Design of a resonant converter for a permanent magnet synchronous machine

by

Jean-François BISSON

THESIS PRESENTED TO ÉCOLE DE TECHNOLOGIE SUPÉRIEURE
IN PARTIAL FULFILLMENT FOR A MASTER'S DEGREE
WITH THESIS IN ELECTRICAL ENGINEERING
M.A.Sc.

MONTREAL, DECEMBER 8, 2021

ÉCOLE DE TECHNOLOGIE SUPÉRIEURE
UNIVERSITÉ DU QUÉBEC

BOARD OF EXAMINERS

THIS THESIS HAS BEEN EVALUATED

BY THE FOLLOWING BOARD OF EXAMINERS

Mr. Kamal Al-Haddad, Thesis Supervisor
Department of Electrical Engineering, École de technologie supérieure

Mr. Louis A. Dessaint, President of the Board of Examiners
Department of Electrical Engineering, École de technologie supérieure

Mr. Ahmed Chériti, Member of the jury
Department of Electrical Engineering and Computer Engineering, Université du Québec à Trois-Rivières

THIS THESIS WAS PRESENTED AND DEFENDED

IN THE PRESENCE OF A BOARD OF EXAMINERS AND PUBLIC

DECEMBER 8, 2021

AT ÉCOLE DE TECHNOLOGIE SUPÉRIEURE

FOREWORD

Global warming is the most challenging problem and potentially the most disastrous threat that our civilization faces nowadays. It has been many decades since this issue is known to mankind, however, efforts to eradicate the global warming threat have been marginal until now. Today, the global warming issue has been acknowledged by a vast majority of political and industry leaders around the world. Regulations like the Carbon Exchange program, greenhouse gases emissions restrictions and international agreements like the Paris Agreement are materialization of the will to move towards clean energies and reduce our fossil fuel consumption. Industries like energy providers and automotive manufacturers are in most cases putting gigantic efforts to replace the fossil fuel based technologies with renewable power sources and electric technologies.

Despites all the efforts put in place nowadays, the aviation industry still does not have the technologies available to go all electric. Effectively, the electric energy storage and the power densities of the available electrodynamic systems are two major blockers in developing a full electric aircraft that could fulfill the needs of the commercial aviation on a large scale.

A lot of research is being done on the batteries to increase their energy density and power density. Nowadays Lithium-Ion batteries have a good energy density, but are still far from fulfilling the needs of a commercial airplane. Fortunately, research continues and new technologies with better energy density and power density continuously emerge. Aside the batteries, the electrodynamic systems performance also need to be improved to fulfill the power density requirements of commercial aviation. Turbine based jet engines have great power densities thanks to their fast rotational speeds. However, electrical machines typically need to reduce their output torque to reach high speeds, which is no use for aeronautical applications.

This research project was initiated with the idea that using electrical resonance to power a permanent magnet synchronous machine could improve its performances, efficiency and

power density, which could ultimately help reaching aviation ready electric propulsion technologies.

ACKNOWLEDGMENT

I would like to sincerely thank, from the bottom of my heart, the following persons for their contribution and support throughout this research project. Without them, it would have been impossible to bring this research project to an end.

Professor Kamal Al-Haddad, research director for this project. Professor Al-Haddad had believed in this research project from the beginning and his support, availability, help for reaching resourceful people within the university network, support with administrative aspects of the master's thesis and intellectual property, have been or great help.

Firas Al-Jilani, David Godin-Lebreux and Renaldo Myrtil for their precious contribution in the detailed implementation of the power electronics aspect of the RPP. Their excellent work during their End of Scholarship Project (PFE) allowed to implement the power electronics circuit of the RPP, and will allow to build a real hardware prototype.

Francis Binette, Gabriel Huard-Desjardins and Sébastien Lavoie for their precious contribution in the detailed implementation of the control electronics aspect of the RPP. Their excellent work during their End of Scholarship Project (PFE) allowed to find solutions for the high frequency and complex control algorithm execution, and also provided detailed interfaces to and from the selected FPGA, as well as detailed design of the conditioning circuits. Their work will make possible to build a real hardware prototype.

My stepmother Irène Fibich and my stepfather Jacques Lauzon, for their generous time spent taking care of my two lovely children, therefore freeing up time for me to work on this research project. This contribution has been significant and without their help, it would not have been possible to complete this research project.

My Parents Diane Parent and Pierre Bisson, as well as my sister Véronique Bisson, for their continuous support throughout this research project.

Finally, I would like to thank my wife, Brigitte Lauzon-Fibich, for all her sacrifices, comprehension, support and for taking care of our two wonderful children while I was working on this research project. She always believed in the success of this project and was always on my side along the way. I love you and thank you for everything.

Conception d'un convertisseur résonant destiné à une machine synchrone à aimants permanents

Jean-François BISSON

RÉSUMÉ

Ce projet de recherche a débuté avec l'hypothèse que le comportement résonant d'un circuit RLC pourrait améliorer le fonctionnement d'une machine synchrone à aimant permanent. L'idée de ce projet de recherche est de connecter un condensateur en série à chaque phase du moteur pendant le fonctionnement à grande vitesse, transformant les circuits électriques de phase en circuits RLC. Le condensateur serait dimensionné spécialement pour que la fréquence naturelle du circuit RLC résultant corresponde à la fréquence électrique du moteur à la vitesse de fonctionnement souhaitée. En raison de la force contre-électromotrice du moteur, il a été constaté que les condensateurs doivent être préchargés afin de fournir l'énergie électrique requise au moteur.

Ce mémoire présente en premier lieu les propriétés de la résonance électrique dont il pourrait être intéressant de bénéficier et présente un concept haut niveau de convertisseur qui pourrait permettre de tirer parti des propriétés de la résonance électrique lors du fonctionnement d'un Moteur Synchrone à Aimant Permanent (PMSM). Ensuite, ce mémoire documente l'élaboration et la conception détaillée du convertisseur. Les trois principaux aspects couverts dans la conception détaillée sont : le circuit d'électronique de puissance du convertisseur résonant, l'électronique de commande du convertisseur résonant et l'algorithme de commande du convertisseur résonant. En troisième lieu, le modèle de simulation est présenté, ainsi que les résultats de simulation démontrant les capacités fonctionnelles du convertisseur résonant. Enfin, les résultats de la simulation sont analysés en détail et les conclusions sur les avantages et les inconvénients du convertisseur résonant proposé sont énumérées.

La simulation du concept de convertisseur résonant, nommé « Resonant Power Processor » (RPP), montre que l'algorithme de contrôle et le circuit électronique du RPP font fonctionner avec succès une machine synchrone à aimant permanent à grande vitesse et à couple élevé simultanément, avec une faible distorsion harmonique des courants de phase et de faibles fluctuations de couple moteur. Profitant du comportement dynamique des circuits RLC des phases du moteur et du circuit de recharge, le RPP permet d'atteindre 263% de la puissance atteignable avec la même tension de batterie de 320V et génère une tension Ligne-Ligne de 485.7Vrms avec une batterie tension de 320V. Le système fait fonctionner avec succès la machine synchrone à aimant permanent à 5 400 tr/min et 14 N.m de couple de sortie.

Les performances du système proposé ont été comparées à un système de base qui se compose d'étages de conversion DC-DC élévateurs de tension et d'un onduleur à 3 niveaux. L'analyse comparative montre que la distorsion harmonique du courant de phase et les ondulations de

couple sont améliorés avec le RPP, mais l'efficacité et les densités de puissance du prototype proposé ne montrent pas d'améliorations en termes d'efficacité et de densité de puissance du système global. Cependant, il est à noter que le prototype virtuel développé dans ce mémoire de maîtrise se veut une preuve de concept et qu'aucune amélioration de l'efficacité et de la densité de puissance n'a encore été apportée. Cela étant dit, des options existent pour amener l'efficacité du système et la densité de puissance en avance sur l'art antérieur.

En conclusion, le RPP proposé et son système sont une technologie prometteuse, en particulier pour le fonctionnement à haute vitesse et à haute densité de puissance d'un PMSM.

Mots-clés : aviation, propulsion, électrique, résonance, convertisseur

Design of a Resonant Converter for a Permanent Magnet Synchronous Machine

Jean-François BISSON

ABSTRACT

This research project initially started with the hypothesis that the resonant behavior of a RLC circuit could improve the operation of a Permanent Magnet Synchronous Machine. The idea of this research project is to connect a capacitor in series to each motor phase during high-speed operation, turning the phase electrical circuits into a RLC circuits. The capacitor would be sized specially for the natural frequency of the resulting RLC circuit to match the electrical frequency of the motor at the desired operation speed. Because of the motor Back-EMF, it was found that the capacitors need to be pre-charged in order to provide the required electrical energy to the motor.

This thesis presents in the first place the properties of the electrical resonance that could be valuable to benefit from and presents a high-level concept of converter that could allow to take advantage of the properties of the electrical resonance during operation of a Permanent Magnet Synchronous Motor (PMSM). Then, this thesis documents the elaboration and detailed design of the converter. The three main aspects covered in the detailed design are: the power electronics circuit of the resonant converter, the control electronics and the control algorithm. In the third place, the simulation model is presented, as well as the simulation results demonstrating the functional capabilities of the resonant converter. Finally, the simulation results are analyzed in details and conclusions about the advantages and disadvantages of the proposed resonant converter are enumerated.

The simulation of the concept of resonant converter, named Resonant Power Processor (RPP), shows that the control algorithm and electronic circuit of the RPP successfully operate a PMSM at high speed and high torque simultaneously, with low THD phase current and low motor torque fluctuations. Taking advantage of the dynamic behavior of the RLC circuits of the motor phases and the recharge cycle, the RPP allows to reach 263% of the power achievable with the same battery voltage of 320V and generates a Line-Line voltage of 485.7Vrms with a battery voltage of 320V. The system successfully operates the PMSM at 5400 rpm and 14 N.m of output torque.

The performances of the proposed system have been compared to a baseline system which consists of boost DC-DC conversion stages and a 3-Level inverter. The comparative analysis shows that the phase current THD and torque ripples are improved with the RPP, but the efficiency and power densities of the proposed prototype do not show improvements in terms of efficiency and power density of the global system. However, it is to be noted that the virtual prototype developed in this master's thesis intents to be a proof of concept and that no

efficiency and power density improvements have been done yet. This being said, options exist to bring the system efficiency and power density ahead of the prior art.

In conclusion, the proposed RPP and its system is a promising technology, especially for high speed and high-power density operation of a PMSM.

Keywords : aviation, propulsion, electric, resonance, converter

TABLE OF CONTENTS

Page

LIST OF TABLES

Page

LIST OF FIGURES

Page

LIST OF ABREVIATIONS

AC	Alternative Current
BOM	Bill of Material
CPS	Capacitor Polarity Selection
CS	Capacitance Setting
DC	Direct Current
EMF	Electromotive Force
EMI	Electromagnetic Interference
EMPRCS	Electric Machine Phase/Recharge Circuit Selection
FFT	Fast Fourier Transform
FOC	Field Oriented Control
FPGA	Field Programmable Gate Array
IGBT	Insulated Gate Bipolar Transistor
IM	Induction Machine
IPMSM	Internal Permanent Magnet Synchronous Machine
LC	Inductive-Capacitive
ME	Maximum Efficiency
MEPA	Maximum Efficiency per Amp
MOSFET	Metal-Oxyde-Silicon Field Effect Transistor
MTPA	Maximum Torque Per Amp
PFE	End of Scholarship Project (Projet de fin d'étude)
PI	Proportional-Integral Controller
PMSM	Permanent Magnet Synchronous Machine

PWM	Pulse Width Modulation
RL	Resistive-Inductive
RLC	Resistive-Inductive-Capacitive
rpm	rotation per minute
RPP	Resonant Power Processor
Si	Silicon
SiC	Silicon Carbide
SPMSM	Surface Permanent Magnet Synchronous Machine
SRM	Switched Reluctance Machine
THD	Total Harmonic Distorsion
T-N curve	Torque as a function of speed curve
VHDL	VHSIC Hardware Description Language
VHSIC	Very High Speed Integrated Circuit
ZCS	Zero Current Switching
ZDAC	Zero d-axis Current
ZVS	Zero Voltage Switching

LIST OF SYMBOLS

Symbol	Description	Unit
α	Resistivity Thermal Coefficient	1/°C
AX	Switch A command for Capacitor module X	-
Br	Remanent Magnetic Field	T
Bs	Saturation Magnetic Field	T
BX	Switch B command for Capacitor module X	-
C	Capacitance	F
CPSX1	Switch CPS_1 command for Capacitor module X	-
CPSX2	Switch CPS_1 command for Capacitor module X	-
CX	Switch C command for Capacitor module X	-
D	Duty Cycle	%
Ea	Back-EMF of phase A	V
Eb	Back-EMF of phase B	V
$E_{BDSW,Cond}$	Conduction energy loss in a bi-directional switch	J
Ec	Back-EMF of phase C	V
EC	Energy in a capacitor	J
E_{cap}	Capacitor Conduction Loss (1 simulation step)	J
E_{diode}	Diode Conduction Loss (1 simulation step)	J
E_{ind}	Inductance Conduction Loss (1 simulation step)	J
E_L	Energy in an inductance	J
$E_{MOSFET,FWD}$	Forward conduction energy loss in a MOSFET	J
$E_{MOSFET,REV}$	Reverse conduction energy loss in a MOSFET	J
$E_{MOSFET.OFF}$	Turn-on Energy loss in a MOSFET	J
$E_{MOSFET.ON}$	Turn-on Energy loss in a MOSFET	J
E_{motor}	Motor Conduction Loss (1 simulation step)	J
$E_{OFF,I}$	IGBT turn-off energy loss	J
$E_{ON,I}$	IGBT turn-on energy loss	J
Ex	Back-EMF of phase X	V
f	Frequency	Hz
fs	Switching Frequency	Hz
Hc	Coercitive Magnetic Induction	A/m
Hs	Saturation Magnetic Induction	A/m
HX	Switch H command for Capacitor module X	-
I	Current	A
I1	Capacitor 1 Current	A
I2	Capacitor 2 Current	A
I3	Capacitor 3 Current	A
I4	Capacitor 4 Current	A

XXX

Symbol	Description	Unit
Ia	Phase A Current	A
Ib	Phase B Current	A
Ic	Phase C Current	A
IC	Collector Current (IGBT)	A
Id	d-axis Current	A
ID	Current in a diode	A
I_d*, Id_req	d-axis current command	A
I_{DS}	Drain-Source current (MOSFET)	A
IF	Forward Direction Current in a diode	A
Iq	q-axis Current	A
I_q*, Iq_req	q-axis current command	A
Ir	Recharge Circuit Current	A
I_R	Reverse Direction Current in a diode	A
φ_a	Flux linkage of phase a	Wb
φ_{ar}	Rotor flux linkage of phase a	Wb
φ_b	Flux linkage of phase b	Wb
φ_{br}	Rotor flux linkage of phase b	Wb
φ_c	Flux linkage of phase c	Wb
φ_{cr}	Rotor flux linkage of phase c	Wb
φ_d	d-axis Flux linkage	Wb
φ_q	q-axis Flux linkage	Wb
φ_r	Rotor flux linkage	Wb
$\varphi_{r,peak}$	Peak rotor flux linkage	Wb
K_{BEMF}, Kbemf	Back-EMF Constant	V.sec/rad
l	Length	m
L	Inductance	H
La	Phase A Inductance	H
Lb	Phase B Inductance	H
Lc	Phase C Inductance	H
Ld	d-axis Inductance	H
Lq	q-axis Inductance	H
Lr	Recharge Inductance	H
Lx	Phase X Inductance	H
N	Number of wire turns	-
P_{cond}	Conduction Losses in a semiconductor	W
P_{Cu}	Copper losses	W
P_e	Eddy Losses	W
P_{F_diode}	Forward Current losses in a diode	W

Symbol	Description	Unit
P_h	Hysteresis Losses	W
P_i	Iron Losses	W
P_p	Number of pole pairs	-
P_{R_diode}	Reverse Current losses in a diode	W
P_{sw}	Switching Losses in a semiconductor	W
q	charge	C
θ_e, theta_e	Electrical angular position	rad
θ_{motor}, theta_motor	Rotor angular position	rad
ρ	Resistivity Factor	Ω.m
$\mathscr{R}$	Magnetic Reluctance	1/H
R	Resistance	Ω
R_ON	R_ON for the MOSFET of the Recharge Circuit	-
ρ_0	Base Resistivity Factor	Ω.m
R_{CE0}	Collector to Emittor Resistance	Ω
$R_{DS(ON)}$	Conduction Resistance in a MOSFET	Ω
R_{EC0}	Emittor to Collector Resistance	Ω
R_s	Phase resistance	Ω
RX	Switch R command for Capacitor module X	-
S	Surface Area	m^2
SX	Inverter MOSFET X command	-
T	Simulation Sample Time	second
t	time (continuous)	second
T°	Temperature	°C
Tdq*	d-axis Torque command	N.m
Tq	Torque	N.m
Tq*, Tq_req	Torque command	N.m
Tq_a	Torque generated by phase A	N.m
Tq_b	Torque generated by phase B	N.m
Tq_c	Torque generated by phase C	N.m
Tqq*	q-axis Torque command	N.m
V	Voltage	V
Va*, Va_req	Phase A voltage command from FOC	V
Vab	Line Voltage a to b	V
Vainv, VinvA_req	Inverter phase A output voltage command	V
Van	Phase Voltage a to n	V
Vb*, Vb_req	Phase B voltage command from FOC	V
Vbc	Line Voltage b to c	V
Vbinv, VinvB_req	Inverter phase B output voltage command	V
Vbn	Phase Voltage b to n	V

Symbol	Description	Unit
V_C	Capacitor Voltage	V
Vc*, Vc_req	Phase C voltage command from FOC	V
Vc_req	Capacitor Voltage command	V
Vc1	Capacitor 1 voltage	V
Vc2	Capacitor 2 voltage	V
Vc3	Capacitor 3 voltage	V
Vc4	Capacitor 4 voltage	V
Vca	Line Voltage c to a	V
VCa	Voltage of the capacitor connected to phase A	V
VCb	Voltage of the capacitor connected to phase B	V
VCc	Voltage of the capacitor connected to phase C	V
V_{CE}	Collector to Emittor Voltage	V
V_{CE0}	Initial Collector to Emittor Voltage Drop	V
Vcinv, VinvC_req	Inverter phase C output voltage command	V
Vcn	Phase Voltage c to n	V
VcX	Capacitor X voltage	V
vd	d-axis Voltage	V
Vd*, Vd_req	d-axis voltage command	V
Vdc	DC Voltage	V
V_{DS}	Drain-Source voltage (MOSFET)	V
V_{EC}	Emittor to Collector Voltage	V
V_{EC0}	Initial Emittor to Collector Voltage Drop	V
V_F	Forward direction voltage in a diode	V
Vin	Input Voltage	V
V_L	Inductance Voltage	V
Vq	q-axis Voltage	V
Vq*, Vq_req	q-axis voltage command	V
V_R	Reverse direction voltage in a diode	V
ω	Angular Speed	rad/sec
ω_e, w_e	Electrical angular speed	rad/sec
ω_{motor}, w_motor	Rotor angular speed	rad/sec
ω_n	Natural Frequency	rad/sec
X	Arbitrary Identificator	-
Ψ_m	Magnetic Flux	Wb
Z^{-1}, 1/Z	Unit Delay (discrete domain)	-
Z_{RLC}	RLC Circuit Impedance	Ω

INTRODUCTION

Global warming nowadays pushes the political and industry leaders to adopt renewable energy sources and electrified propulsion systems instead of fossil fuel based technologies. The energy providers and automotive manufacturers around the world are accelerating their investments in the development of green technologies. However, one of the most fossil fuel consuming industry, the commercial aviation, does not have the technology required to completely electrify their products yet. Two main blockers exist that currently prevents the electrification of the aviation at a large scale. First, the energy density of the batteries is currently insufficient to carry the required energy for long-haul flights. Weight is an important parameter in aviation and unfortunately nowadays the superior efficiency of electrodynamic systems compared to the jet fuel turbine engines is not sufficient to palliate for the lack of energy density of the Lithium-Ion batteries. Also, unlike jet fuel which is being burned along the way, the battery weight remains airborne from take-off to landing, which adds to the complexity of the weight problem. Fortunately, research is ongoing on the batteries side and new technologies emerge on a yearly basis. The second blocker is the power density of the electrodynamic propulsion systems. Modern aircraft propulsion systems get their high power densities from their fast rotational speeds. From previous publications, it has been found that the best efficiency and best power density belongs to the permanent magnet synchronous machine (PMSM). Operating a PMSM at high speed has many challenges. First, for a fixed battery voltage, the speed range in which the maximum torque is available is limited by the motor's back-EMF, which is directly proportional to speed and opposes to the phase voltage. Once the back-EMF exceeds the input voltage, maximum torque is not achievable anymore and speed increase is only possible by reducing the torque using field weakening control. Due to the nature of the aeronautical torque loads, which increase with rotational speed, field weakening control is not a suitable solution.

The research project presented in this master's thesis started from the hypothesis that electrical resonance could help improving the performances of a PMSM based electrodynamic system. The dynamic behavior of the electrical resonance has properties that could be interesting to

benefit from in order to improve the performances of a PMSM drive. First, the electrical resonance has an oscillatory behavior that is compatible with Alternative Current (AC) drives. Effectively, battery powered automotive must convert the DC current from the battery to AC current to the motor. This is typically done by an inverter alone, but resonance could assist the inverter in shaping the phase current in a sinusoidal waveform. Second, the electrical resonance phenomenon can store energy under the form of voltage in a capacitor or under the form of current in an inductance. The stored energy in the form of capacitor voltage may be added to the motor phase voltage to increase its magnitude, and therefore allow for a wider speed range at maximum torque operation. Finally, the unitary power factor of a RLC circuit at its resonance frequency means that potentially no reactive power is consumed, which may improve efficiency.

In order to verify the hypothesis that electrical resonance may improve the performances of a PMSM drive, a novel resonant converter has been developed in this research project. First, a preliminary concept of operation of the converter has been developed after analysis of the properties of the electrical resonance. This preliminary concept consists of a converter that matches a pre-charged capacitor to a motor phase in order to turn the phase circuit into a RLC circuit. The capacitors are sized specifically for the natural frequency of the resulting RLC circuit to match the electrical speed of the motor during operation at the desired speed. In order to permanently have a recharged capacitor linked to all motor phases, a dedicated recharge circuit needs to be implemented to recharge the discharged capacitors before they are connected to a motor phase. The preliminary concept has evolved into a detailed concept of converter. The detailed design of the converter consists of the power electronics, control electronics and control algorithm. The detailed design has been successfully implemented using off the shelf components, and the control algorithm has been synthetized in VHDL code for implementation in a FPGA. The system has then been simulated using Matlab/Simulink and the simulation results are shown in this master's thesis. The results have been deeply analyzed and the results analysis is presented as part of this work.

CHAPTER 1

REVIEW OF LITERACY

1.1 Electric machines in aviation

Aircrafts powered by electric motors are not common nowadays. Actually, manned electric aviation is currently at its first steps. We could recently witness the world tour of the solar powered electric aircraft Solar Impulse (2015-2016) and the crossing of the English Channel by the Airbus E-fan electric aircraft (2015). However, the performances of both aircrafts are still far from the performances of the turbofan powered commercial airliners.

In the past years, the use of electric powered drones has been rapidly increasing and the trend is that it will be increasing in the future. Electric powered drones are electrical aircrafts, however manned drones have not been seen on a large scale yet.

The main obstacle of large scale commercial electric aviation is the energy storage. Nowadays, the specific energy density and volumetric energy density of the lithium-ion battery is about 875 KJ/Kg and 2.43 MJ/L respectively ("Lithium-ion battery," 2021) and the specific energy density and volumetric energy density of jet fuel A-1 is about 43200 KJ/Kg and 35 MJ/L respectively ("Jet fuel," 2021). However, considering that the efficiency of an electric motor drive system is higher than the efficiency of aviation turbomachines, less energy must be airborne. It is therefore mandatory that electric motor drive systems used in aviation both are efficient and have high power densities, because those factors have a direct impact on the airborne energy required for the trip.

Aeronautical propellers and fans must operate at high speeds to generate thrust, and the torque load generated by a propeller or fan increases with speed. To ensure an optimal power density, the electrical machine must operate at its highest torque and highest speed simultaneously. For this reason, flux weakening control is not a suitable option for increasing the rotational speed of a propeller or fan.

Many electric machine types are available. As examples, we have the induction machine (IM), the permanent magnet synchronous machines (PMSM), DC machines (DC) and switch reluctance machines (SRM). All of them have strenghts and flaws. The paper of Finken, Felden and Hameyer (Finken, Felden & Hameyer, 2008) compares the performances of those 4 types of electrical machines. It concludes that the permanent magnet synchronous machine (PMSM) has the best efficiency and best power density amongst the other types of electrical machines. Figure 1.1 shows a comparative table of the characteristics of different electrical machines. Figure 1.2 shows the peak efficiency areas of the different electrical machines on the T-N curve.

	DC	IM	PMSM	SRM		
power density	⊖⊖	⊙	⊕⊕	⊙	⊕⊕	very good
efficiency	⊖	⊕	⊕⊕	⊕	⊕	good
costs	⊕	⊕⊕	⊖	⊕	⊙	neutral
reliability	⊖	⊕⊕	⊙	⊕	⊖	bad
technical maturity	⊕	⊕	⊙	⊙	⊖⊖	very bad
controlability, costs	⊕⊕	⊙	⊕	⊖		

Figure 1.1 Comparative table of the characteristics of electric machines
Taken from Finken et al. (2008)

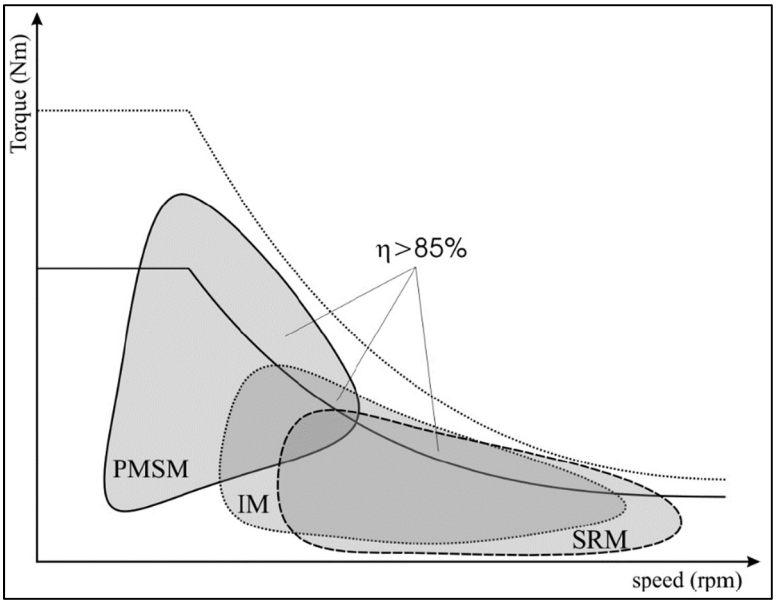

Figure 1.2 Peak efficiency areas of the electrical machines
Taken from Finken et al. (2008)

Because of their superior efficiency and power density, the PMSM appears to be the best candidate for aeronautical applications. Additionally, the peak efficiency area of the PMSM is at the highest torque amongst the other types of electric machines, which may ultimately benefit the power density criteria. The electric powered drones are typically equipped with brushless DC motors, which are PMSMs.

It is to be noted that the reliability of the PMSM is rated neutral (Finken et al., 2008). Safety and reliability are the most important factors to consider in the aviation industry. Successful commercial aviation can only exist with nothing but the best safety and reliability standards. The present thesis does not deeply cover the safety and reliability aspects of the system. However, as the safety and reliability of a PMSM may be improved by design, many other non-functional aspects in the aviation industry ensure that the safety and reliability requirements are met, including quality control, design processes and certification processes. For those reasons, it is reasonably estimated that PMSMs can achieve the levels of safety and reliability required by the civil aviation.

1.2 The Permanent Magnet Synchronous Machine (PMSM)

The permanent magnet synchronous machine (PMSM) is typically powered by three-phased AC current. Its design consists of a stator made of electrical wire coils and magnetically permeable material, and a rotor including permanent magnets. A rotating magnetic field is generated by the AC current circulating in the stator, which attracts the permanent magnets installed on the rotor. The interaction between the stator magnetic field and the permanent magnets magnetic field generates the torque at the shaft. As the magnetic field of the permanent magnets is fixed, the stator currents determine the torque. The frequency of the AC current circulating in the rotor determines the rotor speed, as the stator and rotor magnetic fields are synchronized. The machine is therefore called synchronous. Figure 1.3 shows a cut view of a permanent magnet synchronous machine.

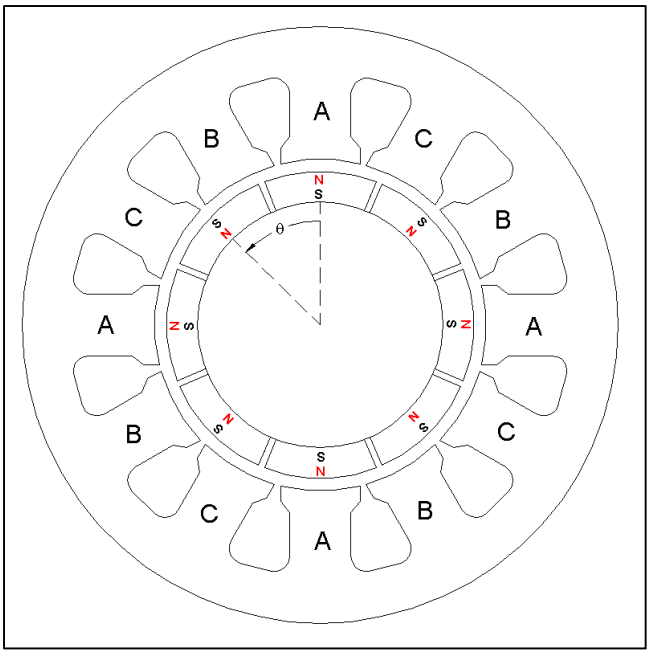

Figure 1.3 Cut view of a 4 pole pairs PMSM

1.2.1 The electrical circuit of the PMSM stator

The electrical circuit of the PMSM stator consists of 3 phases. Each phase has a Back-EMF (E_X), a phase resistance (R_S) and a phase inductance (L_X). When the motor is connected in "Wye" configuration, the phases are connected to a common point called the neutral (n). Figure 1.4 shows a schematic of the PMSM stator electrical circuit connected in "Wye" configuration. One alternative way of connecting the motor phases in in "Delta" configuration. Delta configuration makes the phase voltage equal to the line-to-line voltage but removes the neutral point. The sub sections below explain the features of the phase circuit.

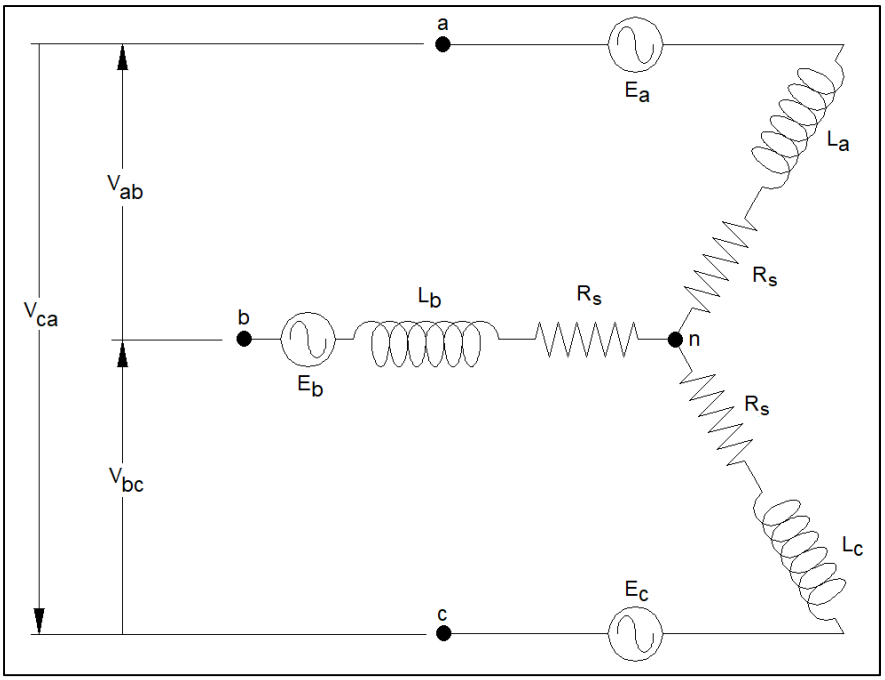

Figure 1.4 Schematic of the PMSM stator electrical circuit

1.2.1.1 The phase resistance (R_S)

The phase resistance is the resistance of the copper wires that form the stator coils. The phase resistance increases with temperature. Resistance is calculated in Equation (1.1) and resistivity factor is calculated in Equation (1.2). Resistance is function of wire section area S, wire length l and resistivity factor ρ. The resistivity factor ρ is function of the resistivity factor at 0°C ρ_0, the temperature coefficient α and the wire temperature $T°$ in °C.

$$R = \frac{\rho \cdot l}{S} \tag{1.1}$$

$$\rho = \rho_0 \cdot (1 + \alpha \cdot T°) \tag{1.2}$$

In order to minimize the copper losses in the machine, it is better to minimize the stator resistance by sizing the wires accordingly and by ensuring proper cooling of the electric machine.

1.2.1.2 The phase inductance (L_X)

The phase inductance is the inductance of the motor phase coil which generate the magnetic fluxes of the stator. The phase inductance may be independent of the rotor position in the case of a non-salient poles machine or may vary with rotor angle in the case of a salient poles machine. The variation of inductance on a salient poles machine is because the reluctance of the magnetic circuit coupled with the stator coils varies as a function of rotor angle. As shown in equation (1.3), the inductance is function of the number of coil turns N squared and the inverse of reluctance $\mathcal{R}$.

$$L = \frac{N^2}{\mathfrak{R}} \tag{1.3}$$

The phase inductance has a fixed component (non-salient inductance) and a component that varies with the rotor angle (salient inductance). The phase inductance matrix [L_{SS}] is calculated in equation (1.4), the non-salient inductance matrix [L_{SS0}] in equation (1.5) and the salient inductance matrix [L_{SS2}] in equation (1.6). L_{S0} is the self inductance, L_{M0} is the mutual inductance, θ is the rotor angle in rad, L_{S2} is the saliency constant and P_P is the number of pole pairs.

$$[L_{SS}] = [L_{SS0}] + [L_{SS2}] \tag{1.4}$$

$$[L_{SS0}] = \begin{bmatrix} L_{S0} & L_{M0} & L_{M0} \\ L_{M0} & L_{S0} & L_{M0} \\ L_{M0} & L_{M0} & L_{S0} \end{bmatrix} \tag{1.5}$$

$$[L_{SS2}] = L_{s2} \cdot \begin{bmatrix} \cos(2P_P\theta_{motor}) & \cos(2P_P\theta_{motor} - \frac{2\pi}{3}) & \cos(2P_P\theta_{motor} + \frac{2\pi}{3}) \\ \cos(2P_P\theta_{motor} - \frac{2\pi}{3}) & \cos(2P_P\theta_{motor} + \frac{2\pi}{3}) & \cos(2P_P\theta_{motor}) \\ \cos(2P_P\theta_{motor} + \frac{2\pi}{3}) & \cos(2P_P\theta_{motor}) & \cos(2P_P\theta_{motor} - \frac{2\pi}{3}) \end{bmatrix} \quad (1.6)$$

From the equations (1.4) to (1.6), and considering a balanced three-phased current, one finds the matrix of the phase inductance L_x in equation (1.7).

$$\begin{bmatrix} L_a \\ L_b \\ L_c \end{bmatrix} = \begin{bmatrix} L_{S0} - L_{M0} - \frac{3}{2}L_{S2}\cos(2P_P\theta_{motor}) \\ L_{S0} - L_{M0} - \frac{3}{2}L_{S2}\cos(2P_P\theta_{motor} - \frac{2\pi}{3}) \\ L_{S0} - L_{M0} - \frac{3}{2}L_{S2}\cos(2P_P\theta_{motor} + \frac{2\pi}{3}) \end{bmatrix} \quad (1.7)$$

1.2.1.3 The Back-EMF (E_X)

The Back-EMF is counter electromotive force induced in the stator coils because of the rotation of the rotor magnetic field. The rotor magnetic field, from the point of view of the stator coils, is function of the rotor angle θ. As per Faraday's law (1.8), the counter electromotive force induced in a coil is function of the number of coil turns N and the gradient of the magnetic flux Ψ_m through the coil. For the purpose of simplifying the equations, the number of stator coil turns is embedded in the rotor flux linkage φ_r as shown in Equation (1.9). One may interpret the rotor flux linkage φ_r as being the rotor flux Ψ_m if the stator coil had only 1 turn. Assuming a sinusoidal Back-EMF profile, the matrix of the three-phased rotor flux linkage $[\varphi_r]$ is calculated at equation (1.10) where $\varphi_{r,peak}$ is the amplitude of the alternating rotor flux linkage φ_r. The matrix of the three-phased Back-EMF is calculated at equation (1.11), where ω_{motor} is the rotor angular speed in rad/sec. The Back-EMF constant K_{BEMF} includes the constants that

define the amplitude of the Back-EMF as shown in equation (1.12). One can observe that the Back-EMF amplitude is directly proportional to the motor speed.

$$E = -N \cdot \frac{d\Psi_m}{dt} \tag{1.8}$$

$$\varphi_r = N \cdot \Psi_m \tag{1.9}$$

$$\begin{bmatrix} \varphi_{ar} \\ \varphi_{br} \\ \varphi_{cr} \end{bmatrix} = \varphi_{r_{peak}} \begin{bmatrix} \cos(P_P\theta_{motor}) \\ \cos(P_P\theta_{motor} - \frac{2\pi}{3}) \\ \cos(P_P\theta_{motor} + \frac{2\pi}{3}) \end{bmatrix} \tag{1.10}$$

$$\begin{bmatrix} E_a \\ E_b \\ E_c \end{bmatrix} = -\frac{d}{dt}\begin{bmatrix} \varphi_{ar} \\ \varphi_{br} \\ \varphi_{cr} \end{bmatrix} = \omega_{motor} \cdot K_{BEMF} \begin{bmatrix} \sin(P_P\theta_{motor}) \\ \sin(P_P\theta_{motor} - \frac{2\pi}{3}) \\ \sin(P_P\theta_{motor} + \frac{2\pi}{3}) \end{bmatrix} \tag{1.11}$$

$$K_{BEMF} = P_p \cdot \varphi_{r_{peak}} \tag{1.12}$$

1.2.1.4 The Electromagnetic Torque

The electromagnetic power developed by the motor is the product of the Back-EMF and the phase current. Neglecting the mechanical losses, one finds in equation (1.13) that electromagnetic power equals the product of torque and speed. The combined torque generated by each phase of the motor makes the electromagnetic torque *Tq* as shown in equation (1.14).

$$EI = Tq \cdot \omega \tag{1.13}$$

$$Tq = K_{BEMF} \cdot \left(I_a \cdot \sin\left(P_p \theta_{motor}\right) + I_b \cdot \sin\left(P_p \theta_{motor} - \frac{2\pi}{3}\right) + I_c \cdot \sin\left(P_p \theta_{motor} + 2\pi/3\right) \right) \quad (1.14)$$

1.2.2 Mathematical model of the PMSM

The matrix of the three-phased stator phase voltage [v_{xn}] can be found at equation (1.15) and the matrix of the three-phased magnetic flux linkage [φ_X] can be found at equation (1.16). The magnetic flux linkage is the sum of the stator magnetic flux generated by the stator currents and the rotor flux linkage which can be found at equation (1.10).

$$\begin{bmatrix} v_{an} \\ v_{bn} \\ v_{cn} \end{bmatrix} = R_s \cdot \begin{bmatrix} I_a \\ I_b \\ I_c \end{bmatrix} + [L_{SS}] \times \frac{d}{dt} \begin{bmatrix} I_a \\ I_b \\ I_c \end{bmatrix} + \begin{bmatrix} E_a \\ E_b \\ E_c \end{bmatrix} \quad (1.15)$$

$$\begin{bmatrix} \varphi_a \\ \varphi_b \\ \varphi_c \end{bmatrix} = [L_{SS}] \times \begin{bmatrix} I_a \\ I_b \\ I_c \end{bmatrix} + \begin{bmatrix} \varphi_{ar} \\ \varphi_{br} \\ \varphi_{cr} \end{bmatrix} \quad (1.16)$$

The matrix of the three-phase stator voltage become in its most familiar expression at equation (1.17).

$$\begin{bmatrix} v_{an} \\ v_{bn} \\ v_{cn} \end{bmatrix} = R_s \cdot \begin{bmatrix} I_a \\ I_b \\ I_c \end{bmatrix} + \frac{d}{dt} \begin{bmatrix} \varphi_a \\ \varphi_b \\ \varphi_c \end{bmatrix} \quad (1.17)$$

1.2.2.1 Mathematical model of the PMSM in the d-q axis

In order to use the field-oriented control on the PMSM, the mathematical model of the PMSM must be transformed into the direct and quadrature axis model. This is done using the Park transform. The Park transform is a combination of the Clarke or Concordia transform to the αβ axis and a rotation operation. Equation (1.18) shows the Clarke transform and the equation (1.19) shows the Concordia transform. One may use Clarke transform to maintain the voltages and current amplitudes, or the Concordia transform to maintain the torque and power values.

From this point, the Clarke transform will be used to the αβ axis, unless otherwise specified. The rotation operation is shown at equation (1.20). The d-q axis model puts the direct axis is in line with a rotor permanent magnet, and the quadrature axis is between 2 rotor permanent magnets. The *x* parameters may be voltage, current or magnetic flux linkage and θ is the rotor angular position in rad.

$$\begin{bmatrix} x_\alpha \\ x_\beta \end{bmatrix} = \frac{2}{3}\begin{bmatrix} 1 & -1/2 & -1/2 \\ 0 & \frac{\sqrt{3}}{2} & -\frac{\sqrt{3}}{2} \end{bmatrix} \cdot \begin{bmatrix} x_a \\ x_b \\ x_c \end{bmatrix} \tag{1.18}$$

$$\begin{bmatrix} x_\alpha \\ x_\beta \end{bmatrix} = \sqrt{\frac{2}{3}} \cdot \begin{bmatrix} 1 & -1/2 & -1/2 \\ 0 & \frac{\sqrt{3}}{2} & -\frac{\sqrt{3}}{2} \end{bmatrix} \cdot \begin{bmatrix} x_a \\ x_b \\ x_c \end{bmatrix} \tag{1.19}$$

$$\begin{bmatrix} x_d \\ x_q \end{bmatrix} = \begin{bmatrix} \cos(P_p\theta_{motor}) & sin(P_p\theta_{motor}) \\ -sin(P_p\theta_{motor}) & cos(P_p\theta_{motor}) \end{bmatrix} \cdot \begin{bmatrix} x_\alpha \\ x_\beta \end{bmatrix} \tag{1.20}$$

One can transition between the three-phased model and the d-q axis model using the transforms and the inverse of the transforms.

$\begin{bmatrix} x_a \\ x_b \\ x_c \end{bmatrix}$ ⇒Clarke or Concordia⇒ $\begin{bmatrix} x_\alpha \\ x_\beta \end{bmatrix}$ ⇒Rotation⇒ $\begin{bmatrix} x_d \\ x_q \end{bmatrix}$

$\begin{bmatrix} x_d \\ x_q \end{bmatrix}$ ⇒Inverse rotation⇒ $\begin{bmatrix} x_\alpha \\ x_\beta \end{bmatrix}$ ⇒Inverse Clarke or Inverse Concordia ⇒ $\begin{bmatrix} x_a \\ x_b \\ x_c \end{bmatrix}$

The equations (1.21) and (1.22) calculate the stator inductances in the d-q axis model and the equations (1.23) and (1.24) calculate the magnetic flux linkage in the d-q axis model. It is to be noted in equations (1.21) and (1.22) that the q-axis inductance is greater than the d-axis inductance. If the d-axis inductance is greater than the q-axis inductance, equations (1.21) and (1.22) are permuted.

$$L_d = L_{S0} - L_{M0} - \frac{3}{2}L_{S2} \tag{1.21}$$

$$L_q = L_{S0} - L_{M0} + \frac{3}{2}L_{S2} \tag{1.22}$$

$$\varphi_d = L_d I_d + \varphi_{r_{peak}} \tag{1.23}$$

$$\varphi_q = L_q I_q \tag{1.24}$$

The matrix of the three-phased stator voltage at equation (1.15) becomes the matrix of the stator voltage in the d-q axis model at equation (1.25). The equations of the stator voltages in the d-q axis model may also be represented as per equations (1.26) and (1.27).

$$\begin{bmatrix} v_d \\ v_q \end{bmatrix} = R_s \begin{bmatrix} I_d \\ I_q \end{bmatrix} + \frac{d}{dt}\begin{bmatrix} \varphi_d \\ \varphi_q \end{bmatrix} \tag{1.25}$$

$$v_d = R_s I_d - P_P \omega_{motor} \varphi_q + \frac{d\varphi_d}{dt} \tag{1.26}$$

$$v_q = R_s I_q + P_P \omega_{motor} \varphi_d + \frac{d\varphi_q}{dt} \tag{1.27}$$

It is to be noted that in steady state operation, the gradients of d-axis flux linkage and q-axis flux linkage are null. Therefore, in steady state operation, the equations of the stator voltages in the d-q axis model may be represented as per equations (1.28) and (1.29).

$$v_d = R_s I_d - P_P \omega_{motor} L_q I_q \tag{1.28}$$

$$v_q = R_s I_q + P_P \omega_{motor} L_d I_d + P_P \omega_{motor} \varphi_{r_{peak}} \tag{1.29}$$

1.2.2.2 Electromagnetic torque in the d-q axis

The electromagnetic torque Tq of the PMSM in the d-q axis model can be calculated using the equations (1.30) or (1.31) as they are equivalent.

$$Tq = \frac{3}{2} P_p \left(\varphi_d I_q - \varphi_q I_d \right) \tag{1.30}$$

$$Tq = \frac{3}{2} P_p \left(\left(L_d - L_q \right) I_d + \varphi_{f_{max}} \right) I_q \tag{1.31}$$

1.2.3 Losses in the PMSM

The PMSM acts as a converter, as it converts the electrical power into mechanical power. In every power conversion, energy is lost and therefore the efficiency of the conversion process cannot reach unity. The PMSM makes no exception to this principle, as the motor input electrical energy exceeds the output mechanical energy. Inversely, when the PMSM is used as a generator, the input mechanical energy exceeds the output electrical energy. The energy losses in a PMSM are due to different phenomenon, either electrical, magnetic or mechanical. In order to be as efficient as possible, the losses must be minimized. The following section reviews the different types of energy losses in a PMSM.

1.2.3.1 Copper Losses

The copper losses are the resistive losses generated by the phase currents in the stator. Those losses are called copper losses because the electrical conductors of the PMSM stator are typically made of copper. The copper losses are function of the electrical resistance and current squared as expressed in equation (1.32). As per equations (1.1) and (1.2), the electrical resistance is function of the section area of the electrical wire, the length of the electrical wire and the temperature of the copper wire. It is to be noted that in a PMSM, the current is of sinusoidal shape and therefore the current is not constant over time. For this reason, the root mean square (rms) value of the current will be used as per equation (1.33). If equation (1.33)

represents the losses of a single phase, then it must be multiplied by 3 to get the total copper losses in the PMSM.

$$P_{Cu} = R_s I^2 \tag{1.32}$$

$$P_{Cu} = \frac{R_s I_{peak}^2}{\sqrt{2}} = R_s I_{rms}^2 \tag{1.33}$$

1.2.3.2 Iron losses

There are 2 distinct types of iron losses; the Eddy current losses and the hysteresis losses. The Eddy current losses (Wildi, T., 2003) are the resistive losses due to the induction of current loops in the stator. As seen precedingly at equation (8), a varying magnetic flux will induce a voltage in a closed loop circuit proportional to the gradient of the magnetic flux through the closed loop. As the magnetic field in PMSM is rotating, the magnetic field from the stator point of view is alternating. If the stator material is electrically conductive, the alternating magnetic field in the stator generates alternating current loops which in turn generates Eddy current losses. Eddy losses are dissipated under the form of heat in the stator and the rotor. Eddy current losses may be significantly reduced by building the stator and the rotor with thin layers of sheet metal electrically isolated from each other. This makes a discontinuity in the eddy current loops and therefore reduce the intensity of the eddy currents in the stator. It is to be noted that as the rotor rotates synchronous with the magnetic field, the magnetic field from the point of view of the rotor is steady and therefore the Eddy current losses in the rotor are mainly due to the current harmonics, which generate the alternating magnetic flux in the rotor (Liang, Li, Qu, Zheng, & Song, 2015). Figure 1.5 shows how Eddy currents are generated with relation to magnetic flux variations.

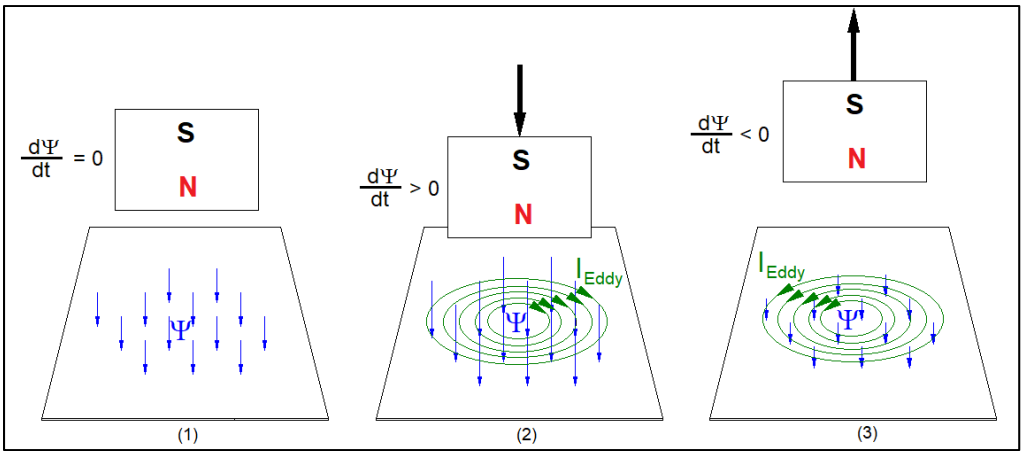

Figure 1.5 Eddy currents in a metal sheet due to varying magnetic flux (1) The permanent magnet is not moving; no Eddy current is generated. (2) The permanent magnet moves towards the metal sheet; the magnetic flux through the metal sheet increases, and clockwise Eddy currents are generated. (3) The permanent magnet moves away from the metal sheet; the magnetic flux through the metal sheet decreases and counter-clockwise Eddy currents are generated

The hysteresis losses are the losses due to the change in direction of the magnetic domains in the magnetically permeable material of the stator. Ferromagnetic materials have a microcrystalline structure in which many magnetic domains exist. When no external magnetic field is present, the magnetic domains cancel each other. When an external magnetic field is applied, the magnetic domains gradually align with the external magnetic field, allowing a greater magnetic induction in the material. When the magnetic field in the material reaches its saturation value H_S, all the magnetic domains are aligned and then we achieve the maximum magnetic induction B_S. After bringing a ferromagnetic material to its maximal induction, if the external magnetic field is removed, the magnetic domains do not all come back to their original orientation and therefore a remanent magnetic field is still present. In order to remove the remanent magnetic field, an external magnetic field of value H_C must be applied in the opposite direction. This cycle is called the magnetization cycle. The dissipated energy during the magnetization cycle is equal to the surface contained in the hysteresis loop. This amount of energy is dissipated in the form of heat at every hysteresis cycle (Baïlon & Dorlot, 2000). Figure 1.6 shows a typical hysteresis loop of a ferromagnetic material.

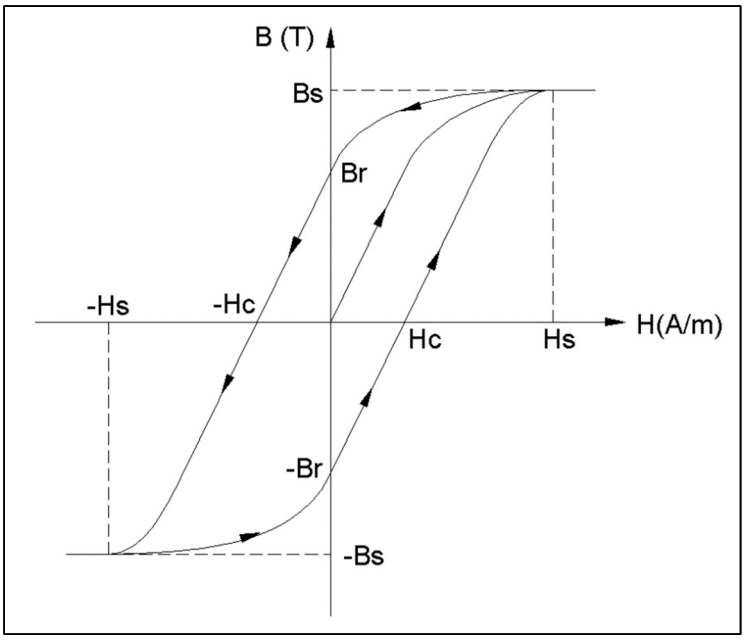

Figure 1.6 Typical hysteresis loop of a ferromagnetic material

The theoretical calculation of the iron losses may be possible for simple magnetic circuit geometries where the magnetic fluxes can be easily predicted. However, for complex geometries and magnetic fluxes distribution, it may be difficult to evaluate. Nowadays, finite element analysis is a powerful tool to simulate the magnetic flux in complex geometries and under varying operating conditions. The paper from L. Ma, M. Sanada, S. Morimoto and Y. Takeda (Ma, Sanada, Morimoto & Takeda, 2003) proposes the equation (1.34) to calculate the iron losses in a finite element.

$$P_i = P_h + P_e = \varepsilon_h (f/100) B_m^{\alpha} + \varepsilon_e (f/100)^2 B_m^2 \qquad (1.34)$$

Where P_i is the total iron loss, P_h is the hysteresis loss, P_e is the Eddy current loss, ε_h is the hysteresis loss coefficient at 100 Hz, ε_e is the Eddy current loss coefficient at 100 Hz and α is a constant function of the hysteresis loop characteristics. B_m is the magnetic field and f is the frequency in Hz. From equation (1.34), it is possible to observe that the iron losses due to the fundamental frequency of the motor are function of the motor speed and motor speed squared.

Also, it is possible to observe that high amplitude and frequency harmonics may generate a significant amount of iron losses.

1.2.3.3 Mechanical losses

The mechanical losses are the losses which are not caused by electromagnetic phenomenon. As examples, we can count among the mechanical losses the friction losses of the bearings, the cooling ventilation, parasitic losses or vibrations.

1.3 Power supply of the PMSM

A PMSM is an alternating current electrical machine. However, in automotive vehicles, the electrical energy storage is typically done using a battery or a fuel cell, and both electrical energy storage technologies provide DC power. Therefore, a device to convert DC power into AC power is required between the battery and the motor in order to properly supply the electrical power to the PMSM. As mentioned earlier in section 1.2.1.3, as the speed of the PMSM increase, the back-EMF increase and more input phase voltage is required to feed current into the machine. To reach high torque at high rotational speeds, it is possible that the DC voltage of the energy storage device needs to be increased. For this reason, one will assume that the prior art DC to AC converter is made of two distinct components: a DC-DC step-up converter and an inverter.

1.3.1 DC-DC Step-Up Converters

The purpose of a DC-DC Step-Up converter is to increase the DC link voltage above the DC voltage of the energy storage device. The paper of K. M. Choo and Al. (Choo, Won, Hong, Lee & Won, 2017) demonstrate that an optimized DC voltage modulation according to the operating condition of the PMSM may reduce the torque ripples of the PMSM, the THD of the phase current and the switching losses in the inverter. Also, (Choo et al., 2017) shows that the dynamic control of the PMSM may be enhanced by modulating the DC-link voltage adequately. Despites the fact that a DC-DC Step-up converter may improve some of the

characteristics of the electrodynamic system, the DC-DC converter generates power losses. As the main objective is to improve the global efficiency of the electrodynamic system, a trade-off may be required between the step-up capability of the converter and the energy storage device voltage. The paper of Estima and Marques Cardoso (Estima & Marques Cardoso, 2012) compares the performances of a PWM inverter supplied by a high voltage DC battery and the performances of a PWM inverter supplied by a low voltage battery and a step-up DC-DC converter. Both configurations are used to power a non-salient poles PMSM. This paper concludes that it is better to operate the DC-link at a voltage close to the battery voltage in order to minimize effect of the DC-DC conversion losses on the total system efficiency. The paper of Yamamoto, Shinohara and Makishima (Yamamoto, Shinohara & Makishima, 2002) makes the same comparison with a salient poles PMSM. It concludes that in the constant torque region where the nominal voltage of the battery is high enough to reach maximum torque, the total system efficiency is lower when using the voltage booster because of the DC-DC conversion losses.

The DC-DC step-up conversion may bring interesting advantages in terms of power density when it is difficult to increase the battery voltage, because of technology or safety reasons. However, it is preferable to minimize the conversion losses by setting the nominal battery voltage to the optimal operating DC link voltage for the PMSM, if the operating condition of the PMSM is known and stable.

1.3.2 DC-DC Step-Up Converter topologies

Many topologies of step-up DC-DC converter exist. Amongst the most popular, one finds the Buck converter, the Boost converter and the Buck-Boost converter. The Buck converters are not interesting when targeting high power operation as they limit the available power. The Buck-Boost converter may be interesting for targeting peak efficiency in a wider range of PMSM speed of operation. However, as per the paper of Joseph, Patel and Pathak (Joseph, Patel & Pathak, 2018), the Boost converter has a superior efficiency compared to the Buck-Boost converter. Therefore, if the main operating condition of the PMSM is at high speed, it is better to choose a Boost converter if the Battery voltage itself cannot be increased.

1.3.2.1 Basic Boost Converter topology

The Basic Boost converter accumulates energy in the inductance L when the transistor Tdc is energized and liberates the accumulated energy in the load when the Tdc transistor is OFF. The Capacitor C damps the voltage oscillations at the inductance output. The Basic Boost Converter can be found in Figure 1.7 and the theoretical conversion ratio of the Basic Boost converter as a function of duty cycle D can be found at Equation (1.35).

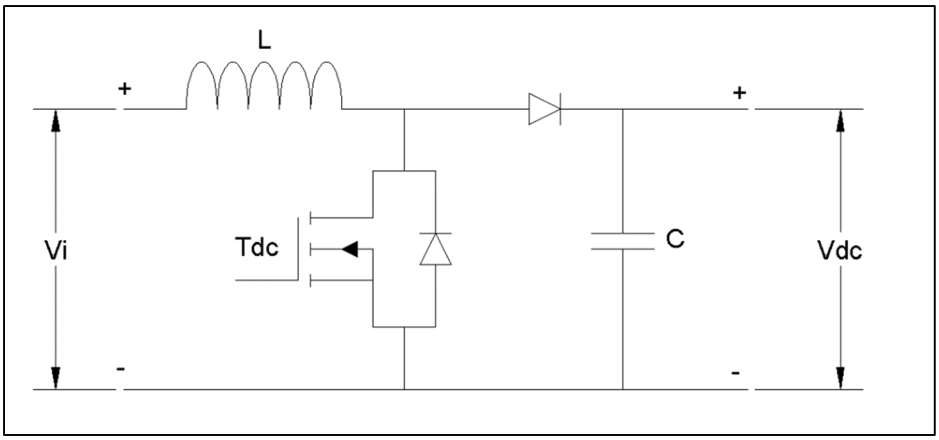

Figure 1.7 Basic Boost converter topology

$$\frac{V_{dc}}{V_i} = \frac{1}{1-D} \tag{1.35}$$

1.3.2.2 Interleaved Boost Converter Topology

The Basic Boost converter can be connected in parallel with other Basic Boost converters to create the Interleaved Boost converter. The paper of A. Thiyagarajan, S. G. Praveen Kumar and A. Nandini (Thiyagarajan, Praveen Kumar & Nandini, 2014) makes the comparison of the performances between a Basic Boost converter and an Interleaved Boost converter. They find that Interleaved Boost configuration reduces the voltage fluctuations at the converter output, increase current output and improve efficiency. However, the Interleaved Boost conversion ratio is the same as the Basic Boost Converter ratio.

1.3.2.3 Tandem Boost Converter Topology

The paper of N. Boujelben, F. Masmoudi, M. Djemel and N. Derbel (Boujelben, Masmoudi, Djemel & Derbel, 2017) makes the comparison of the performances between a Basic Boost converter and a Tandem Boost converter. They find that the Basic Boost converter can be connected in series with other Basic Boost converters in order to increase the conversion ratio and efficiency. However, the Tandem Boost converter cannot increase the output current. The theoretical conversion ratio of the Tandem Boost converter as a function of duty cycle D can be found at equation (1.36) below, where n is the number of Basic Boost converter connected in series.

$$\frac{V_{dc}}{V_i} = \frac{1}{(1 - D_1) \cdot (1 - D_2) \cdot \ldots \cdot (1 - D_n)} \tag{1.36}$$

1.3.2.4 Improved converter topology for high voltage gain

P. Nandankar, A. Dasarwar, G. Karache propose in their paper (Nandankar, Dasarwar & Karache, 2018) an improved topology of DC-DC converter with a high voltage gain and conversion efficiency up to 14% above the Basic Boost converter. Their improved DC-DC step-up converter topology can reach a conversion ratio over 20 at an efficiency above 97%. The proposed topology in (Nandankar et al., 2018) can be found in Figure 1.8 below. The theoretical conversion ratio of the improved converter topology as a function of duty cycle D can be found at Equation (1.37).

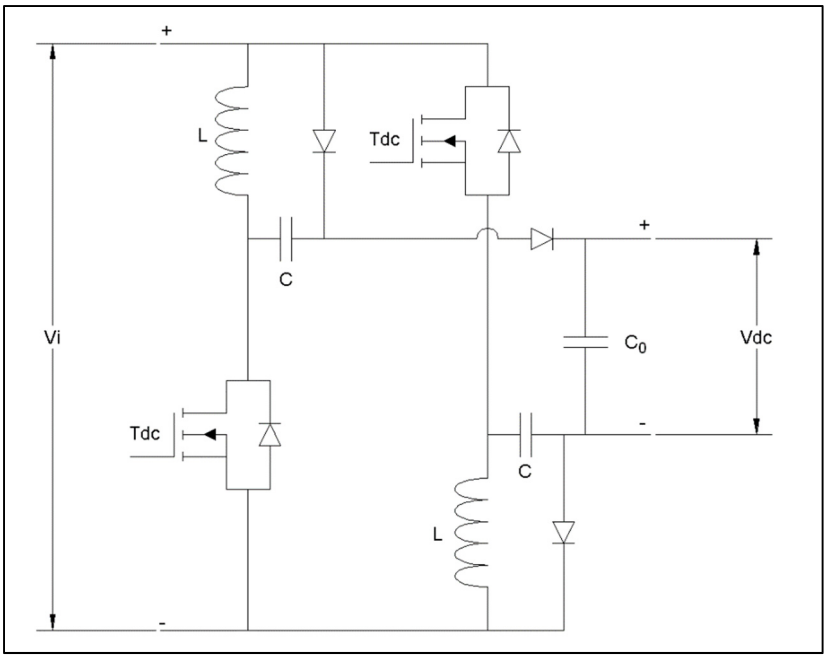

Figure 1.8 Improved converter topology
Adapted from Nandankar et al. (2018)

$$\frac{V_{dc}}{V_i} = \frac{3 - D}{1 - D} \tag{1.37}$$

1.3.3 Inverters

The role of the inverter is to convert the DC link voltage into alternative voltage in order to power the AC electric machine. Amongst the inverter topologies used in the industry nowadays, one finds the 2-Levels inverter topology and some Multi-Level inverter topologies. The Multi-Level inverter can generate many voltage levels, and therefore improve the resolution of the inverter output voltage. The selection of an inverter topology for a given application is of primordial importance to improve the efficiency of the electrodynamic system. Aside its own conversion efficiency, the inverter influences the efficiency of the electric machine, mainly because of the current harmonics generated by the DC-AC conversion (Liang et al., 2015), (Itoh, Sato & Tanaka, 2012).

The Multi-Level inverter has numerous advantages over the Two-Level inverter. Amongst the advantages are the reduction of the current harmonics in the electric machine (Liang et al., 2015), (Narnik, Singla & Sharma, 2012), (Itoh et al., 2012), (Haris, Pathak & Agarwal, 2014), reduction of EMI emissions (Haris et al., 2014), the reduction of the switching losses (Liang et al., 2015), (Tiapkin, Volkov & Tiapkin, 2017), (Haris et al., 2014) and reduction of voltage stress on the switches (Haris et al., 2014). On the other hand, the Multi-Level inverter has some disadvantages compared to the two-level inverter, including the increased complexity and increased cost (Narnik et al., 2012).

Nowadays, the Multi-Level inverters are not commonly used in the industry, as they are complex and costly for the common requirements for operating an AC drive. However, the Three-Level inverter has significant advantages over the Two-Level inverter. For a given switching frequency, the Three-Level inverter generates lower current harmonics compared to the Two-Level inverter, therefore improving the efficiency of the electric machine (Liang et al., 2015). The THD can be improved further by increasing the switching frequency of the multi-level inverter, at the cost of additional switching losses (Itoh et al., 2012). As mentioned previously in this section, Lower EMI emissions and reduction of voltage stress on the switches are other advantages of the Three-Level inverter over the Two-Level inverter.

Figures 1.9 and 1.10 below show the comparison of the output voltage of the Two-Level and Three-Level inverters. It is possible to observe that the output voltage of the inverter becomes smoother as the number of levels increase.

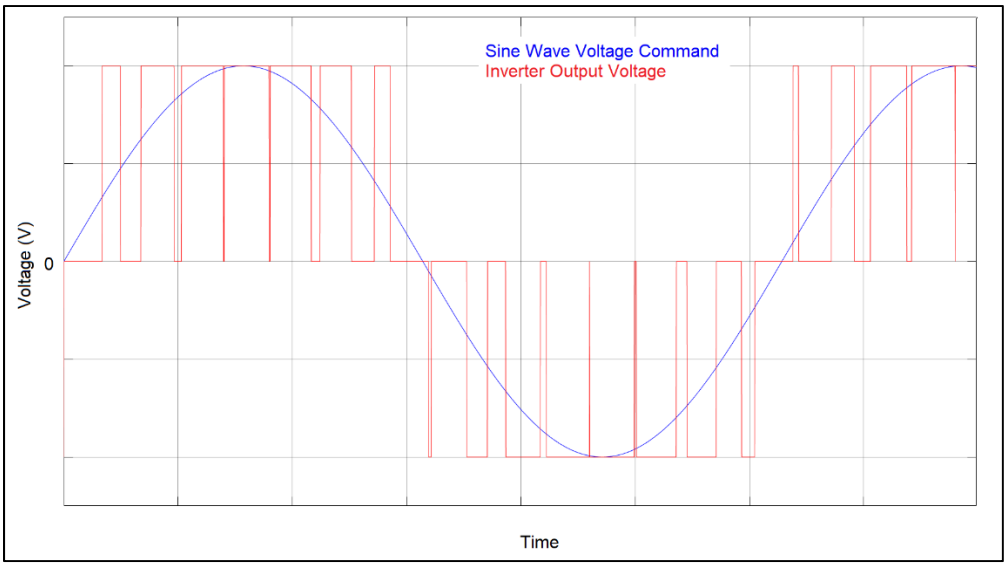

Figure 1.9 Output voltage of a Two-Level inverter

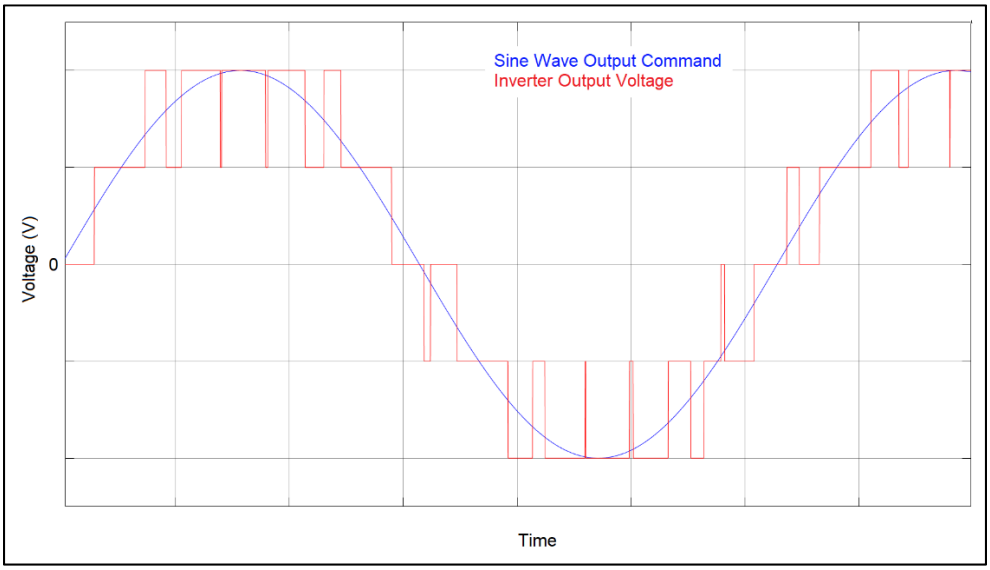

Figure 1.10 Output voltage of a Three-Level inverter

One may conclude that for a high speed PMSM drive, it is preferable to use a Multi-Level inverter as they reduce the current harmonics, which are increasingly generating irons losses as speed increase. Also, as the Back-EMF of the PMSM increase with speed, the DC-link voltage must be increased accordingly, which results in higher voltage stress on the switches of the inverter. As mentioned earlier in this section, using a Multi-Level inverter reduces the voltage stress on the switches.

1.3.4 Inverter topologies

1.3.4.1 Two-Level inverter topology

The Two-Level inverter is the basic inverter configuration. It is made of 6 transistors and a DC-link capacitor to absorb the voltage fluctuations caused by the switching of the transistors. The output Line-Line voltage of the inverter varies between 3 values; [-Vdc, 0, Vdc] where Vdc is the DC-link voltage. See Figure 1.11 for the Two-Level inverter topology.

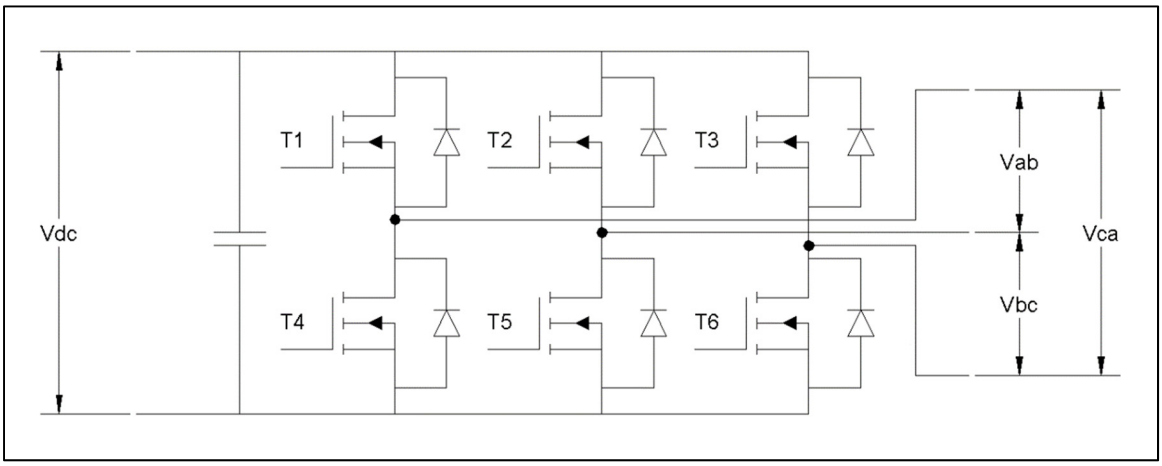

Figure 1.11 Two-Level inverter topology

1.3.4.2 Three-Level inverter topologies

The Multi-Level inverter topologies are mainly the Neutral Point Clamped, I-Type (NPC-I), Neutral Point Clamped, T-Type (NPC-T), Flying Capacitor (FC) and H-Bridge (HB) (Tiapkin et al., 2017), (Rodriguez, Bernet, Steimer & Lizama, 2010), (Narnik et al., 2012). The NPC-I, FC and HB topologies have an architecture which theoretically allows for an unlimited number of levels (Narnik et al., 2012). However, it has not been possible to find literature confirming the existence of NPC-T type inverters with number of Levels higher than 3. Therefore, it is deemed that the NPC-T type inverter is limited to Three levels. As the number of levels increase, the complexity and the number of components also increase. Table 1.1 shows a parts list for different Multi-Level inverter topologies as function of the number of Level m.

The paper of Tiapkin and Volkov (Tiapkin et al., 2017) compares the theoretical (simulated) efficiency of the NPC-I and NPC-T Three-Level inverter topologies. It concludes that the

NPC-I and NPC-T topologies have similar efficiencies, the NPC-T being slightly more efficient at low switching frequency, and the NPC-I being slightly more efficient at high switching frequency.

See Figure 1.12 for the Three-Level Neutral Point Clamped, I-Type (NPC-I) topology, Figure 1.13 for the Three-Level Neutral Point Clamped, T-Type (NPC-T) topology, Figure 1.14 for the Three-Level Flying Capacitor (FC) topology and Figure 1.15 for the Three-Level H-Bridge (HB) topology.

Table 1.1 Parts list of Multi-Level inverters as a function of Level m

Composante	**Multi-Level Inverter Topology**			
	Neutral Point Clamped, I-Type (Note 1)	**Neutral Point Clamped, T-Type** (Note 2)	**Flying Capacitor** (Note 1)	**H-Bridge** (Note 1)
Transistors (Note 1)	6(m-1)	12	6(m-1)	6(m-1)
Feedback Diodes (Note 1)	6(m-1)	12	6(m-1)	6(m-1)
ClampingDiode(Note 1)	3(m-1)(m-2)	0	0	0
DC-Link Capacitors (Note 1)	(m-1)	2	(m-1)	(m-1)/2
Balancing Capacitors (Note 1)	0	0	3(m-1)(m-2)/2	0

Note 1 – Information from (Narnik et al., 2012)
Note 2 – Topology limited to Three-Level

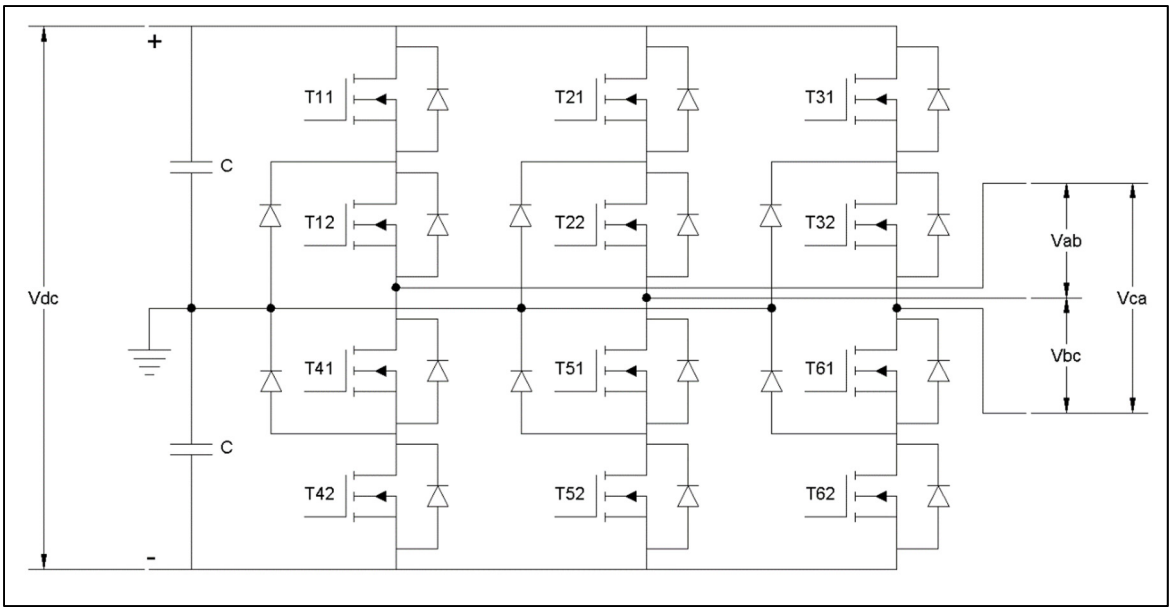

Figure 1.12 Three-Level Neutral Point Clamped, I-Type (NPC-I) Inverter Topology

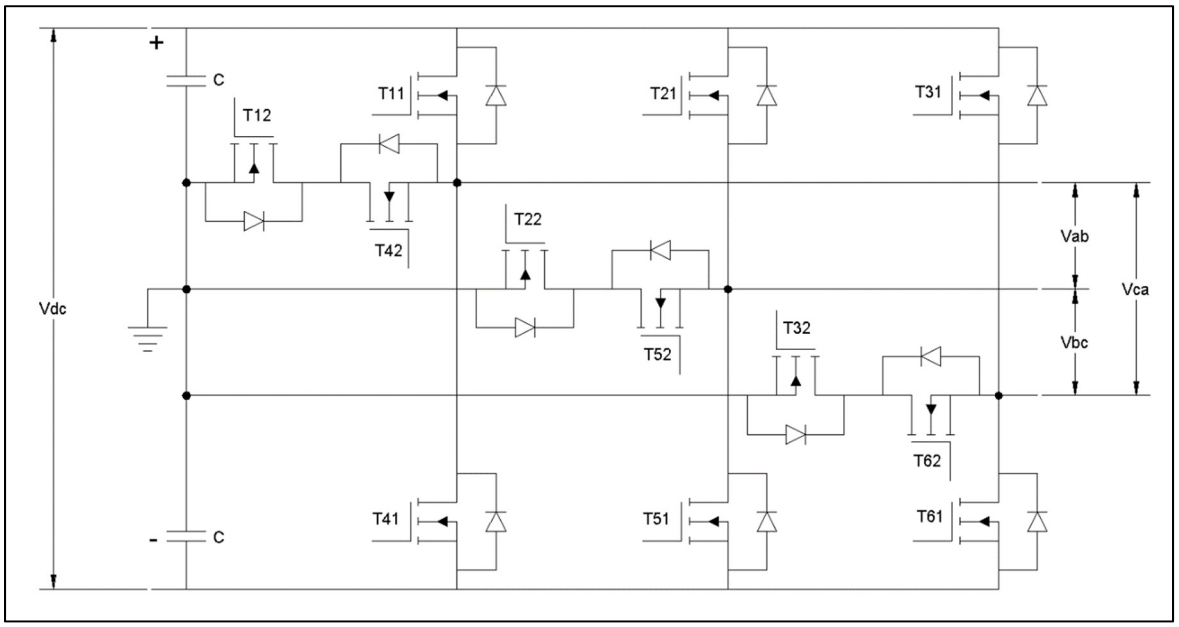

Figure 1.13 Three-Level Neutral Point Clamped, T-Type (NPC-T) Inverter Topology

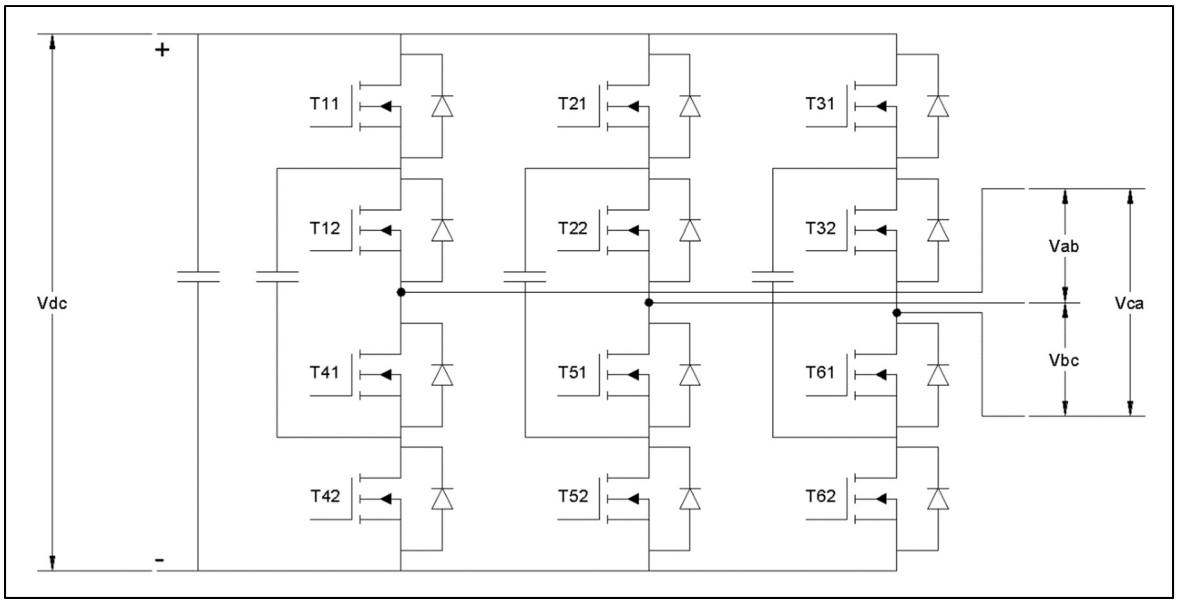

Figure 1.14 Three-Level Flying Capacitor Inverter Topology

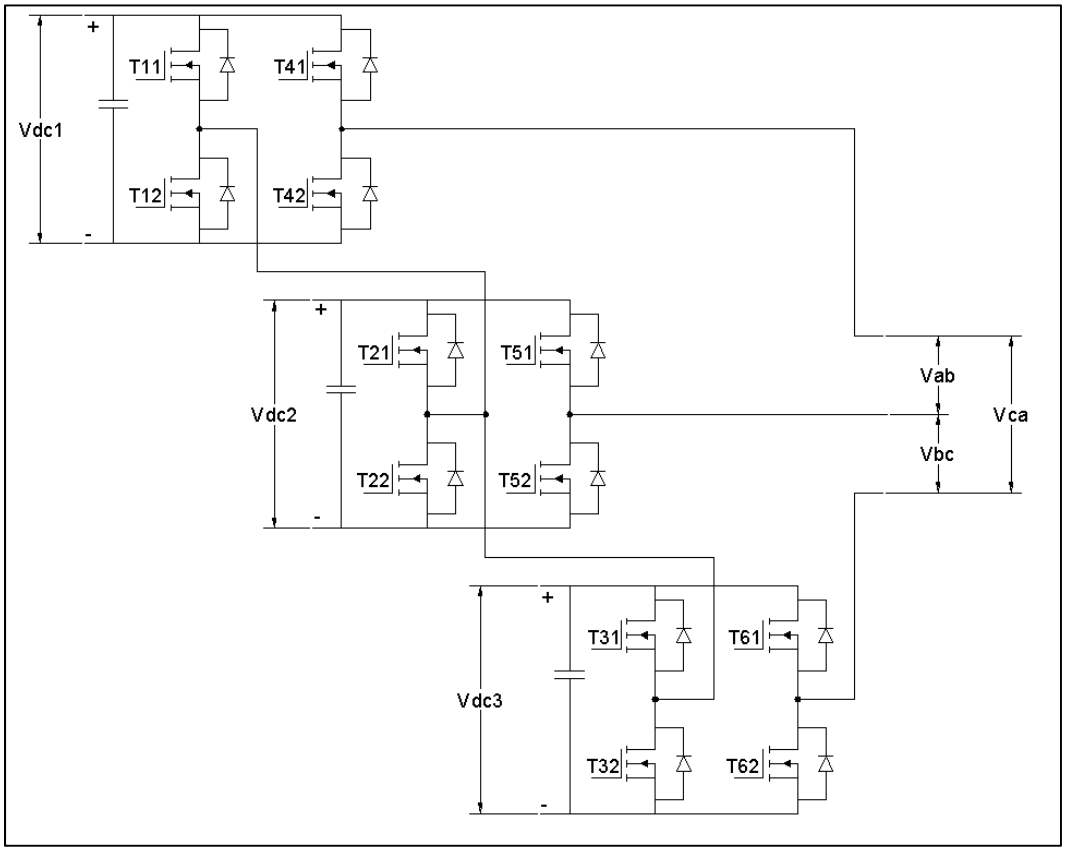

Figure 1.15 Three-Level H-Bridge Inverter topology

1.4 Losses in the semi-conductors

1.4.1 Losses in a diode

The role of a diode is to allow current flow in only one direction (from the anode to the cathode), and to prevent current flow in the opposite direction (cathode to anode). The allowed current direction is here referred as the Forward current and the blocked current direction is here referred as the Reverse current. An ideal diode would have a null resistance or voltage drop in forward direction and an infinite resistance or voltage drop in reverse direction.

As expected, the ideal diode does not exist and therefore a diode generates a voltage drop in forward direction when the current flows in forward direction and allows a small amount of reverse current when the voltage is applied in reverse direction. The voltage drop in forward direction is a function of the forward current and diode temperature. The reverse current is a function of the reverse voltage and the diode temperature. All diode models have different characteristics. Therefore, the voltage drop in forward direction and the reverse current in reverse voltage can typically be found in the data sheet of the diode model. Figures 1.16 and 1.17 below show respectively an example of the voltage drop characteristics and reverse current characteristics of a commercially available diode (ON Semiconductor model RHRG75120, https://www.onsemi.com/pdf/datasheet/rhrg75120-d.pdf).

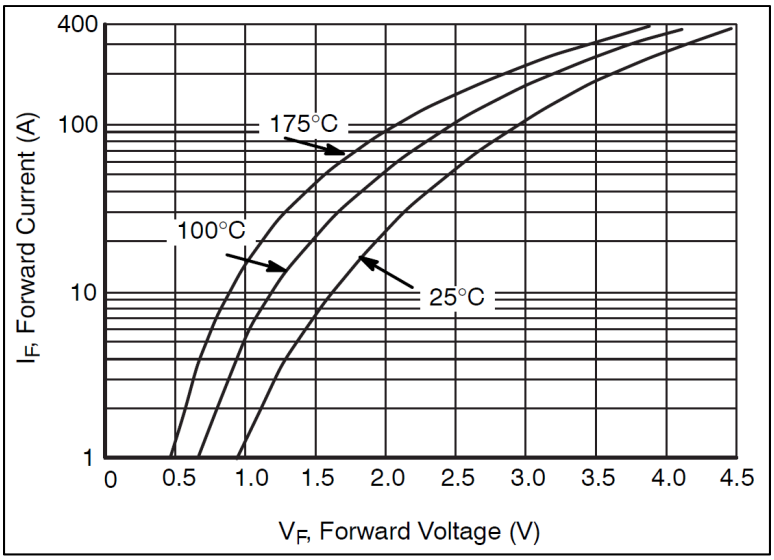

Figure 1.16 Voltage drop in forward current direction for diode On Semi RHRG75120 (https://www.onsemi.com/pdf/datasheet/rhrg75120-d.pdf)

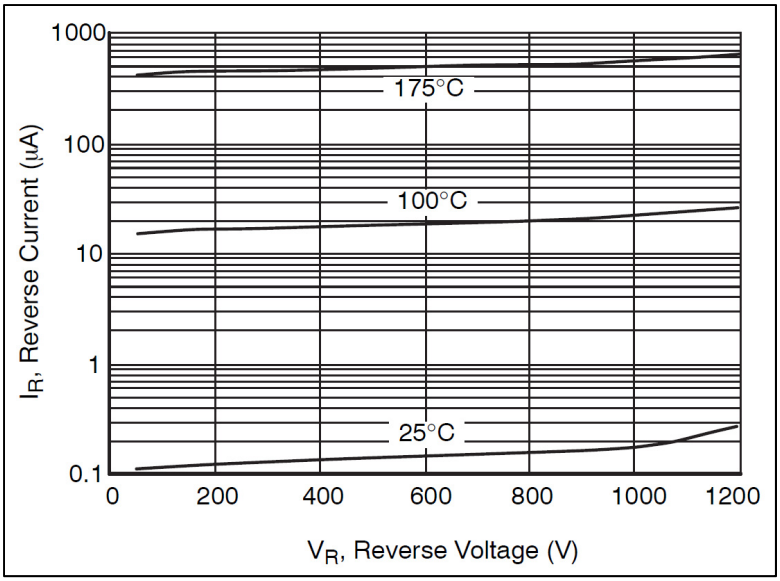

Figure 1.17 Reverse current in reverse voltage direction for diode On Semi RHRG75120 (https://www.onsemi.com/pdf/datasheet/rhrg75120-d.pdf)

The equation of the power loss in a diode in the forward current direction can be found at Equation (1.38) and the equation of the power loss in in a diode in the reverse direction can be found at equation (1.39).

$$P_{F\_diode} = V_F \cdot I_F \tag{1.38}$$

$$P_{R\_diode} = V_R \cdot I_R \tag{1.39}$$

1.4.2 Losses in a Metal-Oxyde Semiconductor Field Effect Transistor (MOSFET)

A Metal-Oxyde Semiconductor Field Effect Transistor (MOSFET) behaves like a unidirectional switch. In forward voltage direction, the MOSFET allows forward current only when the MOSFET's gate is energized and blocks the forward current when the MOSFET's gate is de-energized. Reverse current flow is allowed in a MOSFET because of the intrinsic body diode.

The losses in a MOSFET, in forward current direction, consists of the turn-on losses, the conduction losses, and turn-off losses. The switching losses is the sum of the turn on losses and turn off losses. In reverse current direction, the losses are those of a diode as seen previously in Section 1.4.1. The paper of H. Raee, A. Rabiei and T. Thirnger (Raee, Rabiei & Thirnger, 2013) provides an explanation and a detailed model of the switching losses in a MOSFET. The paper of X. Yu and P. Yeaman (Yu & Yeaman, 2013) proposes a simplified switching losses equation as shown in Equation (1.40) below.

$$P_{sw} = \frac{V_{DS} \cdot I_{DS}}{2} \cdot \left(\frac{(Q_{GD} + Q_{GS}/2) \cdot R_{G\_on}}{V_{DR} - V_{GS(SP)}} + \frac{(Q_{GD} + Q_{GS}/2) \cdot R_{G\_off}}{V_{GS(SP)}} \right) \cdot f_s \tag{1.40}$$

Where V_{DS} is the voltage between the drain and source, V_{DR} is the voltage between the gate and the source, I_{DS} is the current through the drain and source, Q_{GD} is the charge in the GD capacitor, Q_{GS} is the charge in the GS capacitor, R_{G_ON} and R_{G_OFF} are the gate resistance during ON and OFF transitions, f_s is the switching frequency and $V_{GS(SP)}$ is the Voltage gate threshold adjusted with temperature as per the Equation (1.41) below:

$$V_{GS(SP)} = V_{GS(SP)0} \cdot \left(1 - k_1 \cdot (T° - 25)\right) \quad (1.41)$$

Where T° is the MOSFET temperature, $V_{GS(SP)0}$ is the $V_{GS(SP)}$ at 25 °C and k_1 is a constant that can be found using the MOSFET datasheet. See Figure 1.18 below for a schematic of the MOSFET applicable to the switching losses calculation.

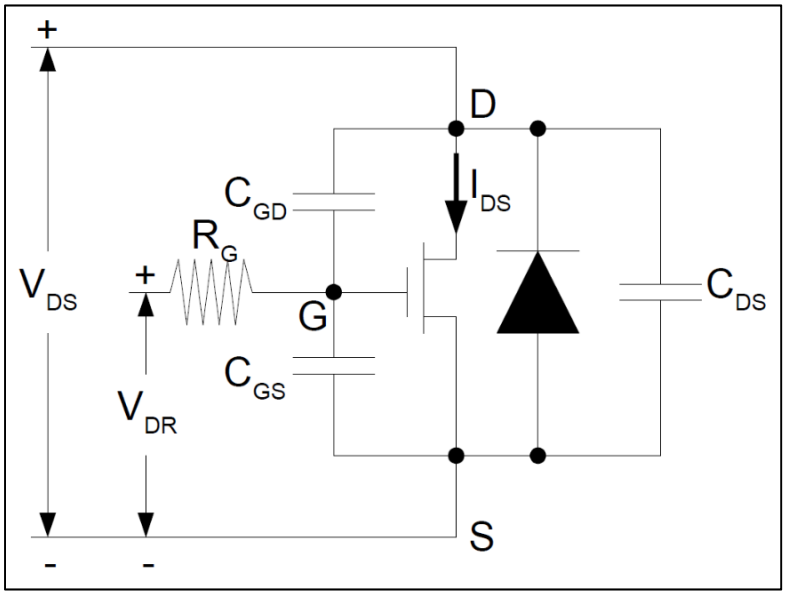

Figure 1.18 MOSFET model schematic

The conduction losses consist of the resistive losses caused by the intrinsic MOSFET's resistance in forward current direction. The intrinsic MOSFET's resistance is known as $R_{DS(ON)}$. The conduction losses equation can be found at Equation (1.42).

$$P_{Cond} = R_{DS(ON)} \cdot I_{DS}^2 \quad (1.42)$$

The conduction resistance is function of V_{GS}, I_{DS} and MOSFET temperature. All MOSFET models have different characteristics. The information to calculate the conduction losses can typically be found in the MOSFET datasheet. As an example, see Figures 1.19 to 1.21.

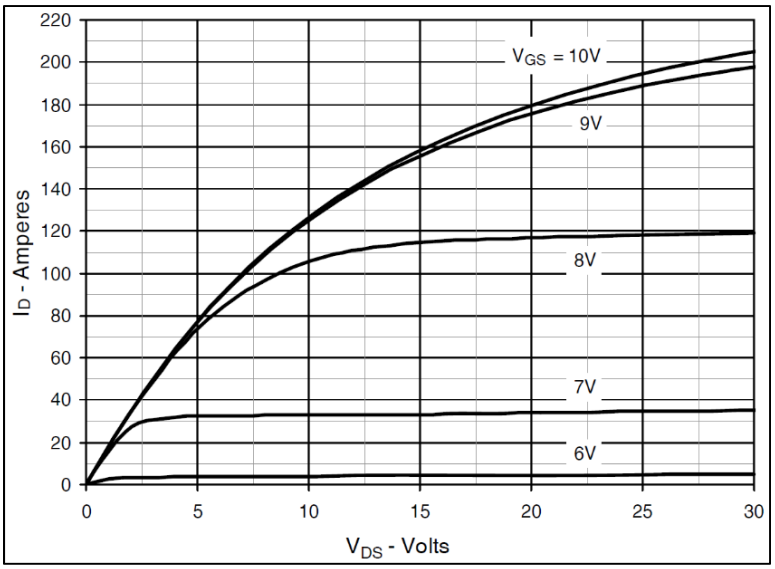

Figure 1.19 Effect of VGS on RDS(ON) (IXYS X-Class HiPerFET IXFB70N100X at 25 °C) (https://www.littelfuse.com/~/media/electronics/datasheets/discrete_mosfets/littelfuse_discrete_mosfets_n-channel_ultra_junction_ixfb70n100x_datasheet.pdf.pdf)

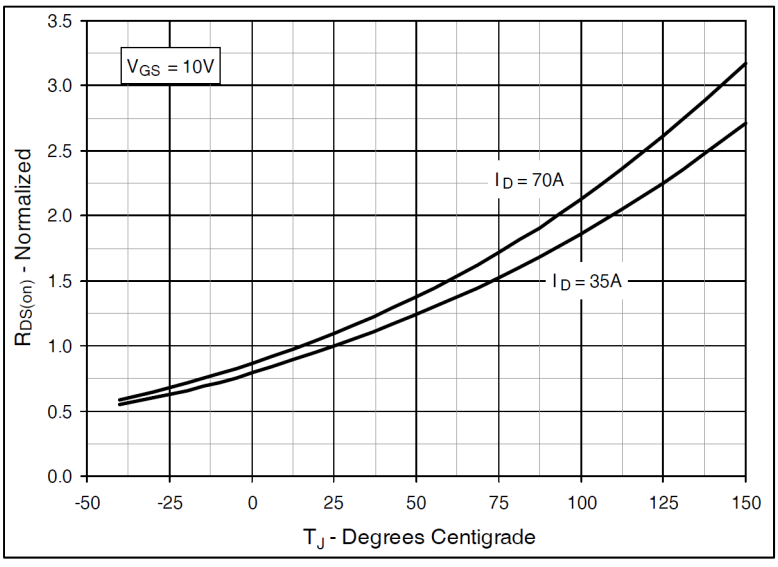

Figure 1.20 Effect of temperature on RDS(ON) (IXYS X-Class HiPerFET IXFB70N100X) (https://www.littelfuse.com/~/media/electronics/datasheets/discrete_mosfets/littelfuse_discrete_mosfets_n-channel_ultra_junction_ixfb70n100x_datasheet.pdf.pdf)

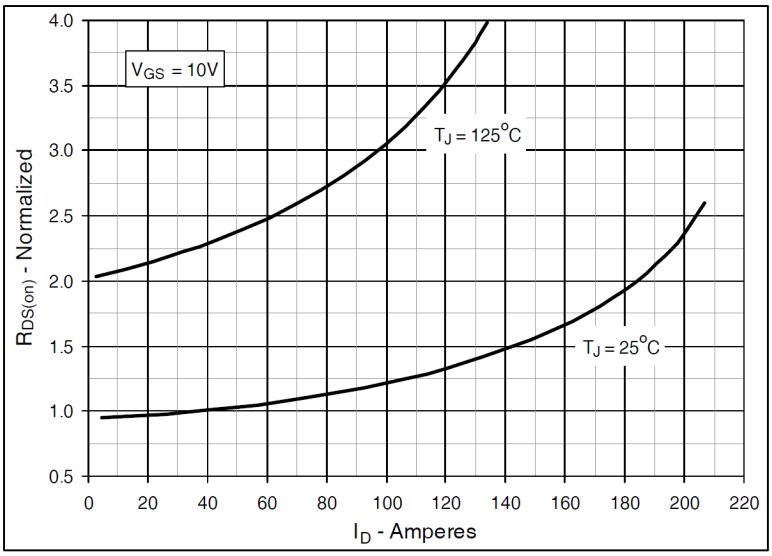

Figure 1.21 Effect of current on RDS(ON) (IXYS X-Class HiPerFET IXFB70N100X at 35A) (https://www.littelfuse.com/~/media/electronics/datasheets/discrete_mosfets/littelfuse_discrete_mosfets_n-channel_ultra_junction_ixfb70n100x_datasheet.pdf.pdf)

1.4.3 Losses in an Insulated Gate Bipolar Transistor (IGBT)

The Insulated Gate Bipolar Transistor (IGBT) is another semi-conductor device that can be used as a unidirectional on-off switch, similarly to the MOSFET. However, unlike the MOSFET, the IGBT does not have an embedded body diode and therefore cannot conduct in reverse current direction. To allow reverse direction free wheeling current, a diode must be added in parallel with the IGBT.

The losses in an IGBT, in forward current direction, consists of the turn-on losses, the conduction losses, and turn-off losses. The switching losses is the sum of the turn on losses and turn off losses. In reverse current direction, the losses are those of a diode as seen previously in Section 1.4.1. The paper of Z. Chen, L. Yuan, Z. Zhao and X.Sun (Chen, Yuan, Zhao & Sun, 2012) proposes the switching losses equation as shown in Equation (1.43) below.

$$P_{SW} = \frac{6}{\pi} \cdot f_s \cdot \left(E_{ON,I} + E_{OFF,I}\right) \cdot \frac{V_{dc}}{V_{ref}} \cdot \frac{\widehat{\imath_I}}{i_{ref}} \tag{1.43}$$

Where P_{SW} is the switching losses, f_s is the switching frequency, $E_{ON,I}$ is the turn on energy (typically found in the IGBT datasheet) and $E_{OFF,I}$ is the turn off energy (typically found in the IGBT datasheet), V_{dc} is the DC-link voltage, V_{ref} is the reference DC-link voltage $\hat{\imath}_I$ is the peak AC current (assumed to be sinusoidal) and I_{ref} is the reference AC current. The voltage and current corrections in Equation (1.43) are because the switching losses are function of the collector current in "ON" state and voltage across the IGBT (V_{CE}) in "OFF" state. For the instantaneous switching loss energy, the Equations (1.44) and (1.45) may be used:

$$E_{ON,IGBT} = \left(E_{ON,I}\right) \cdot \frac{V_{CE}}{V_{ref}} \cdot \frac{I_C}{i_{ref}} \tag{1.44}$$

$$E_{OFF,IGBT} = \left(E_{OFF,I}\right) \cdot \frac{V_{CE}}{V_{ref}} \cdot \frac{I_C}{i_{ref}} \tag{1.45}$$

Where V_{CE} is the collector-emitter voltage and I_C is the collector current. It is to be noted that the turn-off energy losses of the diode due to the reverse recovery process is embedded in the turn-off energy definition. Figures 1.22 and 1.23 are examples on how the collector current and collector-emitter voltage impacts the switching losses.

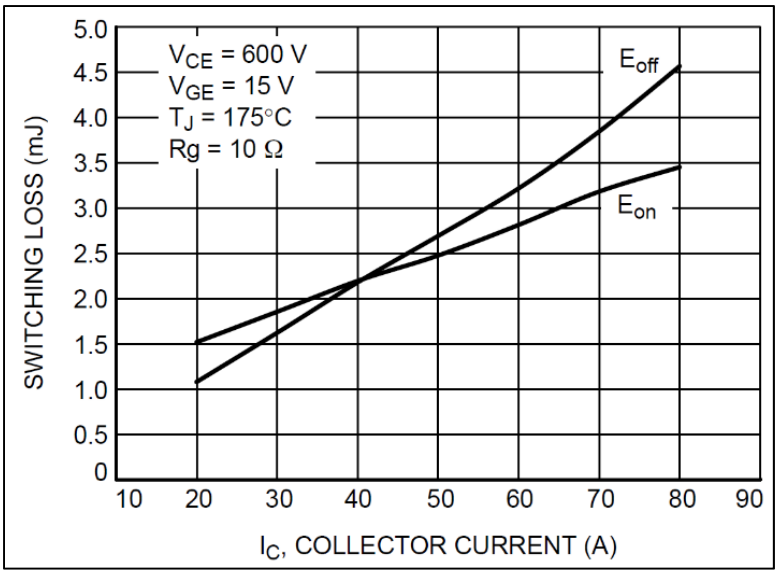

Figure 1.22 Effect of collector current on switching losses (NGTB40N120FL2WAG) (https://www.onsemi.com/pdf/datasheet/ngtb40n120fl2wa-d.pdf)

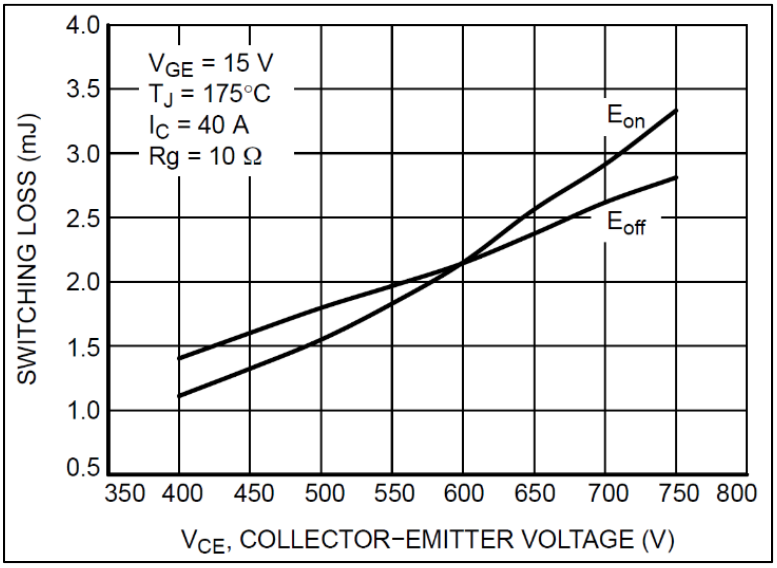

Figure 1.23 Effect of collector-emitter voltage on switching losses (NGTB40N120FL2WAG) (https://www.onsemi.com/pdf/datasheet/ngtb40n120fl2wa-d.pdf)

The voltage and current corrections proposed in Equation (1.43) provide an approximation of the effect of the collector-emitter voltage and collector current on the switching losses.

Aside the collector-emitter voltage and collector current, the IGBT junction temperature and gate resistance RG have an impact on the switching losses. Figures 1.24 and 1.25 show the effect of the IGBT junction temperature and gate resistance R_G on the switching losses.

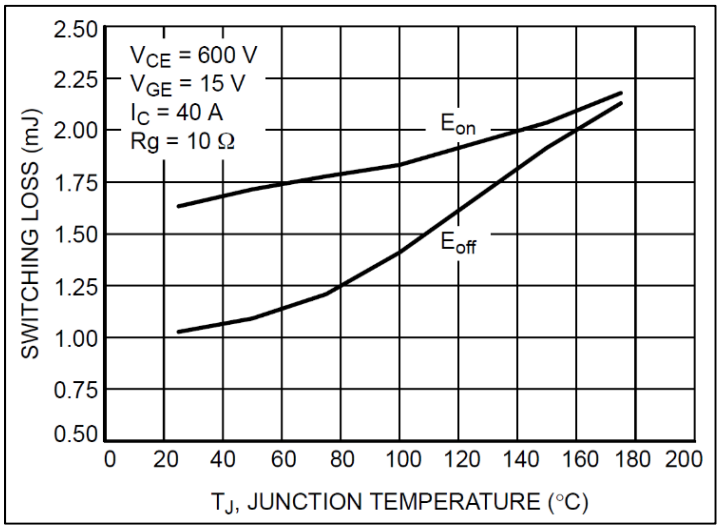

Figure 1.24 Effect of IGBT junction temperature on switching losses (NGTB40N120FL2WAG) (https://www.onsemi.com/pdf/datasheet/ngtb40n120fl2wa-d.pdf)

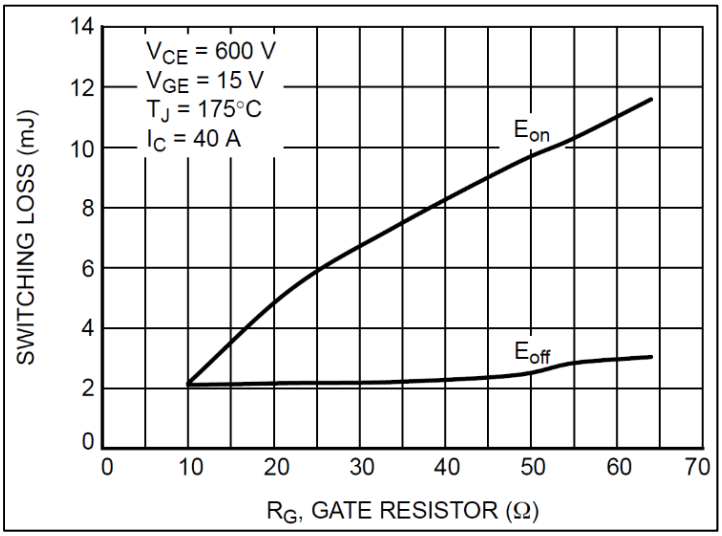

Figure 1.25 Effect of gate resistor on switching losses (NGTB40N120FL2WAG) (https://www.onsemi.com/pdf/datasheet/ngtb40n120fl2wa-d.pdf)

The paper of Z. Chen, L. Yuan, Z. Zhao and X.Sun (Chen et al., 2012) proposes the forward conduction losses and reverse conduction losses at Equations (1.46) and (1.47) respectively.

$$P_{cond,FWD} = V_{CE} \cdot I_C \tag{1.46}$$

$$P_{cond,REV} = V_{EC} \cdot I_D \tag{1.47}$$

Where $P_{cond,FWD}$ is the conduction power loss in forward direction (through the IGBT), $P_{cond,REV}$ is the conduction power loss in reverse direction (through the diode), V_{CE} is the voltage drop across the IGBT, V_{EC} is the voltage drop across the diode and I_C is the collector current. The voltage drop across the diode and the IGBT are of similar nature and may be modeled using a voltage bias and an internal resistance as per Equations (1.48) and (1.49) below.

$$V_{CE} = V_{CE0} + R_{CE0} \cdot I_C \tag{1.48}$$

$$V_{EC} = V_{EC0} + R_{EC0} \cdot I_D \tag{1.49}$$

Figures 1.26 and 1.27 below show the impact of IGBT temperature and gate to emitter voltage (V_{GE}) on the IGBT voltage bias and IGBT internal resistance. Figure 1.28 shows the impact of diode temperature on the diode voltage bias and diode internal resistance. See Figure 1.29 for a schematic of the IGBT model.

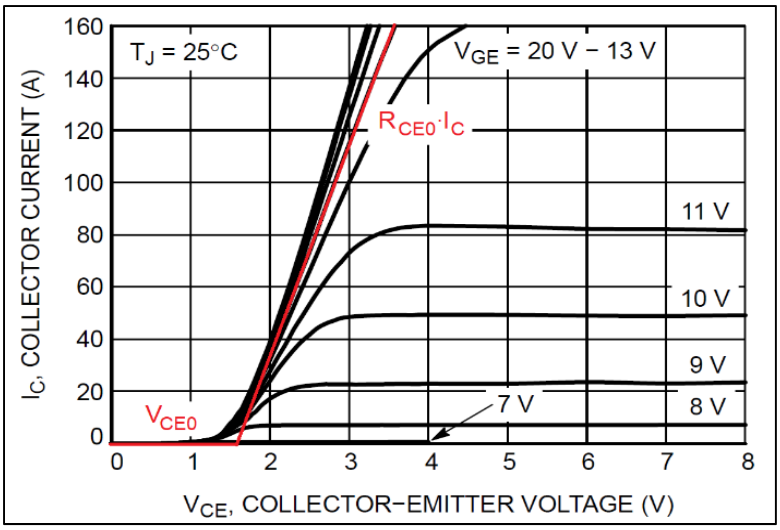

Figure 1.26 Collector Current as a function of Collector-Emitter Voltage and Gate to Emitter voltage (TJ = 25°C) (NGTB40N120FL2WAG) (https://www.onsemi.com/pdf/datasheet/ngtb40n120fl2wa-d.pdf)

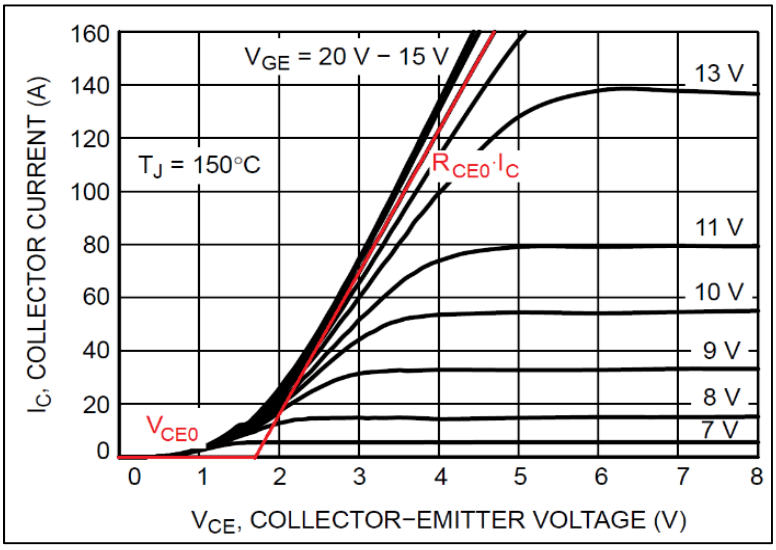

Figure 1.27 Collector Current as a function of Collector-Emitter Voltage and Gate to Emitter Voltage (TJ = 150°C) (NGTB40N120FL2WAG) (https://www.onsemi.com/pdf/datasheet/ngtb40n120fl2wa-d.pdf)

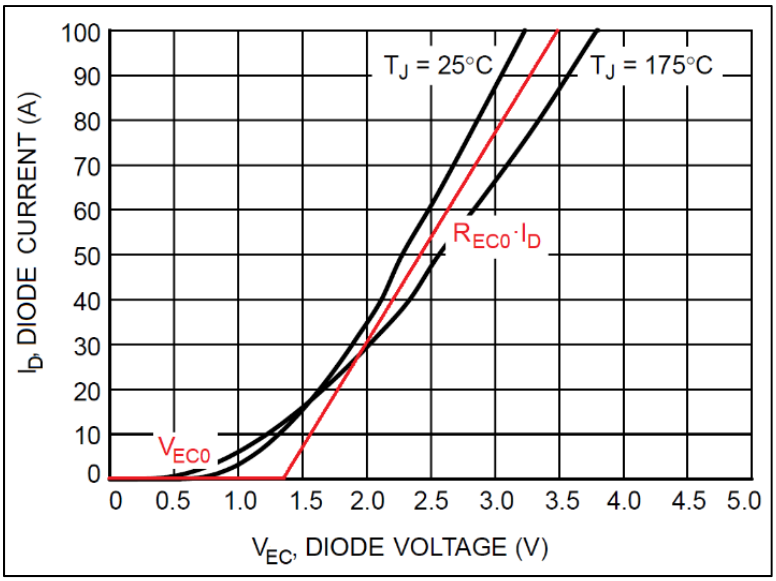

Figure 1.28 Diode Current as a function of Emitter-Collector Voltage and diode temperature (NGTB40N120FL2WAG) (https://www.onsemi.com/pdf/datasheet/ngtb40n120fl2wa-d.pdf)

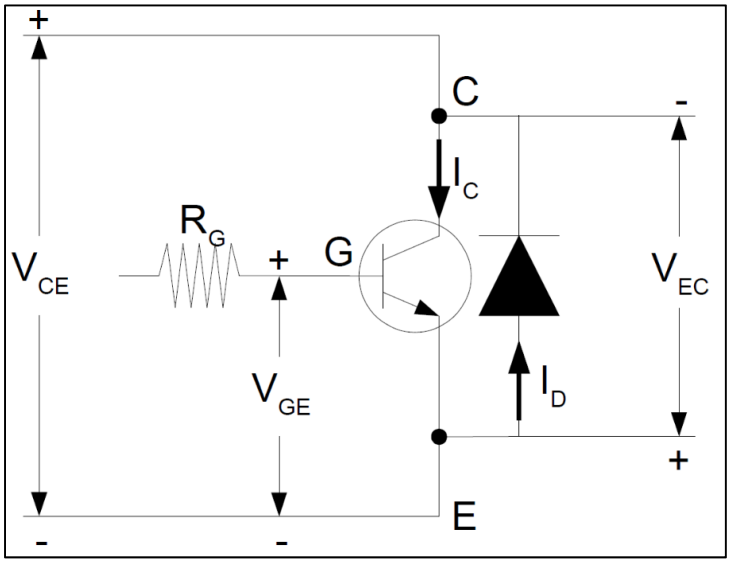

Figure 1.29 IGBT model schematic

1.5 PMSM Control

Nowadays Field Oriented Control (FOC) is the main control strategy used in the industry to control PMSMs. The Field Oriented Control of a PMSM Drive requires a precise knowledge of the rotor position and phase currents in real time. The rotor position is mandatory to calculate the voltage and current vectors in the d-q space, and the phase currents are inputs to the d-q axis current PI controllers that generate the output voltage commands to the inverter. For high speed machines and high number of pole pair machines, the rotor position and phase current data acquisition must be done at high frequency. Figure 1.30 shows the structure of a PMSM Field Oriented Controller. It is to be noted that the structure of the PMSM FOC shown in Figure 1.30 is a speed controller accepting a speed request ω^*. For torque control operation, the speed control PI can be bypassed by accepting an external torque request $T_q{}^*$.

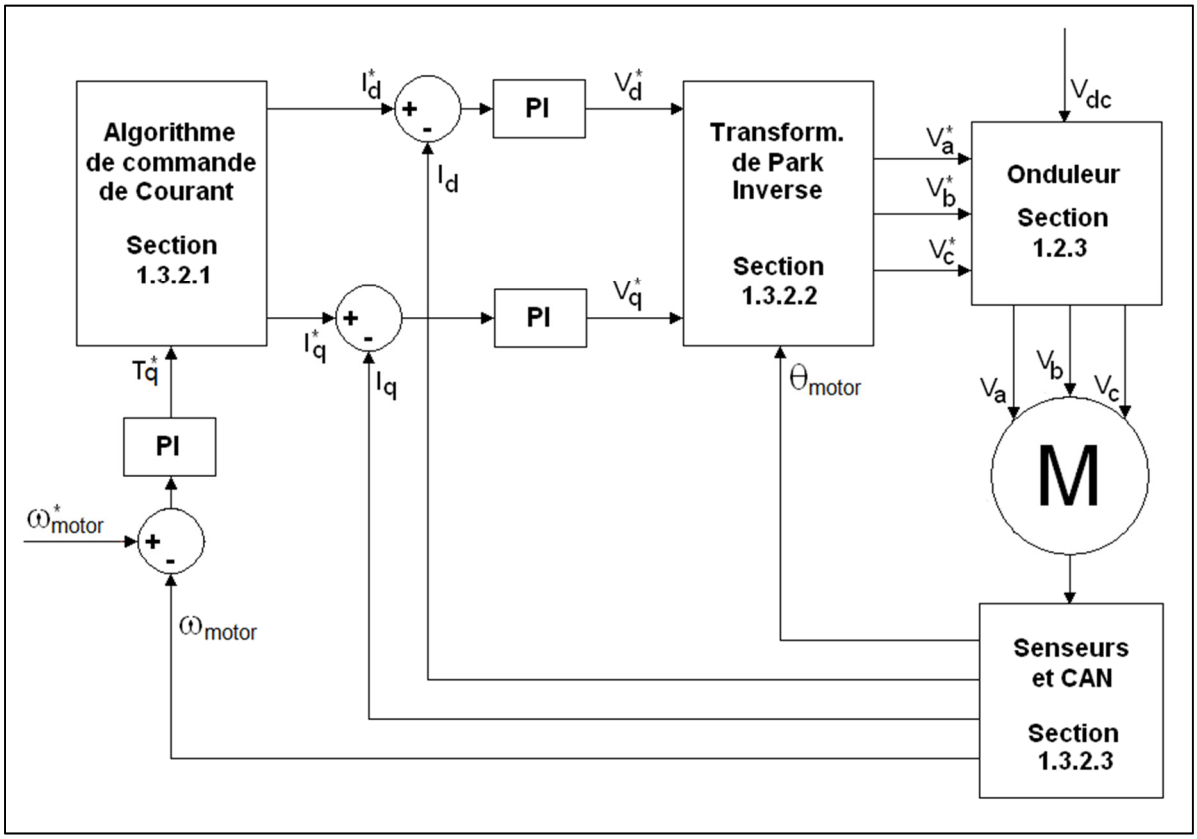

Figure 1.30 PMSM Field Oriented Controller Structure

1.5.1 Torque Control Algorithm

The Torque Control Algorithm accepts a torque request and schedules the phase currents for the PMSM output torque to match the torque request. Equation (1.50) links the electromagnetic torque command T_q^* to the current commands in the d-q space.

$$T_q^* = \frac{3}{2} P_p \left(\varphi_f + \left(L_d - L_q\right) i_d^*\right) i_q^* \tag{1.50}$$

An infinity of d-axis current and q-axis current combinations are possible to reach the commanded torque. The d-axis Current Control determines the d-axis current command for a given motor configuration and point of operation. The structure of the Torque Control Algorithm is shown in Figure 1.31 below.

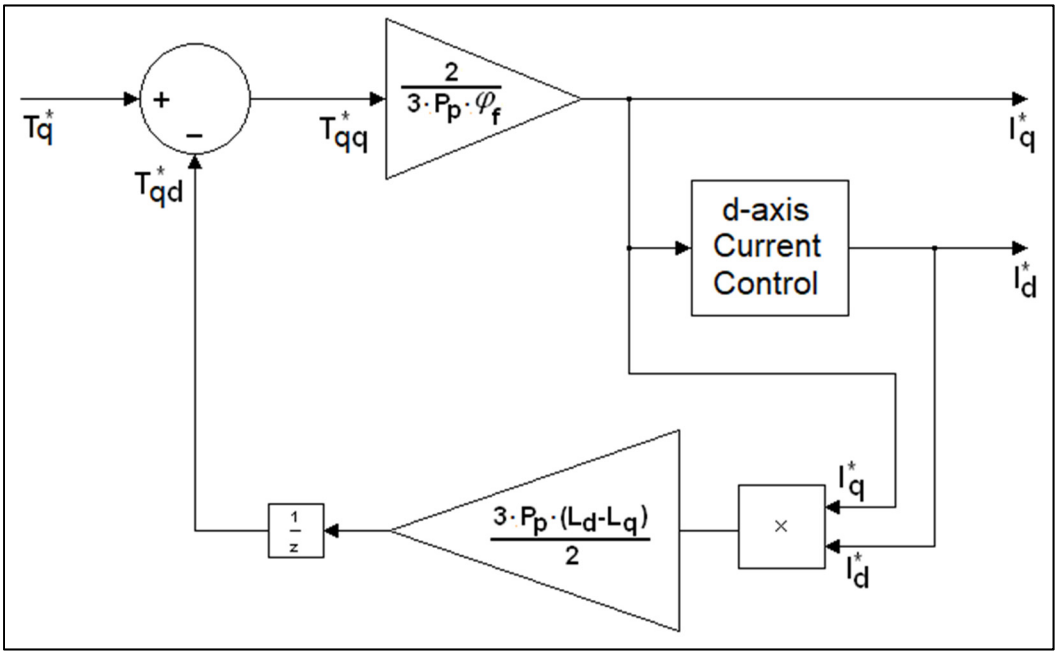

Figure 1.31 Torque Control Algorithm

1.5.2 d-axis Current Control

The d-axis Current Control algorithm has an influence on the motor efficiency and performance, depending on the motor configuration and motor operating conditions. The

following section presents different d-axis Current Control strategies which improves the motor performances when used with the proper motor configuration and operating condition.

1.5.2.1 Zero d-axis Current Control

The Zero d-axis Current (ZDAC) control strategy consists of fixing the d-axis current command I_d^* to zero ($I_d^* = 0$). For surface mounted PMSMs, where typically the d-axis inductance is equal to the q-axis inductance, no reluctant torque is generated by the difference in d-axis and q-axis inductances. Therefore, it is useless to command d-axis current when operating a surface mounted PMSM, unless field weakening operation is required to reach high speed. The ZDAC command ensures that the only current consumed by the PMSM generates torque, which allows to reach optimal efficiency.

1.5.2.2 Maximum Torque Per Amp Control

The Maximum Torque Per Amp (MTPA) control strategy consists of generating the d-axis and q-axis current combination that minimize the amplitude of the phase current vector for a given torque command. The paper of Morimoto, Sanada and Takeda (Morimoto, Sanada & Takeda, 1994) proposes Equation (1.51). Equation (1.51) determines the d-axis current command I_d^* which ensures the maximum torque per amp as a function of the q-axis current command I_q^* and PMSM characteristics.

$$i_d^* = \frac{\varphi_f}{2\left(L_q - L_d\right)} - \sqrt{\frac{\varphi_f^2}{4\left(L_q - L_d\right)^2} + i_q^{*2}} \tag{1.51}$$

The paper of Halder, Agarwal and Srivastava (Halder, Agarwal & Srivastava, 2015) compares the efficiency of ZDAC and MTPA control strategies on a salient poles PMSM. They found that for a given operating condition, the required phase current to reach a given torque is higher when using ZDAC compared to MTPA. One may conclude that MTPA control improves the efficiency of the PMSM compared to the ZDAC control.

1.5.2.3 Field Weakening Control

When the PMSM speed increase, the impedance of the phase inductances increases proportionally to the PMSM speed. Additionally, the Back-EMF, which opposes to the phase voltage, also increase proportionally to the PMSM speed. It therefore comes a speed of operation where the phase voltage is not enough to inject the maximum torque per amp current in the motor phases. In order to increase the speed of the PMSM, Field Weakening operation is required. Field Weakening operation use the d-axis current to reduce the magnetic flux linkage φ_f. Referring to equation (1.31), one can observe that the electromagnetic torque T_e decreases as the magnetic flux linkage decrease for a given phase current. Field Weakening Control is also called constant power control. The paper of Zhao and Liang (Zhao & Liang, 2009) proposes the Equation (1.52) for the Field Weakening d-axis current command, where V_{max} is the maximum available phase voltage.

$$i_d^* = \frac{-\varphi_f + \sqrt{\left(\frac{V_{max}}{\omega}\right)^2 - \left(L_q \cdot i_q^*\right)^2}}{L_d} \tag{1.52}$$

1.5.2.4 Maximum Efficiency Control

The MTPA control provides a good efficiency. However, the maximum efficiency is not achieved using MTPA control. The MTPA control ensures the maximum torque per amp but not the maximum power per amp. The control strategy which ensures maximum power per amp is called the Maximum Efficiency (ME) control.

The paper of Pohlenz and Böcker (Pohlenz & Böcker, 2010) compares the efficiency of MTPA control and their proposed ME control applied to a salient poles PMSM. For this study, the maximum efficiency of the IPMSM has been measured experimentally and the I_d^* and I_q^* components are generated by lookup tables as a function of speed ω_{motor} and torque command T_q^*. Despites that the MTPA and ME commands provide similar efficiencies, the ME command creates a small flux weakening, which has the effect of slightly decreasing the torque but slightly more increasing speed, which in turns generate more output mechanical power.

Pohlenz and Böcker conclude that the increased efficiency of the ME control is due to the reduction of core and iron losses made possible by the additional flux weakening current. The ME control proposed by Pohlenz and Böcker improve the motor efficiency by a maximum of 0.3% in the lower half of the output torque range.

Figures 1.32 and 1.33 are taken from (Pohlenz et al., 2010). Figure 1.32 shows the efficiency improvement of the proposed ME control compared to MTPA control over the torque range at a speed of 2000 rpm. Figure 1.33 shows the efficiency improvement of the proposed ME control compared to MTPA at various speeds.

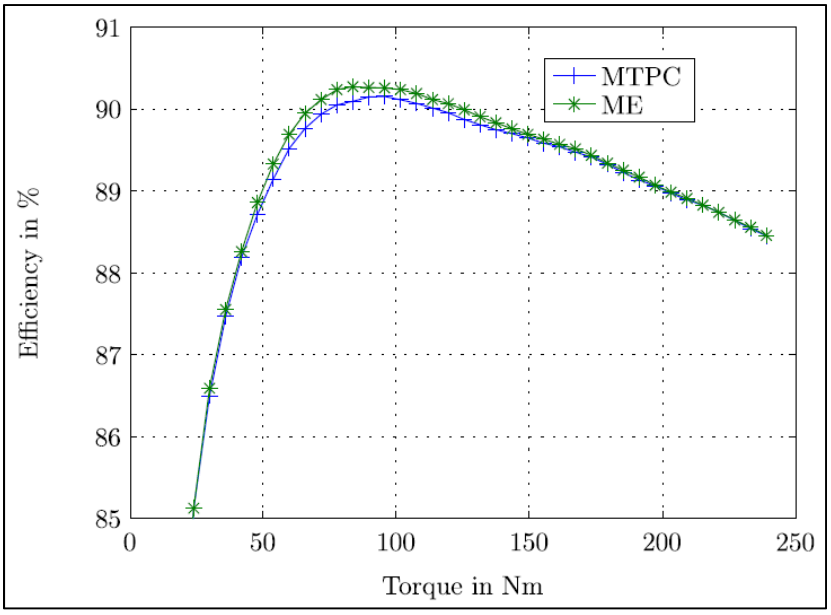

Figure 1.32 Efficiency vs torque for MTPA (MTPC) and ME @ 2000 rpm
Taken from Pohlenz et al. (2010)

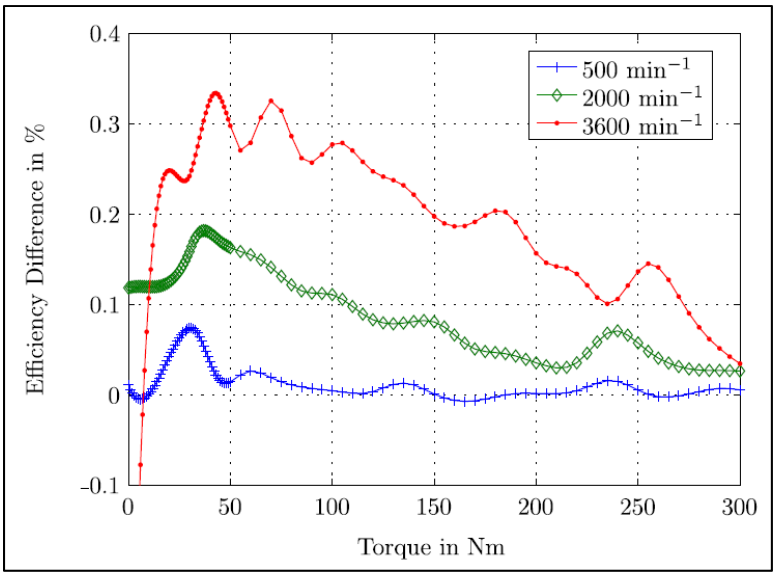

Figure 1.33 Difference of efficiencies between ME and MTPA at varying speed
Taken from Pohlenz et al. (2010)

The paper of Ni et Al. (Ni et al., 2015) proposes a model-based ME control. The iron losses of the PMSM are calculated analytically from the Bertotti formula. Also, the effect of d-axis and q-axis current on the d-axis and q-axis inductances, due to the magnetic saturation of the stator, are considered. The ME control proposed in (Ni et al., 2015) improves the motor efficiency by 0.5% at low power and by 0.2% at rated power compared to MTPA control. See Figure 1.34 for a comparison between the efficiency of the proposed ME (MEPA) control in (Ni et al., 2015) compared to the MTPA control.

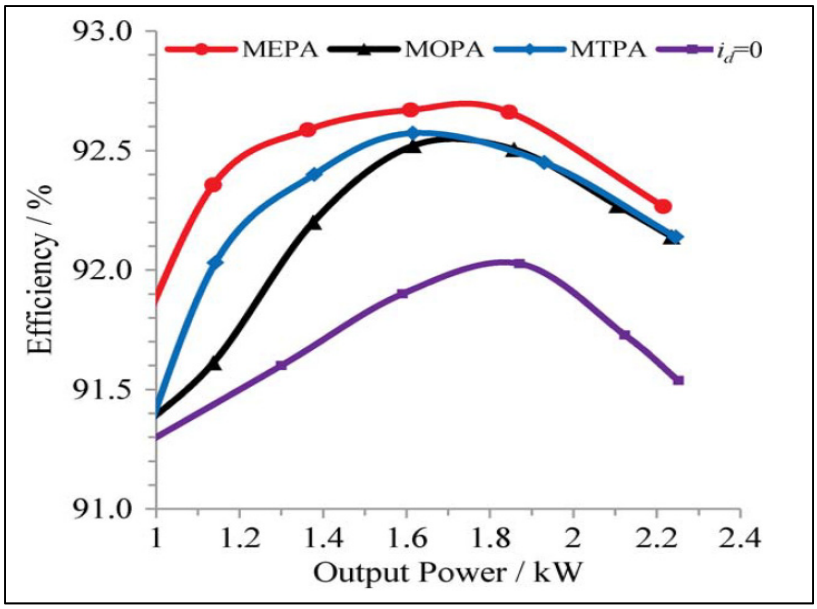

Figure 1.34 Efficiency comparison versus output power under different control algorithms at rated speed
Taken from Ni et al. (2015)

The paper of Guo et Al. (Guo et al., 2016) proposes a model-based ME control for a SPMSM. The iron losses are analytically calculated from the Bertotti formula and the effect current harmonics on the copper losses and iron losses is considered in the calculation of the total losses of the SPMSM. The ME control proposed in (Guo et al., 2016) improves the efficiency by approximately 0.4% in the low torque and high-speed region compared to the ZDAC control. See Figure 1.35 for a comparison between the efficiency of the proposed ME control in (Guo et al., 2016) compared to the ZDAC control.

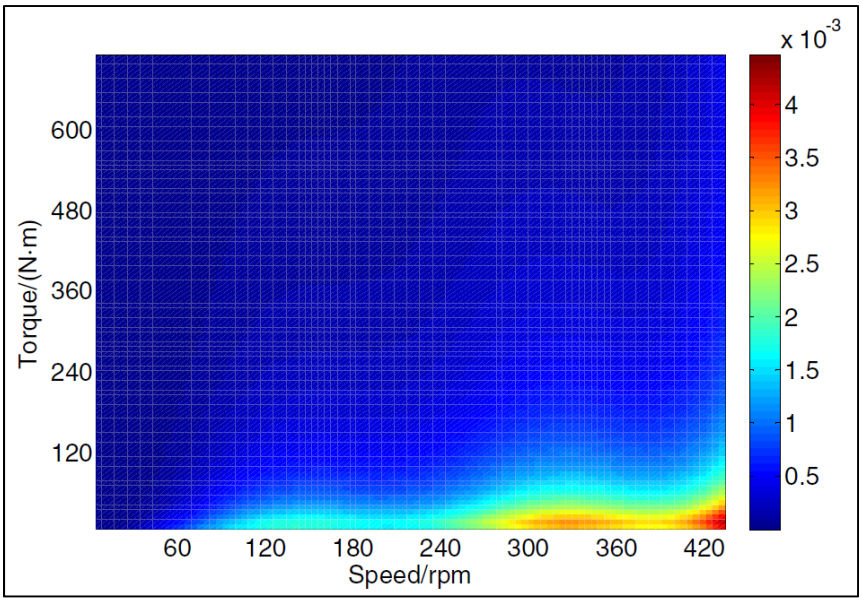

Figure 1.35 Difference between ME efficiency and ZDAC efficiency
Taken from Guo et al. (2016)

1.6 Electrical Resonance

The electrical resonance is a phenomenon where the energy is exchanged between a capacitance and an inductance at the natural frequency of the LC circuit. The capacitance holds the energy in the form of voltage, comparable to mechanical potential energy. The inductance holds the energy in the form of current, comparable to mechanical kinetic energy. The equation of the energy contained in a capacitance can be found at equation (1.53) and the equation of the energy contained in an inductance can be found at equation (1.54). It is to be noted that a resistor does not accumulate energy, it only dissipates it.

$$E_C(t) = \frac{q(t)^2}{2 \cdot C} \tag{1.53}$$

$$E_L(t) = \frac{L \cdot I(t)^2}{2} \tag{1.54}$$

1.6.1 Dynamics of the electrical resonance

A RLC circuit is composed of a resistance, an inductance and a capacitance connected in series. The equations of the voltage at the terminals of each passive components of the RLC circuit can be found at Equations (1.55) to (1.57) below. The voltage balance equation of the RLC circuit can be found at (1.58) and the transfer function of the RLC circuit in the Laplace domain can be found at equation (1.59). V_{in} is the input voltage of the RLC circuit and $V_{C_{t=0}}$ is the initial voltage in the capacitor.

$$V_R(t) = R \cdot I(t) = R \cdot \frac{dq(t)}{dt} \tag{1.55}$$

$$V_L(t) = L \cdot \frac{dI(t)}{dt} = L \cdot \frac{dq^2(t)}{dt^2} \tag{1.56}$$

$$V_C(t) = \frac{q(t)}{C} \tag{1.57}$$

$$\sum V = 0 = V_{in}(t) - R \cdot \frac{dq(t)}{dt} - L \cdot \frac{dq^2(t)}{dt^2} - \frac{q(t)}{C} \tag{1.58}$$

$$q(s) = \frac{V_{in}(s)}{L} \cdot \frac{1}{(s+a)^2 + \omega^2} + I_{t=0} \cdot \frac{1}{(s+a)^2 + \omega^2} + q_{t=0} \cdot \frac{s}{(s+a)^2 + \omega^2} + \frac{R \cdot q_{t=0}}{L} \cdot \frac{1}{(s+a)^2 + \omega^2} \tag{1.59}$$

Where:

$$a = \frac{R}{2L} \tag{1.60}$$

$$\omega = \sqrt{\frac{1}{L \cdot C} - \left(\frac{R}{2L}\right)^2} \tag{1.61}$$

It is to be noted that ω is the oscillatory frequency of the RLC circuit. If the resistance of the RLC circuit is neglected, the transfer function of the LC circuit in the Laplace domain can be found at equation (1.62) and the undamped oscillatory frequency at equation (1.63). The undamped oscillatory frequency is also known as the natural frequency ω_n.

$$q(s) = \frac{V_{in}(s)}{L} \cdot \frac{1}{s^2 + \omega_n^2} + I_{t=0} \cdot \frac{1}{s^2 + \omega_n^2} + q_{t=0} \cdot \frac{s}{s^2 + \omega_n^2} \tag{1.62}$$

$$\omega_n = \sqrt{\frac{1}{L \cdot C}} \tag{1.63}$$

In power electronic circuits, a basic design objective is to reduce the resistance in order to minimize the copper losses. Therefore, the resistance may be neglected if it does not significantly modify the LC circuit dynamic behavior. One can observe that the structure of the transfer function at equation (1.62) makes the time domain representation of charge and current with no external voltage and no initial current, and with the capacitor pre-charged (i.e. $q_{t=0} \neq 0$) as per Equations (1.64) and (1.65).

$$q(t) = q_{t=0}.\cos(\omega_n \cdot t) \tag{1.64}$$

$$I(t) = \frac{dq(t)}{dt} = -q_{t=0} \cdot \omega_n \cdot \sin(\omega_n \cdot t) \tag{1.65}$$

The time domain undamped current follows a sinusoidal shape and the amplitude of the oscillating current is $q_{t=0} \cdot \omega_n$.

1.6.2 Step response of the LC circuit

If a voltage step is applied to an inert LC circuit, the current oscillates around zero and the capacitor voltage oscillates around the voltage of the DC source. One can observe that the structure of the transfer function at equation (1.62) makes the time domain representation of capacitor voltage as per Equation (1.66).

$$V_{in}(s) = \frac{V_{in}}{s}$$

$$q(s) = \frac{V_{in}}{L} \cdot \frac{1}{s(s^2 + \omega_n^2)}$$

$$q(t) = \frac{V_{in}}{L \cdot \omega_n^2} \cdot \left(1 - \cos(\omega \cdot t)\right)$$

$$V_C(t) = V_{in} \cdot \left(1 - \cos(\omega \cdot t)\right) \tag{1.66}$$

Per the equation (1.66), the maximum capacitor voltage is twice the input voltage. When considering the effect of the power dissipation by the resistor, one finds that the maximum capacitor voltage is still greater than the input voltage when the RLC circuit in underdamped. An example of the step response of an underdamped RLC circuit can be found at Figure 1.36.

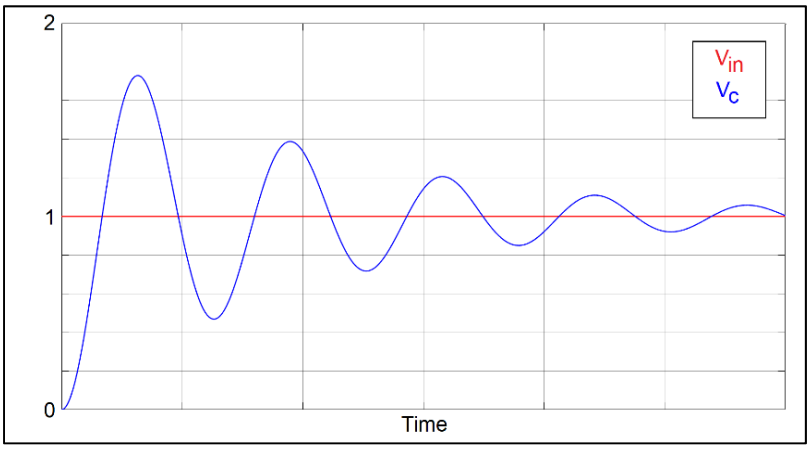

Figure 1.36 Step response of an underdamped RLC circuit

1.6.3 Impedance of the RLC circuit

The impendence formula of the RLC circuit can be found at Equation (1.67). The impedance of the RLC circuit is function of the AC frequency.

$$Z_{RLC} = R + i \cdot \omega \cdot L + \frac{1}{i \cdot \omega \cdot C} \tag{1.67}$$

One finds that at low frequency, the impedance of the capacitance is the most significant, unlike at high frequency where the impedance of the inductance is the most significant. If the AC frequency is equal to the natural frequency of the RLC circuit as defined in Equation (1.61), the impedance of the RLC circuit becomes only resistive as the impedance of the inductance and the capacitor cancel each other. This behavior can be observed on the bode plot of the transfer function of Equation (1.68).

$$\frac{I(s)}{V_{in}(s)} = \frac{s}{L \cdot s^2 + R \cdot s + \frac{1}{C}} \tag{1.68}$$

One sees on Figure 1.37 that at the natural frequency of the RLC circuit, the phase shift between the current and the input voltage is null and the gain is the DC gain of the RL circuit. As the input voltage is in phase with the current, the power factor is 1.

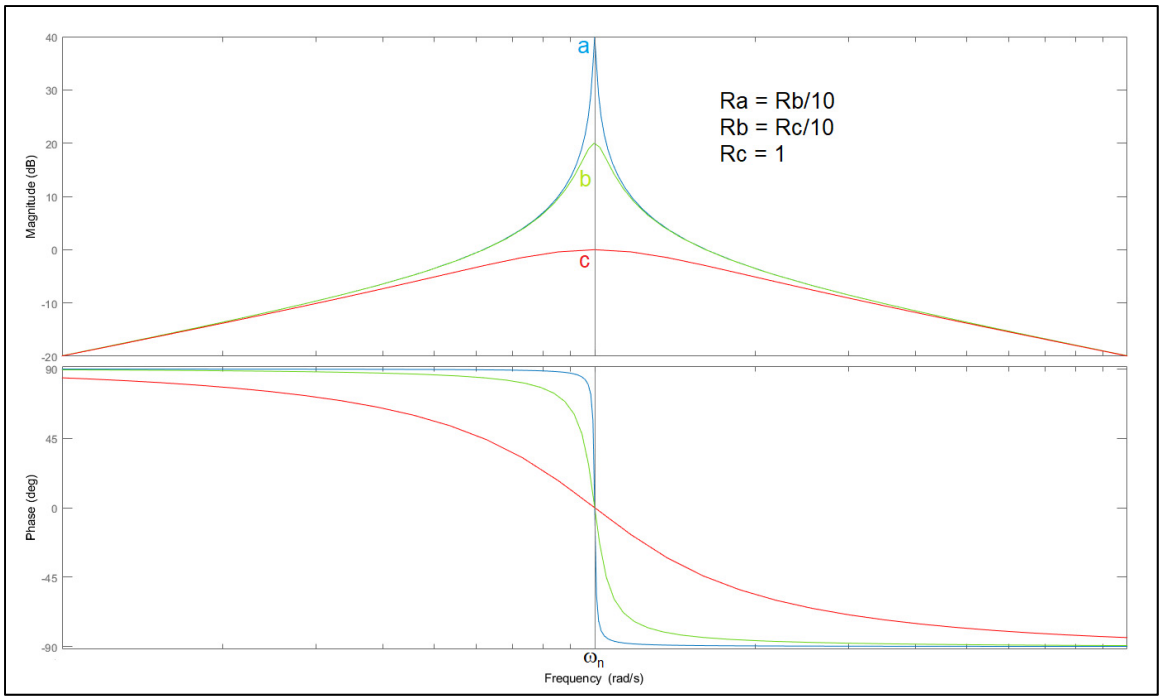

Figure 1.37 I/V Transfer Function Frequency Response of a RLC circuit with varying resistors

1.6.4 Accumulation of energy in the RLC circuit

As already mentioned, the resistor dissipates the energy in the form of heat when current circulates through it. However, for the following demonstration, the energy dissipation by the resistor will be neglected. As shown on Equations (1.53) and (1.54), the capacitor and the inductance can both store energy. Using equations (1.64) and (1.65) above, one finds that the energy is exchanged between the capacitor and the inductance at the natural frequency of Equation (1.63), and that the energy contained in the LC circuit is a constant which does not vary in time. The mathematical demonstration is performed at Equation (1.69).

$$E_L(t) = \frac{L \cdot I(t)^2}{2} = \frac{L}{2} \cdot (-q_{t=0} \cdot \omega_n \cdot \sin(\omega_n \cdot t))^2$$

$$E_C(t) = \frac{q(t)^2}{2 \cdot C} = \frac{1}{2 \cdot C} \cdot (q_{t=0} \cdot \cos(\omega_n \cdot t))^2$$

$$E_L(t) + E_C(t) = \frac{L \cdot q_{t=0}^2 \cdot \omega_n^2}{2} = \frac{q_{t=0}^2}{2 \cdot C} \tag{1.69}$$

If an AC source, alternating at the natural frequency, powers the LC circuit, one can observe on equations (1.70) and (1.71) that the amplitude of both charge and current increase with time, and therefore the energy contained in the LC circuit also. When neglecting the resistance, the energy accumulation is infinite. However, when considering the effect of energy dissipation in the resistor, there is a point where the input power will be completely dissipated by the resistor and the energy contained in the resonating RLC circuit will remain constant over time. The steady state current amplitude of the RLC circuit is determined at equation (1.72).

$$V_{in}(t) = V_{in} \cdot \cos(\omega_n \cdot t)$$

$$q(s) = \frac{V_{in}}{L} \cdot \frac{s}{s^2 + \omega_n^2} \cdot \frac{1}{s^2 + \omega_n^2} = \frac{V_{in}}{L} \cdot \frac{s}{(s^2 + \omega_n^2)^2}$$

$$q(t) = \frac{V_{in}}{2 \cdot L \cdot \omega_n} \cdot t \cdot \sin(\omega_n \cdot t) \tag{1.70}$$

$$I(t) = \frac{V_{in}}{2 \cdot L \cdot \omega_n} \cdot (t \cdot \omega_n \cdot \cos(\omega_n \cdot t) + \sin(\omega_n \cdot t)) \tag{1.71}$$

$$I_{max} = \frac{V_{in}}{R} \tag{1.72}$$

1.6.5 Applications of electrical resonance

Nowadays, many concepts and applications take advantage of the properties of electrical resonance. The electrical resonance phenomenon is being used in DC/DC power conversion (Lee, Kim, Jeong & Choi, 2016), (Van Den Bossche, Stoyanov, Dukov, Valchev & Marinov, 2016), (Mishima, Takeuchi & Nakaoka, 2011), (Rahman, Chiu & Hsieh, 2018), (Law, Cheng & Yeung, 2005), (Eno, Thompson & Coppins, 2005), DC/AC power conversion (Hori & Matsuse, 1999), (Marchesoni, Puglisi & Rebora, 1995), (Peng & Adams, 2000), (Peretz & Ben-Yaakov, 2005), (Wei, Zhu, Bartarseh & Vaidya, 1998) and induction heating (Pholsriphim, Nurach & Lenwari, 2017), (Fathy et al., 2005), (Saha, Lee & Nakaoka, 2006). More related to the topic of this research project, electrical resonance is also used in powering electrical machines. Amongst the previous art and previous research, electrical resonance has been used to power switched reluctance motors (Alaee, Afjei & Ataei, 2007), (Benny Yeung, 2004), induction motors (Marchesoni et al., 1995), (Kapoor & Tripathi, 1996), (Murai,

Ishikawa & Lipo, 1994), (Potter, Shirsavar & McCulloch, 2003), (Suh, Choi & Sul, 1996) and permanent magnet synchronous motors (Shahbazi, Madani & Ebrahimi, 2009), (Kernstock & Plassnegger, 2012), (Hucheng, Weiguo, Manfeng & Ruiqing, 2007), (Taniguchi, Saegusa & Morizane, 2005).

Those concepts take advantage of the soft switching techniques made possible by the current and voltage dynamics of the RLC circuit. Soft switching consists of switching the semiconductors when the current is null (Zero Current Switching, ZCS) or when the voltage is null (Zero Voltage Switching, ZCS). Typically, in soft switching resonant circuits, the semiconductor switching open circuit is done at zero current, and the semiconductor switching close circuit is done at zero voltage. As seen previously, the current and voltage in a resonating RLC circuit are sinusoidal, and therefore reaches null current and null voltage naturally without interrupting the energy input. Switching off the semiconductors during zero current condition and switching on the semi conductors during zero voltage has the effect of reducing the switching losses in the semiconductors.

It is obviously impossible to list and resume every thesis and research article written about using the resonance phenomenon in power conversion or electrical motorization. The references listed above consist of examples of research articles describing applications of electrical resonance and do not consist of the exhaustive list of publications about using the resonance phenomenon in power conversion or electrical motorization. It is to be noted that despites the fact that all publications about the applications of electrical resonance could not be referenced above, the unreferenced publications on this topic are not considered of lesser value.

CHAPTER 2

DEFINITION OF THE PROBLEM

As previously seen, operating a PMSM at high speed and high torque represents a significant technical challenge. PMSMs generate a Back-EMF which is function of speed, and this Back-EMF opposes the phase voltage from the inverter. For a fixed voltage, once the battery voltage is not sufficient to inject enough q-axis current to generate the maximum motor torque, the PMSM control needs to be operated in field weakening current mode, which increase speed but reduce torque. Typically, field weakening control maintains the PMSM output power, which means that the motor torque shall decrease as the speed increase. When the PMSM is used for an aeronautical propeller, the load increase with speed, and therefore field weakening operation cannot reach the desired operating point, which is both at high torque and high speed, as shown in Figure 2.1 below:

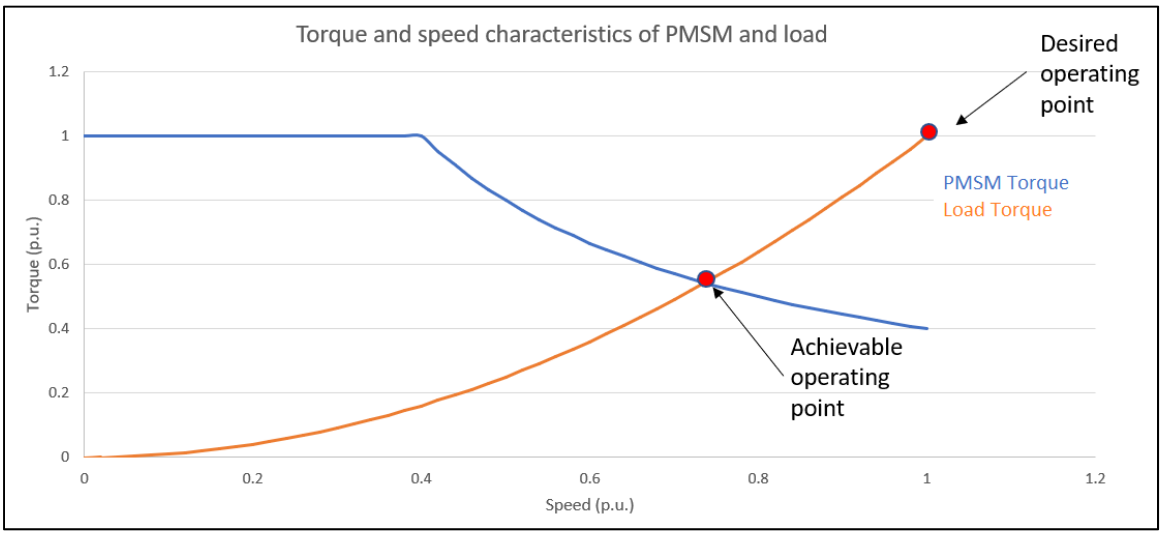

Figure 2.1 Torque and speed characteristics of the PMSM and the propeller load

To reach the desired operating point, the phase voltage must be increased to at least the voltage of the Back-EMF at the desired operating speed. However, this has drawbacks. First, considering a fixed battery voltage, the DC link voltage to the inverter needs to be increased using a DC-DC converter. As mentioned previously, energy conversion, including DC-DC step-up voltage conversion, generates losses and therefore reduce global efficiency of the

system. Also, increasing the phase voltage generates more current harmonics, because the PWM switching generates higher voltage steps which in turns generates higher current ripples. To reduce the current harmonics in the PMSM, a multi-level inverter may be used. As previously seen, the multi-level inverter generates multiple levels of phase voltage, which improve the current harmonics in the motor.

When operating a PMSM at high speed, the resolution of the emulated voltage sine wave by the PWM switching is reduced, and therefore current harmonics may become significant. Pushing the PMSM speed further, one can understand that at some point, the benefits of the multi-level inverter will vanish if the inverter switching frequency does not allow to fully use the benefits of the multi-level voltage steps (i.e. if the half period of the Back-EMF is too short to modulate the phase voltage using all voltage levels). To counter this problem, the multi-level inverter switching frequency must be increased, therefore increasing the switching losses to the benefit of improving the phase current harmonics.

Bringing a PMSM to maximum speed at maximum torque requires significant energy conversion steps, and the sum of all losses dedicated to energy conversion (combined step-up voltage conversion and phase current modulation by the inverter) may become significant as the motor torque and speed both increase simultaneously. It can be easily understood that as the motor speed and torque increase, more input electrical power to the PMSM is required. This requires the DC-DC step-up conversion to increase it power conversion by converting more battery current to a higher voltage and a lower current at the inverter input. A search of the available off-the-shelf DC-DC step-up converters available in the market nowadays shows that DC-DC step-up converters are not widely available for high power applications. Using off-the-shelf applications would require using multiple DC-DC converters in parallel or in series, for increased cost and additional weight.

CHAPTER 3

HYPOTHESIS

As seen previously, the electrical resonance presents very interesting properties for operating an AC machine. Unlike in most structural applications where a resonant behavior shall be avoided or at least largely damped, resonance could be of great help to shape AC current and even amplify it compared to a simple inductive circuit. It is therefore believed that the following properties of the electrical resonance phenomenon, when used in combination with a PMSM, can improve the efficiency and power density of the PMSM.

3.1 Hypothesis #1

Hypothesis 1: Current and voltage sinusoidal behavior of the resonant RLC circuit may reduce PWM induced current harmonics, therefore improve motor efficiency.

As mentioned previously in section 1.6, the current and voltage in an RLC circuit naturally follows a sinusoidal profile and the frequency of the free oscillating current is similar to the natural frequency of the RLC circuit when the resistance is low. As the phase resistance of a PMSM is typically very low in order to optimize the efficiency of the motor, one can estimate the RLC circuit current oscillatory frequency as being equal to the natural frequency of the LC circuit.

In most recent DC/AC conversion technologies for PMSM, the sinusoidal current profile is exclusively generated from the PWM switching pattern of the semiconductors in the inverter. The switching can induce current harmonics in the motor and therefore iron losses. At high frequency, the current harmonics can be particularly harmful to the PMSM as seen in section 1.2.3. Adding a capacitor to each motor phases will make the motor phases RLC circuits where the current and voltage naturally follows a sinusoidal profile. If the capacitor is sized in order for the natural frequency of the RLC circuit to match the electrical frequency of the motor at

the desired operating speed, then the PWM inverter contribution for shaping the AC current may be reduced, therefore reducing the current harmonics in the motor.

3.2 Hypothesis #2

Hypothesis 2: The Current/Voltage gain of an RLC circuit at the natural frequency being that of the DC gain of the RL circuit, lower AC input voltage may be required to reach the desired current, therefore improving efficiency.

As mentioned previously in section 1.6, the Current/Voltage (I/V) gain of an RLC circuit at the natural frequency is that of the DC gain of the RL circuit. Typically, the I/V gain of a RL circuit is equal to the DC gain at 0 Hz and decreases as the input voltage frequency increase. It is therefore understood that with any RL circuit, the phase circuit's I/V gain at any operating electrical frequency of the motor will be lower than the DC gain. Figure 3.1 below shows the difference in frequency response between a RL circuit, which is a typical motor phase circuit, and the RLC circuit.

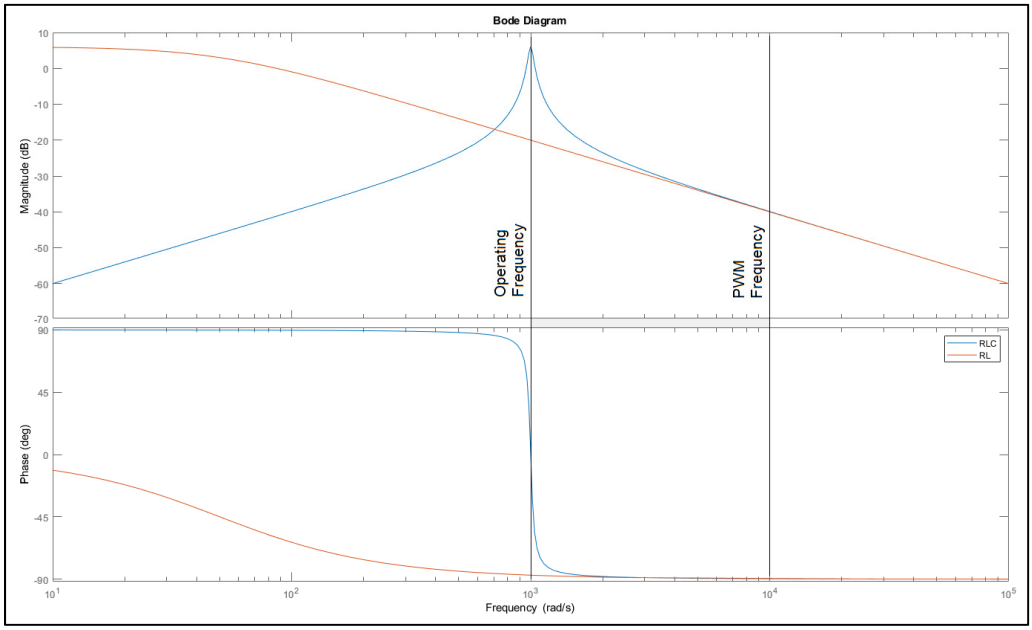

Figure 3.1 Comparison of the I/V gain frequency response between a LC and RLC circuit

From Figure 3.1, one can observe that the gain at the natural frequency of the RLC circuit is significantly above the gain of the RL circuit at the same frequency. Additionally, the gain difference between the operating frequency and the PWM frequency is significantly higher on the RLC circuit compared to the RL circuit, when the natural frequency of the RLC circuit matches the operating (or electrical) frequency of the motor. This behavior could potentially help reducing the current harmonics generated by the PWM switching at higher frequency.

3.3 Hypothesis #3

Hypothesis 3: The voltage amplification capability of the RLC circuit may bring the capacitor's voltage above the battery voltage, and therefore allow operating the motor at higher speeds while in MTPA.

As seen in section 1.2.1.3 previously, the motor's Back-EMF amplitude increase linearly with speed. Therefore, there is an operating speed where the power supply voltage is not enough to allow MTPA control. Typically, field weakening control is required to bring the motor speed past this speed. However, field weakening control maintains constant power, and therefore reduces torque as the speed increase. Adding the voltage of a pre-charged capacitor to the voltage of the inverter may allow MTPA control over a wider speed range. If the natural frequency of the RLC circuit matches the electrical frequency of the PMSM, the AC input voltage profile, generated by the PWM inverter, may be decreased below the motor's back-EMF, therefore potentially reducing the current harmonics induced by the PWM switching.

As seen in Figure 1.36, the resonant behavior of the RLC circuit itself has the capability to bring the capacitor's voltage above the battery voltage. Therefore, this phenomenon may be exploited in a way to bring the capacitor's voltage above the battery voltage. Figure 3.2 shows the capacitor voltage behavior in the RLC circuit when current is allowed to oscillate freely. On Figure 3.3, one can see that adding a diode to the circuit of Figure 3.2 allows to clamp the capacitor voltage at its maximum value. If the capacitor's polarity can be inverted with a H-bridge, one can see at Figure 3.4 that, when the polarity switch is done at zero current (ZCS),

the voltage in the capacitor is being gradually increased until the energy dissipated in the resistor is equal to the energy input. In this case, the capacitor voltage cannot be increased further.

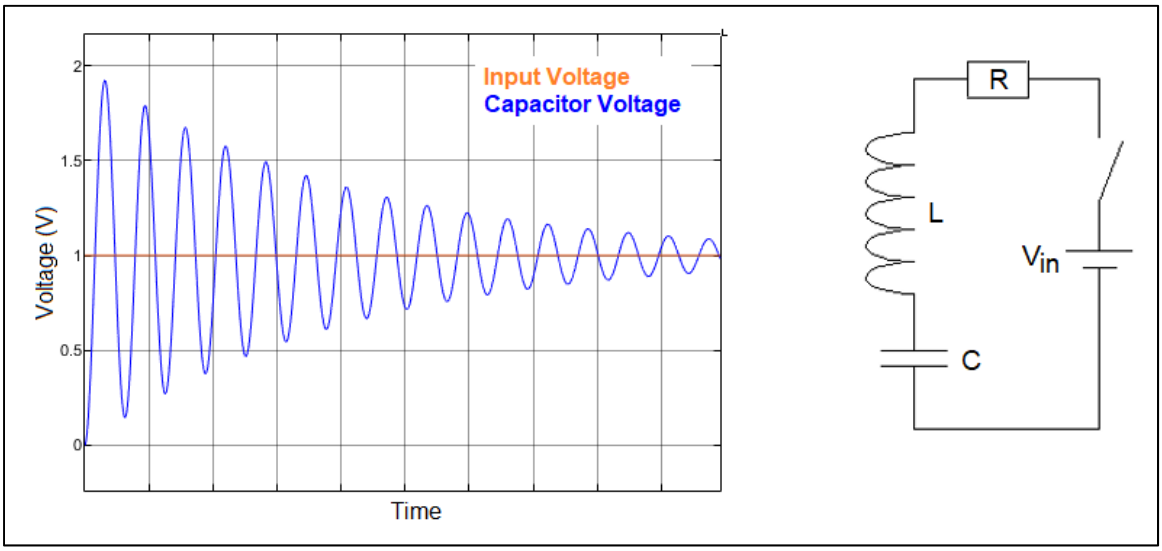

Figure 3.2 Free oscillating RLC circuit with 1V step input

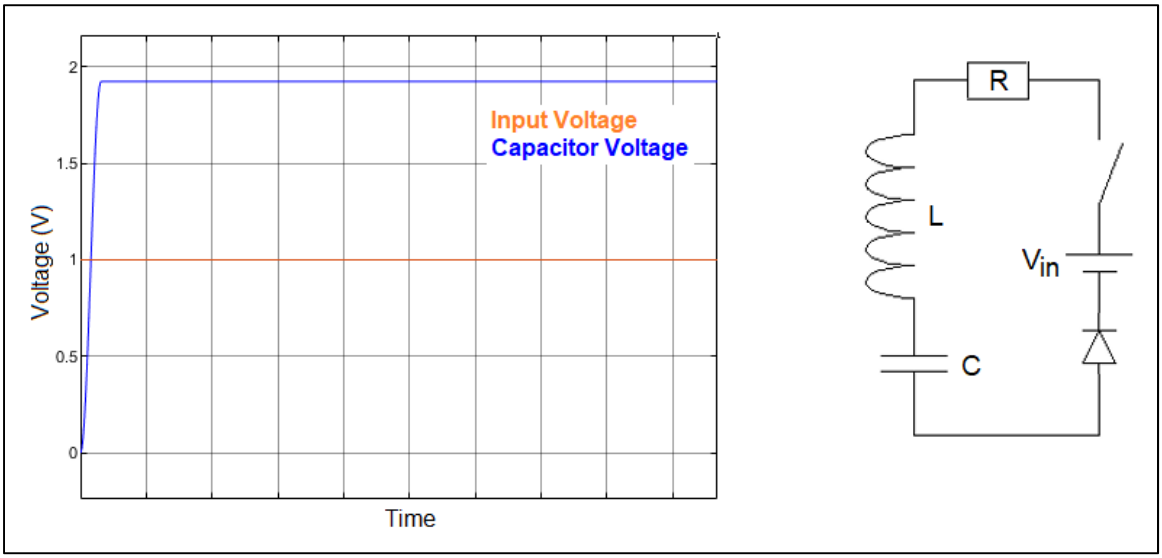

Figure 3.3 Clamped oscillating RLC circuit with 1V step input

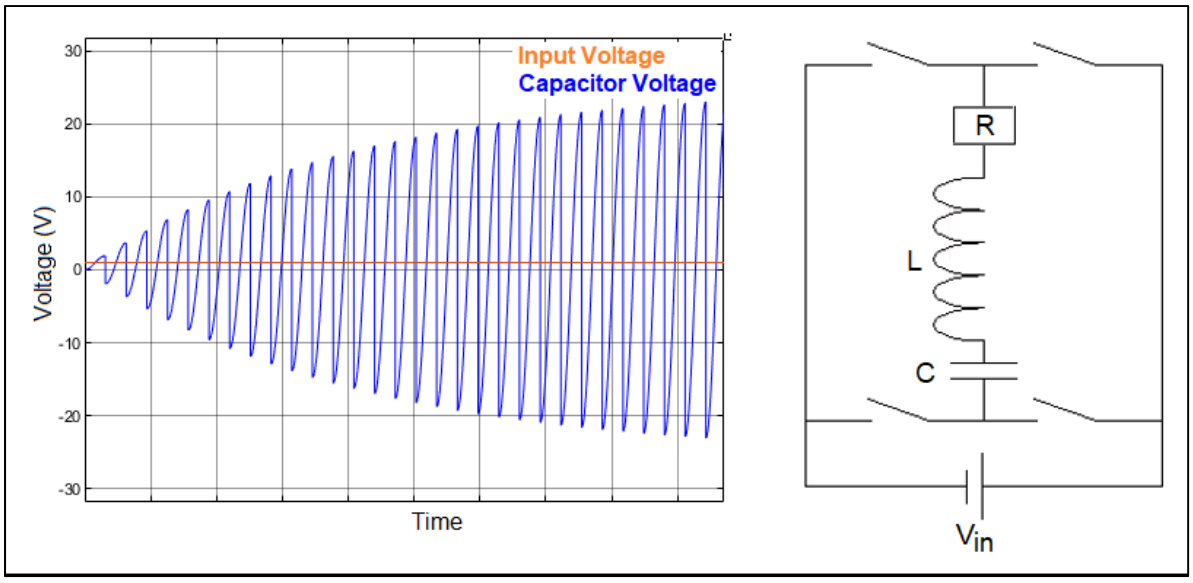

Figure 3.4 Oscillating RLC circuit with capacitor polarity inversion and 1V input

3.4 Hypothesis #4

Hypothesis 4: Unitary power factor at the natural frequency of the RLC circuit simplify the capacitor energy release schedule.

As seen previously in section 1.6, the power factor of an RLC circuit operating at its natural frequency is unitary. This means that in this particular frequency of operation, the input voltage and current vectors are in phase. This could simplify the timing of the capacitor's energy release in the motor phase.

CHAPTER 4

CONCEPT OF OPERATION OF THE RESONANT POWER PROCESSOR

In order to confirm the hypothesis enumerated in the previous section, a concept of converter has been developed during this master's project. This converter has been designed to use the properties of the electrical resonance for the supply of electrical power to the PMSM. In addition to supply power to the PMSM, the resonant dynamic behavior of the RLC circuit is used to pre-charge the capacitors of the converter before they are discharged in the motor phases. The use of an RLC circuit as the capacitor recharge circuit allows the pre-charged capacitors to reach voltages above the battery voltage.

The proposed converter allows to increase the phase voltage of a PMSM by adding the voltage of a pre-charged capacitor to the phase voltage. The functioning principle is that a Capacitor, embedded in a Configurable Capacitor Module, is being recharged through a dedicated Recharge Circuit before it is being discharged in a phase of the PMSM. The Capacitors are connected in series with the electrical machine phases; therefore, each motor phase becomes an RLC circuit. Each Capacitor can be connected to a maximum of one electric machine phase or one Recharge Circuit at once.

The scheduling of the capacitor pre-charge and discharge sequences is ensured by the control algorithm, which is implemented by software in a microcontroller (or by VHDL in a FPGA). The control algorithm also manages the routing of the capacitor discharge energy to the required motor phase and the routing of the discharged capacitors to the recharge circuit by commanding several switches. Finally, the control algorithm sets the capacitors polarity as per the needs of the conversion cycle.

It is to be noted that using the resonant behavior of the converter over a wide speed range require changing the converter's capacitance as a function of motor speed. As seen previously, the natural frequency of an RLC circuit is function of the values of resistance, inductance and capacitance. The motor phase inductances are typically fixed, as well as the phase resistance.

Therefore, the only option to match the RLC circuit natural frequency with the operating electrical frequency is by adjusting the capacitances according to the operating speed. In aerospace propulsion, operating speeds are typically steady over long period of times, and the speed set points are often pre-determined by design. The converter's capacitor banks may therefore be tuned to match a limited number of operating speed set points.

The proposed converter has been named "Resonant Power Processor", also referred as RPP in this present document. The detailed concept of operation is presented in this section.

4.1 Electrodynamic System Architecture

A PWM inverter is connected upstream of the Resonant Power Processor in order to make the electric machine phase voltage equal to the sum of the PWM inverter voltage and charged Capacitor voltage. See figure 4.1 for a visual representation of the system architecture. The system architecture presented herein is for powering a 3 phases PMSM. It is to be noted that the Resonant Power Processor is a component within the system.

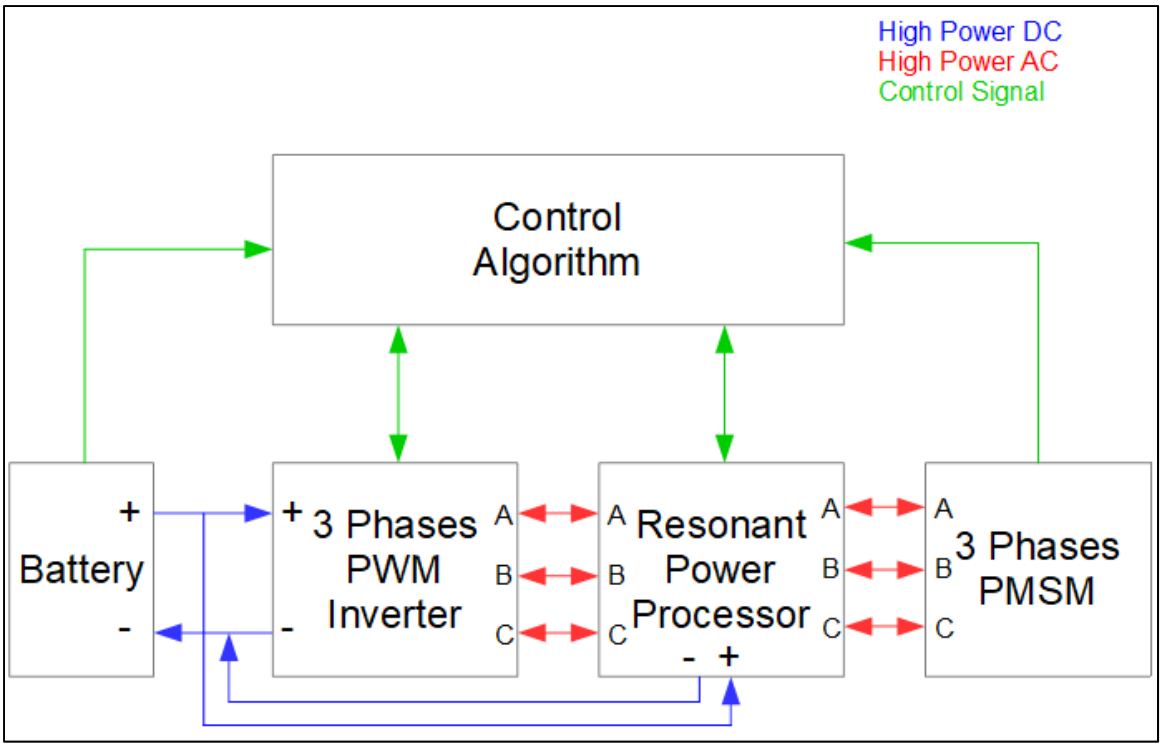

Figure 4.1 System architecture

4.1.1 Resonant Power Processor Architecture

The Resonant Power Processor contains 4 Configurable Capacitor Modules. Each Configurable Capacitor Module has the following configuration features: Electric Machine Phase/Recharge Circuit Selection (EMPRCS), Capacitor Polarity Selection (CPS) and Capacitance Setting (CS). The EMPRCS matches the Capacitors with electric machine phases or with the Recharge Circuit through a configuration of bidirectional switches (AX, BX, CX or RX switches, see Figure 4.3). Each Configurable Capacitor Module can be linked to only one electric machine phase or the Recharge Circuit at a time. CPS sets the polarity of the Capacitors with regards to the motor phase or the Recharge Circuit through H bridges (CPS switches, see Figure 4.3). CS sets the variable capacitance of the capacitors in order to match, as much as possible, the phase's RLC circuit natural frequency with the electrical frequency of the electric machine. Optimal operating condition is when the phase's RLC circuit natural frequency matches the electrical frequency of the electric machine. See Figure 4.3 for the

topology of the Variable Capacitor Module. EMPRCS, PS and CS features are managed by the Control Algorithm (See Section 4.1.2).

One Recharge Circuit is present in the Resonant Power Processor. The recharge circuit recharges the capacitors of the Resonant Power Processor in alternance in order to store the required amount of energy in each capacitor before it is discharged in an electric machine phase. Using the bi-directional switches of the Configurable Capacitor Module, the Recharge Circuit is connected in series to a Capacitor to be charged. The controlled DC voltage source of the Recharge Circuit can either apply the voltage of the DC source through a transistor or provide 0 Volt through a diode to allow current free wheeling to complete the charging process. A recharge inductor is connected in series with the recharging capacitor in order to benefit from the resonant dynamics of a RLC circuit during recharge. The recharge time is mainly driven by the natural frequency of the recharge inductance and capacitance combination and by the amount of energy to be added in the capacitor. As only one Recharge Circuit is present in the converter for 3 motor phases, the natural frequency of the Recharge circuit must be a least 3 times the natural frequency of the motor phase RLC circuit to prevent converter overrun. See Figure 4.4 for the topology of the Recharge Circuit. The capacitor recharge is managed by the Control Algorithm (See Section 4.1.2).

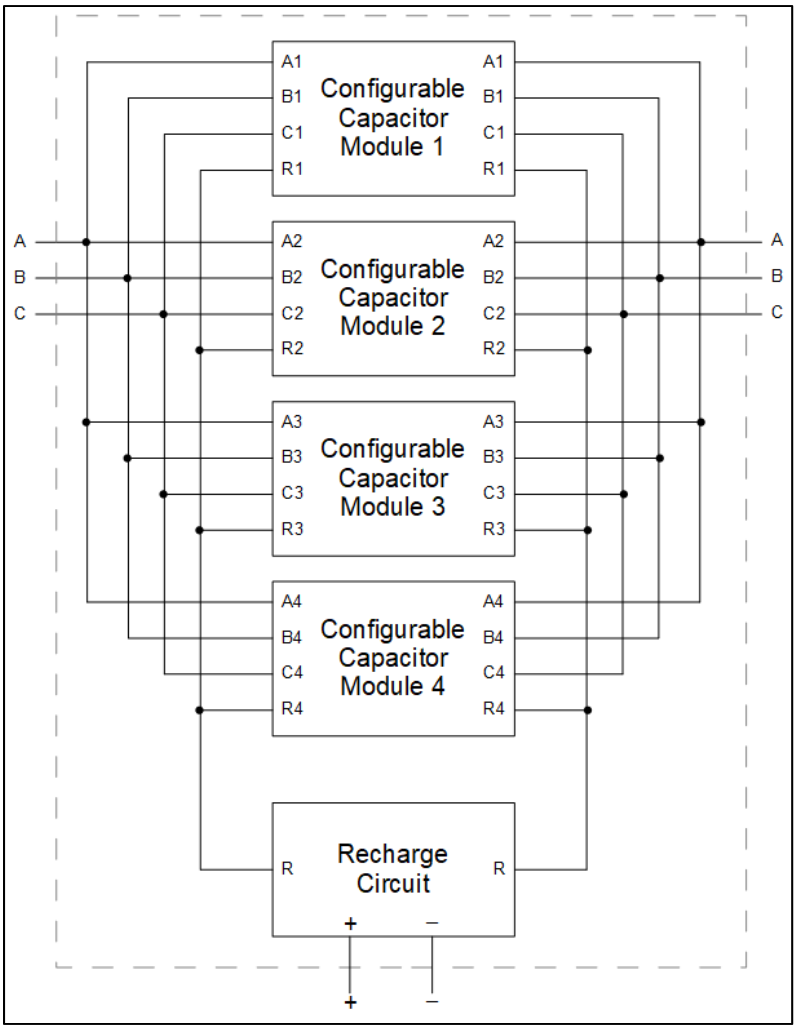

Figure 4.2 Resonant power Processor Architecture

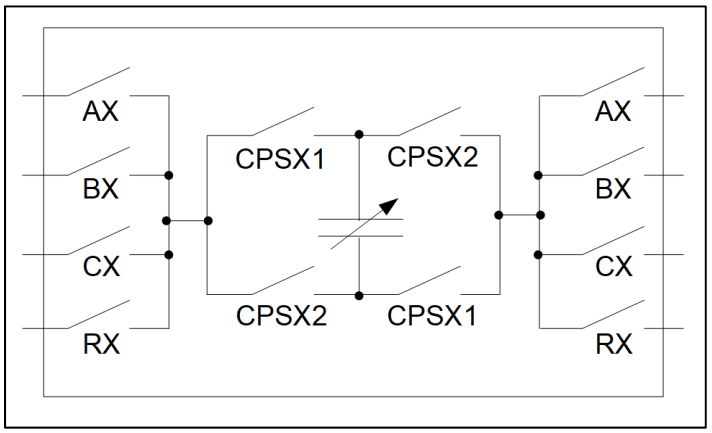

Figure 4.3 Topology of a Configurable Capacitance Module (Configurable Capacitor Module X)

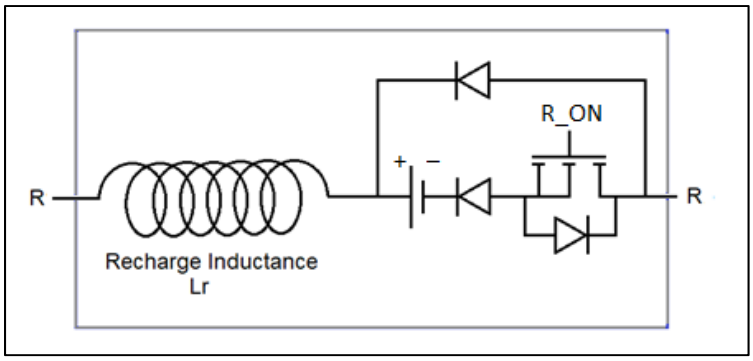

Figure 4.4 Topology of the Recharge Circuit

4.1.2 Control Algorithm

The Control Algorithm has 4 layers:

- Analog to Digital Signal Conversion: Converts the raw signal of the current sensors, voltage sensors and resolver position to digital data for the control algorithm.
- Main Sequencer: Oversees the system operation, matches the charged capacitors to electric machine phases for the discharge cycle and matches discharged capacitors to recharge circuits. Also schedules the recharging and discharging for the capacitors.
- Capacitor Module Controls: For each Configurable Capacitor Module, manages the Capacitor Module Control State Machine and operation for each State.
- RPP switches commands: Converts the digital Boolean value of the switch's statuses to electrical signals for the gate drivers.

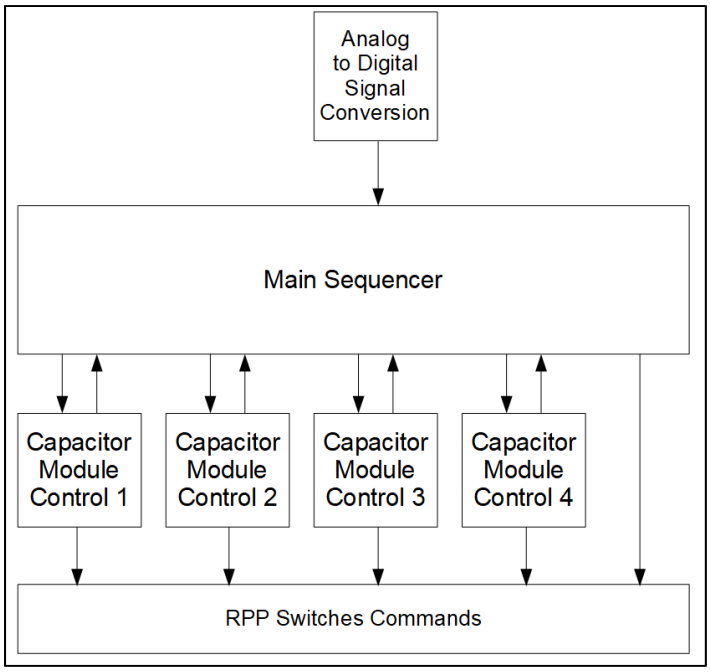

Figure 4.5 Control Algorithm architecture

4.1.2.1 Main Sequencer

The Main Sequencer is responsible for the following operations:

- Activation of the RPP when the motor speed threshold is reached.
- Electric machine phase selection for capacitor discharge and command of the phase selection bidirectional switches (AX, BX and CX switches).
- Recharge Circuit selection for capacitors recharge (RX switches).
- Setting of the Discharge Available signals for the Capacitor Module Controls.
- Setting the Recharge Available signals for the Capacitor Module Controls.
- Capacitor Voltage Request Calculation. The Capacitor Voltage Request is the voltage at which the capacitors must be charged before the Discharge cycle begins.

4.1.2.2 Capacitor Module Control

There is one Capacitor Module Control per Configurable Capacitor Module. Each Capacitor Control Module is responsible for the following operations:

- Processing Discharge Available signal from the Main Sequencer (Trigger for setting Discharging State).
- Processing Recharge Available signal from the Main Sequencer (Trigger for setting Recharging State).
- Determining the Recharge Cycle Done Boolean parameter.
- Determining the Discharge Cycle Done Boolean parameter.
- Determining the State of the Configurable Capacitor Module. The Configurable Capacitor Module States are: Discharged, Recharging, Recharged and Discharging.
- Determining the command of the Capacitor Polarity switches (CPSX1 and CPSX2 switches)
- Determining the capacitance of the capacitor modules through the capacitance setting switches (HX switches).
- Managing the capacitor recharge process to ensure that the recharged capacitor voltage is as per the Capacitor Voltage Request (R_ON transistor).

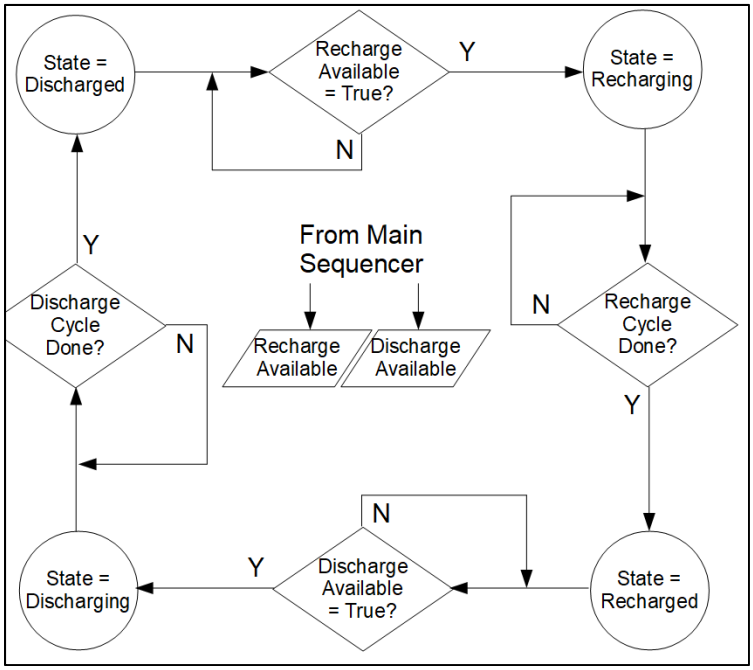

Figure 4.6 Capacitor Module Control State Machine

Discharged State:

In Discharged State, the capacitor has the lowest voltage of the cycle. In this State, the Capacitor Module Control is in standby for a Recharge Available signal from the Main Sequencer. In Discharged State, the following operations are performed:

- Setting of the Capacitors Polarity Switches to OFF (CPSX1 and CPSX2 switches) to isolate the capacitor from the rest of the circuit.
- Setting the variable capacitor's capacitance according to the Variable Capacitors Capacitance Request.

Recharging State:

In Recharging State, the Capacitor is connected in series to a Recharge Circuit. In Recharging State, the following operations are performed:

- Setting of the capacitor's polarity and command of the Capacitor Polarity Switches. The polarity of the Capacitor is set in a way that the positive voltage terminal of the capacitor (at initialization of the Recharging State) is connected to the input of the Recharge Circuit.
- Command of the Recharge Circuit selection bidirectional switches (RX switches).
- Monitoring of the recharge energy input and command of the recharge transistor (R_ON) while the capacitor energy is lower than the Capacitor Energy Request.
- Release the recharge transistor (R_ON) when the capacitor energy reaches the Capacitor Energy Request. Current is afterwards free wheeling until current is null.
- Detecting that the capacitor recharge is completed and setting Recharge Cycle Done signal.

Recharged State:

In Recharged State, the capacitor has the highest voltage of the cycle. In this State, the Capacitor Module Control is in standby for a Discharge Available signal from the Main Sequencer. In Recharged State, the following operations are performed:

- Setting of the Capacitors Polarity Switches to OFF (CPSX1 and CPSX2 switches) to isolate the capacitor from the rest of the circuit.

Discharging State:

In Discharging State, the Capacitor is connected in series with an electric machine phase. The electrical machine phase selection is performed by the Main Sequencer. In discharging state, the capacitor can only be connected to one electric machine phase at a time. In Discharging State, the following operations are performed:

- Setting of the capacitor's polarity and command of the Capacitor Polarity Switches. The polarity setting of the Capacitor depends on the desired capacitor polarity for a given discharge cycle.
- Detecting that the capacitor discharge cycle is completed and setting of the Discharge Cycle Done signal.

4.1.2.3 Control of the PWM inverter

Field Oriented Control can be used to control the electrodynamic system. As previously seen in section 1.5, the optimal Field Oriented Control strategy for a surface mounted (flat poles) PMSM is Zero D-Axis Current. If the PMSM was a salient poles machine, the optimal control algorithm would be Maximum Torque Per Amp (MTPA). However, in a system where it is important to match the capacitor's capacitance with the inductances of the PMSM, having to deal with a salient poles PMSM would add challenges. For this reason, operation of a flat poles PMSM is considered in this project. As seen in section 1.5 above, ZDAC Field Oriented Control strategy provides optimal control efficiency. It has been seen previously that the Maximum Efficiency control may slightly improve the efficiency, but in the high speed and low power region.

The PWM inverter voltage command is equal to the phase voltage command (generated by ZDAC Field Oriented Control) minus the actual voltage of the capacitor connected in series with the electric machine phase. Doing so allows to use the Field Oriented Control as is and therefore the capacitor's voltage is removed from the final voltage command to the inverter.

For a 3 phases inverter powering a 3 phases electric machine through the Resonant Power Processor, the inverter voltage commands are:

$$Va_{inv} = V_a^* - VC_a \quad (4.1)$$

$$Vb_{inv} = V_b^* - VC_b \quad (4.2)$$

$$Vc_{inv} = V_c^* - VC_c \quad (4.3)$$

Where:

Vx_{inv} is the inverter output voltage command for phase x (A, B or C).

V_x^* is the Field Oriented Control voltage command for phase x (A, B or C).

VCx is the real time voltage of the capacitor connected to phase x (A, B or C).

CHAPTER 5

IMPLEMENTATION OF THE RESONANT POWER PROCESSOR AND ITS SYSTEM

Bringing a concept to a functional prototype often requires more effort than developing the concept itself. Especially in the case of the Resonant Power Processor, many power electronics and control electronics features are not typically used in powering AC motors. Therefore, off the shelf components could not be found easily. The following section explains the implementation of the Resonant Power Processor. The descriptions are for the detailed design of the key components and the whole system.

Because of the dynamic response of an RLC circuit, the motor cannot be started with the capacitances in the circuit because at low frequency, the dynamic current response of an RLC circuit makes it impossible to circulate enough current in the motor phases. From the motor start to a pre-determined speed threshold, the Resonant Power Processor must be as much as possible invisible to the power electronic circuit, in order to allow only the inverter to power the motor. Activation of the RPP may be done from the speed where the RLC circuit gain exceeds the RL circuit gain. The design of the Resonant Power Processor includes this possibility. The capacitance being connected through a H-Bridge, closing both legs of the H-Bridge allows to bypass the capacitors.

It is assumed that a dedicated 16 Vdc power supply is available for the control electronics and for the gate drivers of the semi conductors. It is also assumed that the 16 Vdc power supply will be converted to +/- 15 Vdc, 5 Vdc and 2.5 Vdc for the instrumentation signals. This project does not cover the design of the power supplies in the system. However, those aspects will have to be taken care of when the first functional prototype will be materialized.

Based on a preliminary simulation and analysis, the maximum currents, voltages and powers in the different components have been found theoretically. From this data the requirements for all the components have been determined. The requirements for all the components can be

found in ANNEX I. ANNEX I also includes the functional requirements of the current and voltage sensors. The detailed implementation of the Resonant Power Processor's power electronic components as per the requirements has been performed by a team of three graduating students as an end of scholarship project (PFE - Projet de fin d'étude). A special thanks goes to Firas Al-Jilani, David Godin-Lebreux and Renaldo Myrtil for their work in implementing the detailed Power Electronic circuit components of the Resonant Power Processor. The final report provided by the team can be found in (Al-Jilani, Godin-Lebreux & Myrtil, 2020).

5.1 Electrical machine (PMSM)

For the project it was decided to use an off the shelf PMSM. One available PMSM was the ABB/Baldor BSM33C-6177MHQ. It has a continuous power of approximately 3 kW at 320 Vdc, which is an interesting power range for a proof of concept. It has 4 pairs of poles and has a sinusoidal back-EMF profile. It is a flat poles machine, meaning that the direct-axis inductance is equal to the quadrature-axis inductance. As the inductance does not vary with the rotor position, the natural frequency of the phase circuit will be stable through the electrical cycle. Motor specifications may be found at (https://www.baldor.com/catalog/BSM33C-3177MHQ).

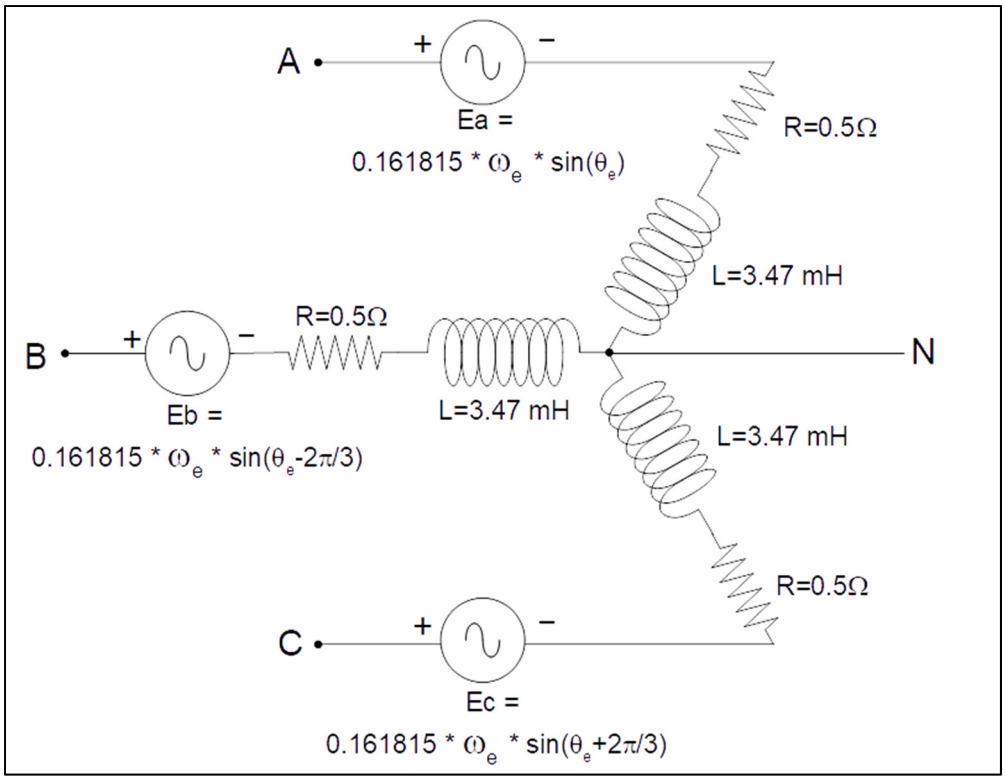

Figure 5.1 Electrical model of the ABB/Baldor BSM33C-6177MHQ PMSM (ω_e is the electrical frequency in rad/sec and θ_e is the electrical angle in rad)

In order to properly perform the Park transforms, the motor shall be equipped with a position encoder or resolver, which informs the control system of the rotor position. For this project, a 14 bits optical encoder has been assumed. A 14 bits resolver allows for a rotor angular position resolution of 0.022 degrees. As the motor owns 4 pairs of poles, the electrical angular position resolution 0.088 degrees.

5.2 3 Phases 2 Levels Inverter

Inverters are well known power electronic devices. They are typically used to power 3 phases devices such as motors by generating a line-to-line voltage of either 0V or +/- the DC link voltage. Operation of the RPP in combination with a 3 phases inverter requires specific characteristics that are not fulfilled by the typical 2 level inverter. Therefore, the typical inverter needs to be slightly modified to fulfill the requirements enumerated below:

- The inverter shall allow to control the voltage for each motor phase independently.
- The inverter shall generate a phase to neutral voltage of 0V or +/- $V_{dc}/2$.
- The inverter shall allow for free-wheeling phase current when the phase voltage is 0V.
- The inverter shall allow the phase current to be in the direction of the phase voltage or in the opposite direction of the phase voltage.
- The inverter shall allow to generate a positive voltage on all 3 phases simultaneously or a negative phase voltage on all 3 phases simultaneously.

The proposed topology of the modified 3 phases inverter is shown in Figure 5.2 below. It is essentially a Three-Level Neutral Point Clamped T-Type 3 level inverter as shown in Figure 1.13 of Section 1.3.4.2. The main difference is that the ground connection of the Three-Level Neutral Point Clamped is the connection to the motor neutral point on the proposed inverter. This allows to trade the 3 levels inverter capability with the capability to supply all negative or all positive phase voltages simultaneously. Also, the bi-directional switches commands are commanded by a NOR gate of both MOSFET commands on the same leg, unlike the Three-Level Neutral Point Clamped T-Type inverter. The output voltage of the proposed topology as a function of its semi-conductor devices status can be found in Table 5.1 below. It is to be noted that the bi-directional switches are ON when the MOSFETS of the same leg are OFF. The switching frequency of the inverter is set to 10 kHz and the Pulse length resolution is 1% (1 μs). The design of the modified inverter is detailed in ANNEX II.

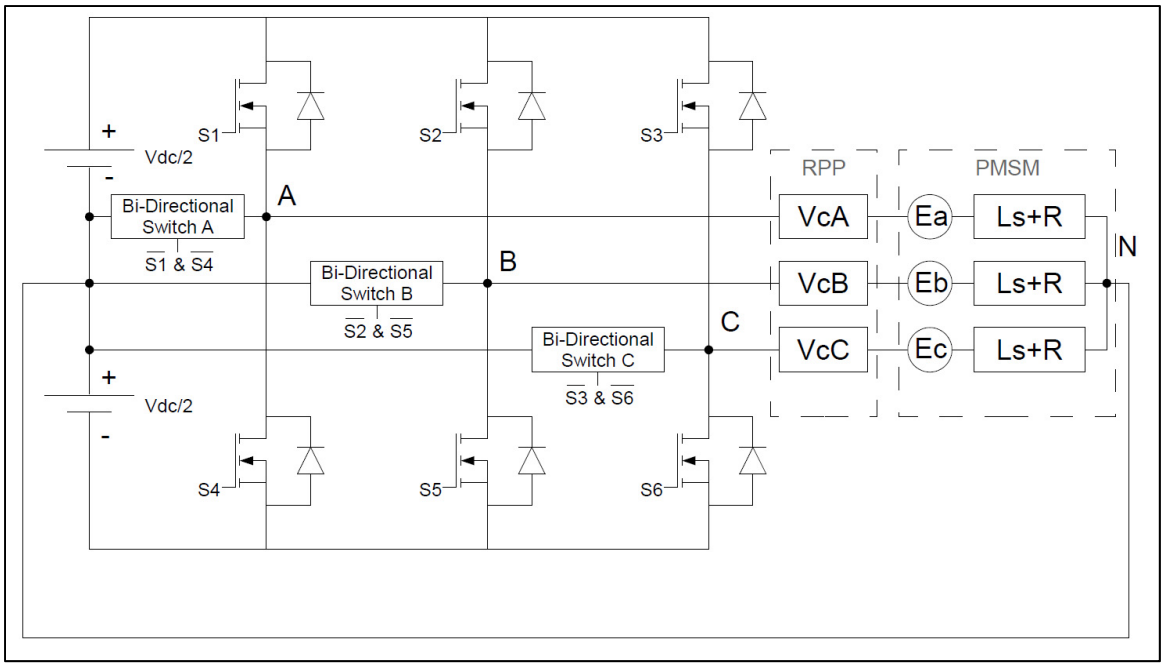

Figure 5.2 Proposed Modified 3 Phases 2 Level Inverter

Table 5.1 Inverter output voltage as a function of the semi-conductor's state

S1	S4	S2	S5	S3	S6	Van	Vbn	Vcn
0	0	0	0	0	0	0	0	0
0	0	0	0	0	1	0	0	-Vdc/2
0	0	0	0	1	0	0	0	Vdc/2
0	0	0	1	0	0	0	-Vdc/2	0
0	0	0	1	0	1	0	-Vdc/2	-Vdc/2
0	0	0	1	1	0	0	-Vdc/2	Vdc/2
0	0	1	0	0	0	0	Vdc/2	0
0	0	1	0	0	1	0	Vdc/2	-Vdc/2
0	0	1	0	1	0	0	Vdc/2	Vdc/2
0	1	0	0	0	0	-Vdc/2	0	0
0	1	0	0	0	1	-Vdc/2	0	-Vdc/2
0	1	0	0	1	0	-Vdc/2	0	Vdc/2
0	1	0	1	0	0	-Vdc/2	-Vdc/2	0
0	1	0	1	0	1	-Vdc/2	-Vdc/2	-Vdc/2
0	1	0	1	1	0	-Vdc/2	-Vdc/2	Vdc/2
0	1	1	0	0	0	-Vdc/2	Vdc/2	0
0	1	1	0	0	1	-Vdc/2	Vdc/2	-Vdc/2

Table 5.1 Inverter output voltage as a function of the semi-conductor's state (Continued)

S1	S4	S2	S5	S3	S6	Van	Vbn	Vcn
0	1	1	0	1	0	-Vdc/2	Vdc/2	Vdc/2
1	0	0	0	0	0	Vdc/2	0	0
1	0	0	0	0	1	Vdc/2	0	-Vdc/2
1	0	0	0	1	0	Vdc/2	0	Vdc/2
1	0	0	1	0	0	Vdc/2	-Vdc/2	0
1	0	0	1	0	1	Vdc/2	-Vdc/2	-Vdc/2
1	0	0	1	1	0	Vdc/2	-Vdc/2	Vdc/2
1	0	1	0	0	0	Vdc/2	Vdc/2	0
1	0	1	0	0	1	Vdc/2	Vdc/2	-Vdc/2
1	0	1	0	1	0	Vdc/2	Vdc/2	Vdc/2

5.3 Resonant Power Processor (Power Electronics, Instrumentation and Control Signals)

The Resonant Power Processor is the subsystem between the inverter and the motor. It applies a phase voltage boost equal to the capacitor voltage in addition to convert the phase circuit into an RLC circuit. Optimal operation of the RPP is when the natural frequency of the RLC circuit matches the electrical frequency of the PMSM. The Resonant Power Processor has 4 Configurable Capacitor Modules and 1 Recharge Circuit. A total of 3 Configurable Capacitor Module are always connected to the motor phases. It is therefore essential to have at least one Configurable Capacitor Module that is available to be recharged through the Recharge Circuit at all times. Figure 5.3 below shows the detailed architecture of the Resonant Power Processor in terms of Power Electronics and instrumentation electronics. The current and voltage transducers have been determined by the team of Firas Al-Jilani, David Godin-Lebreux and Renaldo Myrtil in (Al-Jilani et al., 2020).

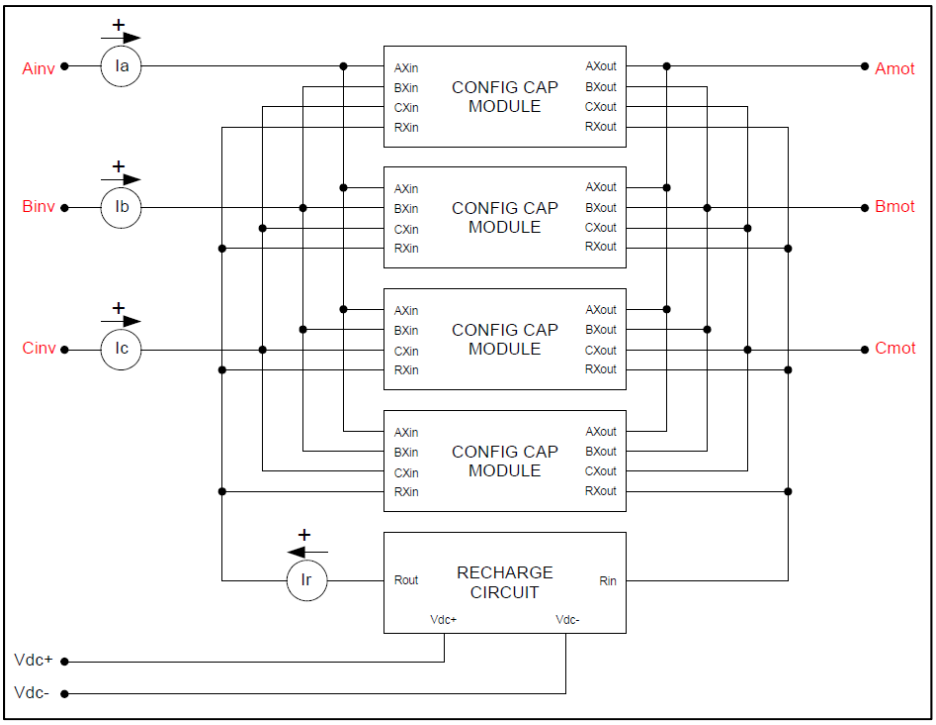

Figure 5.3 Resonant Power Processor Architecture

5.3.1 Configurable Capacitor Module

The Configurable Capacitor Module has three roles. The first role is to configure the circuit to route the capacitor to the PMSM phase or recharge circuit it shall be routed to (Electric Machine Phase/Recharge Circuit Selection, EMPRCS). This is done through the AX, BX, CX and RX switches. The second role is to set the capacitor's polarity in order to apply the voltage in the desired direction (Capacitor Polarity Selection, CPS). This is done through the H-Bridge connection and the CPSX1 and CPSX2 switches. The third role of the Configurable Capacitor Module is to adjust the capacitance of the capacitors according to the operating speed of the PMSM (Capacitance Setting, CS). This is done using the HX switch. Figure 5.4 shows the Configurable Capacitor Module sub-assembly. The voltage transducer has been determined by the team of Firas Al-Jilani, David Godin-Lebreux and Renaldo Myrtil in (Al-Jilani et al. 2020).

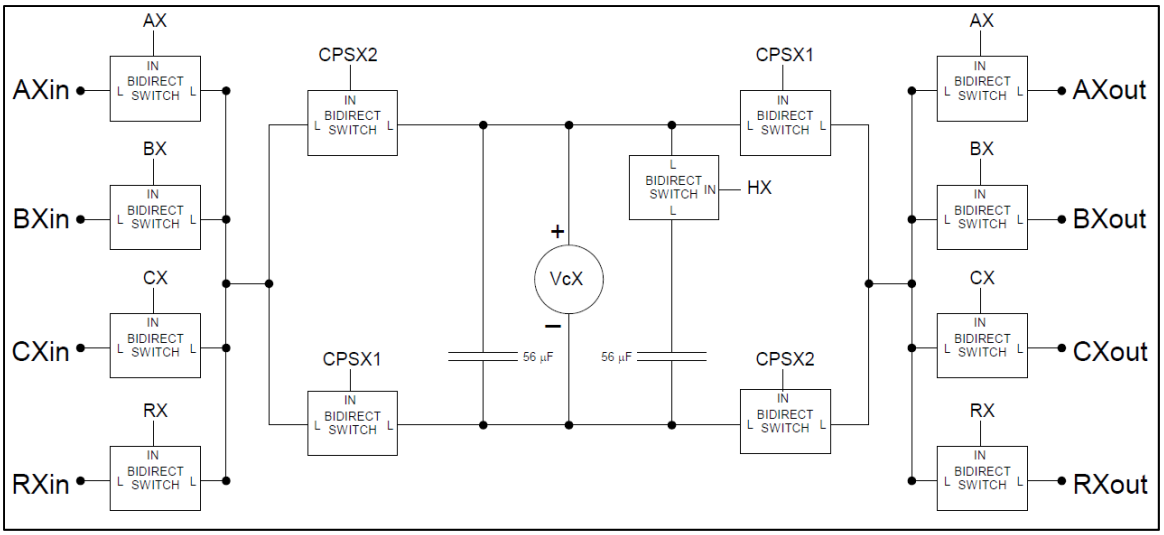

Figure 5.4 Configurable Capacitor Module architecture

5.3.1.1 56 µF Capacitor Banks

No 56 µF capacitors which comply to the requirements were available off the shelf. For this reason, a capacitor bank has been developed by the team of Firas Al-Jilani, David Godin-Lebreux and Renaldo Myrtil. The capacitors must be bi-polar as the current and voltage through them will constantly change direction and polarity. Kemet film capacitors have been selected for the application. The 56 µF capacitor bank detailed design is documented in (Al-Jilani et al., 2020) and in ANNEX II. The implementation of the 56 µF capacitor banks makes the actual capacitance being 55 µF instead of 56 µF. However, as per the requirements in ANNEX I, 55 µF is within the tolerance range. Despites that the implementation of the capacitor banks makes it 55 µF, the capacitor banks will still be referred as the 56 µF capacitor banks throughout this document.

5.3.1.2 Variation of the capacitance

As mentioned previously, the power capacitor's capacitance must be adjusted to match the resonant frequency with the motor speed when the motor speed varies. Even if one operating speed is targeted by the proposed system, transient speed excursions are inevitable, especially

during motor run-up. It is to be remembered that below a pre-determined speed, the Resonant Power Processor configures itself to allow the inverter to power the PMSM alone. For this design, a variable capacitor with 2 possible capacitance values has been implemented. The capacitance value may be either 56 µF or 112 µF, depending on the selected configuration. Two 56 µF capacitors are connected in parallel making a 112 µF capacitance. One of the capacitors may be removed from the circuit by opening the Bi-directional switch HX, and then the capacitance becomes 56 µF.

5.3.1.3 Bi-directional switch (IGBT)

The Bi-Directional switches are a key element in the design of the Resonant Power Processor. They must prevent current to circulate when they are OFF, and they must allow the current to circulate with the minimum resistance or losses as possible when they are ON. They must transition from one state to the other as quickly as possible to the command signal in order to prevent shoot-through in the circuit. Because of the operating frequency and response time requirements, relays are unfit for this application. Instead, semi-conductors have been selected to create the Bi-directional switches. The principle is that the control signal is directed simultaneously to two IGBTs connected in anti-parallel. When the control signal is OFF, both IGBTs and diodes prevent the current to circulate. When the control signal is ON, the current flows through the first IGBT and through the second diode. This applies for both current directions. The IGBT based bi-directional switches have been simulated in (Al-Jilani et al., 2020) and the simulation results show that this setup is suitable for a Bi-Directional switch. The IGBTs part number and the Gate Drivers part number have been determined by the team of in (Al-Jilani et al., 2020).

5.3.2 Recharge Circuit

The Recharge circuit has the role to recharge each capacitor at the desired voltage level before it is discharged in a motor phase. The current in the Recharge Circuit is unidirectional, thanks to the feature to select the polarity of the capacitors (CPS). The Recharge circuit may either apply the DC-Link voltage to the recharge circuit (power branch) or zero volt (Free wheeling

branch). When the DC-link voltage is applied, the current circulates in the power branch through the MOSFET and through the voltage source. When 0 Volt is applied, the current circulates in the free-wheeling branch through the diode. The diode connected to the power branch is for protection purpose only. With enough confidence in the switching schedule, the power branch diode would not be necessary. Figure 5.5 shows the topology of the Recharge Circuit.

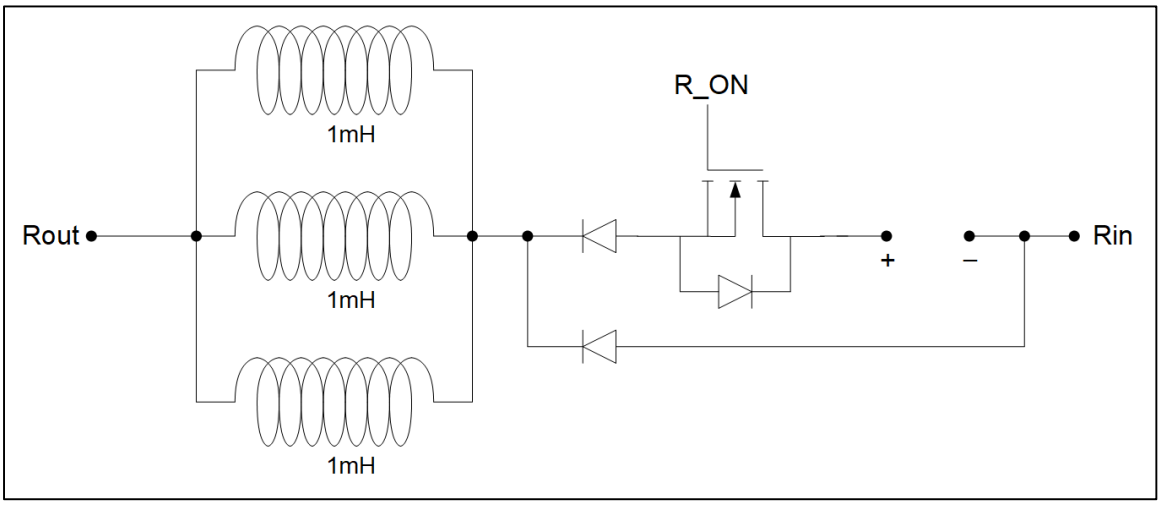

Figure 5.5 Recharge Circuit Architecture

5.4 Implementation of the control algorithm

The control algorithm's primary role is to control the PMSM speed to a fixed target by managing the motor torque, and therefore the phase currents. This is achieved by operating both the inverter and the Resonant Power Processor simultaneously. At low speed, the Resonant Power Processor is offline and does not contribute to the phase voltages of the PMSM. When the PMSM speed reaches the RPP activation speed, the RPP goes online and the RPP's capacitors voltages are added to the PMSM phase voltages.

When the RPP is offline, the control algorithm consists of a typical Field Oriented Control with ZDAC control algorithm (the Baldor/ABB BSM33C-6177MHQ PMSM is a flat poles machine), and only the inverter supplies power to the PMSM.

When the RPP is online, the control algorithm manages the capacitor's recharge and discharge cycles. The recharge cycle recharges the configurable capacitor modules in alternance to a specific voltage target. The discharge cycle discharges the capacitors into motor phases. The control algorithm also configures the capacitance of the capacitors using the HX switches and the polarity of the capacitors using the capacitor polarity switches (CPSX1 and CPSX2) of each Capacitor Module. The Field Oriented Control with ZDAC control algorithm remains responsible for commanding the inverter's output voltage, but the RPP's capacitors voltages are subtracted from the FOC voltage command (See Equations 4.1 to 4.3).

The control algorithm contains 5 layers; The Electrical Frequency Calculation, the Main Sequencer, the Capacitor Modules Control, the Field Oriented Control and the inverter command. The control algorithm executes its code at a frequency of 1 MHz, or every 1 µs. Initial simulations used an algorithm execution frequency of 100 kHz, however it was decided to try to execute the control algorithm at a faster frequency than required in order to demonstrate capability of operation at higher motor speed. The control algorithm has been synthetized in VHDL code for implementation in a FPGA. As the system requires a fast execution of the control algorithm, and as the control algorithm generally consists of simple operations that can be implemented as a flow chart, the FPGA was deemed the best type of microcontroller for this application.

The detailed implementation of the Resonant Power Processor' control electronics as per the requirements has been performed by a team of three graduating students as an end of scholarship project (PFE - Projet de fin d'étude). A special thanks goes to Francis Binette, Gabriel Huard-Desjardins and Sébastien Lavoie for their work in implementing the detailed Control Electronic components of the Resonant Power Processor. The final report provided by the team can be found in (Binette, Huard-Desjardins & Lavoie, 2021). Their report lists all the components and control electronic sub assemblies required to materialize the control electronics of the Resonant Power Processor. Their report also details the interfaces between the sensors of the Power Electronics and the control FPGA.

The following section is structured in order to represent the data flow of the control algorithm through those 5 layers.

Table 5.2 Inputs of the Control Algorithm

Parameter	Description	Unit	Min	Max	Type
Ia	Motor phase A current	A	-50.0	50.0	fix(1,16,9)
Ib	Motor phase B current	A	-50.0	50.0	fix(1,16,9)
Ic	Motor phase C current	A	-50.0	50.0	fix(1,16,9)
Ir	Recharge circuit current	A	0.0	200.0	fix(1,16,7)
Vc1	Capacitor 1 voltage	V	-400.0	400.0	fix(1,16,6)
Vc2	Capacitor 2 voltage	V	-400.0	400.0	fix(1,16,6)
Vc3	Capacitor 3 voltage	V	-400.0	400.0	fix(1,16,6)
Vc4	Capacitor 4 voltage	V	-400.0	400.0	fix(1,16,6)
Vdc	DC-Link (Battery) voltage	V	0.0	400.0	fix(1,16,6)
theta_motor	Rotor angular position	rad	0.0	6.2828	fix(1,12,8)
w_motor	Rotor angular speed	Rad/sec	-750.0	750.0	fix(1,12,1)
sawtooth	10 kHz Inverter PWM carrier signal	N/A	0.0	1.0	fix(1,16,14)

Table 5.3 Outputs of the Control Algorithm

Parameter	Description	Unit	Min	Max	Type
A1	RPP Switch A1 command	N/A	false	true	Boolean
B1	RPP Switch B1 command	N/A	false	true	Boolean
C1	RPP Switch C1 command	N/A	false	true	Boolean
R1	RPP Switch R1 command	N/A	false	true	Boolean
CPS11	RPP Switch CPS11 command	N/A	false	true	Boolean
CPS12	RPP Switch CPS12 command	N/A	false	true	Boolean
H1	RPP Switch H1 command	N/A	false	true	Boolean
A2	RPP Switch A2 command	N/A	false	true	Boolean
B2	RPP Switch B2 command	N/A	false	true	Boolean
C2	RPP Switch C2 command	N/A	false	true	Boolean
R2	RPP Switch R2 command	N/A	false	true	Boolean
CPS21	RPP Switch CPS21 command	N/A	false	true	Boolean
CPS22	RPP Switch CPS22 command	N/A	false	true	Boolean

Table 5.3 Outputs of the Control Algorithm (Continued)

Parameter	Description	Unit	Min	Max	Type
H2	RPP Switch H2 command	N/A	false	true	Boolean
A3	RPP Switch A3 command	N/A	false	true	Boolean
B3	RPP Switch B3 command	N/A	false	true	Boolean
C3	RPP Switch C3 command	N/A	false	true	Boolean
R3	RPP Switch R3 command	N/A	false	true	Boolean
CPS31	RPP Switch CPS31 command	N/A	false	true	Boolean
CPS32	RPP Switch CPS32 command	N/A	false	true	Boolean
H3	RPP Switch H3 command	N/A	false	true	Boolean
A4	RPP Switch A4 command	N/A	false	true	Boolean
B4	RPP Switch B4 command	N/A	false	true	Boolean
C4	RPP Switch C4 command	N/A	false	true	Boolean
R4	RPP Switch R4 command	N/A	false	true	Boolean
CPS41	RPP Switch CPS41 command	N/A	false	true	Boolean
CPS42	RPP Switch CPS42 command	N/A	false	true	Boolean
H4	RPP Switch H4 command	N/A	false	true	Boolean
R_ON	RPP MOSFET R_ON command	N/A	false	true	Boolean
S1	Inverter MOSFET S1 command	N/A	false	true	Boolean
S2	Inverter MOSFET S2 command	N/A	false	true	Boolean
S3	Inverter MOSFET S3 command	N/A	false	true	Boolean
S4	Inverter MOSFET S4 command	N/A	false	true	Boolean
S5	Inverter MOSFET S5 command	N/A	false	true	Boolean
S6	Inverter MOSFET S6 command	N/A	false	true	Boolean

5.4.1 Electrical frequency calculation

The electrical frequency is equal to the number of pole pairs multiplied with the rotor angular speed. This simple equation is shown at Equation (5.1) below:

$$w\_e = P_p \cdot w\_motor \tag{5.1}$$

Table 5.4 Constants of the Electrical Frequency Calculation

Parameter	Description	Unit	Value
Pp	Number of pole pairs	N/A	4

Table 5.5 Inputs of the Electrical Frequency Calculation

Parameter	Description	Unit	Min	Max	Type
w_motor	Rotor angular speed	Rad/sec	-750.0	750.0	fix(1,12,1)

Table 5.6 Outputs of the Electrical Frequency Calculation

Parameter	Description	Unit	Min	Max	Type
w_e	Electrical frequency of the PMSM	rad/sec	-4800	4800	fix(1,16,3)

5.4.2 Main Sequencer Algorithm

The Main sequencer algorithm performs the following sub-tasks:

Initialization of the boolean parameters

The state of some booleans remain from cycle to cycle until a command to change its' states occurs. In some cases, a control cycle will not command a change on a boolean parameter, therefore its state will remain the same as the previous cycle. The previous cycle parameter value must be remembered by the DSP. This sub-task initializes the states of those Booleans to the previous cycle value. See Figure 5.6 below.

Calculation of Rotor Position for every Phase

The rotor position is computed from every phase point of view. The rotor position relative to each phase is a signal used by the Motor Phase Scheduling sub-function in order the determine the moment where the charge capacitor can start its discharge cycle and in what motor phase to discharge. See Figure 5.6 below.

Determination of the Resonant Power Processor Status

The Resonant Power Processor Status sub-function determines if the Resonant Power Processor (RPP) is online or offline based on the motor speed. This is done by generating the

BOOST_ON signal, which is an input to the Configurable Capacitor Modules. When the Boolean “BOOST_ON” is true, the RPP is online. See Figure 5.6 below.

Operation of the Resonant Power Processor

If the Resonant Power Processor is online (“BOOST_ON” Boolean is set to true), then the Main Sequencer performs the tasks enumerated below. Otherwise, the Resonant Power Processor goes offline and creates a pass-through path for the phase currents without any additional contribution to the system.

- Scheduling the Recharge Circuit

This sub-task schedules the recharge circuit to recharge each capacitor in alternance. This sub-task monitors the capacitor module’s states and when a capacitor is discharged and the recharge circuit is available, it matches the discharged capacitor with the recharge circuit using the “RX” switches. It ensures that only one capacitor is commanded to be recharged at a time. This sub-task generates the “Rec_AvailX” signal when the Capacitor X is ready for recharge. The “Rec_AvailX” is an input to the Configuration Capacitor Modules.

- Scheduling the Motor phases

The logic monitors the capacitor module’s states and when a capacitor is charged, it waits for a motor phase zero back-EMF threshold to enable the discharge of the capacitor in the selected rotor phase. Because at the resonant frequency the power factor is 1, the capacitor discharge process can be timed with the Back-EMF zero crossing of the motor phases. Every time a motor phase crosses the zero Back-EMF position, a charged capacitor is matched to the motor phase. This is done by scheduling the phase selection switches (AX, BX and CX). The control algorithm ensures that only one motor phase is connected to a Configurable Capacitor Module at the same time. This logic generates the “Dis_AvailX” signal, which are inputs to the Configurable Capacitor Modules.

- Calculation of the Capacitor Voltage Request

Depending on the operating speed of the PMSM, the capacitor voltage needs to be adjusted to provide the optimal efficiency, lower current harmonics and torque ripples. This is done by generating the Vc_req parameter, which is an input to the Configurable Capacitor Modules. See Figure 5.11 below.

- Multiplexing of the rotor angle from capacitors' point of view

The rotor position data provides the rotor position from the motor phases point of view. However, from the point of view of the different Configurable Capacitor Modules, a signal routing operation needs to be performed. This sub-task computes the rotor angle from the capacitor's point of view (theta_e1 to theta_e4 signals) as a function of the phase selection switches (AX, BX and CX) and recharge circuit selection switches (RX). The rotor angle from capacitors point of view are inputs to the different Configurable Capacitor Modules and are used to manage the discharge cycle. See Equation (5.2) below.

$$\begin{bmatrix} A1 & B1 & C1 & R1 \\ A2 & B2 & C2 & R2 \\ A3 & B3 & C3 & R3 \\ A4 & B4 & C4 & R4 \end{bmatrix} \times \begin{bmatrix} theta\_eA \\ theta\_eB \\ theta\_eC \\ 0 \end{bmatrix} = \begin{bmatrix} theta\_e1 \\ theta\_e2 \\ theta\_e3 \\ theta\_e4 \end{bmatrix} \tag{5.2}$$

- Multiplexing of the current sensor data.

The current sensors are measuring the three phase currents and the recharge current. However, from the point of view of the different Configurable Capacitor Modules, a signal routing operation needs to be performed for each Configurable Capacitor Module to access its current amplitude information. This sub-task computes the current from the capacitor's point of view (I1 to I4) as a function of the phase selection switches (AX, BX and CX) and recharge circuit selection switches (RX). The current from the capacitor's point of view are inputs to the different Configurable Capacitor Modules and are used to determine the moment when the recharge cycle is completed. Also, those current signals are used by the Configurable Capacitor Modules to determine when to interrupt the recharge energy input. See Equation (5.3) below.

$$\begin{bmatrix} A1 & B1 & C1 & R1 \\ A2 & B2 & C2 & R2 \\ A3 & B3 & C3 & R3 \\ A4 & B4 & C4 & R4 \end{bmatrix} \times \begin{bmatrix} Ia \\ Ib \\ Ic \\ Ir \end{bmatrix} = \begin{bmatrix} I1 \\ I2 \\ I3 \\ I4 \end{bmatrix} \tag{5.3}$$

- Multiplexing of the capacitor's voltage data.

The capacitor voltage data provides the Capacitors' voltage data for each Configurable Capacitor Module. However, from the point of view of the different motor phases, a signal routing operation needs to be performed for each motor phase to have the voltage of the capacitor connected to it. This sub-task computes the capacitor's voltage from the motor phase point of view (VcA, VcB and VcC signals) as a function of the configuration phase selection switches (AX, BX and CX), and as a function of the Capacitor Polarity Switches (CPSX1 and CPSX2). The capacitor voltage from the motor phase point of view is used to set the phase voltage command to the inverter. See Equations (5.4) and (5.5) below.

$$\begin{bmatrix} -1 & 1 \end{bmatrix} \times \begin{bmatrix} CPS11 & CPS21 & CPS31 & CPS41 \\ CPS12 & CPS22 & CPS32 & CPS42 \end{bmatrix} = \begin{bmatrix} sign1 & sign2 & sign3 & sign4 \end{bmatrix} \tag{5.4}$$

$$\begin{bmatrix} A1 & A2 & A3 & A4 \\ B1 & B2 & B3 & B4 \\ C1 & C2 & C3 & C4 \\ 0 & 0 & 0 & 0 \end{bmatrix} \times \begin{bmatrix} sign1 & 0 & 0 & 0 \\ 0 & sign2 & 0 & 0 \\ 0 & 0 & sign3 & 0 \\ 0 & 0 & 0 & sign4 \end{bmatrix} \times \begin{bmatrix} Vc1 \\ Vc2 \\ Vc3 \\ Vc4 \end{bmatrix} = \begin{bmatrix} VcA \\ VcB \\ VcC \\ 0 \end{bmatrix} \tag{5.5}$$

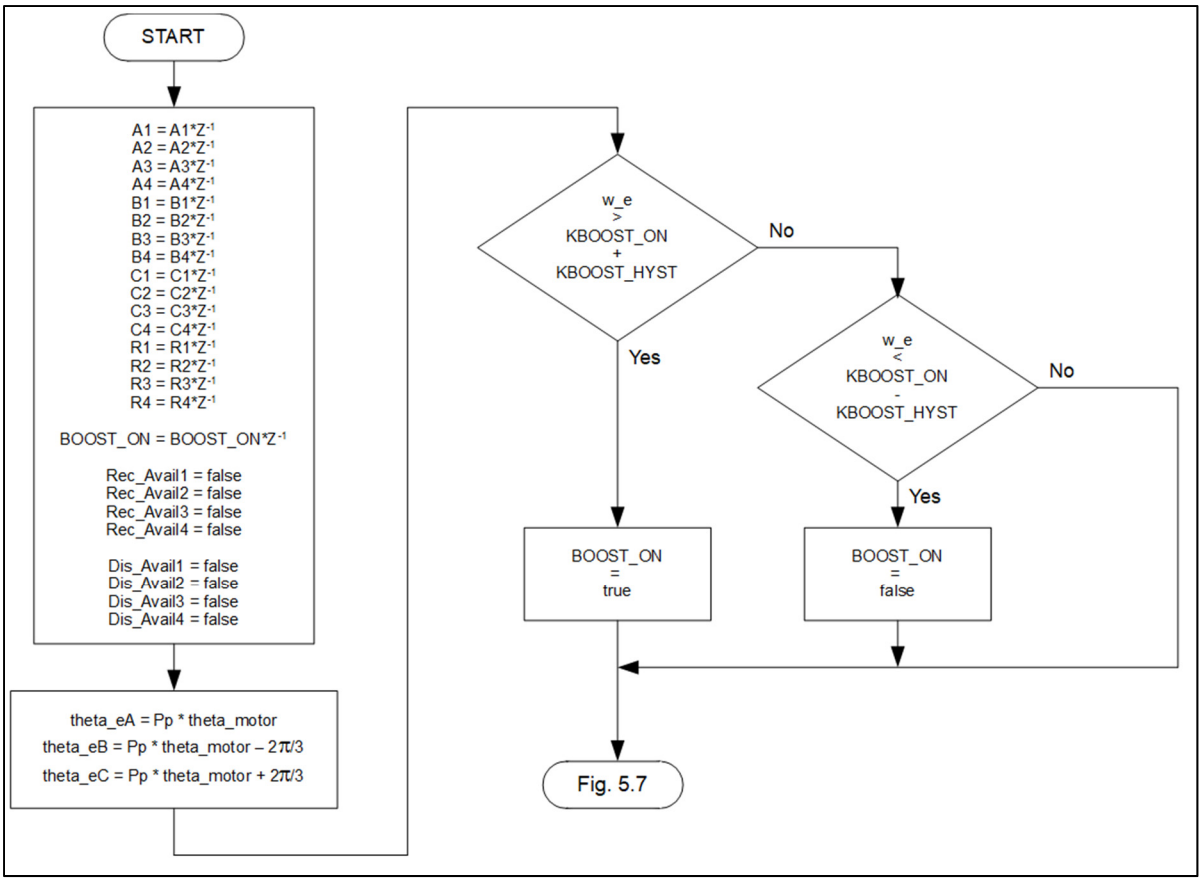

Figure 5.6 Main Sequencer Algorithm (1/6)

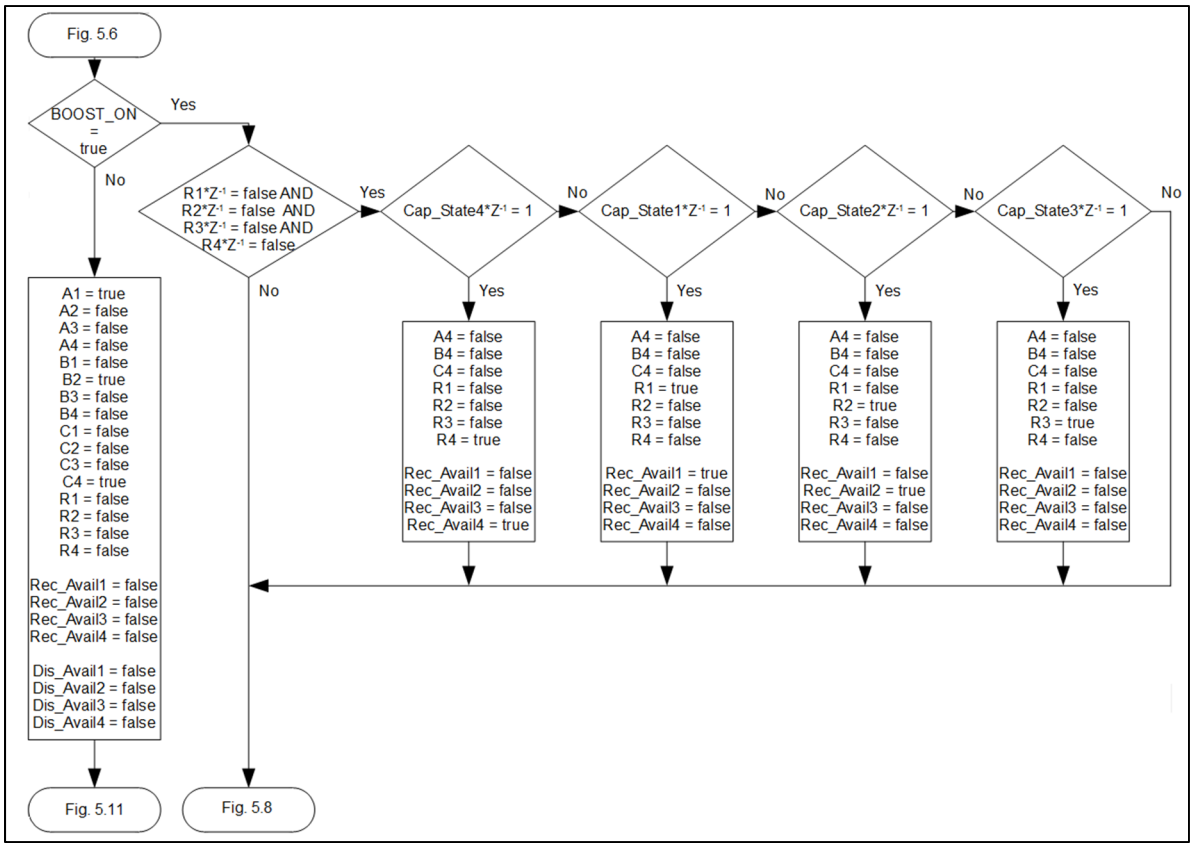

Figure 5.7 Main Sequencer Algorithm (2/6)

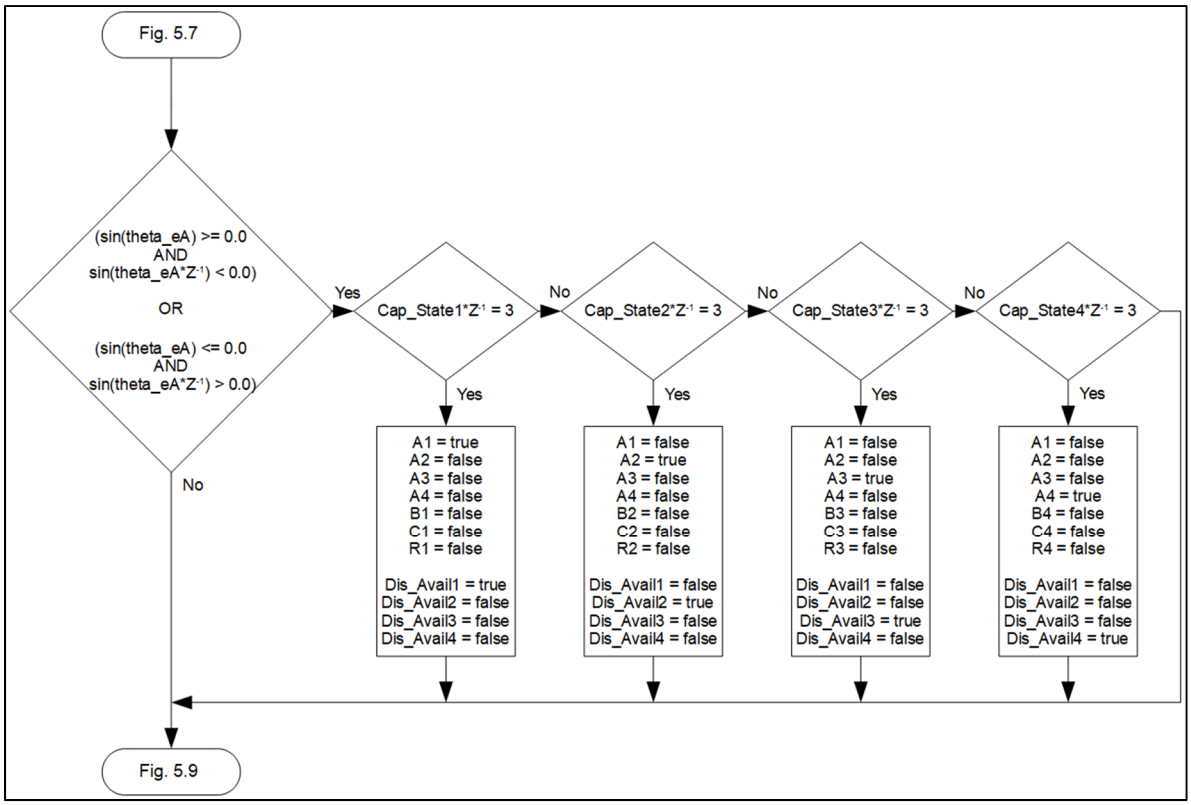

Figure 5.8 Main Sequencer Algorithm (3/6)

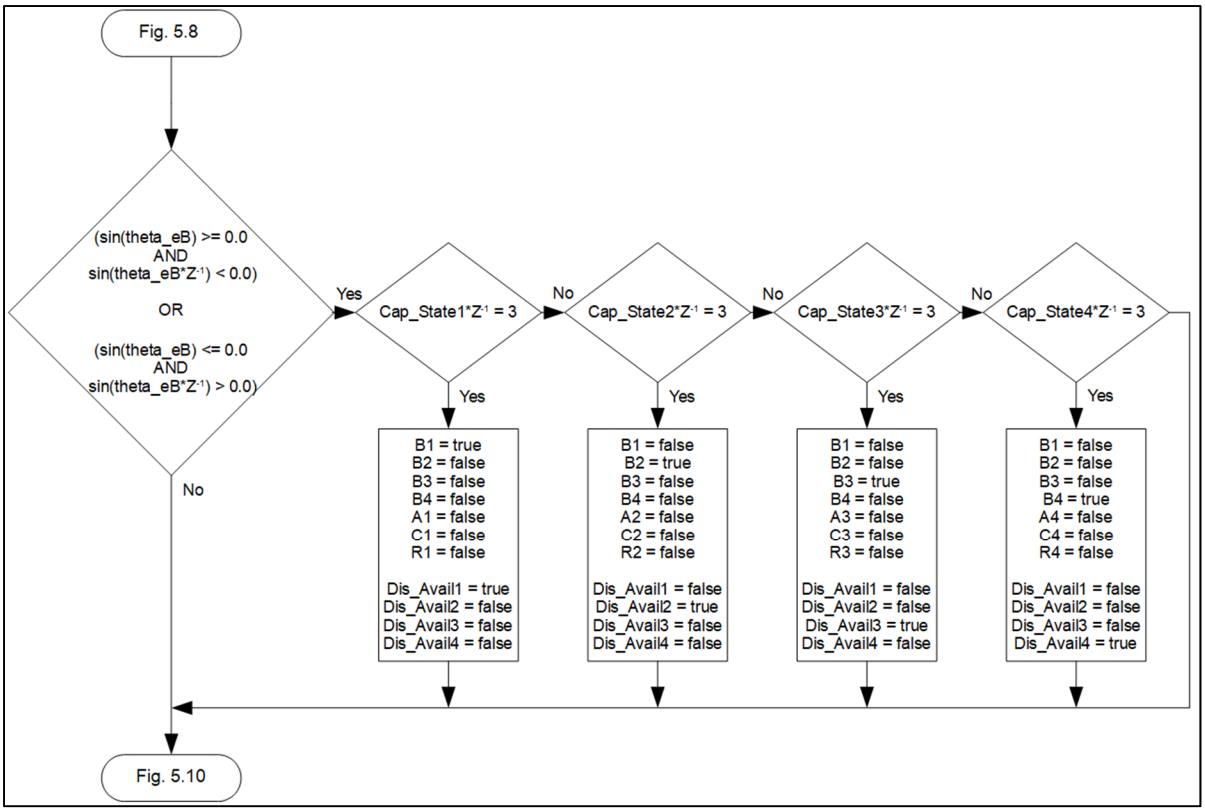

Figure 5.9 Main Sequencer Algorithm (4/6)

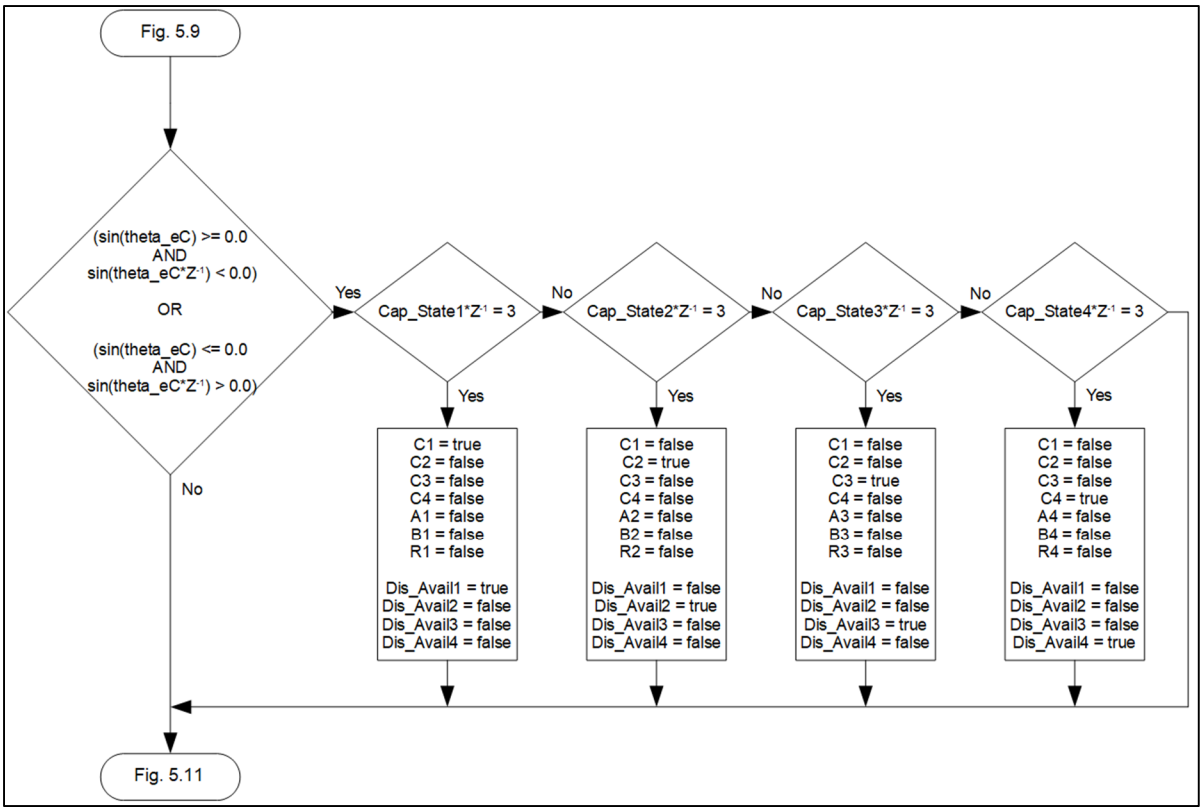

Figure 5.10 Main Sequencer Algorithm (5/6)

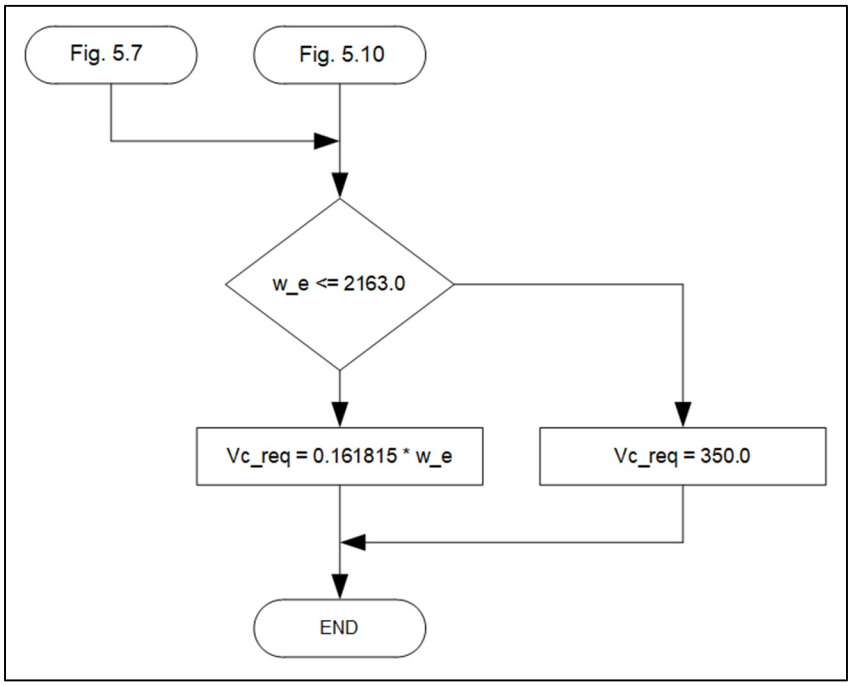

Figure 5.11 Main Sequencer Algorithm (6/6)

Table 5.7 Constants of the Main Sequencer Algorithm

Parameter	Description	Unit	Value
Pp	Number of pole pairs	N/A	4
KBOOST_ON_FREQ	RPP activation electrical frequency	Rad/sec	1131.0
KBOOST_ON_HYST	RPP activation electrical frequency hysteresis	Rad/sec	5.0

Table 5.8 Inputs of the Main Sequencer Algorithm

Parameter	Description	Unit	Min	Max	Type
Ia	Motor phase A current	A	-50.0	50.0	fix(1,16,9)
Ib	Motor phase B current	A	-50.0	50.0	fix(1,16,9)
Ic	Motor phase C current	A	-50.0	50.0	fix(1,16,9)
Ir	Recharge circuit current	A	0.0	200.0	fix(1,16,7)
Vc1	Capacitor 1 voltage	V	-400.0	400.0	fix(1,16,6)
Vc2	Capacitor 2 voltage	V	-400.0	400.0	fix(1,16,6)
Vc3	Capacitor 3 voltage	V	-400.0	400.0	fix(1,16,6)
Vc4	Capacitor 4 voltage	V	-400.0	400.0	fix(1,16,6)
theta_motor	Rotor angular position	rad	0.0	6.2828	fix(1,12,8)
w_e	Electrical frequency of the PMSM	rad/sec	-4800.0	4800.0	fix(1,16,3)
Cap_State1_LP	Configurable Capacitor Module 1 State, last pass (Z^{-1})	N/A	1	4	fix(0,3,0)
Cap_State2_LP	Configurable Capacitor Module 2 State, last pass (Z^{-1})	N/A	1	4	fix(0,3,0)
Cap_State3_LP	Configurable Capacitor Module 3 State, last pass (Z^{-1})	N/A	1	4	fix(0,3,0)
Cap_State4_LP	Configurable Capacitor Module 4 State, last pass (Z^{-1})	N/A	1	4	fix(0,3,0)
CPS11_LP	RPP CPS11 Switch Command, last pass (Z^{-1})	N/A	false	true	Boolean
CPS12_LP	RPP CPS12 Switch Command, last pass (Z^{-1})	N/A	false	true	Boolean
CPS21_LP	RPP CPS21 Switch Command, last pass (Z^{-1})	N/A	false	true	Boolean
CPS22_LP	RPP CPS22 Switch Command, last pass (Z^{-1})	N/A	false	true	Boolean
CPS31_LP	RPP CPS31 Switch Command, last pass (Z^{-1})	N/A	false	true	Boolean
CPS32_LP	RPP CPS32 Switch Command, last pass (Z^{-1})	N/A	false	true	Boolean
CPS41_LP	RPP CPS41 Switch Command, last pass (Z^{-1})	N/A	false	true	Boolean
CPS42_LP	RPP CPS42 Switch Command, last pass (Z^{-1})	N/A	false	true	Boolean

Table 5.9 Outputs of the Main Sequencer Algorithm

Parameter	Description	Unit	Min	Max	Type
Rec_Avail1	Recharge Available signal to Configurable Capacitor Module 1	N/A	false	true	Boolean
Dis_Avail1	Discharge Available signal to Configurable Capacitor Module 1	N/A	false	true	Boolean
Rec_Avail2	Recharge Available signal to Configurable Capacitor Module 2	N/A	false	true	Boolean
Dis_Avail2	Discharge Available signal to Configurable Capacitor Module 2	N/A	false	true	Boolean
Rec_Avail3	Recharge Available signal to Configurable Capacitor Module 3	N/A	false	true	Boolean
Dis_Avail3	Discharge Available signal to Configurable Capacitor Module 3	N/A	false	true	Boolean
Rec_Avail4	Recharge Available signal to Configurable Capacitor Module 4	N/A	false	true	Boolean
Dis_Avail4	Discharge Available signal to Configurable Capacitor Module 4	N/A	false	true	Boolean
theta_e1	Electrical angle from the point of view of capacitor 1	rad	0.0	6.2828	fix(1,16,10)
theta_e2	Electrical angle from the point of view of capacitor 2	rad	0.0	6.2828	fix(1,16,10)
theta_e3	Electrical angle from the point of view of capacitor 3	rad	0.0	6.2828	fix(1,16,10)
theta_e4	Electrical angle from the point of view of capacitor 4	rad	0.0	6.2828	fix(1,16,10)
I1	Motor phase A current	A	-50.0	50.0	fix(1,16,7)
I2	Motor phase B current	A	-50.0	50.0	fix(1,16,7)
I3	Motor phase C current	A	-50.0	50.0	fix(1,16,7)
I4	Recharge circuit current	A	0.0	200.0	fix(1,16,7)
VcA	Capacitor X voltage from the point of view of phase A	V	-400.0	400.0	fix(1,16,6)
VcB	Capacitor X voltage from the point of view of phase B	V	-400.0	400.0	fix(1,16,6)

Table 5.9 Outputs of the Main Sequencer Algorithm (Continued)

Parameter	Description	Unit	Min	Max	Type
VcC	Capacitor X voltage from the point of view of phase C	V	-400.0	400.0	fix(1,16,6)
A1	RPP Switch A1 command	N/A	false	true	Boolean
B1	RPP Switch B1 command	N/A	false	true	Boolean
C1	RPP Switch C1 command	N/A	false	true	Boolean
R1	RPP Switch R1 command	N/A	false	true	Boolean
A2	RPP Switch A1 command	N/A	false	true	Boolean
B2	RPP Switch B1 command	N/A	false	true	Boolean
C2	RPP Switch C1 command	N/A	false	true	Boolean
R2	RPP Switch R1 command	N/A	false	true	Boolean
A3	RPP Switch A1 command	N/A	false	true	Boolean
B3	RPP Switch B1 command	N/A	false	true	Boolean
C3	RPP Switch C1 command	N/A	false	true	Boolean
R3	RPP Switch R1 command	N/A	false	true	Boolean
A4	RPP Switch A1 command	N/A	false	true	Boolean
B4	RPP Switch B1 command	N/A	false	true	Boolean
C4	RPP Switch C1 command	N/A	false	true	Boolean
R4	RPP Switch R1 command	N/A	false	true	Boolean
Vc_req	Capacitor voltage target	V	-400.0	400.0	fix(1,16,6)
BOOST_ON	RPP Online Signal	N/A	false	true	Boolean

5.4.3 Capacitor Modules Control

Each capacitor module is managed independently by a Capacitor Module Control Algorithm. Each Capacitor Module Control Algorithm performs the following sub-tasks:

Capacitor Module State Machine.

The Capacitor Module Control State Machine determines the state of every Configurable Capacitor Module. Each Capacitor Module has the following states:

- Discharged (1)
- Recharging (2)
- Recharged (3)
- Discharging (4)

The transition criteria between the states are described below:

Transition from Discharged (1) to Recharging (2)

The transition from Discharged (1) to Recharging (2) state is done when the “Rec_AvailX” signal is received from the Main Sequencer.

Transition from Recharging (2) to Recharged (3)

The transition from Recharging (2) to Recharged (3) state is done when the recharge current drops below 0.1 Amps.

Transition from Recharged (3) to Discharging (4)

The transition from Recharged (3) to Discharging (4) state is done when the “Dis_AvailX” signal is received from the Main Sequencer.

Transition from Discharging (4) to Discharged (1)

The transition from Discharging (4) to Discharged (1) state is done when the value of the sinus of the electrical angular position of the rotor, from the capacitor’s point of view, enters the band between +/- 0.1.

See Figure 5.12 below for the flowchart diagram of the Capacitor Modules Control.

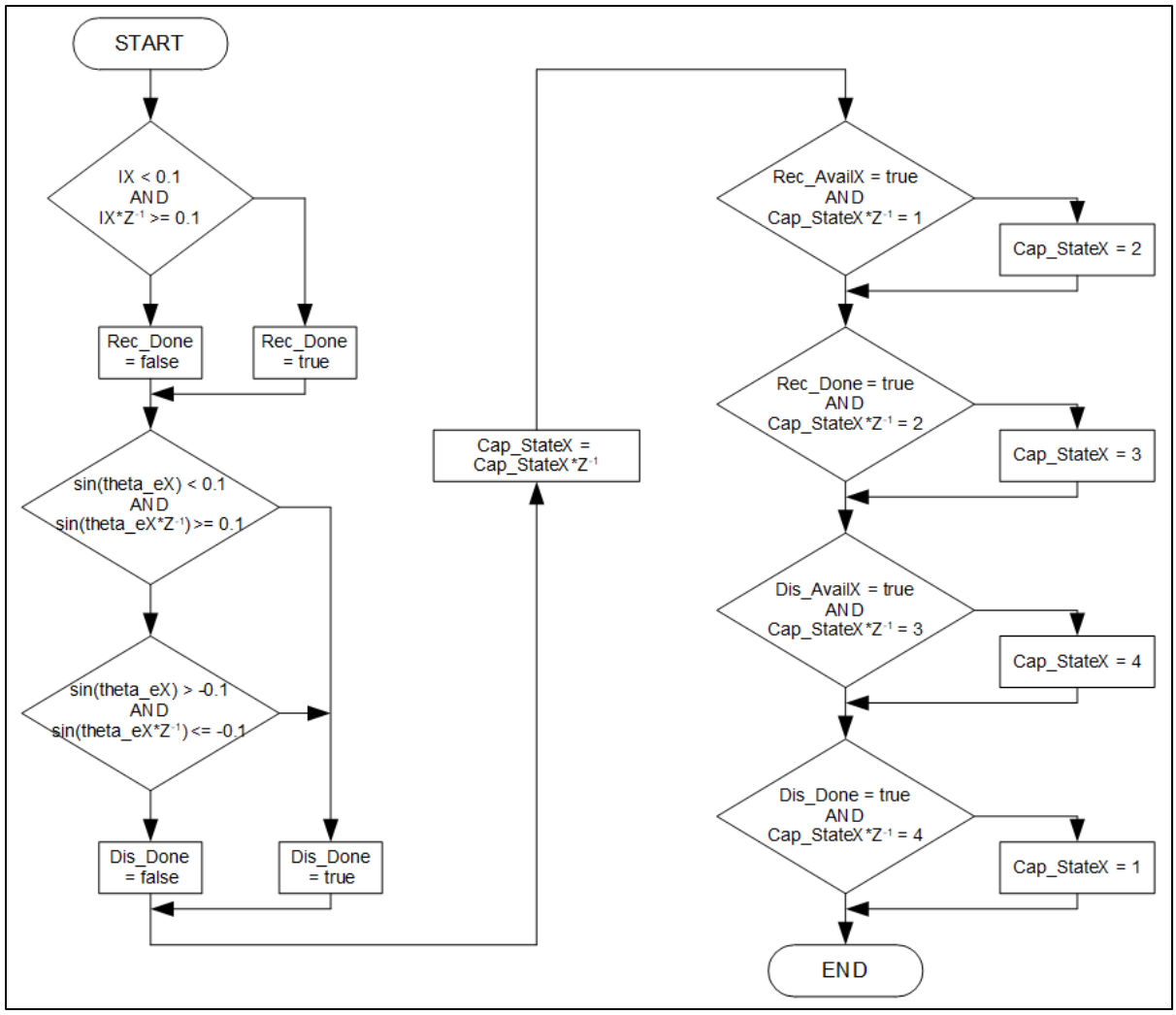

Figure 5.12 Capacitor Modules State Machine Flowchart

Command of the Capacitor Polarity Switches

The Capacitor Polarity Switches (CPSX1 and CPSX2) are used to set the capacitor polarity as per the point of view of the motor phases or the recharge circuit. During the discharging phase, the capacitor's polarity must be opposite to the back-EMF polarity to benefit from the capacitor's contribution. During the Recharging phase, the capacitor's initial polarity must be the same as the DC voltage source to increase the capacitor energy during the recharge cycle. As it is impossible to predict the capacitor's terminals polarity, the capacitor's need to set the polarity to adapt to the discharge or recharge circuits. The Capacitor Polarity Switches Command sets the polarity of the capacitor to properly recharge and discharge the capacitors

according to the operating condition. See Figure 5.13 for the flow chart of the Capacitor Polarity Switches Command.

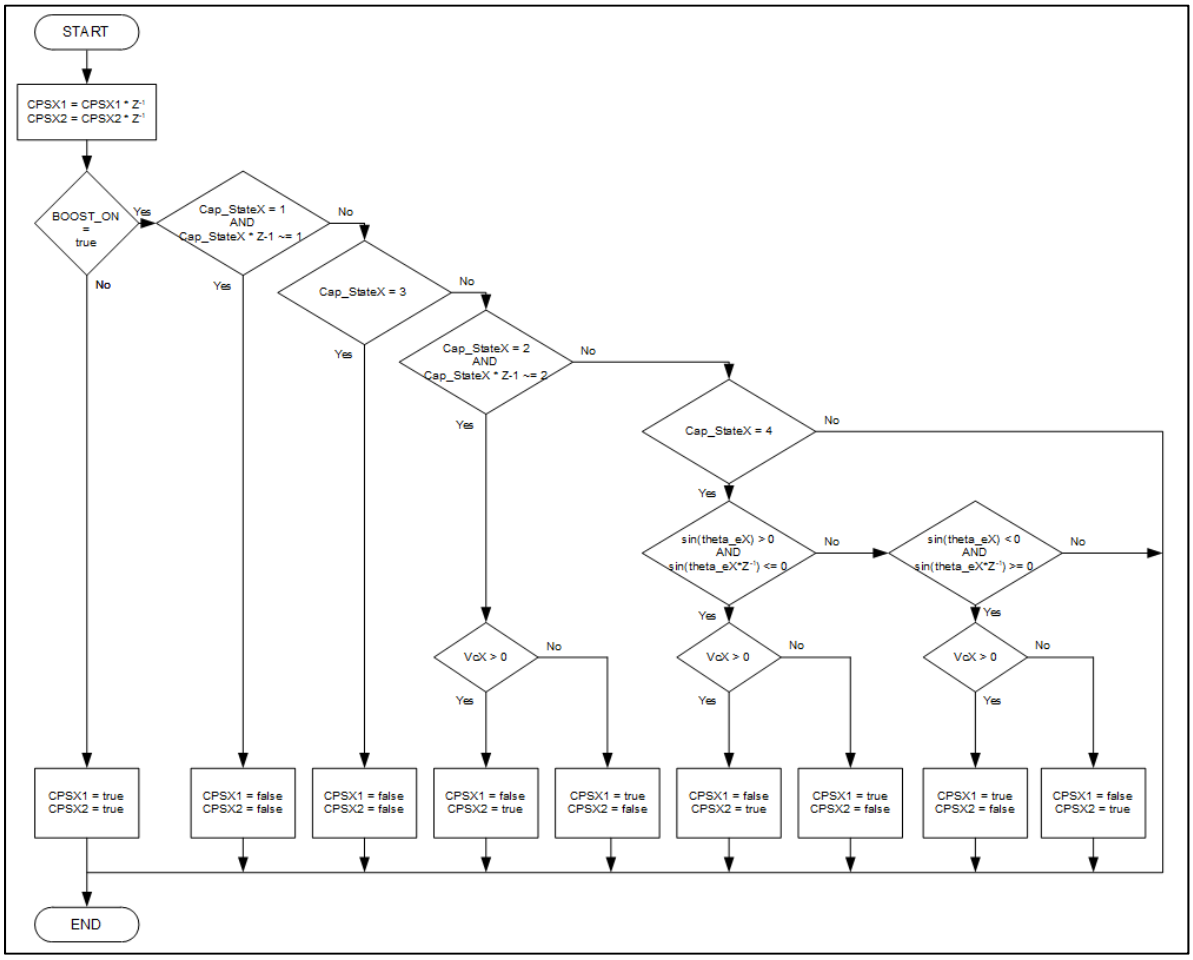

Figure 5.13 Capacitor Polarity Switch Algorithm Flowchart

Setting of the Capacitance

To allow the PMSM to vary through a wide speed range, the Capacitance of the Configurable Capacitor Modules must be set according to the operating speed. The Configurable Capacitor Module has two different capacitance values: 56 µF or 112 µF. The capacitance value is 56 µF when the "H" switch is open (H = false) and 112 µF when the "H" switch is closed (H = true). To minimize the stress on the power electronic components, the capacitance changes are done when the Configurable Capacitor Module is in "Discharged" state. See Figure 5.14 for the flow chart of the Capacitor Setting logic.

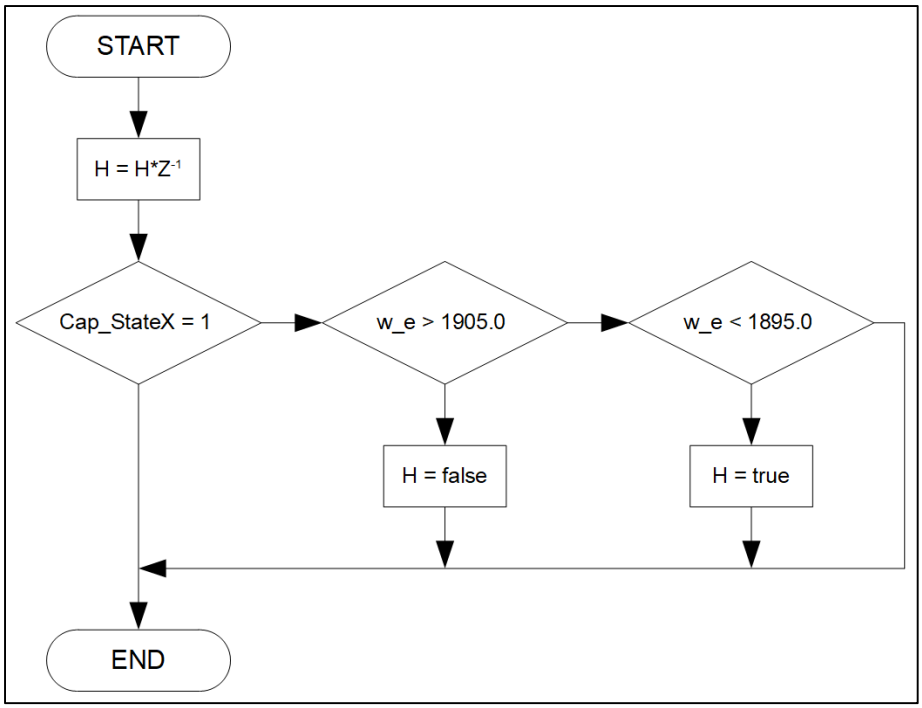

Figure 5.14 Capacitance Setting Logic Flowchart

Scheduling of the Recharge Cycle

The role of the Recharge Circuit is to recharge each capacitor to the pre-determined voltage target. The recharge Circuit Controls the "R_ON" switch. When the "R_ON" switch is ON (R_ON = true), the battery voltage is added to the capacitor's voltage. When "R_ON" is set to ON, the energy from the battery is added to the capacitor's energy. When the "R_ON" switch is OFF (R_ON = false), the battery does not provide energy to the capacitor. The Recharge Circuit operates at Zero Current Switching (ZCS), however the "R_ON" switches can be closed or opened at any moment during the recharge process as a free-wheeling path is available for the recharge current through the bypass diode. The recharge control monitors the initial capacitor's energy and the input energy from the battery. When the energy input required to reach pre-determined voltage target is reached, the "R_ON" switch is commanded OFF (false) and therefore the recharge cycle is completed in free-wheeling while no energy is added to the RLC circuit. See Figure 5.15 for the flow chart of the Recharge Circuit control logic.

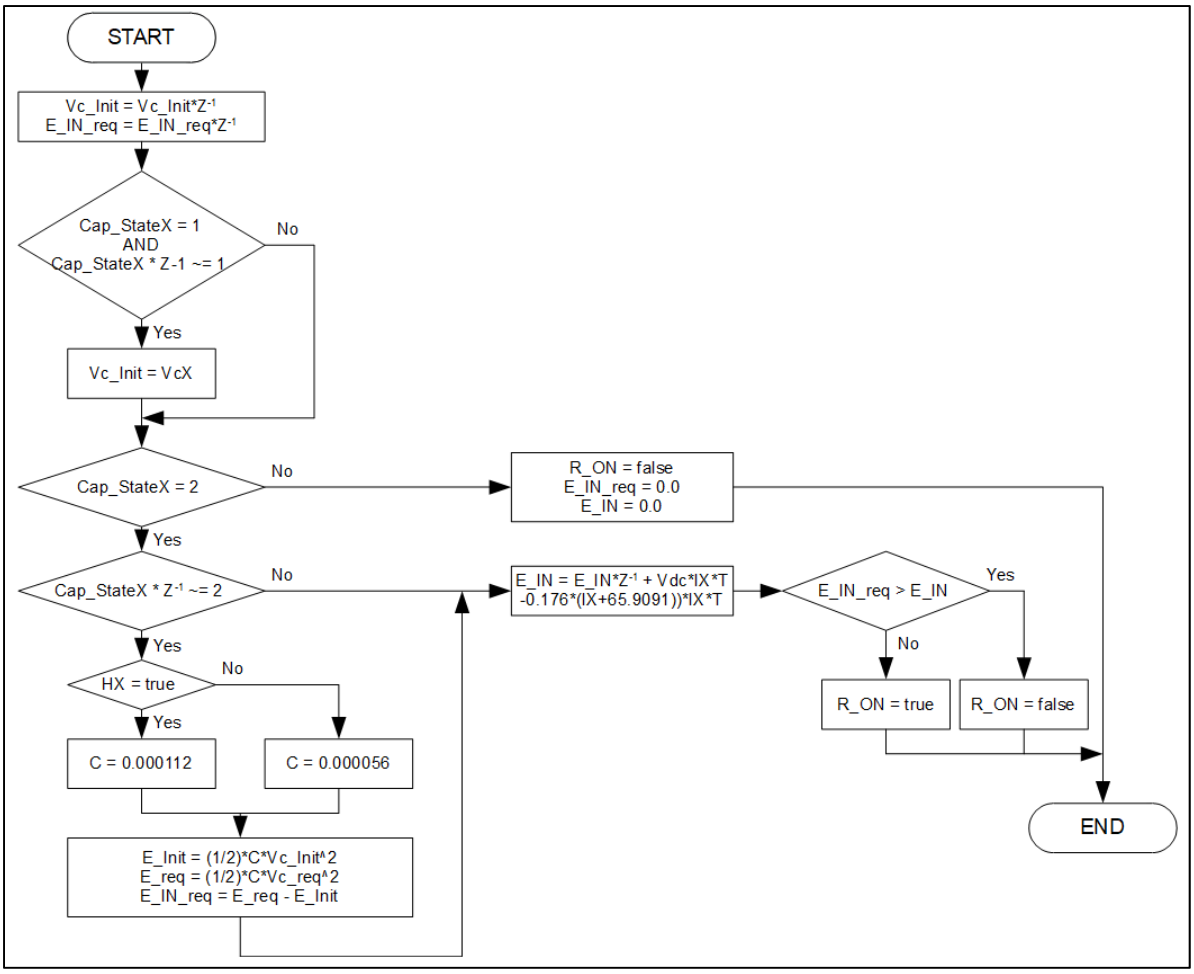

Figure 5.15 Recharge Circuit Control Algorithm Flowchart

Table 5.10 Constants of the of the Capacitor Module Control

Parameter	Description	Unit	Value
T	Control Algorithm sample time	second	0.000001

Table 5.11 Inputs of the of the Capacitor Module Control

Parameter	Description	Unit	Min	Max	Type
Rec_AvailX	Recharge available signal	N/A	false	true	Boolean
Dis_AvailX	Discharge available signal	N/A	false	true	Boolean
IX	Current in the capacitor X	A	-400.0	400.0	fix(1,16,7)
theta_eX	Electrical angle from the point of view of capacitor X	rad	0.0	6.2828	fix(1,16,10)
VcX	Capacitor X voltage	V	-400.0	400.0	fix(1,16,6)
w_e	Electrical frequency of the PMSM	rad/sec	-4800	4800	fix(1,16,3)
Vc_req	Capacitor voltage target	V	-400.0	400.0	fix(1,16,6)
Vdc	DC-Link (Battery) voltage	V	0.0	400.0	fix(1,16,6)
BOOST_ON	RPP Online Signal	N/A	false	true	Boolean

Table 5.12 Outputs of the of the Capacitor Module Control

Parameter	Description	Unit	Min	Max	Type
Cap_StateX	Capacitor X state	N/A	1	4	fix(0,3,0)
CPSX1	CPSX1 switch command	N/A	false	true	Boolean
CPSX2	CPSX2 switch command	N/A	false	true	Boolean
HX	HX switch command	N/A	false	true	Boolean
R_ONX	R_ON switch command	N/A	false	true	Boolean

5.4.4 Field Oriented Control (FOC)

The Field Oriented Control algorithm implemented for this system consists of a speed control with the objective of controlling the PMSM to a speed of 5400 rpm. The control algorithm controls the motor torque through the phase currents to maintain the PMSM speed at this constant speed. The structure of the Field Oriented Control algorithm implemented is shown in Figure 5.16.

5.4.4.1 Input Parameters Conditioning

Equations (5.6) and (5.7) are used to calculate parameters used for the Field Oriented Control algorithm. See Figure 5.16 (1).

$$theta\_e = Pp \cdot theta\_motor \tag{5.6}$$

$$w\_motor\_req = Speed\_req \cdot \frac{2\pi}{60} \tag{5.7}$$

5.4.4.2 Park Transform

As described in Section 1.2.2.1, the Park transform is used to convert the phase currents in the d-axis and q-axis currents. The equation of the Park Transform used in the control algorithm is shown in Equation (5.8) below. See Figure 5.16 (2).

$$\frac{2}{3} \cdot \begin{bmatrix} \cos(theta\_e) & \sin(theta\_e) \\ -\sin(theta\_e) & \cos(theta\_e) \end{bmatrix} \times \begin{bmatrix} 1 & -\frac{1}{2} & -\frac{1}{2} \\ 0 & \frac{\sqrt{3}}{2} & -\frac{\sqrt{3}}{2} \end{bmatrix} \times \begin{bmatrix} Ia \\ Ib \\ Ic \end{bmatrix} = \begin{bmatrix} Id \\ Iq \end{bmatrix} \tag{5.8}$$

5.4.4.3 Closed loop motor control (Speed control)

The Closed loop motor control algorithm is made of 3 layers described as follow. See Figure 5.16 (3):

Speed Control

The speed control closes loop on the speed error between the speed command and the actual PMSM speed. The speed control is a Proportional-Integral (PI) controller which generates a torque request. The integrator used in the PI is a Backward Euler integrator which is saturated within -15.6 N.m to 15.6 N.m. The torque request output is limited between -15.6 N.m and 15.6 N.m to not saturate the integrators of the Field Oriented Control downstream.

Torque Control

The torque request is converted to a q-axis current request. The conversion is done as per the Equation (5.9) below.

$$Iq\_req = \frac{2}{3 \cdot K_{BEMF}} \cdot Tq\_req \tag{5.9}$$

Current Control

The current control algorithm is a Zero d-axis current control (ZDAC), because the PMSM selected for this system is a flat poles electric machine. Therefore, the d-axis current request is always set to zero. The current control is a Proportional-Integral (PI) controller which generates d-axis voltage request and q-axis voltage request. The integrators used in the PIs are Backward Euler integrators.

5.4.4.4 Inverse Park Transform

The inverse Park transform is used to convert the phase voltage command from the direct-quadrature system to the ABC phase system. The equation of the Inverse Park Transform used in the control algorithm is shown in Equation (5.10) below. See figure 5.16 (4):

$$\begin{bmatrix} 1 & 0 \\ -1/2 & -\sqrt{3}/2 \\ -1/2 & -\sqrt{3}/2 \end{bmatrix} \times \begin{bmatrix} \cos(theta\_e) & -\sin(theta\_e) \\ \sin(theta\_e) & \cos(theta\_e) \end{bmatrix} \times \begin{bmatrix} Vd\_req \\ Vq\_req \end{bmatrix} = \begin{bmatrix} Va\_req \\ Vb\_req \\ Vc\_req \end{bmatrix} \tag{5.10}$$

5.4.4.5 Capacitor Voltage Compensation

Because the phase voltage is the sum of the inverter voltage and the capacitor's voltage, the FOC voltage command must be compensated to deliver a phase voltage which is sinusoidal. The inverter voltage command is determined as per equation (5.11) below. See Figure 5.16 (5).

$$\begin{bmatrix} Va\_req \\ Vb\_req \\ Vc\_req \end{bmatrix} - \begin{bmatrix} VcA \\ VcB \\ VcC \end{bmatrix} = \begin{bmatrix} VinvA\_req \\ VinvB\_req \\ VinvC\_req \end{bmatrix} \tag{5.11}$$

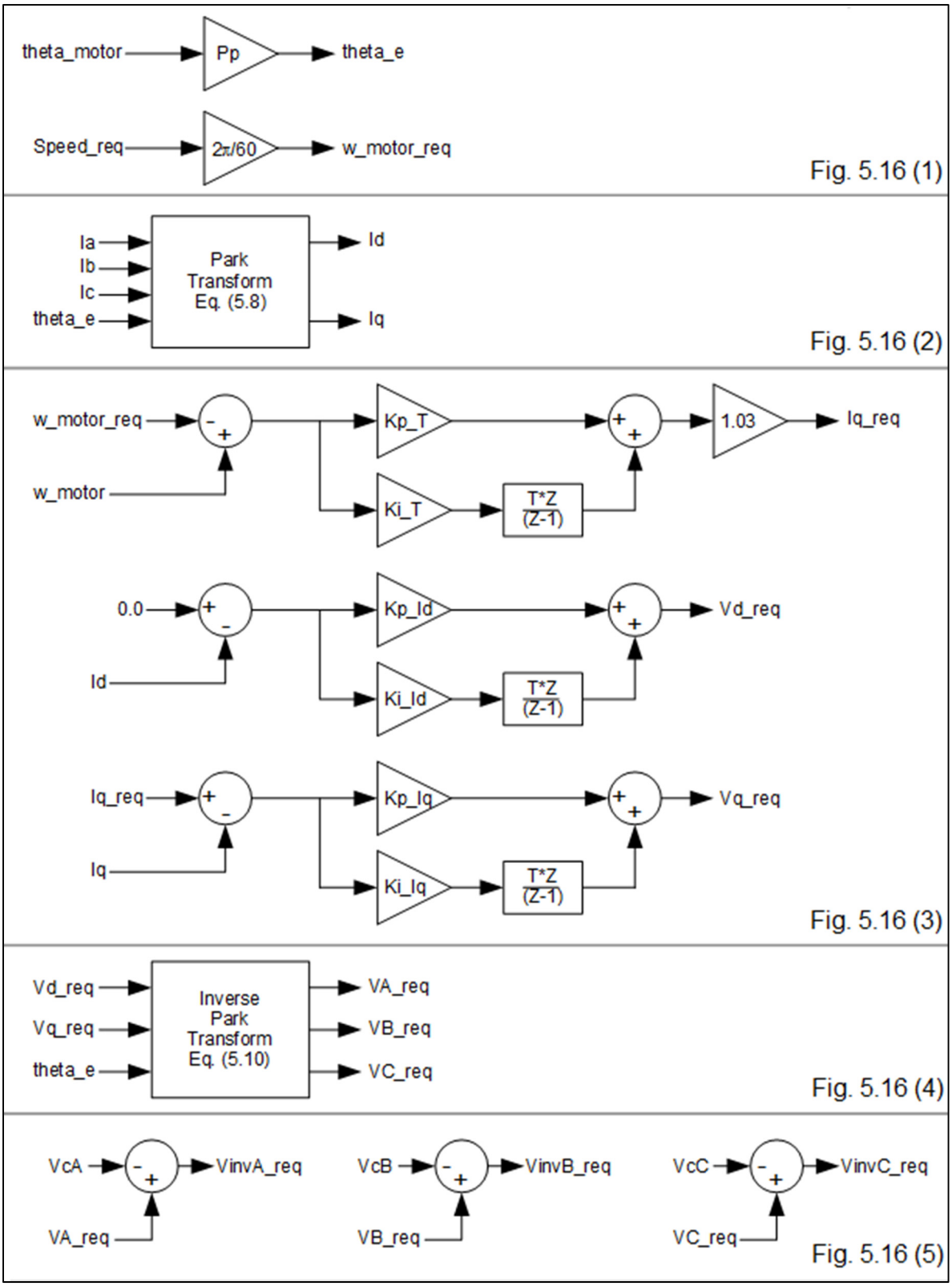

Figure 5.16 Field Oriented Control Algorithm

Table 5.13 Constants of the Field Oriented Control

Parameter	Description	Unit	Value
T	Control Algorithm sample time	second	0.000001
Speed_req	Motor speed target	rpm	5400
Pp	Number of pole pairs	N/A	4
Kp_T	Speed Control Proportional gain	N/A	1.0
Ki_T	Speed Control Integral gain	N/A	5.0
Kp_Id	d-axis current Control Proportional gain	N/A	20.0
Ki_Id	d-axis current Control Integral gain	N/A	100.0
Kp_Iq	q-axis current Control Proportional gain	N/A	20.0
Ki_Iq	q-axis current Control Integral gain	N/A	100.0

Table 5.14 Inputs of the Field Oriented Control

Parameter	Description	Unit	Min	Max	Type
Ia	Motor phase A current	A	-50.0	50.0	fix(1,16,9)
Ib	Motor phase B current	A	-50.0	50.0	fix(1,16,9)
Ic	Motor phase C current	A	-50.0	50.0	fix(1,16,9)
theta_motor	Rotor angular position	rad	0.0	6.2828	fix(1,12,8)
w_motor	Motor shaft speed	Rad/sec	-1000	1000	fix(1,12,1)
VcA	Capacitor X voltage from the point of view of phase A	V	-400.0	400.0	fix(1,16,6)
VcB	Capacitor X voltage from the point of view of phase B	V	-400.0	400.0	fix(1,16,6)
VcC	Capacitor X voltage from the point of view of phase C	V	-400.0	400.0	fix(1,16,6)

Table 5.15 Outputs of the Field Oriented Control

Parameter	Description	Unit	Min	Max	Type
VinvA_req	Phase A inverter voltage command	V	-400.0	400.0	fix(1,16,5)
VinvB_req	Phase B inverter voltage command	V	-400.0	400.0	fix(1,16,5)
VinvC_req	Phase C inverter voltage command	V	-400.0	400.0	fix(1,16,5)

CHAPTER 6

SIMULATION OF THE SYSTEM

The whole system has been modeled and simulated in the Matlab/Simulink environment. The simulation is performed at fixed step, and the simulation time step is set to 1 µs (1 MHz). This sample time is relatively small considering the electrical frequency of 360 Hz at the maximum operation speed, however it matches the operating frequency of the FPGA and allows for a better accuracy of the dynamic behavior calculation. It also provides a better simulation of the phase current harmonics. The following section describe in details the simulation model used to generate the results provided in Section 7.

6.1 Simulation settings

The integrators used to simulate the continuous domain dynamics of the system are continuous domain integrators, and the solver used is Runge-Kutta (ode4). The simulation parameters are resumed in Table 6.1 below.

Table 6.1 Matlab/Simulink Simulation Parameters

Solver type	Fixed-Step
Solver	Runge-Kutta
Fixed-Step Size	0.000001 sec.

6.2 Simulation Model

The simulation model includes the Control, the Inverter, the Resonant Power Processor (RPP) and the Permanent Magnet Synchronous Motor (PMSM). Each of those modules have been implemented in distinct Matlab/Simulink Subsystems. Figure 6.1 shows the schematic of the architecture of the simulation model. Figure 6.1 also shows the data flow between the different subsystems of the simulation model. In the next sections, the simulation model is further broken down and each subsystem is detailed in a comprehensive manner.

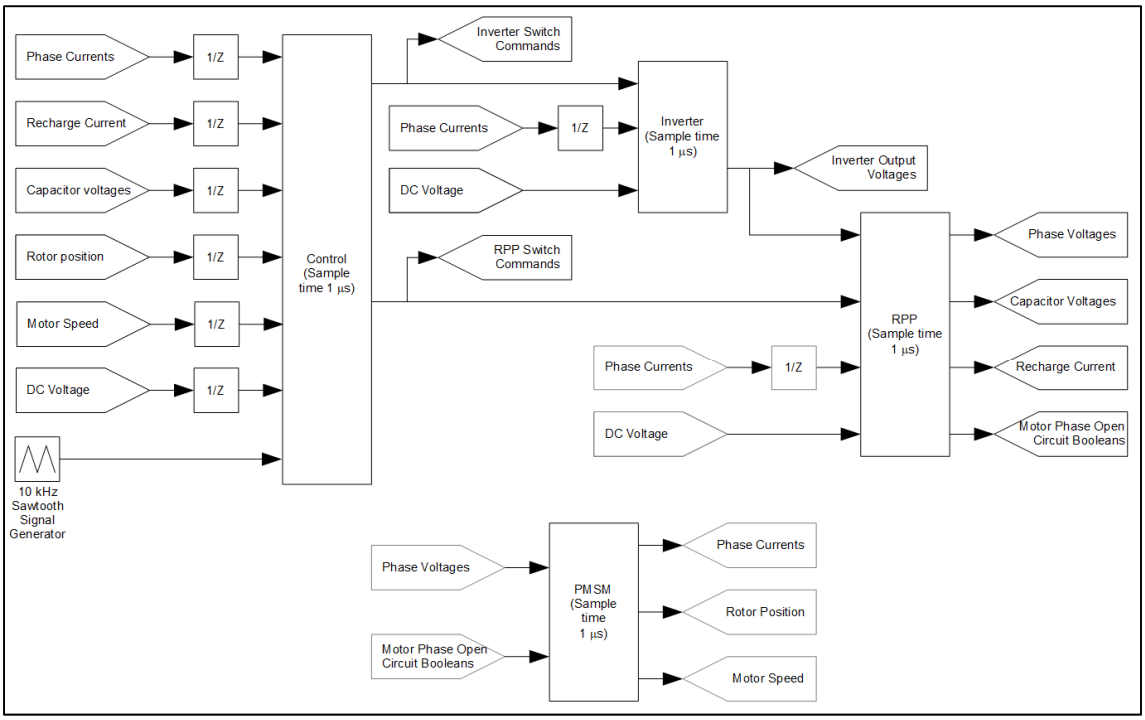

Figure 6.1 Schematic of the architecture of the simulation model

6.2.1 Simulation of the Control Algorithm

The Control algorithm described in Section 5.4 has been modeled in Matlab/Simulink. The flowcharts of the Main Sequencer and the Capacitor Modules control have been implemented using the StateFlow Simulink tool. The electrical frequency determination, the Field Oriented Control and the inverter command have been implemented in Simulink. The whole Control Algorithm has been successfully compiled in VHDL code language for implementation in FPGA format. For details of the Control Algorithm, see Section 5.4.

6.2.2 Simulation of the inverter

The inverter is a 3 phases 2 level inverter. Its role is to generate the commanded phase voltages. It outputs the phase voltages according to the status of the commands of the S1 to S6 MOSFETs. See Figure 6.2 for schematics of the implementation of the inverter simulation.

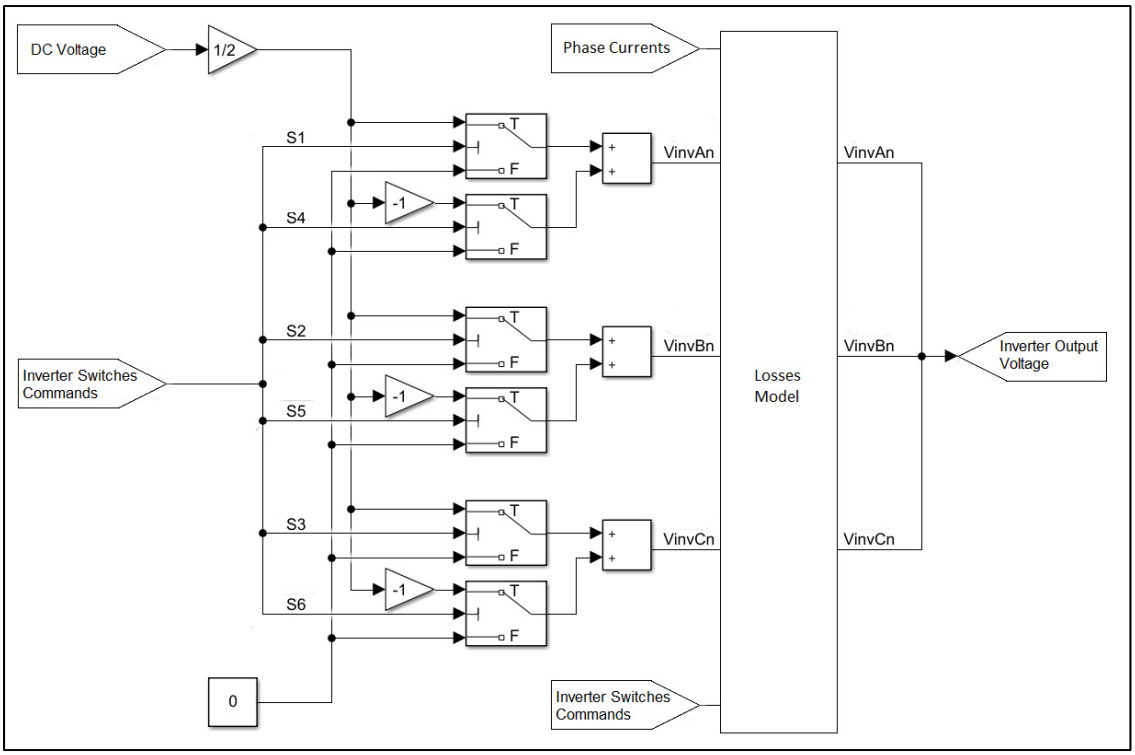

Figure 6.2 Inverter Sub-System Simulation Model

6.2.3 Simulation model of the Permanent Magnet Synchronous Machine (PMSM)

The Permanent Magnet Synchronous Machine (PMSM) has been modeled in Matlab/Simulink. As previously mentioned, the PMSM used for this project is the ABB/Baldor BSM33C-6177MHQ. The standard PMSM model embedded in Matlab/Simulink was not used because it does not provide the capability to reset the phase currents to zero amps when the motor phase is open circuit. Because the RPP can be configured to open the phases circuits, even momentarily, this behavior needs to be represented in the simulation to provide accurate results.

The ABB/Baldor BSM33C-6177MHQ has a sinusoidal back-EMF profile with a Back-EMF constant of 0.161815 V.sec/rad (phase to neutral voltage at electrical frequency) and has a phase inductance of 3.47 mH. Both values have been confirmed by experimental measurements on the machine itself.

It is to be mentioned that the PMSM simulation model used for this project neglects some second order magnetic and thermal characteristics of the PMSM. First, the phase inductances are deemed to be a constant. As the ABB/Baldor BSM33C-6177MHQ PMSM is a flat poles machine, the phase inductance does not change with the rotor angular position. However, the phase currents themselves may modify the phase inductances because of the magnetic saturation of the stator. Second, the thermal effects on the phase resistance and back-EMF constant are neglected. As seen previously, the phase resistance increases with temperature. Also, the permanent magnets strength decreases with temperature, and therefore does the Back-EMF constant.

To simulate the preliminary concept of the Resonant Power Processor, the simulation model of the PMSM is deemed acceptable. However, for an accurate system efficiency assessment, the PMSM simulation model should consider the magnetic saturation and thermal effect on the PMSM performances. It should also consider the iron losses caused by the phase current harmonics. See Figure 6.3 for a schematic of the PMSM simulation model architecture.

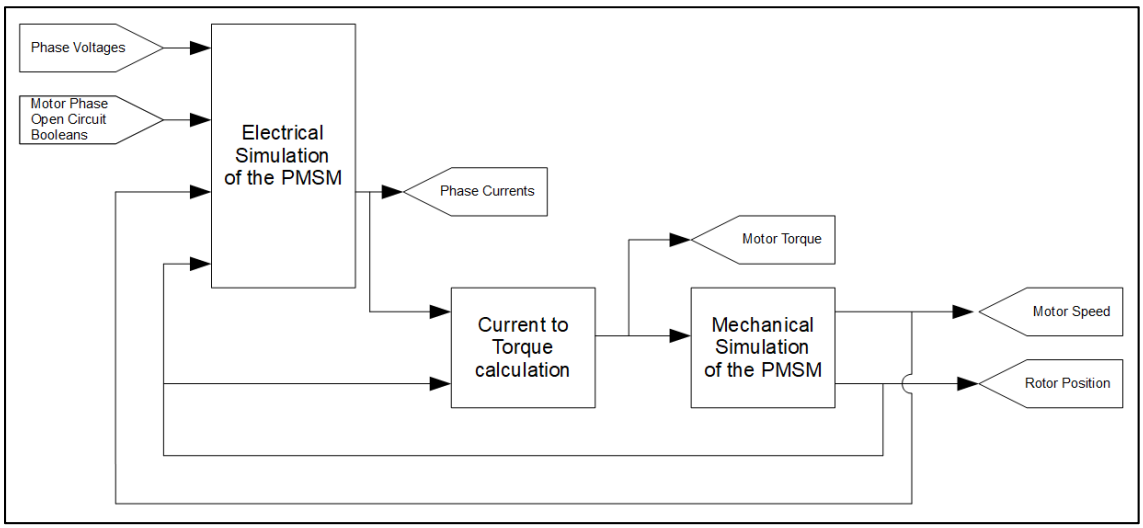

Figure 6.3 Architecture of the PMSM simulation model

6.2.3.1 Electrical simulation of the PMSM

The electrical simulation of the PMSM converts the phase voltages into phase currents. It considers the back-EMF which is generated by the PMSM's shaft rotation. The first step of the PMSM electrical simulation is to calculate the back-EMF as a function of the rotor position and motor speed. The back-EMF is calculated for the 3 phases with a 120° phase shift. Once the Back-EMF is calculated for every phase, the phase currents are calculated as a function of the input phase voltage and motor Back-EMF. The phase current calculation is being performed by resolving the differential equation of Equation (6.1) below:

$$Vxn - Ex = (L \cdot s + R) \cdot Ix \tag{6.1}$$

Where Vxn is the input phase X voltage, Ex is the back-EMF of the phase X, and Ix is the phase X current. When the switches configurations in the Resonant power Processor (RPP) opens a motor phase, the corresponding "OpenX" signal is being routed to the integrator of the differential equation. When the "OpenX" Boolean is true, the phase current integrator is being reset to zero amps, which emulates an open circuit condition. See Figure 6.4 for a schematic of the phase voltage to phase current transfer function as implemented in Matlab/Simulink.

The current to electromagnetic torque calculation is a function of the phase currents and rotor position. The current to electromagnetic torque calculation is done through the equations (6.2) to (6.5) below:

$$Tq_a = Ia \cdot Pp \cdot Kbemf \cdot \sin(theta\_e) \tag{6.2}$$

$$Tq_b = Ib \cdot Pp \cdot Kbemf \cdot \sin(theta\_e - 2\pi/3) \tag{6.3}$$

$$Tq_c = Ic \cdot Pp \cdot Kbemf \cdot \sin(theta_e + 2\pi/3) \tag{6.4}$$

$$Tq = Ta + Tb + Tc \tag{6.5}$$

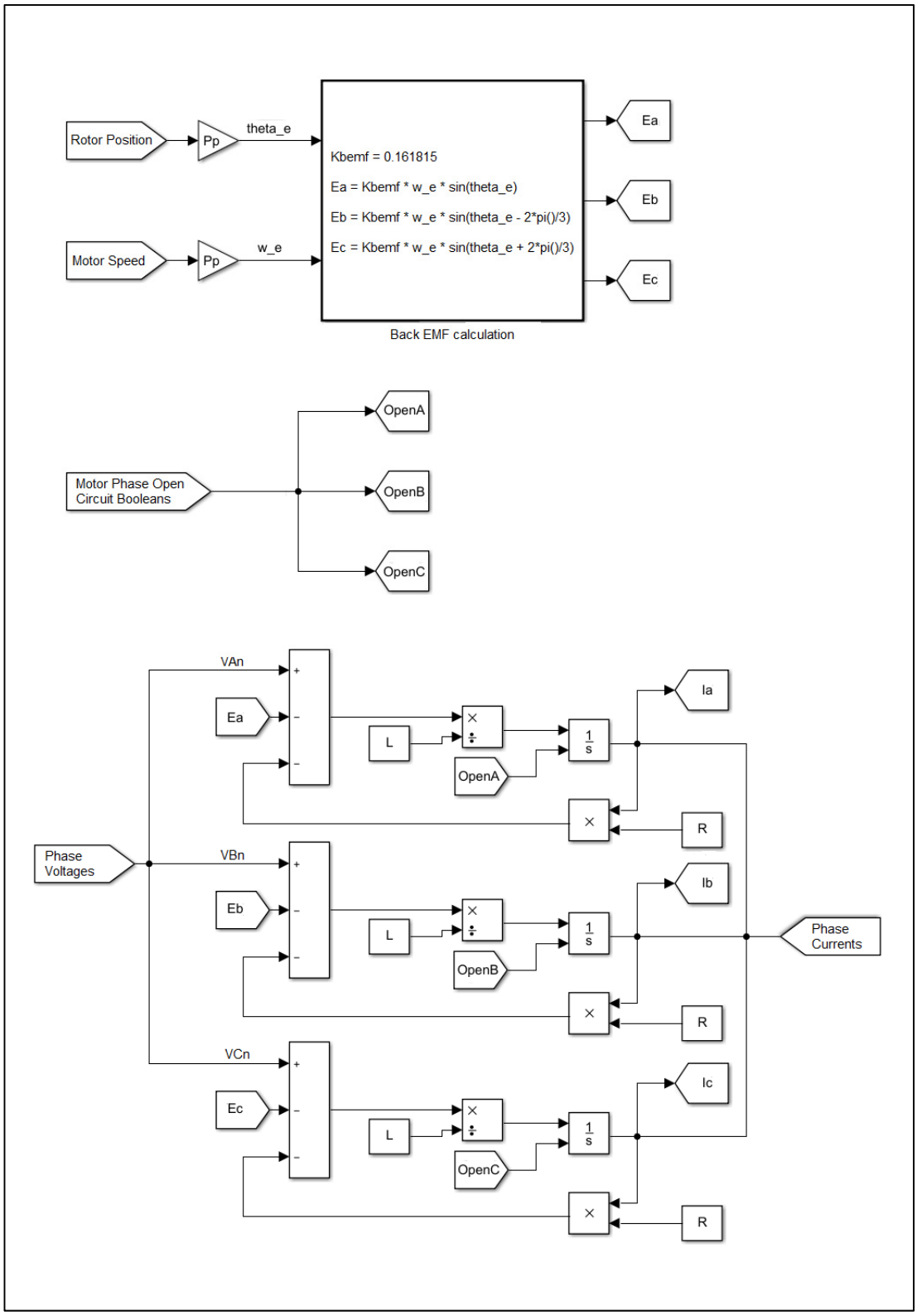

Figure 6.4 Schematic of the architecture of the electrical simulation of the PMSM Mechanical simulation of the PMSM

Torque load

The torque load applied to the PMSM is representative of a propeller. Here, the simulated propeller generates a torque which is function of speed squared. The simulated propeller is defined such that its torque load is 14 N.m at a speed of 5400 rpm. This means that at this condition, the PMSM generates an output power of 7.9 kW. The equation of the torque load can be found at Equation (6.6) below.

$$T_{load} = 0.000044 \cdot \omega_{motor}^2 \tag{6.6}$$

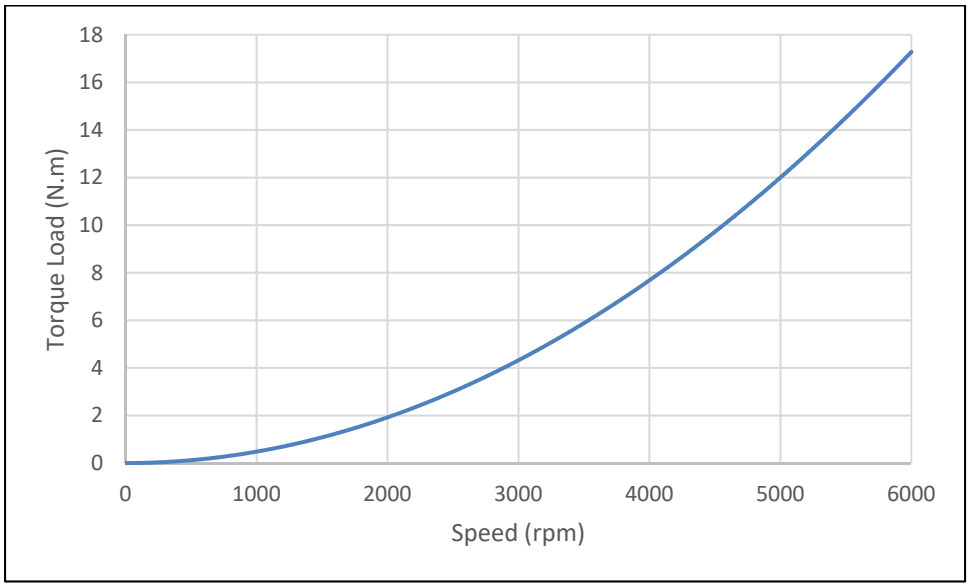

Figure 6.5 Propeller torque load as a function of speed

Torque to speed calculation

The motor speed and the rotor position are calculated as a function of the torque applied to the motor shaft. The torque applied to the motor shaft is the difference between the electromagnetic torque generated by the PMSM and the load torque generated by the propeller. The inertia of the drive train, which includes the PMSM rotor and the propeller's inertia, determines the acceleration of the drivetrain. The rotor speed to rotor position integrator is wrapped between 0 and 2π to replicate the signal of the position resolver. See Figure 6.6 for a schematic of the Torque to Speed model.

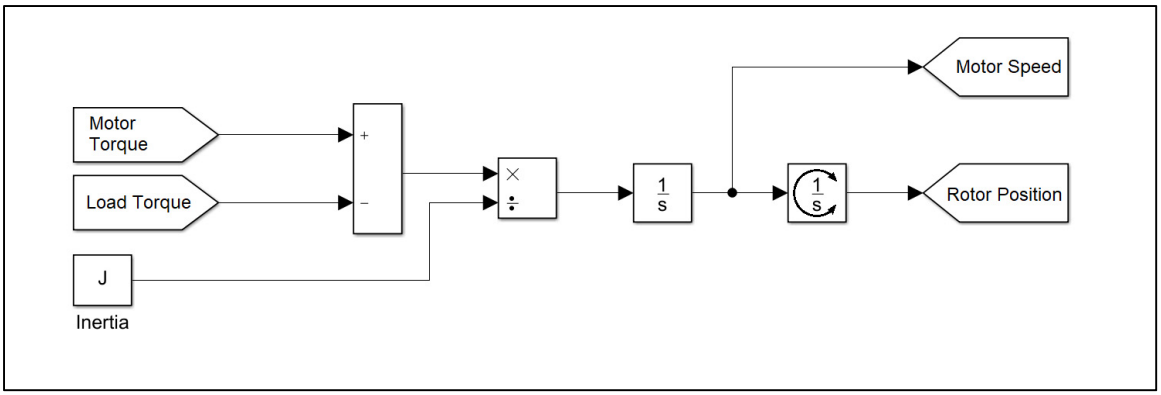

Figure 6.6 Schematic of the Torque to Speed model

6.2.4 Simulation Model of the Resonant Power Processor (RPP)

The Resonant Power Processor consists of 4 identical Configurable Capacitor Modules and one Recharge Circuit. Each of those components have been implemented and simulated in distinct Matlab/Simulink subsystems. Figure 6.7 shows the data flow between the different simulation components of the RPP model.

Figure 6.8 shows how the Multiplexed Capacitor Modules Voltages are converted into the capacitor voltage applied to each motor phase and to the recharge circuit. The control algorithm ensures that only one of the A, B, C or R switches will be on at a time for a given Configurable Capacitor Module. Also, the control algorithm ensures that for each motor phase and the recharge circuit, only one of the 4 Configurable Capacitor Module can be connected simultaneously to a motor phase or a recharge circuit. Therefore, the capacitor voltage applied to each motor phase and to the recharge circuit can be calculated as the sum of each Configurable Capacitor Module's voltage linked to a given motor phase or the recharge circuit as per Figure 6.8.

Figure 6.9 shows how the Capacitor Modules Open Circuit Flags are converted into Open Circuit flags for the motor phases and the Recharge Circuit. The different switch configurations of the Resonant Power Processor may create an open circuit condition at the point of view of the motor phases or Recharge circuit. For each Configurable Capacitor Module, Open Circuit Flags related to each motor phases or to the Recharge Circuit are true when the status of their

respective switches is off. Additionally, if the Capacitor Polarity Switches (CPSX1 and CPSX2) of a configurable capacitor module are both set to off, then all the Open Circuit flags of this Configurable Capacitor Module will be set to true. Figure 6.9 shows that the Open Circuit Flag of the motor phase or recharge circuit is true if all the open circuit flags for this motor phase or recharge circuit are true. The Open Circuit flags are used to force the current of the motor phases or recharge circuit to zero.

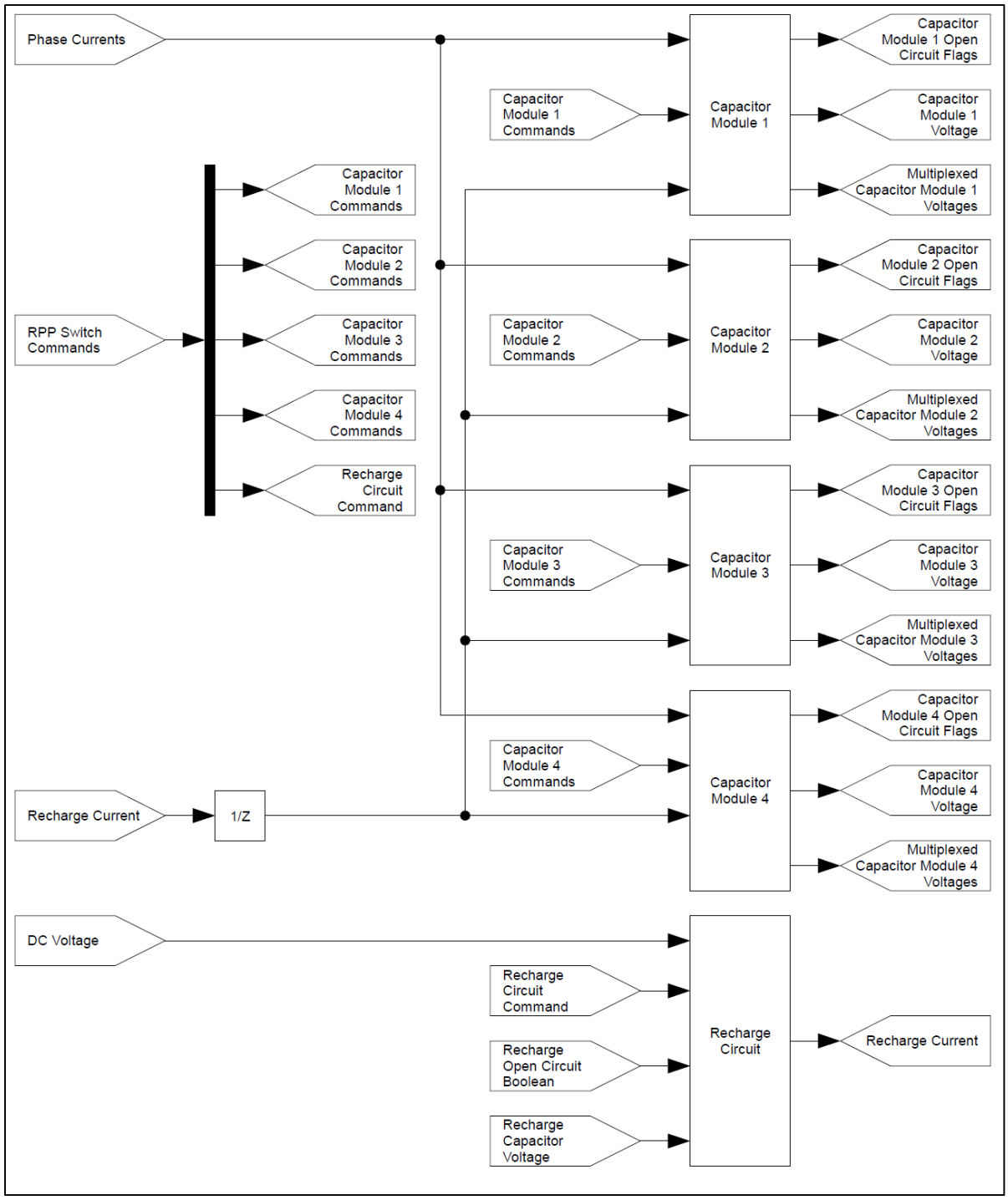

Figure 6.7 Architecture of the Resonant Power Processor simulation model

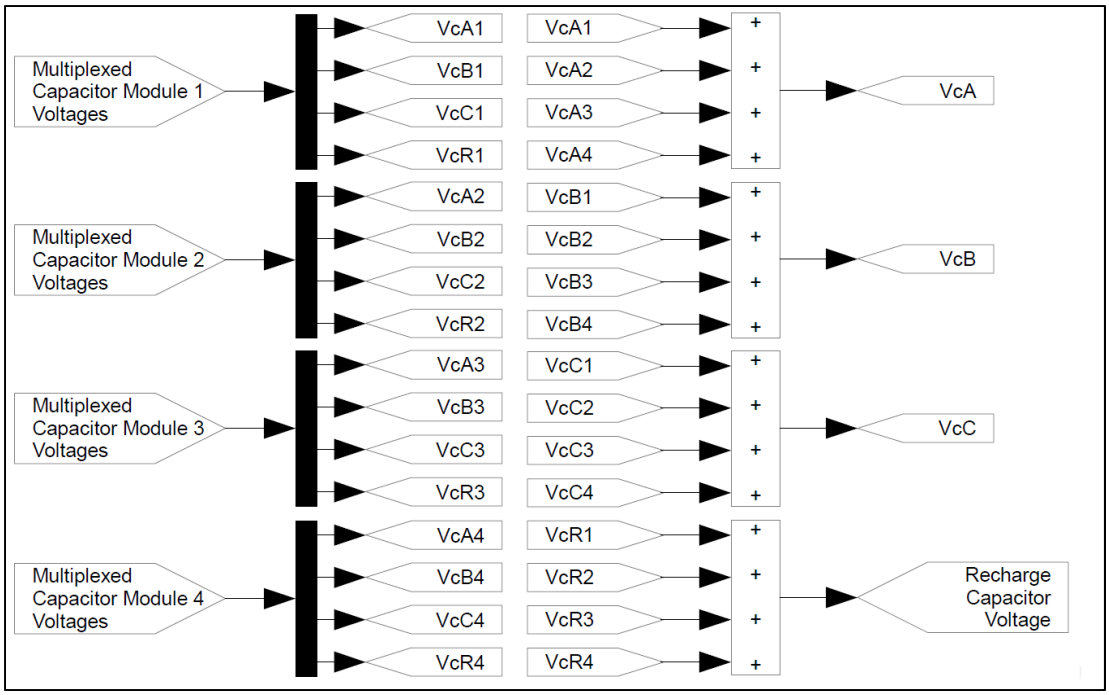

Figure 6.8 Calculation of the capacitor voltages at the point of view of the motor phases and recharge circuit

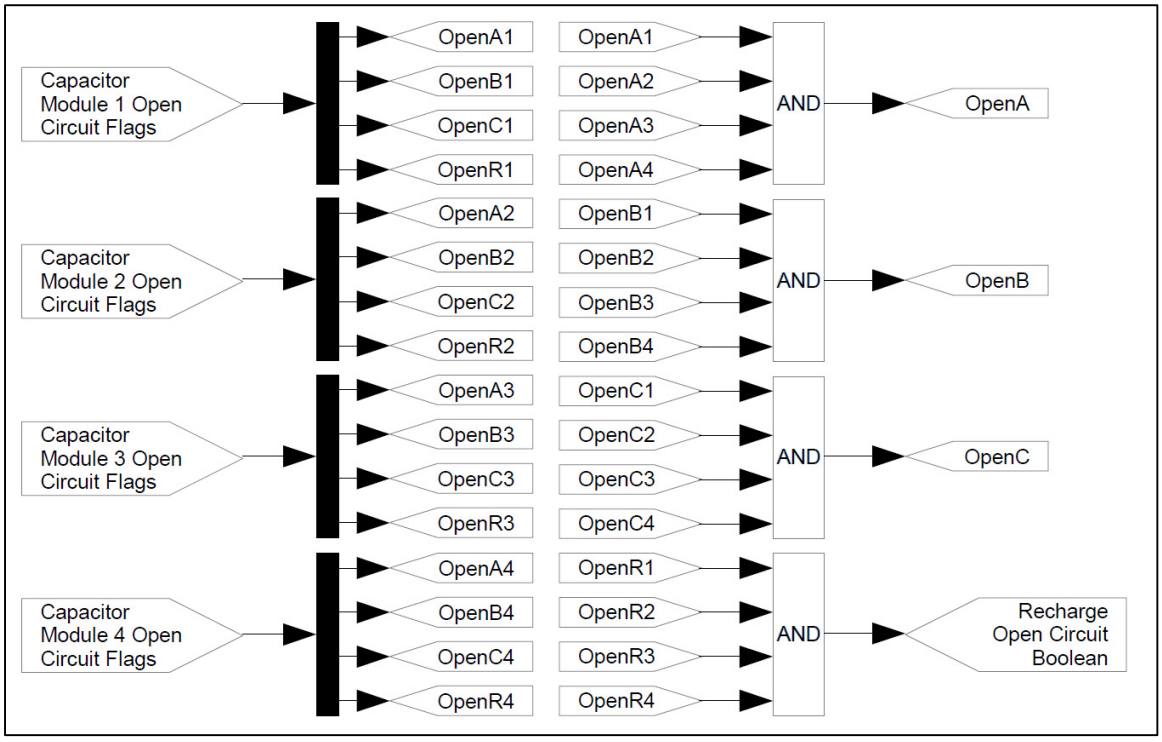

Figure 6.9 Determination of the Open Circuit flags for the motor phases and recharge circuit

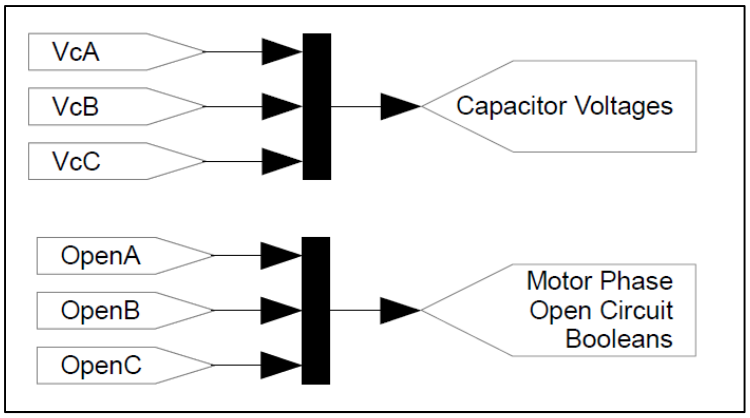

Figure 6.10 Multiplexing of the Capacitor Voltages and the Motor Phase Open Circuit Booleans

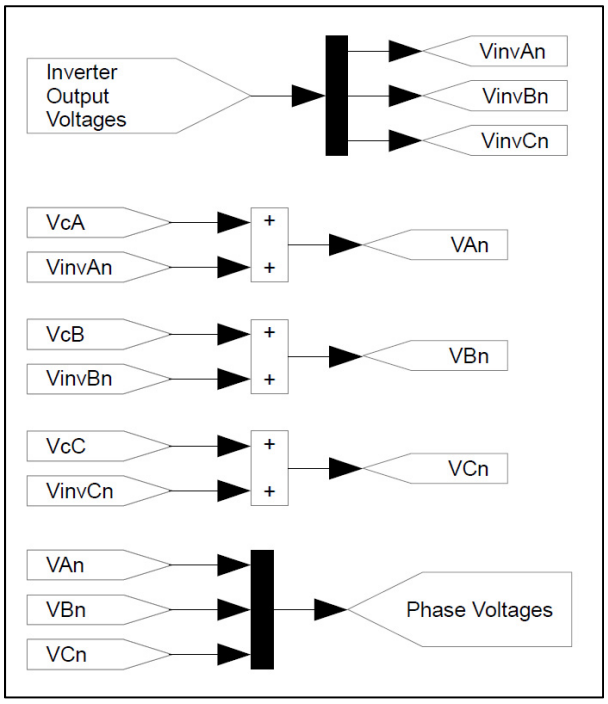

Figure 6.11 Calculation of the phase voltages

6.2.4.1 Simulation of the Capacitor Modules

The Resonant Power Processor contains 4 Capacitor Modules. The Capacitor Modules can be seen as sub-components of the Resonant Power Processor and are strictly identical. The capacitor Module sub-model simply consists of the dynamic model of a capacitor and signal routing operations implemented as matrix operations, and which are function of the RPP

switches states. Figure 6.12 shows the architecture of the Capacitor Module simulation model, including the data flow between the different model components.

The Current Routing block generates the Open Circuit signals of the Capacitor Module (Open_AX to Open_RX) and the current circulating in the capacitor (Icap). See Equation 6.7 for the matrix operation generating the Icap signal and see Figure 6.13 for the logic that determines the Open_AX to Open_RX signals. The Voltage Routing matrix operation can be found at equation 6.8.

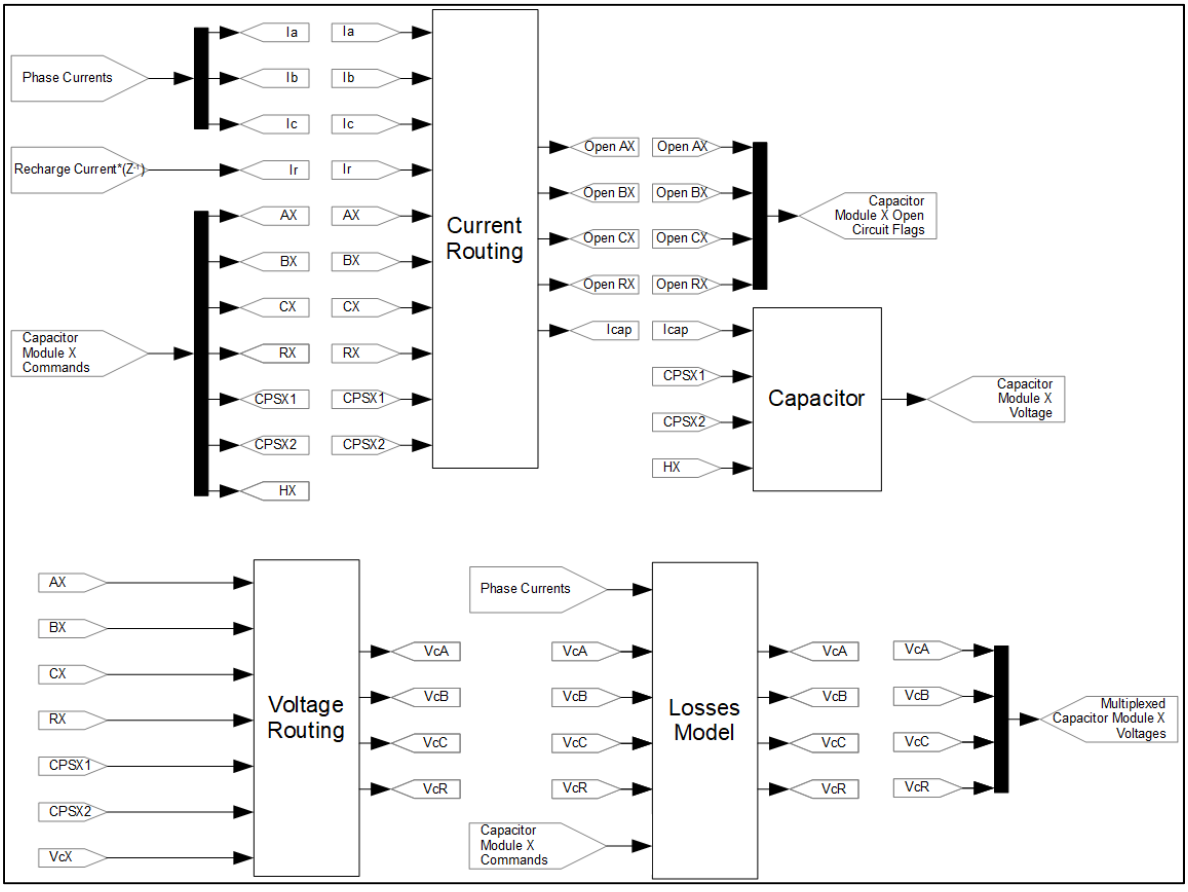

Figure 6.12 Architecture of the Configurable Capacitor Module simulation model

$$Icap = (CPSX1 - CPSX2) \cdot [AX \quad BX \quad CX \quad RX] \cdot \begin{bmatrix} Ia \\ Ib \\ Ic \\ Ir \end{bmatrix} \tag{6.7}$$

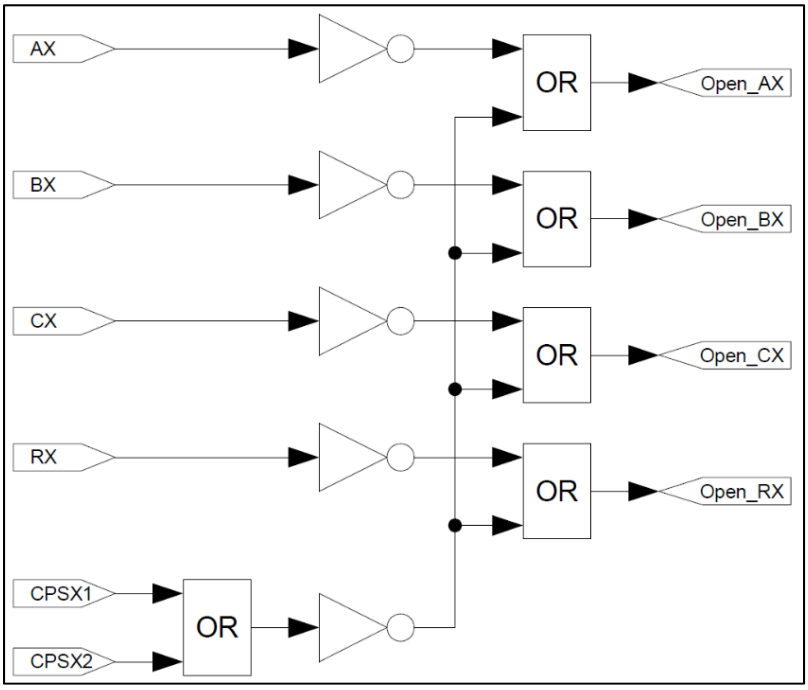

Figure 6.13 Open Circuit signals determination logic

$$\begin{bmatrix} VcA \\ VcB \\ VcC \\ VcR \end{bmatrix} = (CPSX2 - CPSX1) \cdot VcX \cdot \begin{bmatrix} AX \\ BX \\ CX \\ RX \end{bmatrix} \tag{6.8}$$

6.2.4.2 Capacitor Simulation Model

The Capacitor Model encloses the dynamic model of the capacitor, and the capacitor configurator which is used to determine the capacitance "C" of the capacitor as a function of the HX switch and the capacitor polarity as a function of the CPSX1 and CPSX2 switches.

The dynamic model of the capacitor integrates the current flowing in the capacitor to determine the capacitor charge "CapQ". Depending on the HX, CPSX1 and CPSX2 switches configuration, the integrator is being reset to a different charge. Both CPSX1 and CPSX2 switches being true simultaneously will reset the capacitor charge to 0 Coulomb as both terminals of the capacitor will be shorted. The HX switch transitioning from true to false will

divide the capacitor charge in two. The Capacitor Configurator logic determines the integrator reset Boolean, the capacitor charge reset value and the capacitor's capacitance. The Capacitor model architecture is shown at Figure 6.14 below, and the Capacitor Configurator algorithm is shown at Figure 6.15.

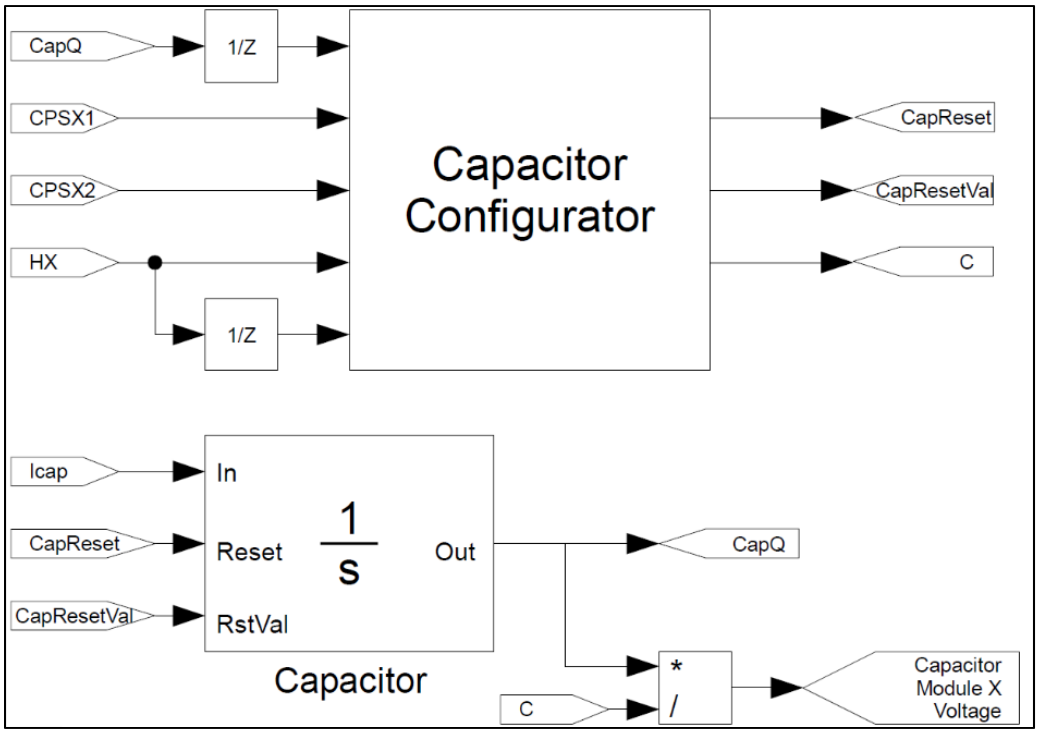

Figure 6.14 Capacitor Model Architecture

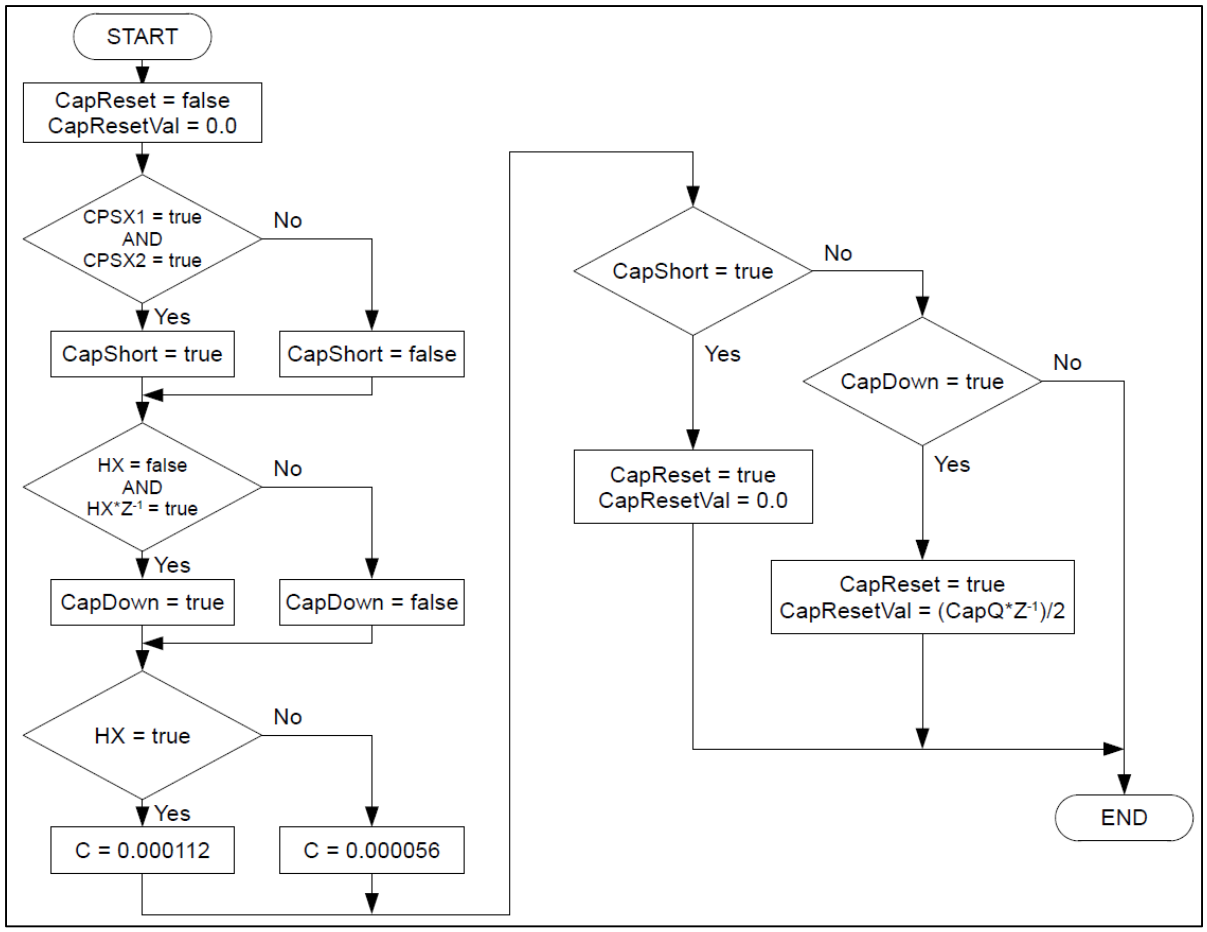

Figure 6.15 Capacitor Configurator Flowchart

6.2.4.3 Simulation Model of the Recharge Circuit

The recharge circuit consists of the recharge inductance and the semiconductors that control the recharge energy. The Recharge Circuit solves the differential equation shown at Equation (6.9) below:

$$V_C X + V_{in} = (L \cdot s + R) \cdot I \tag{6.9}$$

Where V_cX is the capacitor's voltage, V_{in} is the input voltage, L is the Recharge Inductance (0.333 mH), R is the Recharge Resistance (0.0016 Ω) and I is the Recharge Current. Depending on the status of the Recharge Circuit Command (R_ON), the input voltage may be the battery voltage when R_ON is set to true or 0 Volt when R_ON is set to false. The "Recharge Open

Circuit Boolean" resets the current to 0 Amps when true. The integrator's output is saturated between 0 Amps and positive infinite because the Recharge Circuit's diodes prevent reverse current.

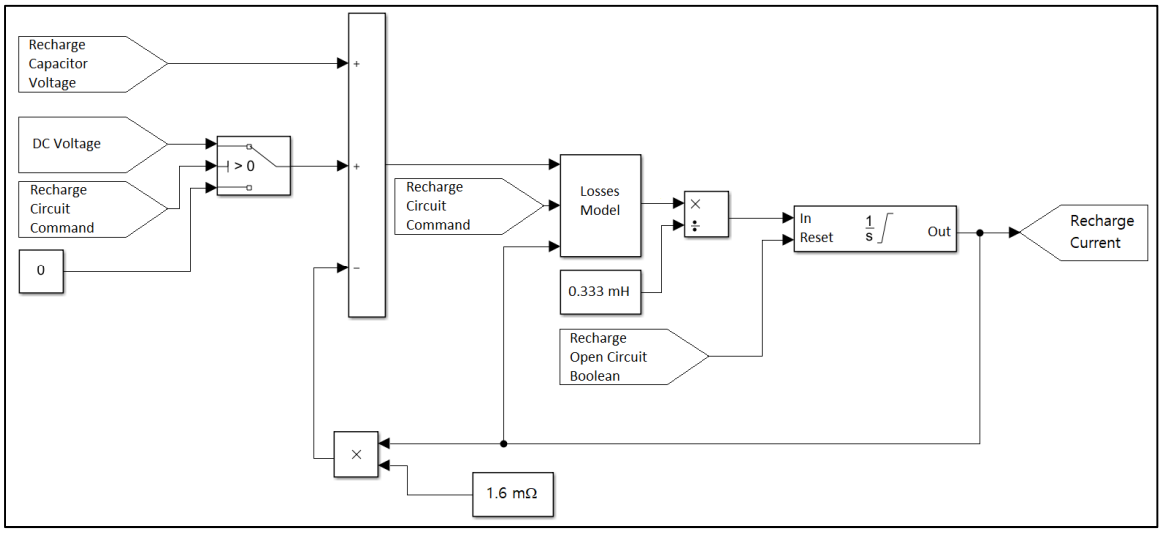

Figure 6.16 Recharge Circuit Model Architecture

6.2.5 Simulation of the system losses

Because the losses in the system cannot be neglected, the conduction losses have been considered in the dynamic model described in Sections 6.2.2 and 6.2.4. The losses are modeled in the form of voltage drops across the current paths, and the power losses are quantified by multiplying the current with the voltage drops. Because their fast dynamics cannot be modeled, the switching losses are not considered in the dynamic simulation of the system. However, the switching losses are quantified in an open loop implementation based on the switching losses equations described in this section. The system losses are calculated based on the voltages, currents and semiconductors state generated by the simulation model. As the simulation model does not include a thermal model of the system, a temperature of 100°C for each component is assumed. The following section describes the calculation of the losses of the system. System losses have been implemented in distinct Matlab subsystems in the form of Matlab code. Matlab codes modeling the system losses can be found in ANNEX IV to VI.

6.2.5.1 Simulation of the Inverter Losses

As previously seen in Section 5.2, the modified inverter topology includes 6 MOSFETs and 3 bi-directional switches made of 2 MOSFETs each in anti-parallel configuration. The inverter switching frequency is fixed at 10 kHz. The semi-conductor losses consist of 2 categories; the switching losses and the conduction losses. The switching losses occur every time a MOSFET changes state. As the state transition time is in the range of nanoseconds, the simulation sample time is too long to capture the semiconductors' dynamic. The switching losses are applied on one simulation time step when the MOSFET state transitions. The conduction losses apply when current circulates through the semiconductor components (MOSFET, Bi-Directional Switches), therefore the conduction losses must be continuously monitored. See equations (6.10) to (6.13) for the calculation of the energy losses per simulation time step. Equations (6.10) to (6.13) are based on the MOSFET losses equations previously seen in section 1.4, and on the parameters defined in Table 6.2 below.

6.2.5.2 MOSFET switching losses

When a MOSFET transitions from false to true, the dissipated energy can be found as per Equation (6.10) below:

$$E_{MOSFET,ON} = \frac{V_{DS} \cdot I_X}{2} \cdot \left(\frac{(Q_{GD} + Q_{GS}/2) \cdot R_{G\_ON}}{V_{DR} - V_{GS(SP)}} \right)$$

$$E_{MOSFET,ON} = \frac{160.0 \cdot I_X}{2} \cdot \left(\frac{\left(\left(190 + \frac{84}{2} \right) \cdot 10^{-9} \right) \cdot 0.3}{15.0 - 6.0} \right) \tag{6.10}$$

$$= I_X \cdot 6.187 \cdot 10^{-7}$$

When a MOSFET transitions from true to false, the dissipated energy can be found as per Equation (6.11) below:

$$E_{MOSFET,OFF} = \frac{V_{DS} \cdot I_X}{2} \cdot \left(\frac{(Q_{GD} + Q_{GS}/2) \cdot R_{G\_ON}}{V_{GS(SP)}} \right)$$

$$E_{MOSFET,OFF} = \frac{160.0 \cdot I_X}{2} \cdot \left(\frac{\left(\left(190 + \frac{84}{2} \right) \cdot 10^{-9} \right) \cdot 0.3}{6.0} \right) \tag{6.11}$$

$$= I_X \cdot 9.28 \cdot 10^{-7}$$

6.2.5.3 MOSFET conduction losses

A MOSFET conducts in forward direction only when its status is ON. Otherwise, it blocks the current in forward direction. In reverse direction, the current circulates through the body diode of the MOSFET.

When the MOSFET is ON and conducts current in the forward direction, the conduction loss in terms of energy per simulation cycle can be found at Equation (6.12) below:

$$E_{MOSFET,FWD} = R_{DS,ON} \cdot I_X^2 \cdot T$$
$$E_{MOSFET,FWD} = 1.06 \cdot I_X^2 \cdot 10^{-6} \tag{6.12}$$

When the MOSFETs conducts current in the reverse direction (through the body diode), the conduction loss in terms of energy per simulation cycle can be found at Equation (6.13) below:

$$E_{MOSFET,REV} = V_F \cdot |I_X| \cdot T$$
$$E_{MOSFET,REV} = 1.5 \cdot |I_X| \cdot 10^{-6} \tag{6.13}$$

6.2.5.4 Losses in the bi-directional switches

The Bi-directional switches being made of 2 MOSFETs in anti-parallel configuration, the losses of the bi-directional switches consist of the combined losses of the 2 MOSFETs. At all times when current circulates through a bi-directional switch, the current goes through the drain and source of one MOSFET and through the body diode of the other MOSFET. Therefore, the conduction loss of the bi-directional switch is the sum of the conduction losses

of the MOSFET and body diode of the second MOSFET. Because only the current in forward direction generates switching losses (reverse direction current passes through the body diode), the switching loss of only one MOSFET is considered for the bi-directional switch loss calculation. The voltage through the bi-directional switches is +/- $V_{dc}/2$ while switching.

Table 6.2 MOSFET losses calculation parameters

Parameter	Description	Value	Unit
$R_{DS,ON}$	Conduction Resistance of the MOSFET	1.06	Ω
V_F	MOSFET Body Diode Voltage Drop	1.5	V
Q_{GD}	GD Capacitor Charge	190.E-9	C
Q_{GS}	GS Capacitor Charge	84.E-9	C
R_{G_ON}	Gate resistance during ON transition	0.3	Ω
R_{G_OFF}	Gate resistance during OFF transition	0.3	Ω
V_{DR}	Gate Driver Voltage	15.0	V
$V_{GS(SP)}$	Gate to source voltage threshold	6.0	V
V_{DS}	Drain to Source Voltage ($V_{dc}/2$)	160.0	V
T	Simulation sample time	1.E-6	second

6.2.5.5 Simulation of the Resonant Power Processor (RPP) Losses

The Resonant Power Processor contains 4 Configurable Capacitor Modules and one Recharge Circuit. The losses calculation for the Resonant Power Processor (RPP) includes the total of the losses in each Configurable Capacitor Module and in the Recharge Circuit. Details of the RPP losses calculation can be found in the following sections.

6.2.5.6 Losses in the Configurable Capacitor Modules

When the Resonant Power Processor (RPP) is offline, the current in each Configurable Capacitor Module goes through two bi-directional switches and two sets of two bi-directional switches in parallel. When the RPP is online, the current in each Configurable Capacitor Module goes through 4 bidirectional switches in series. If the high capacitance configuration is not selected, the current circulates in only one 56μF capacitor. If the high capacitance configuration is selected (HX is true), the current circulates in two 56 μF capacitors in parallel and the conduction loss of the HX switch is added to the Configurable Capacitor Module's

losses. For simplification of the simulation model, in the case the HX switch is “ON”, the current is assumed to be identical between the two 56μF capacitors. The bidirectional switches being made of two IGBTs in anti-parallel configuration, the losses in the bidirectional switches are the conduction losses of the IGBT and of the diode simultaneously. The losses in the capacitor bank consists of the resistive losses generated by the Equivalent Series Resistance (ESR). The current through the Recharge Circuit goes through the recharge inductance, one diode and one MOSFET when the R_ON transistor state is “ON”.

6.2.5.7 Switching Losses in the Bi-Directional Switches

Considering that when the RPP is online, half of the Bi-Directional switches are upstream of the capacitor and the other half are downstream, one finds that the voltage across the Bi-Directional switches upstream of the capacitor is equal to the phase voltage and that the voltage across the Bi-Directional switches upstream of the capacitor is equal to the sum of the phase voltage and capacitor voltage. As the current flows through the diode of at least one IGBT of the Bi-Directional switch, the switching losses apply to only the other IGBT which conducts current in forward direction.

It is to be noted that the Bi-Directional switches are not used for PWM switching, therefore their switching frequency is relatively low compared to the inverter’s witching frequency. Also, switching of the RPP bi-directional switches is done at zero current (or close to zero current), therefore based on Equations (1.44) and (1.45), switching losses at zero current are negligible. For those reasons, the switching losses of the bi-directional switches in the Configurable Capacitor Modules are neglected.

6.2.5.8 Conduction Losses in the Bi-Directional Switches

Each Bi-Directional switch in the model generate switching losses and conduction losses. The conduction losses in a Bi-Directional switch can be found at equation (6.14) below, where I_{BDSW} is the current in the Bi-Directional Switch.

$$E_{BDSW,Cond} = (V_{CE0} + R_{CE0} \cdot I_{BDSW} + V_{EC0} + R_{EC0} \cdot I_{BDSW}) \cdot I_{BDSW} \cdot T$$
$$E_{BDSW,Cond} = (1.6 + 0.016 \cdot I_{BDSW} + 1.3 + 0.028 \cdot I_{BDSW}) \cdot I_{BDSW} \quad (6.14)$$
$$\cdot 0.000001 = |I_{BDSW}| \cdot (2.9 + 0.044 \cdot |I_{BDSW}|) \cdot 10^{-6}$$

Table 6.3 IGBT losses calculation parameters

Parameter	Description	Value	Unit
$E_{ON,I}$	Nominal IGBT switch ON energy	1.8E-3	J
$E_{OFF,I}$	Nominal IGBT switch OFF energy	1.4E-3	J
V_{ref}	Reference voltage	600.0	V
i_{ref}	Reference current	40.0	A
V_{CE0}	IGBT voltage bias	1.6	V
R_{CE0}	IGBT internal resistance	0.016	Ω
V_{EC0}	Diode voltage bias	1.3	V
R_{EC0}	Diode internal resistance	0.028	Ω
T	Simulation sample time	1.E-6	second

6.2.5.9 Losses in the Capacitor

The losses in the capacitor consists of the resistive losses generated by the Equivalent Series Resistance (ESR) of the capacitor. As previously seen in Section 5.3.1.1, the capacitor consists of a capacitor bank of 5 capacitors (2x 60 µF, 1x 70 µF and 2x 80 µF). The capacitor bank has 2 legs with different capacitances in each leg. Therefore, the current will not be equal in each leg of the capacitor bank. The leg 1 (2x 60 µF capacitors) has an equivalent capacitance of 30 µF, and the leg 2 (1x 70 µF and 2x 80 µF) has an equivalent capacitance of 25 µF. Knowing that the voltage across both legs of the capacitor bank is identical, one finds that the equations of the current in each leg of the capacitor bank as a function of the capacitor bank current at equations (6.15) and (6.16) below:

$$I_{Cap,leg1} = \frac{30}{55} \cdot I_{Cap} \quad (6.15)$$

$$I_{Cap,leg2} = \frac{25}{55} \cdot I_{Cap} \quad (6.16)$$

$$R_{Cap,leg1} = 2 \cdot R_{Cap,60} \tag{6.17}$$

$$R_{Cap,leg2} = R_{Cap,70} + 2 \cdot R_{Cap,80} \tag{6.18}$$

$$E_{Cap} = R_{Cap,leg1} \cdot \left(I_{Cap,leg1}\right)^2 \cdot \Delta t + R_{Cap,leg2} \cdot \left(I_{Cap,leg2}\right)^2 \cdot T$$

$$E_{Cap} = 2.2959 \cdot 10^{-9} \cdot I_{Cap}^2 \tag{6.19}$$

The losses through the insulation layers are neglected and the self-inductance of the capacitor is also neglected as the capacitor is always connected in series with a significantly higher inductance (either the motor phases or the recharge inductance).

Table 6.4 Capacitor losses calculation parameters

Parameter	Description	Value	Unit
$R_{Cap,60}$	Equivalent Series Resistance (ESR) of 60 µF capacitor	0.0024	Ω
$R_{Cap,70}$	Equivalent Series Resistance (ESR) of 70 µF capacitor	0.0014	Ω
$R_{Cap,80}$	Equivalent Series Resistance (ESR) of 80 µF capacitor	0.0014	Ω
T	Simulation sample time	1.E-6	second

6.2.5.10 Losses in the Recharge Circuit

The losses in the recharge circuit consist of the conduction losses in the recharge inductance, the conduction losses in the diodes, the conduction losses in the MOSFET and the switching losses of the MOSFET.

6.2.5.11 Losses in the recharge inductance

As previously seen in Section 5.3.2, the recharge inductance consists of 3 identical inductances connected in parallel. The conduction losses in the inductance are the resistive losses caused by the inductance's resistance.

$$E_{ind} = \frac{R_{ind,1}}{3} \cdot I_R^2 \cdot T$$
$$E_{ind} = 1.6 \cdot 10^{-9} \cdot I_R^2 \quad (6.20)$$

6.2.5.12 Losses in the recharge diodes

The recharge circuit diodes losses are always applied when the recharge current circulates in the recharge circuit. Either if the recharge MOSFET is ON or OFF, a diode is present on both possible current paths. The information to model the diode losses are found in the diode's datasheet. The losses in the recharge diodes can be found at Equation (6.21) below:

$$E_{diode} = (V_{FO} + R_{F0} \cdot I_R) \cdot I_R \cdot T$$
$$E_{diode} = (0.8 \cdot |I_R| + 0.0017 \cdot I_R^2) \cdot 10^{-6} \quad (6.21)$$

6.2.5.13 Losses in the recharge MOSFET

The losses in the recharge MOSFET are calculated with the same approach as it was discussed in Sections 6.2.5.2 and 6.2.5.3.
When the recharge MOSFET transitions from false to true:

$$E_{MOSFET,ON} = \frac{V_{DS} \cdot |I_R|}{2} \cdot \left(\frac{(Q_{GD} + Q_{GS}/2) \cdot R_{G\_ON}}{V_{DR} - V_{GS(SP)}} \right)$$
$$E_{MOSFET,ON} = \frac{320.0 \cdot |I_R|}{2} \cdot \left(\frac{\left(\left(190 + \frac{84}{2} \right) \cdot 10^{-9} \right) \cdot 0.3}{15.0 - 3.5} \right) \quad (6.22)$$
$$= |I_R| \cdot 9.683 \cdot 10^{-7}$$

When the recharge MOSFET transitions from true to false:

$$E_{MOSFET,OFF} = \frac{V_{DS} \cdot |I_R|}{2} \cdot \left(\frac{(Q_{GD} + Q_{GS}/2) \cdot R_{G\_ON}}{V_{GS(SP)}} \right)$$

$$E_{MOSFET,OFF} = \frac{320.0 \cdot |I_R|}{2} \cdot \left(\frac{\left(\left(190 + \frac{84}{2} \right) \cdot 10^{-9} \right) \cdot 0.3}{3.5} \right) \tag{6.23}$$

$$= |I_R| \cdot 3 \cdot 10^{-6}$$

When the recharge MOSFET is true:

$$E_{MOSFET,FWD} = R_{DS,ON} \cdot I_R^2 \cdot T$$
$$E_{MOSFET,FWD} = 1.78 \cdot I_R^2 \cdot 10^{-7} \tag{6.24}$$

Table 6.5 Recharge Circuit losses calculation parameters

Parameter	Description	Value	Unit
$R_{ind,1}$	Resistance of a 1mH inductance	0.005	Ω
$R_{DS,ON}$	Conduction Resistance of the MOSFET	0.178	Ω
Q_{GD}	GD Capacitor Charge	190.E-9	C
Q_{GS}	GS Capacitor Charge	84.E-9	C
R_{G_ON}	Gate resistance during ON transition	0.3	Ω
R_{G_OFF}	Gate resistance during OFF transition	0.3	Ω
V_{DR}	Gate Driver Voltage	15.0	V
$V_{GS(SP)}$	Gate to source voltage threshold	3.5	V
V_{DS}	Drain to Source Voltage (V_{dc}/2)	320.0	V
V_{F0}	Diode forward voltage drop	0.8	V
R_{FO}	Diode forward conduction resistance	0.0017	Ω
T	Simulation sample time	1.E-6	second

6.2.5.14 Simulation of the Permanent Magnet Synchronous Motor (PMSM) Losses

The losses in the PMSM typically consist of the electrical losses and mechanical losses. The electrical losses consist of the resistive losses in the motor coils and the iron losses caused by the current harmonics. The mechanical losses consist of the drag in the rotative components, caused either by the air drag or the bearings drag.

As there is no accurate model available to simulate the motor thermal and electromagnetic behavior, the motor losses could not be quantified. Therefore, the following assumptions are made:

- The mechanical losses are neglected.
- The iron losses are assessed qualitatively as a function of the phase current harmonics.
- The resistive losses are calculated as per Equation (6.25) below.

$$E_{motor} = R_s \cdot (I_A^2 + I_B^2 + I_C^2) \cdot T \tag{6.25}$$

Table 6.6 Motor losses calculation parameters

Parameter	**Description**	**Value**	**Unit**
R_s	Motor Phase Resistance	0.5	Ω
T	Simulation sample time	1.E-6	second

CHAPTER 7

PRESENTATION OF THE RESULTS

This section presents the results of the research project. Because no hardware prototype was built, experimental results are not available. However, the simulation results presented herein are deemed sufficient to demonstrate the proof of concept and to have a good approximation of the system performances. First, the simulation has been performed with a time step of 1 µs (1 MHz). This simulation time step is deemed sufficient to capture the pertinent system dynamics, as the electrical frequency (Fundamental frequency) is 360 Hz and the switching frequency is 10 kHz. The simulation time step allows to have a 1% resolution on the pulse width, which is representative of the real system implementation. Also, the conduction losses have been embedded in the dynamic model, which improve the realism of the simulation. The switching losses of the semiconductors have not been embedded in the dynamics of the simulation model because their dynamic is too fast, however the switching losses have been calculated based on the voltages, currents and semiconductor devices status, as per Section 6.

Even if a functional prototype has not been built, the virtual prototype has been developed assuming commercially available components and specifications. Their specifications were available from the supplier's data sheets. This allowed not only to be able to model the system losses accurately, but also to estimate the weight of the Resonant Power Processor. The weight estimation of the RPP is a mandatory parameter to assess the power density of the proposed system compared to the baseline system. The weight estimate has been done for the power electronic components, which represents most of the converter weight. The control electronics, the wires, the cooling system and the mechanical packaging of the RPP have not been considered in the estimation of the weight.

7.1 Simulation Results

The simulation results are presented in two distinct aspects. First, the system behavior is detailed during the entire motor run-up, with more detailed results during key transitions of the run-up process. This first aspect of the simulation results will mainly focus on the following parameters: Motor speed and torque, efficiency, control performance, output power quality, phase voltages and currents, and RPP capacitors. Second, the operation of the Resonant Power Processor and its control algorithm in steady state is detailed to demonstrate the correct implementation of the control algorithm presented in Section 5.4. The results presented in this section are analysed in detail in the Section 8.

7.1.1 Motor Run-up

The model simulates a motor run-up from 0 rpm to 5400 rpm with a propeller load attached to the output shaft as defined in Section 6.2.3.2. During the run-up, the Resonant Power Processor goes through 3 important transitions: The Resonant Power Processor transition from Offline to Online, the capacitance transition from 112 µF to 56 µF and the stabilization towards steady state operation. Once the motor run-up is completed and stabilization is reached, the system is in steady state. The following sections shows the different steps towards reaching steady state operation and provide detailed results of the system performances in steady state. As mentioned earlier, the load is a propeller which generates torque as a function of speed squared and is sized to generate a torque of 14 N.m at 5400 rpm. The motor speed and torque of the PMSM during the run-up are shown in Figure 7.1, the PMSM mechanical power during the run-up is shown at Figure 7.2, and direct and quadrature voltage commands and currents are shown in Figure 7.3. The motor phase voltages, capacitors currents and voltages and the DC Link voltage and current are shown in Figures 7.4 to 7.6 respectively. Finally, the neutral line current is shown in Figure 7.7.

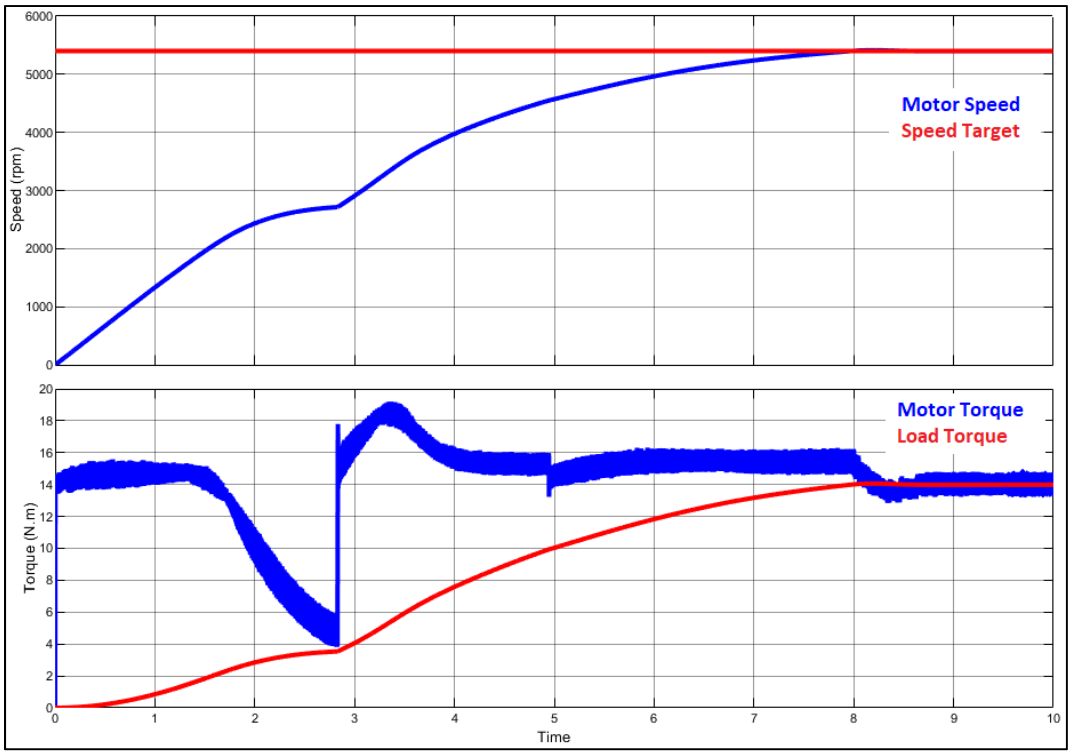

Figure 7.1 Motor Torque and Speed during Run-Up

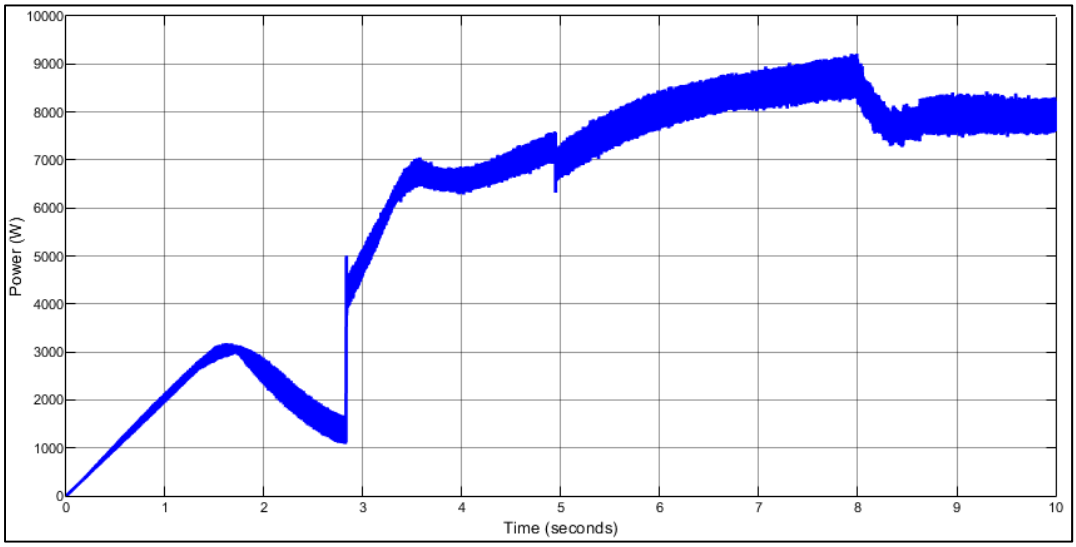

Figure 7.2 Motor mechanical power during Run-Up

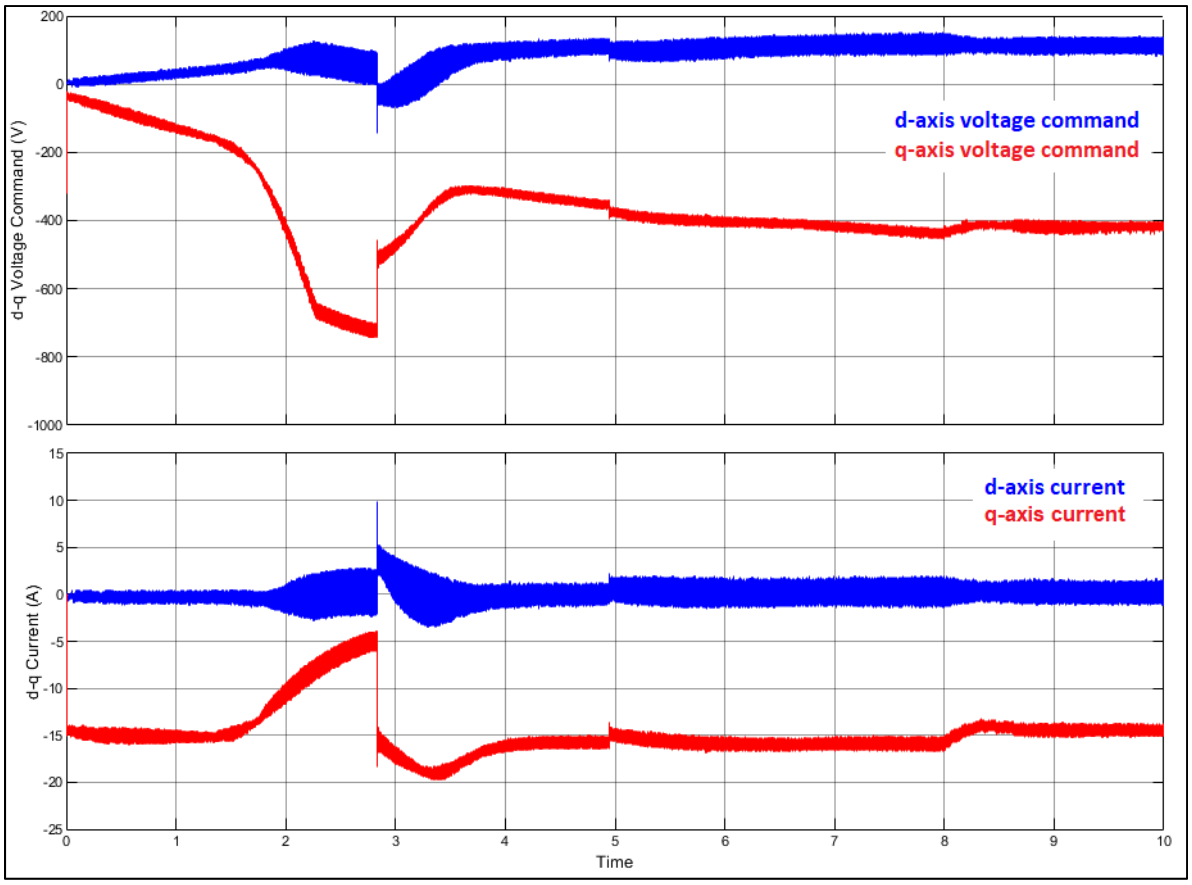

Figure 7.3 d-q Axis Voltage and Current during run-up

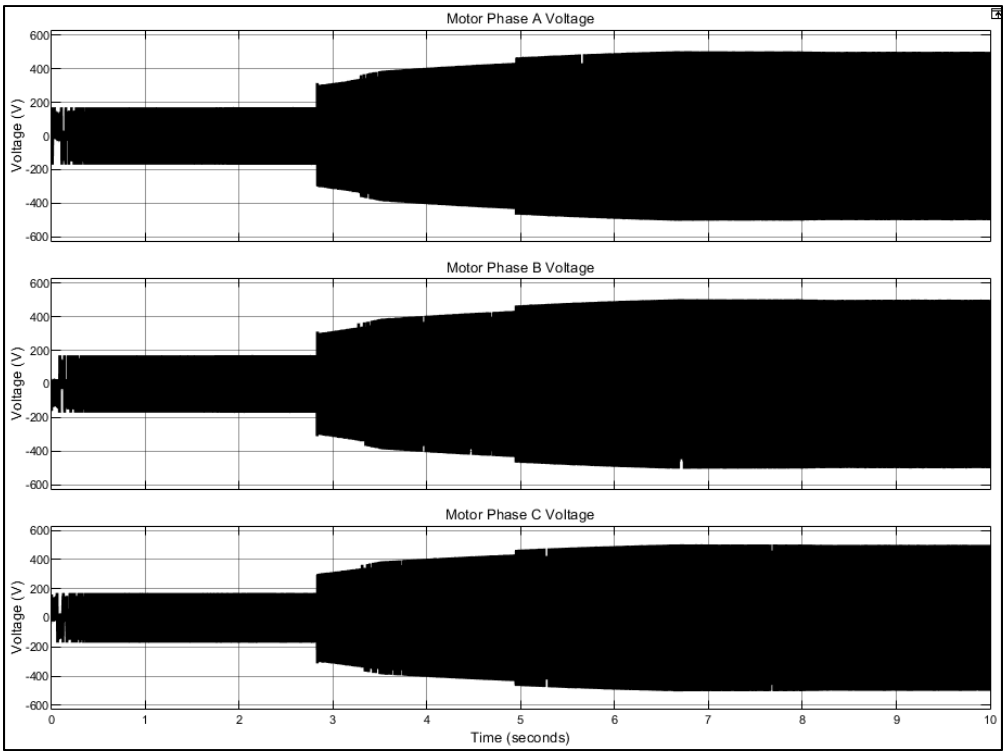

Figure 7.4 Motor Phase Voltages during Run-Up

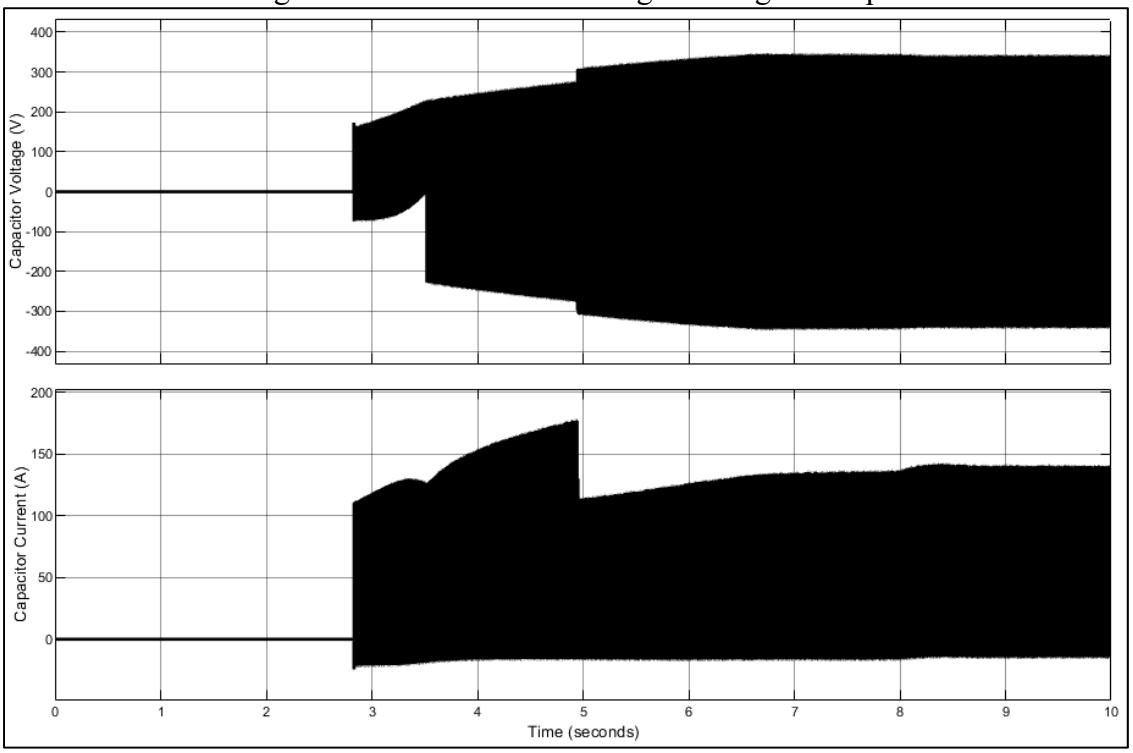

Figure 7.5 Capacitors Voltages and Currents during Run-Up

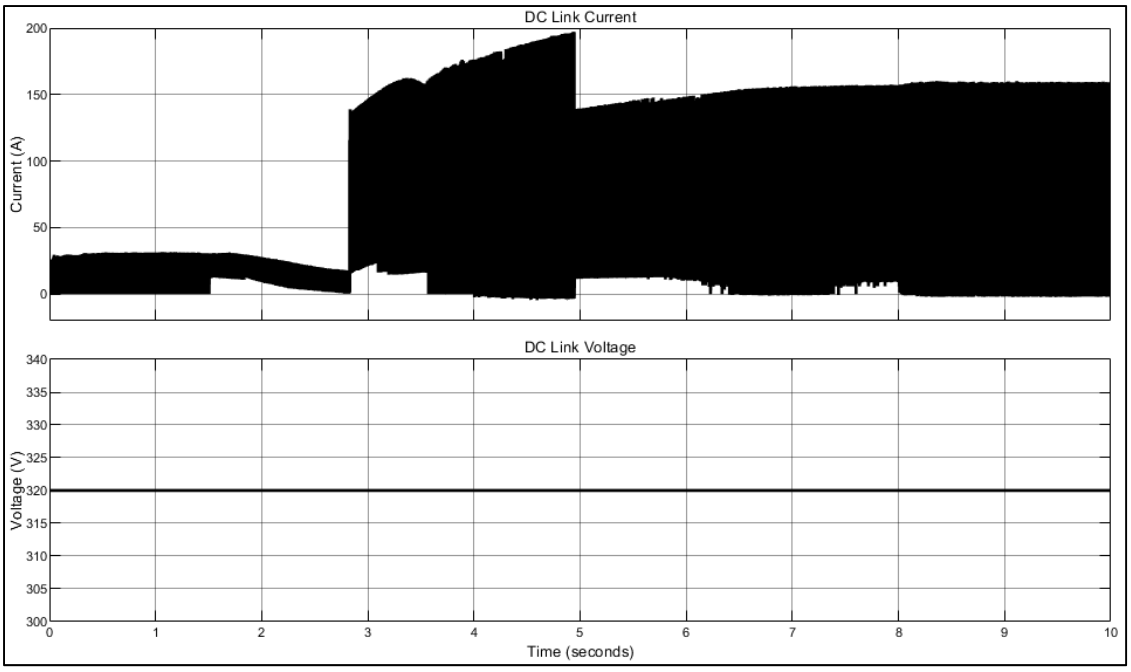

Figure 7.6 DC Link Current and Voltage during Run-up

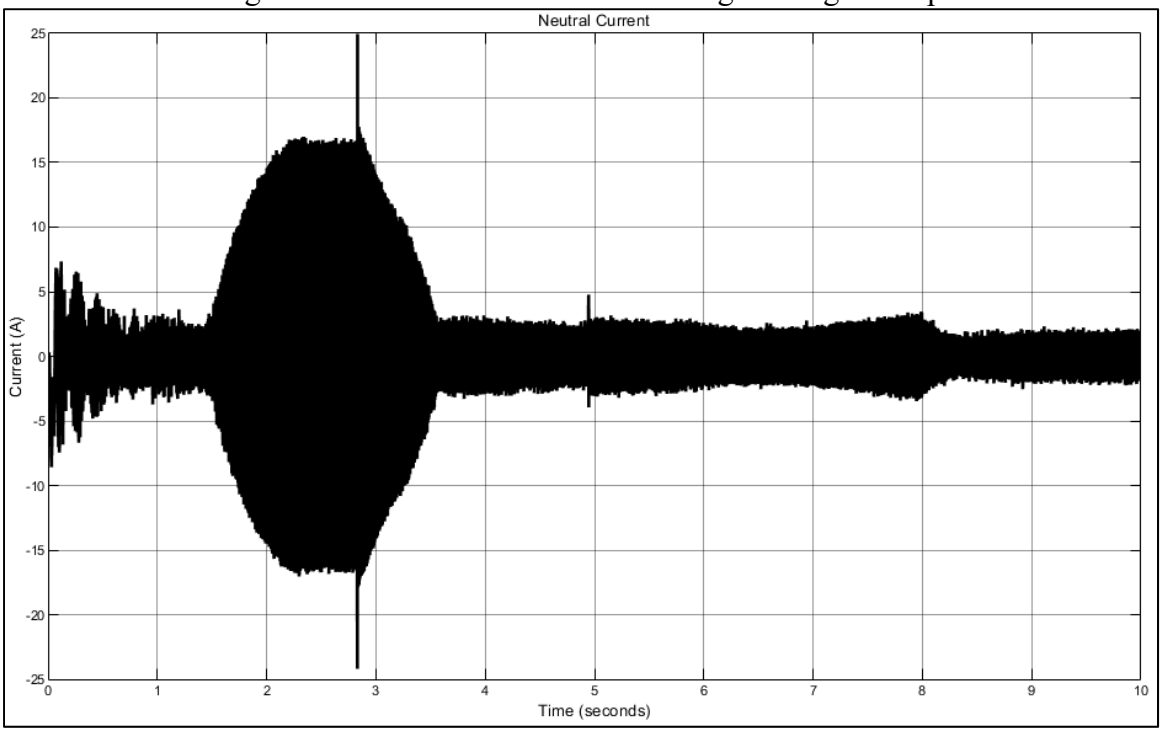

Figure 7.7 Neutral Current

7.1.2 1st transition – Resonant Power Processor transition from Offline to Online

During the 1st transition, the RPP goes from Offline Status to Online status. When in Offline status, the RPP provides a direct connection between the motor and the inverter. When the RPP goes online, the recharged capacitors are connected in alternance to a motor phase to create a phase voltage boost that overcomes the motor Back-EMF. All capacitors, after the discharge cycle, are connected to the recharge circuit to be recharged in alternance. The threshold for transition between the Offline and Online statuses is when the motor speed reaches 2714 rpm (2700 rpm plus hysteresis).

The time window of the transition is between 2.82 and 2.84 seconds. Figure 7.8 shows the motor speed and motor torque during the 1st transition. Figure 7.9 shows the inverter output phase voltage commands. Figure 7.10 shows the motor phase voltages, which is the combined voltage of the inverter and the capacitors. Figure 7.11 shows the phase currents. Figure 7.12 shows the DC-Link current and Voltage. Figure 7.13 shows the voltages and currents of all the Configurable Capacitor Modules. Figure 7.14 shows all Configurable Capacitor Modules phase selection switches (AX, BX, CX and RX) statuses. Finally, Figure 7.15 shows all Configurable Capacitor Modules polarity setting switches (CPSX1 and CPSX2) statuses.

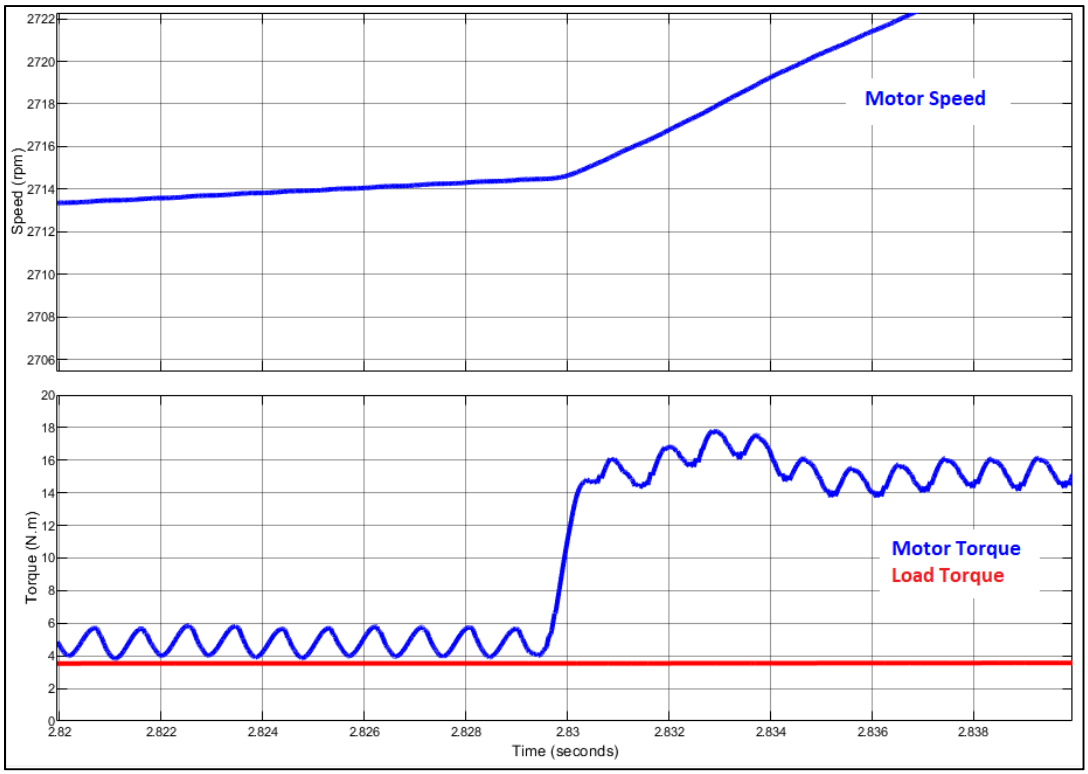

Figure 7.8 Motor Torque and Motor Speed during 1st transition

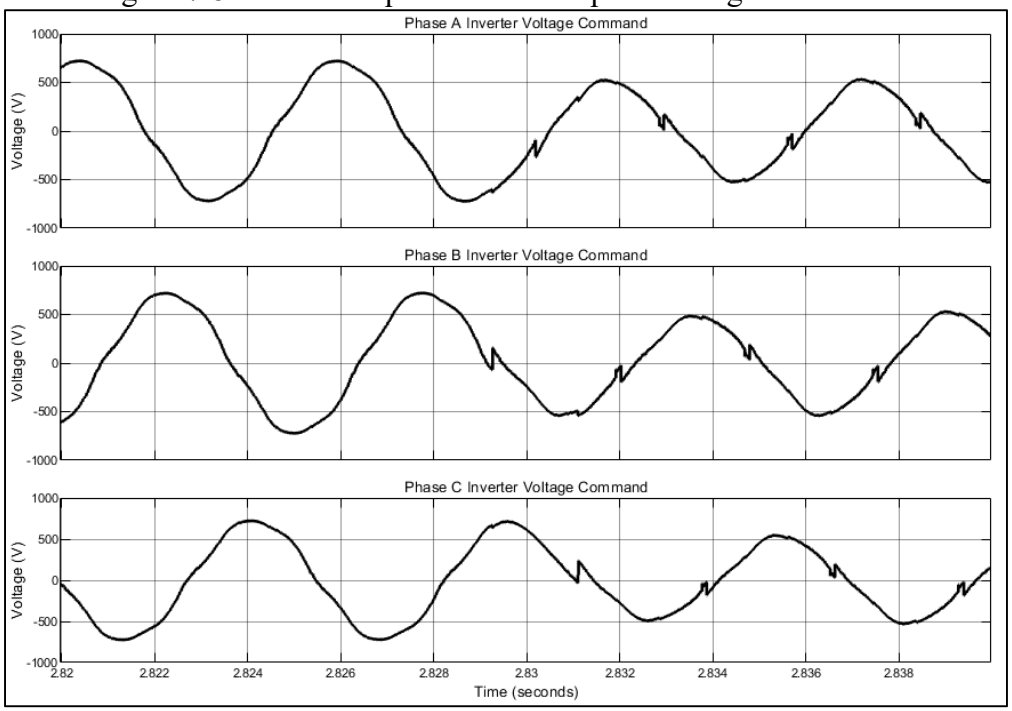

Figure 7.9 Inverter output voltage commands during 1st transition

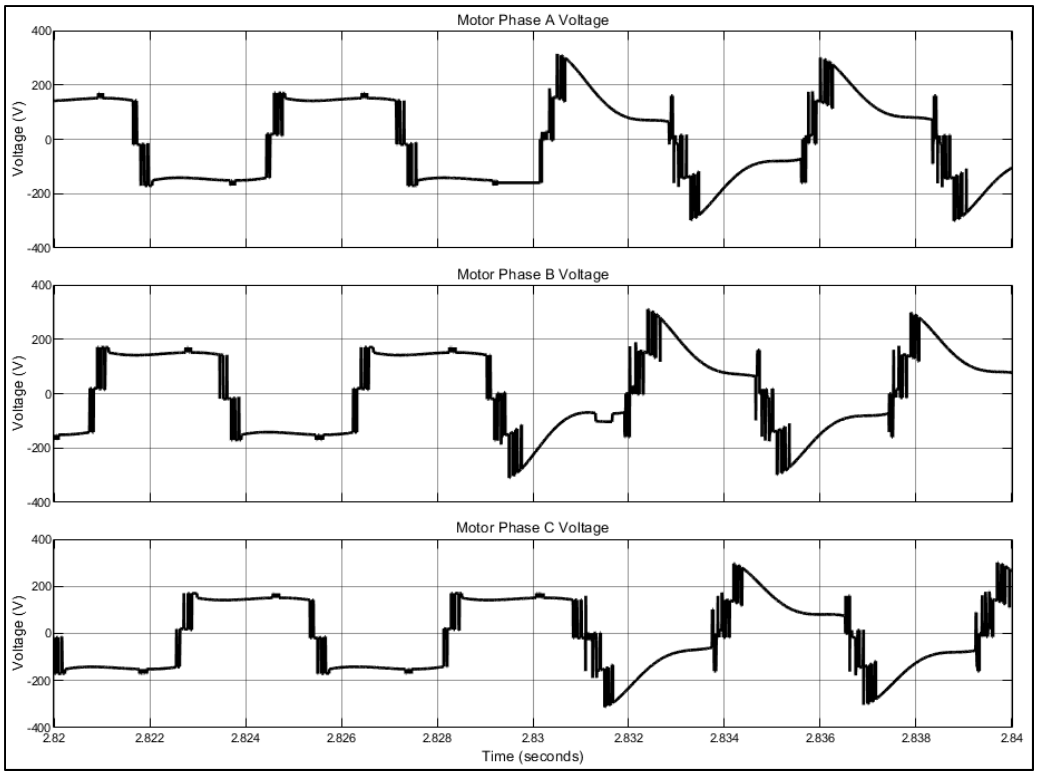

Figure 7.10 Motor Phase Voltages (Inverter + capacitors) during 1st transition

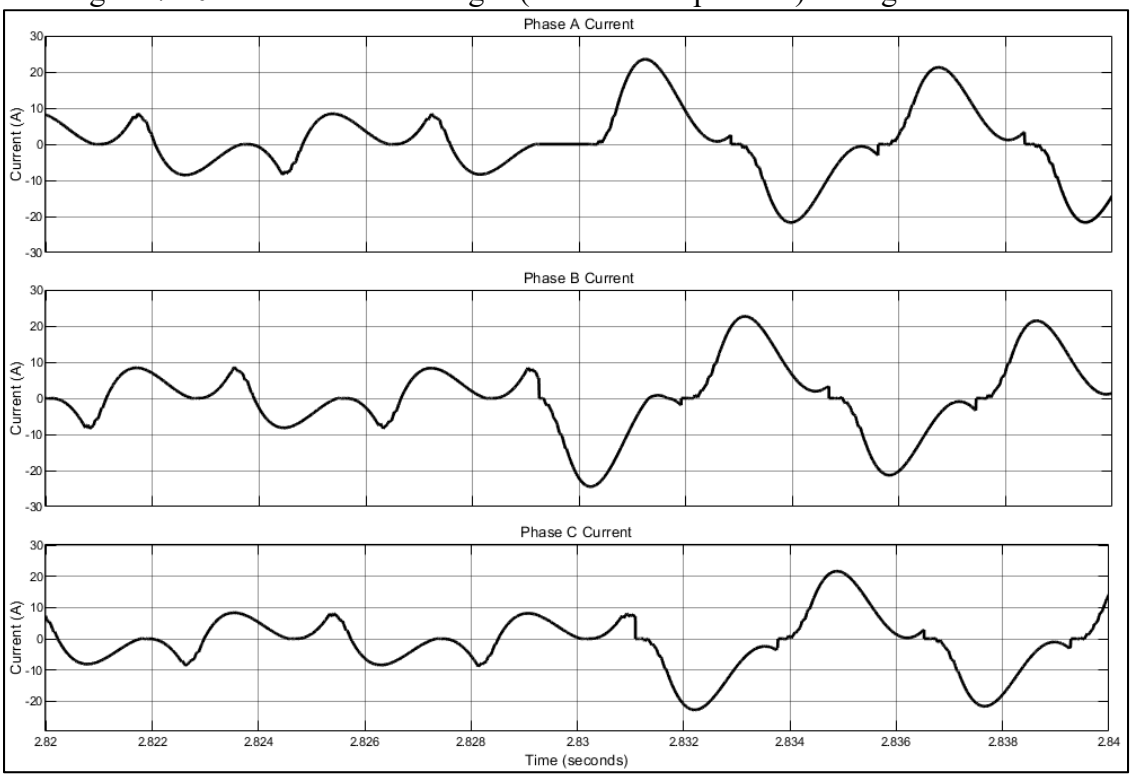

Figure 7.11 Phase Currents during 1st transition

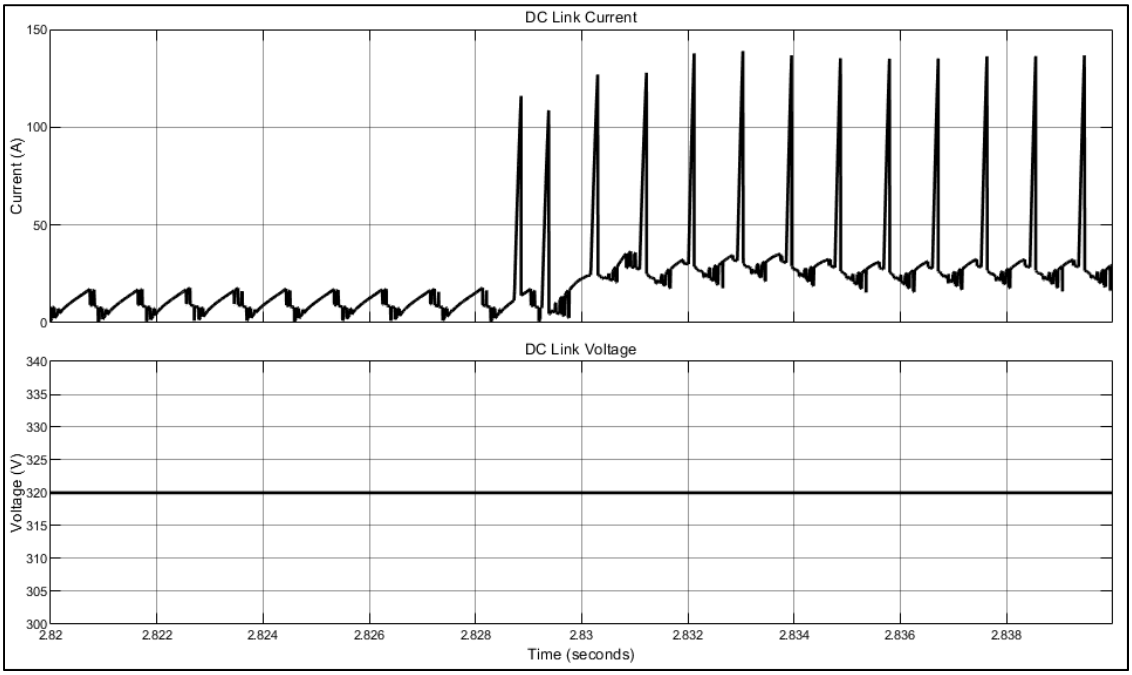

Figure 7.12 DC-Link Current and Voltage during 1st transition

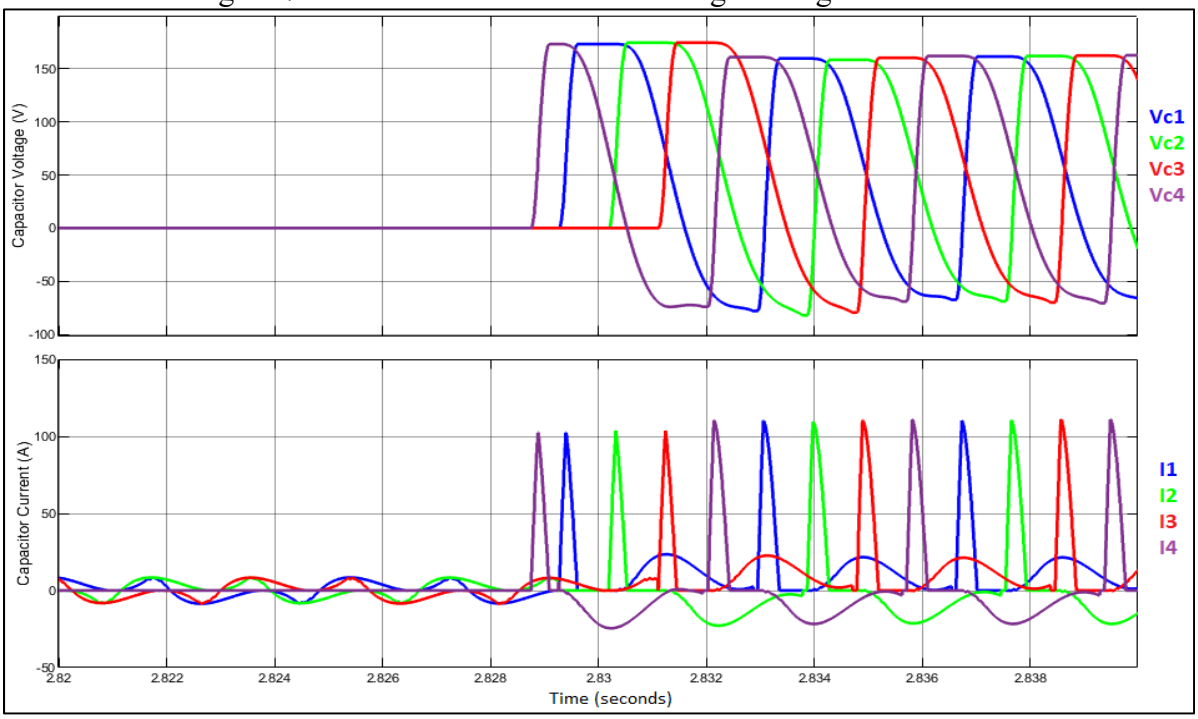

Figure 7.13 Configurable Capacitor Modules voltages and currents during 1st transition

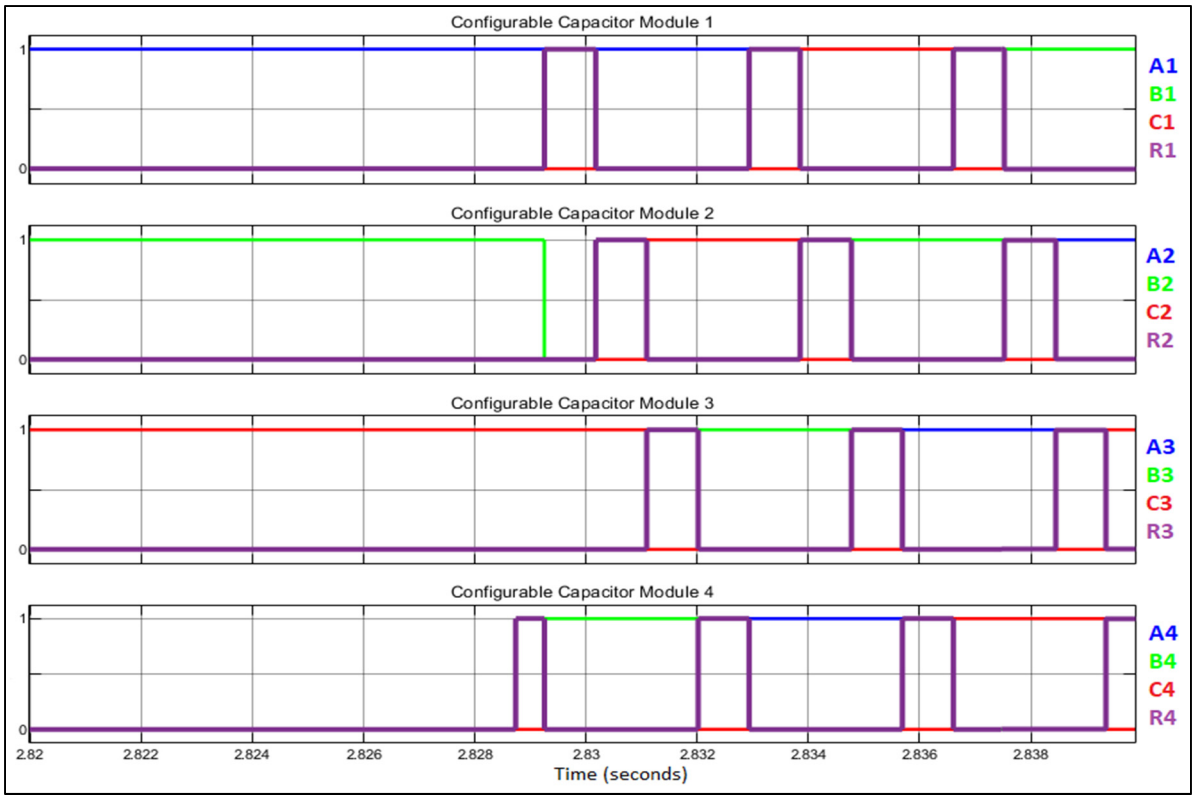

Figure 7.14 Configurable Capacitor Modules Switches A, B, C and R during 1st transition

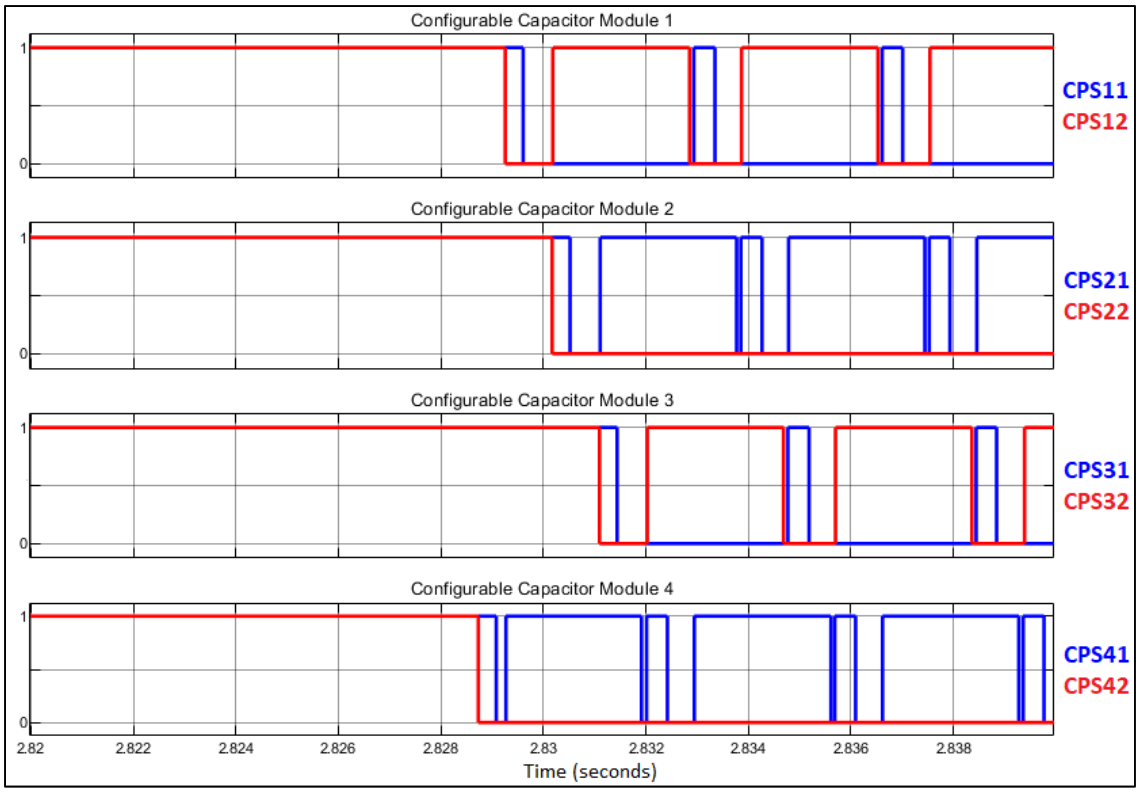

Figure 7.15 Configurable Capacitor Switches CPSX1 and CPSX2 during 1st transition

7.1.3 2nd transition - Capacitor Modules Capacitance Transition from 112 µF to 56 µF.

When the motor speed reaches 4536 rpm (plus the hysteresis band of +/- 12 rpm), the electrical frequency of the motor reaches the point where the gain of the RLC circuit with a 56 µF capacitor exceeds the gain of the RLC circuit with a 112 µF capacitor. This moment is the optimal moment to transition from the high capacitance configuration to the low capacitance configuration. The change of capacitance is done using the HX switches of the Configurable Capacitor Modules. As mentioned previously, in order to limit as much as possible the current rush between the 56 µF capacitor banks, the transition to and from high capacitance configuration is done with the Configurable Capacitor Modules at "Discharged" state.

The time window of the transition is between 4.94 and 4.96 seconds. Figure 7.16 shows the motor speed and motor torque during the 1st transition. Figure 7.17 shows the inverter output phase voltage commands. Figure 7.18 shows the motor phase voltages, which is the combined

voltage of the inverter and the capacitors. Figure 7.19 shows the phase currents. Figure 7.20 shows the DC-Link current and Voltage. Figure 7.21 shows the voltages and currents of all the Configurable Capacitor Modules. Figure 7.22 shows all Configurable Capacitor Modules phase selection switches (AX, BX, CX and RX) statuses. Finally, Figure 7.23 shows all Configurable Capacitor Modules polarity setting switches (CPSX1 and CPSX2) statuses.

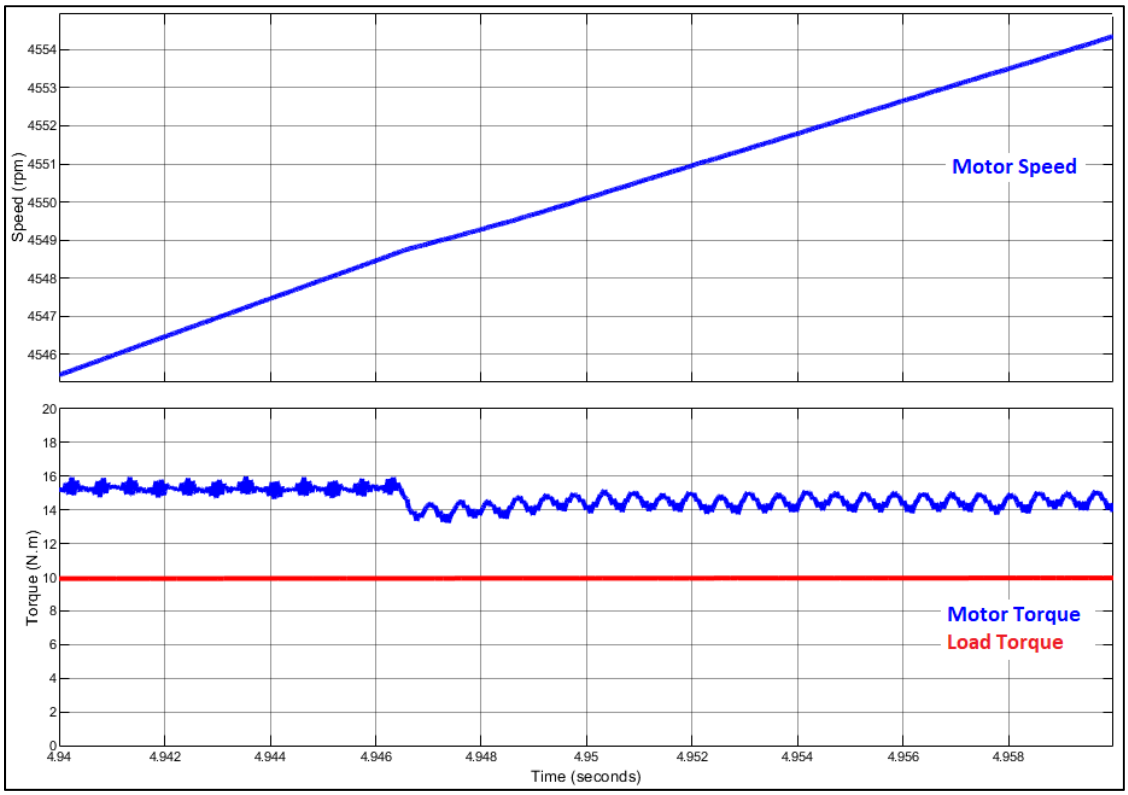

Figure 7.16 Motor Torque and Motor Speed during 2nd transition

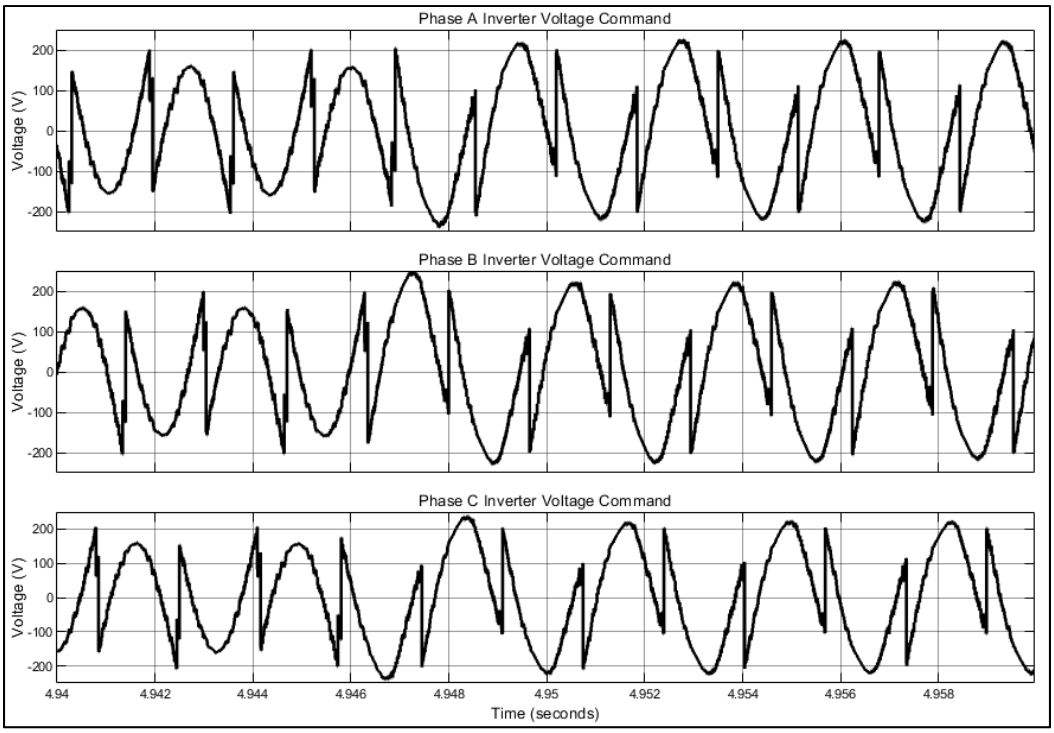

Figure 7.17 Inverter output voltage commands during 2nd transition

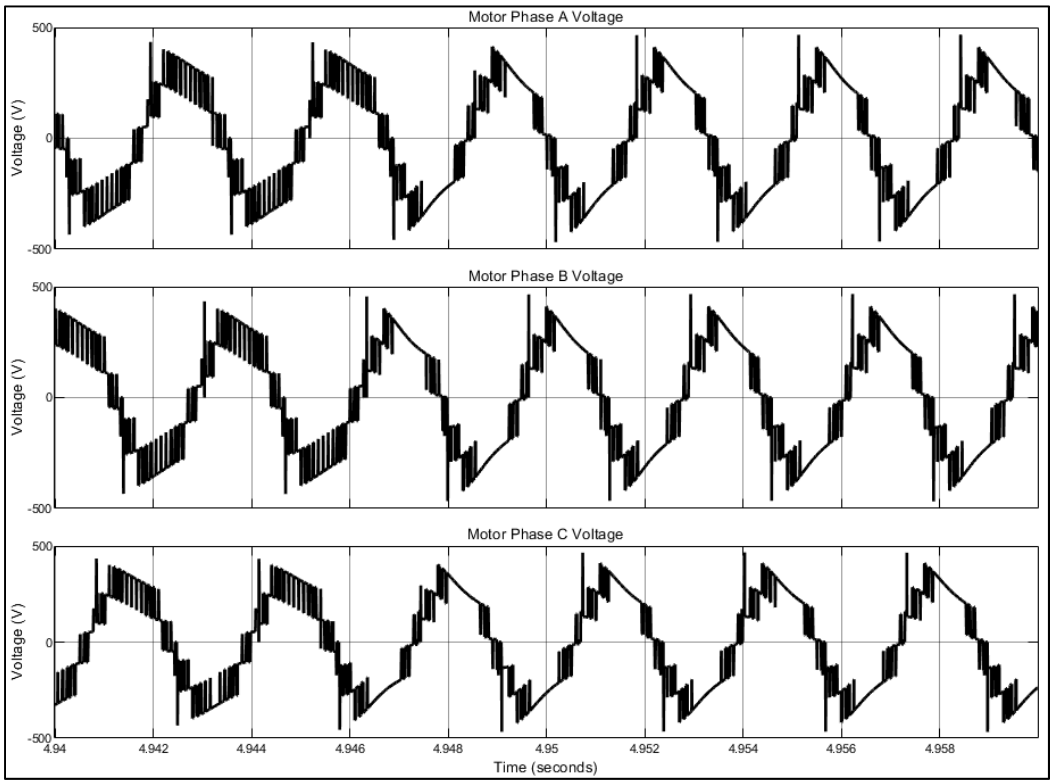

Figure 7.18 Motor Phase Voltages (Inverter + capacitors) during 2nd transition

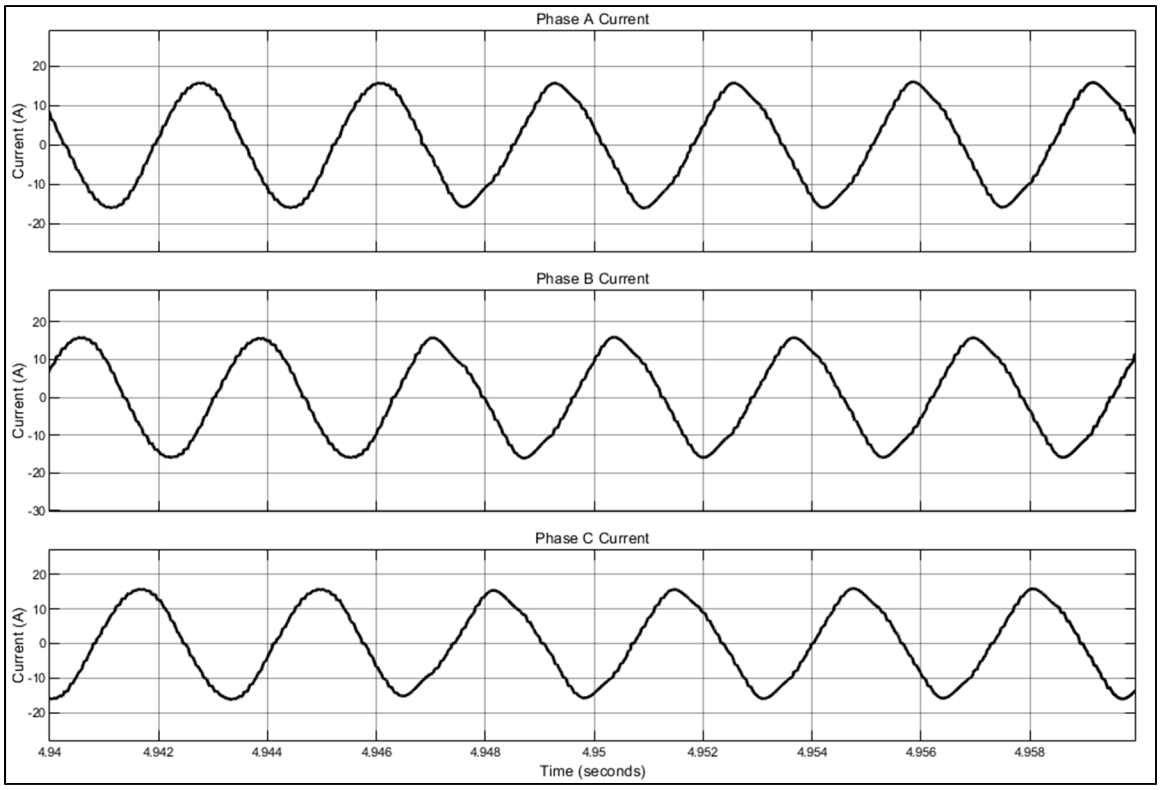

Figure 7.19 Phase Currents during 2nd transition

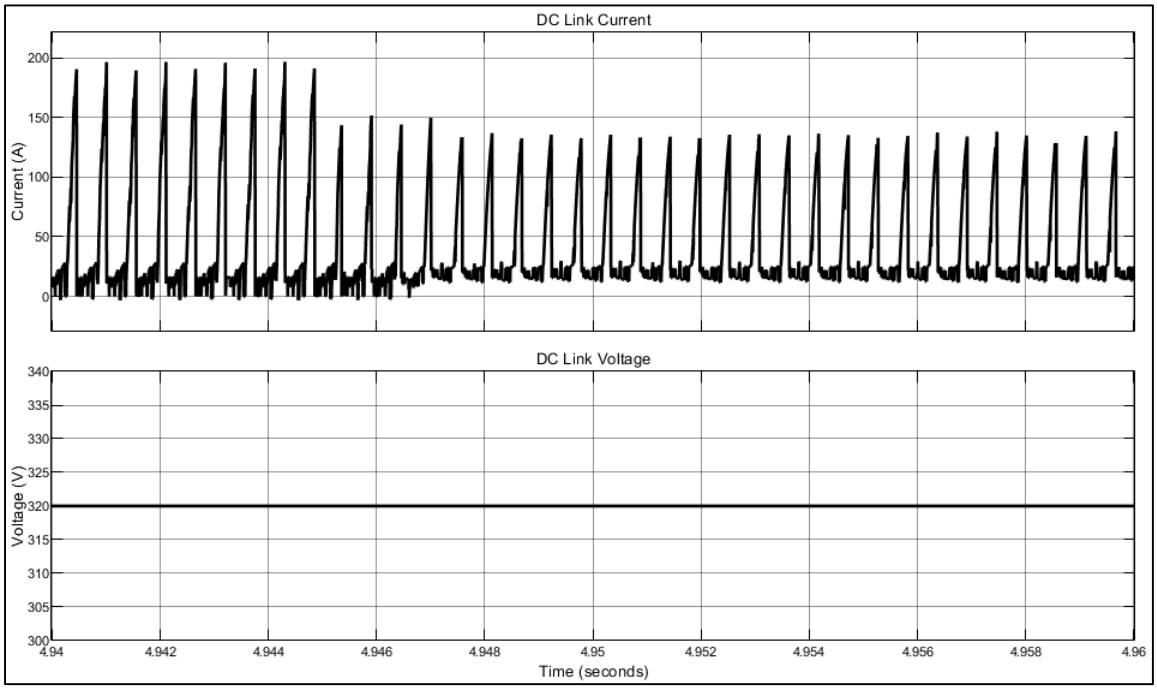

Figure 7.20 DC-Link Current and Voltage during 2nd transition

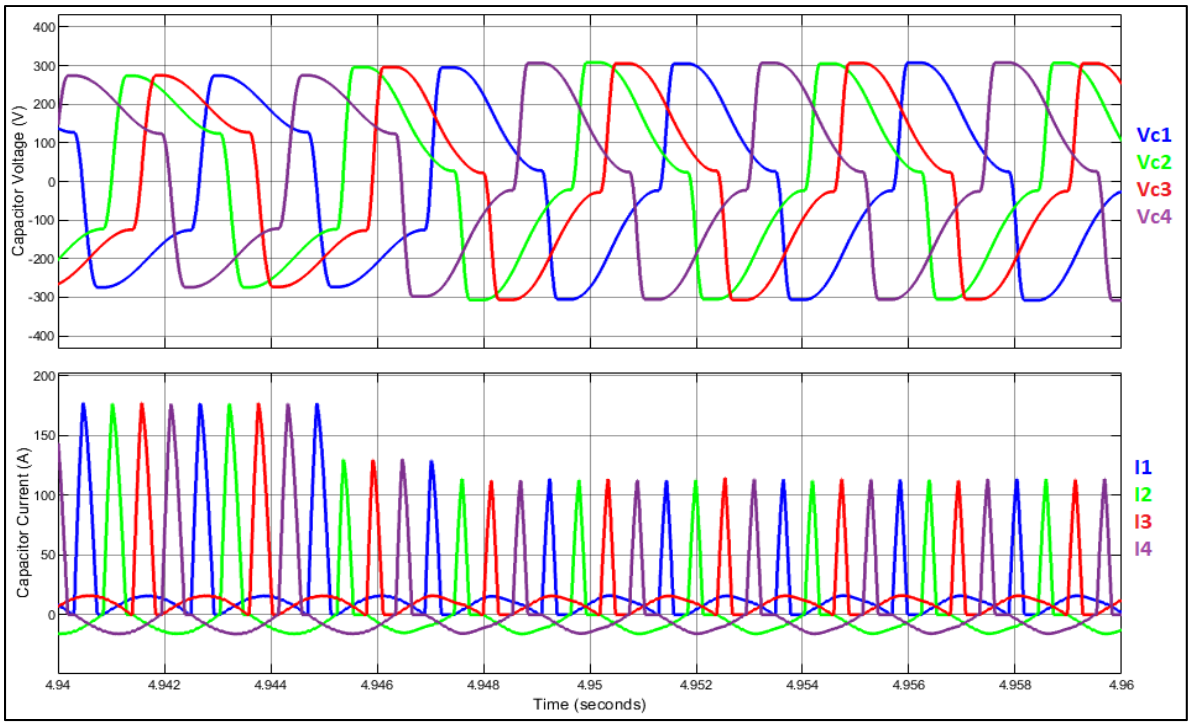

Figure 7.21 Configurable Capacitor Modules voltages and currents during 2nd transition

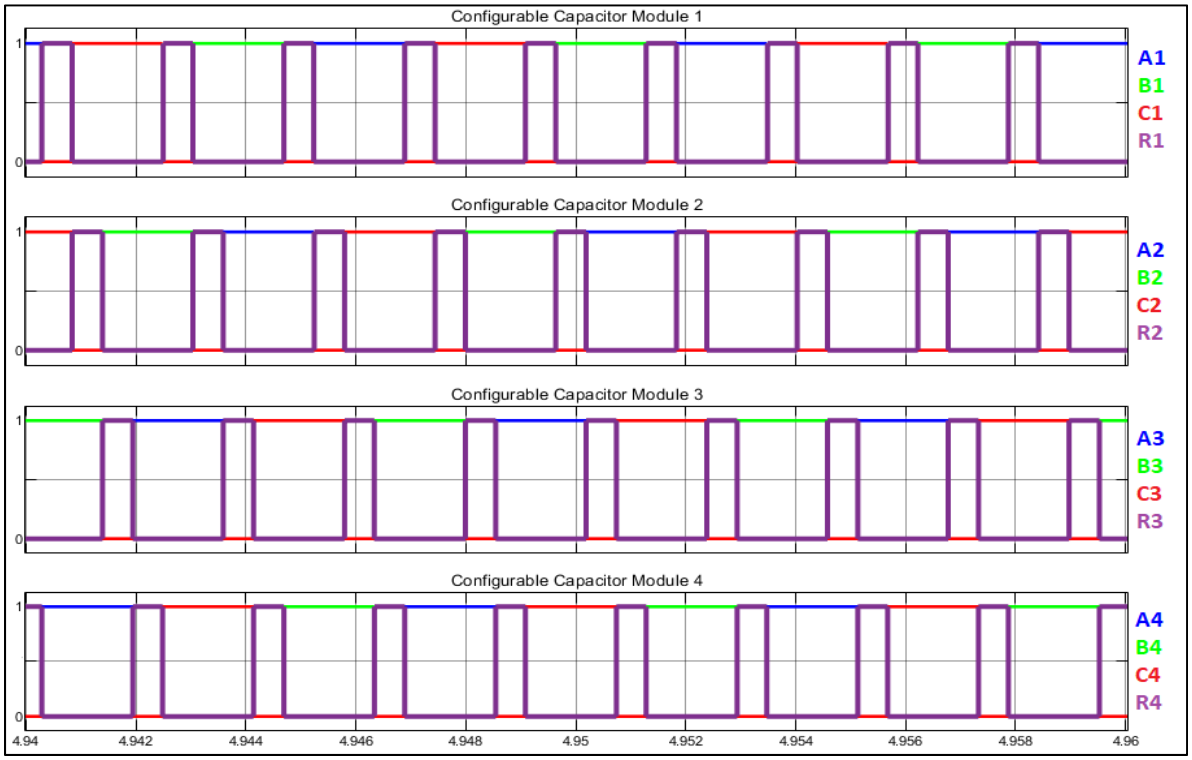

Figure 7.22 Configurable Capacitor Modules Switches A, B, C and R during 2nd transition

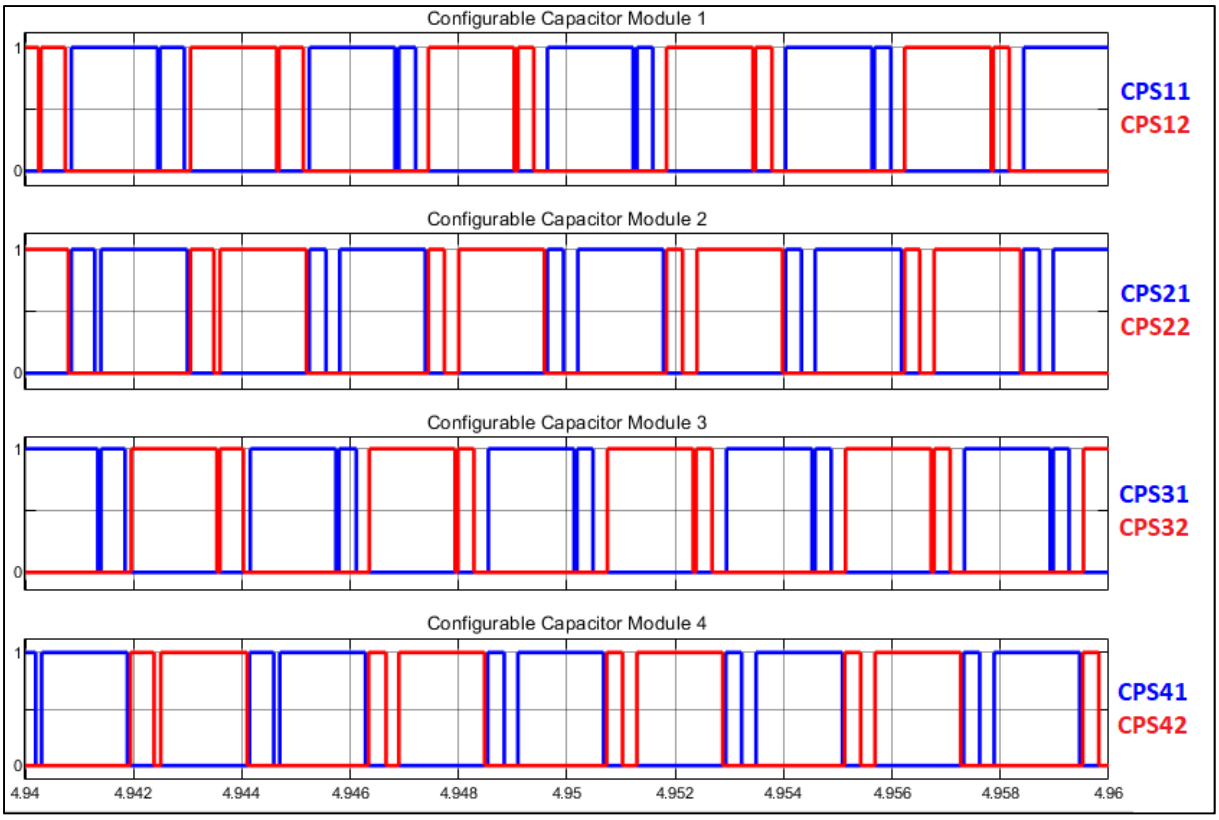

Figure 7.23 Configurable Capacitor Switches CPSX1 and CPSX2 during 2nd transition

7.1.4 3rd transition – Stabilization towards steady state operation

The 3rd transition is the transition between maximum torque operation during run-up and the stabilization at 5400 rpm and 14 N.m of torque. During this phase, the configuration of the Resonant Power Processor does not change and only the Field Oriented Control adjusts its control parameters to command the required torque to maintain a steady state operation at the target speed and torque. The 3rd transition occurs between 7.8 and 8.8 seconds of simulation time. Figure 7.24 shows the motor speed and torque during the stabilisation transition. Figure 7.25 shows the d and q axis voltage commands and the d and q axis currents during the 3rd transition.

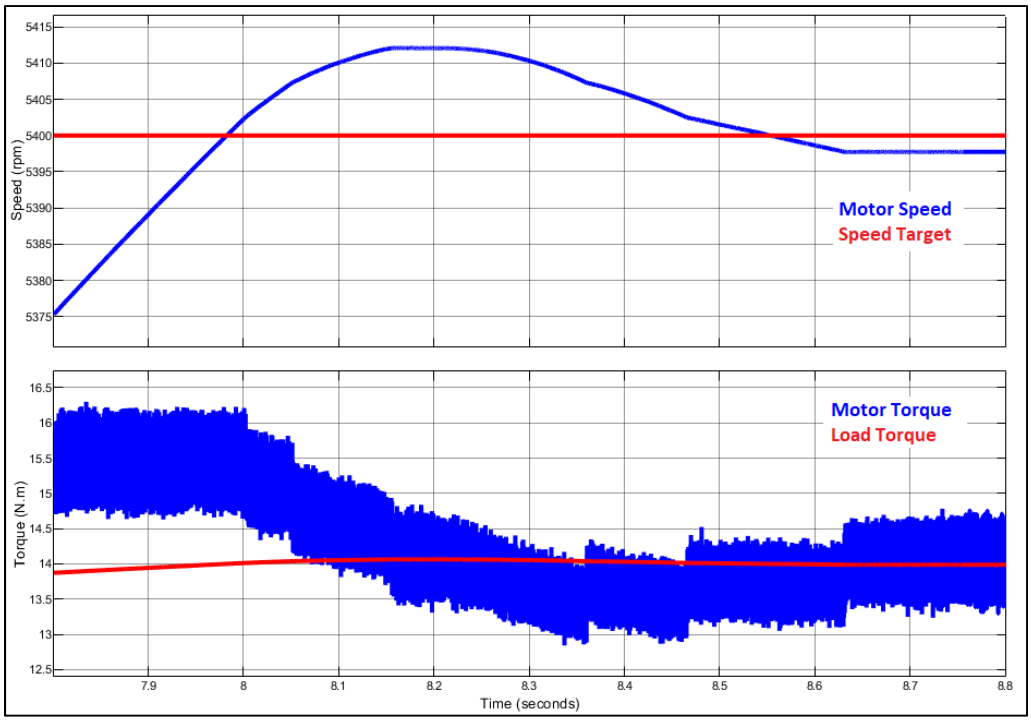

Figure 7.24 Motor Torque and Motor Speed during 3rd transition

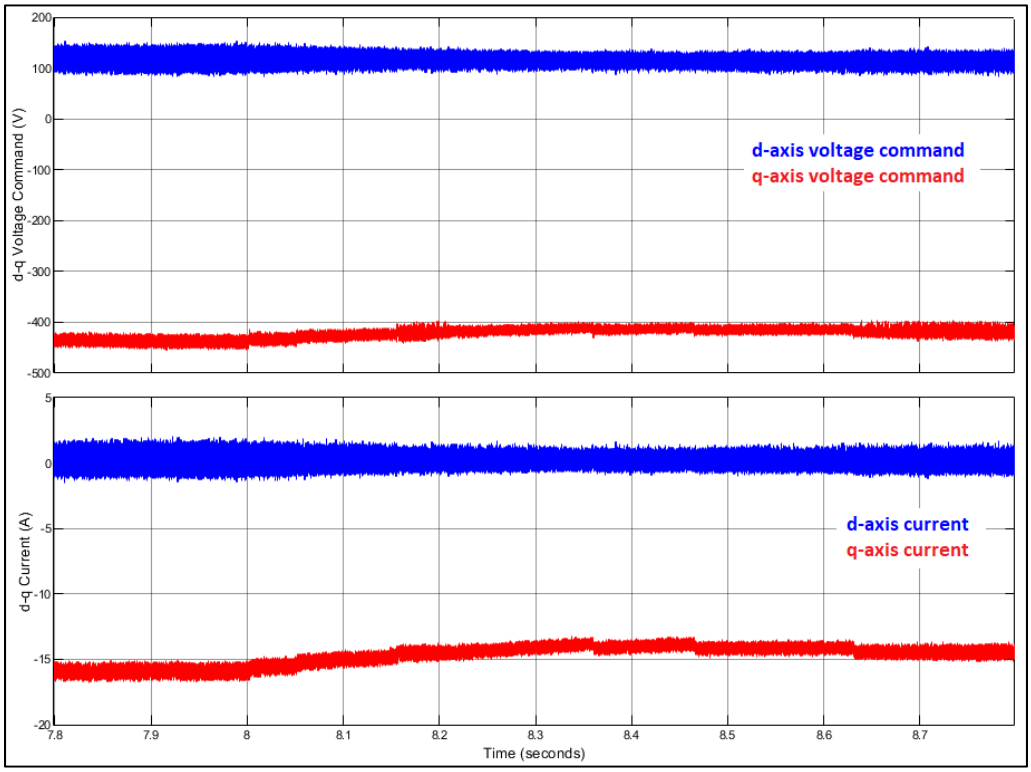

Figure 7.25 d-q Axis Voltage and Current during 3rd transition

7.1.5 Steady State Operation at 5400 rpm

The target operating point is at a speed of 5400 rpm and a motor output torque of 14 Nm. As mentioned earlier in section 1, aircraft engines typically operate at steady speed and torque for long periods of times, unlike an automotive vehicle which typically constantly changes speed and torque over the drive cycle. In this section, the performances of the proposed system will be analyzed at this specific point of operation.

The operation in steady state is defined by the time period between 9 and 10 seconds. The steady state operation results are divided in 3 distinct aspects. The first aspect of the steady state results shows the electrical behavior of the system. The second aspects describe the performances of the system in steady state in terms of efficiency, energy consumption and power density. The 3rd aspect covers the performances of the control algorithm.

7.1.5.1 Electrical behavior of the system in Steady State

For clarity of the figures, a 10 ms time window (between 9 seconds and 9.01 seconds) has been selected to show the behaviors of the system in detail. This section shows the electrical parameters (currents and voltages) in the different components in the system and details the operation of the Resonant Power Processor. Figures 7.26 to 7.28 show the inverter output phase voltage commands, the motor phase voltages, which is the combined voltage of the inverter and the capacitors, and the phase currents. Figure 7.29 shows the DC-Link current and Voltage. Figure 7.30 shows the voltages and currents of all the Configurable Capacitor Modules. Figure 7.31 shows all Configurable Capacitor Modules polarity setting switches (CPSX1 and CPSX2) statuses. Finally, Figure 7.32 shows the electrical and control parameters of the Configurable Capacitor Module 1 as an example.

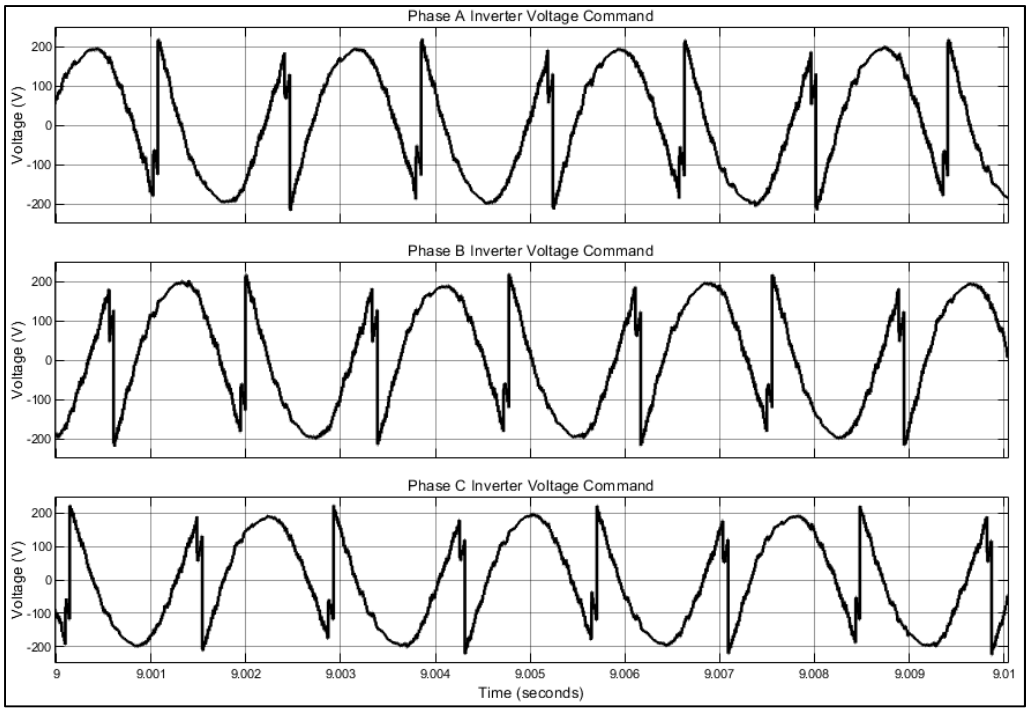

Figure 7.26 Inverter output voltage commands during Steady State

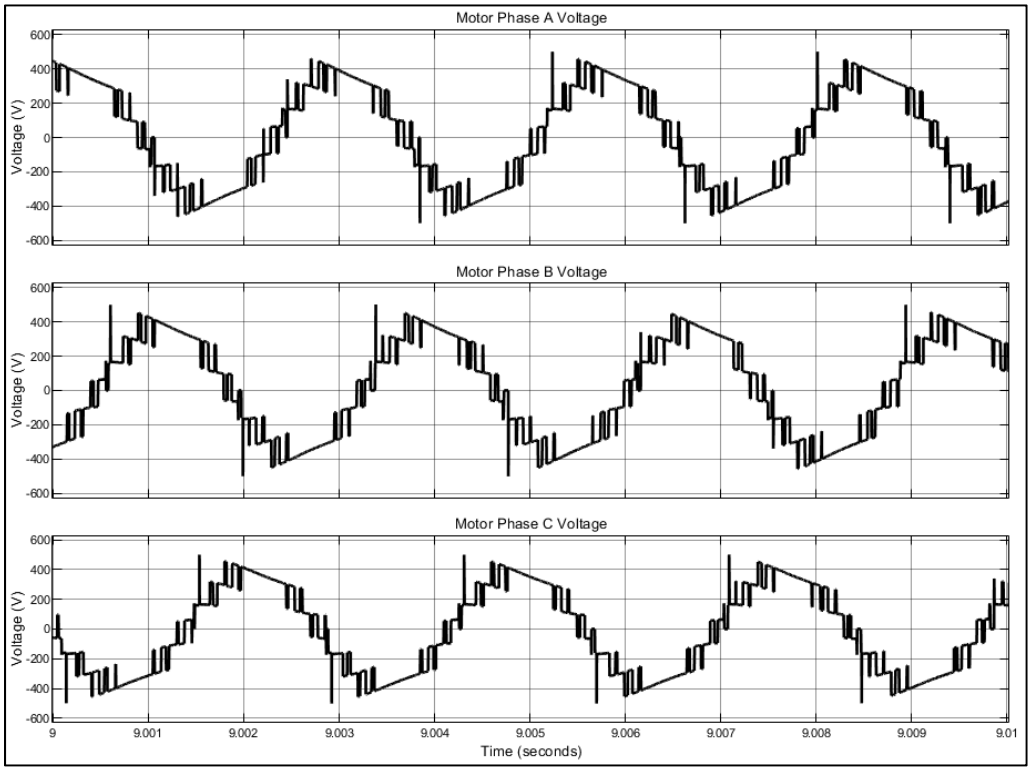

Figure 7.27 Motor Phase Voltages (Inverter + capacitors) during Steady State

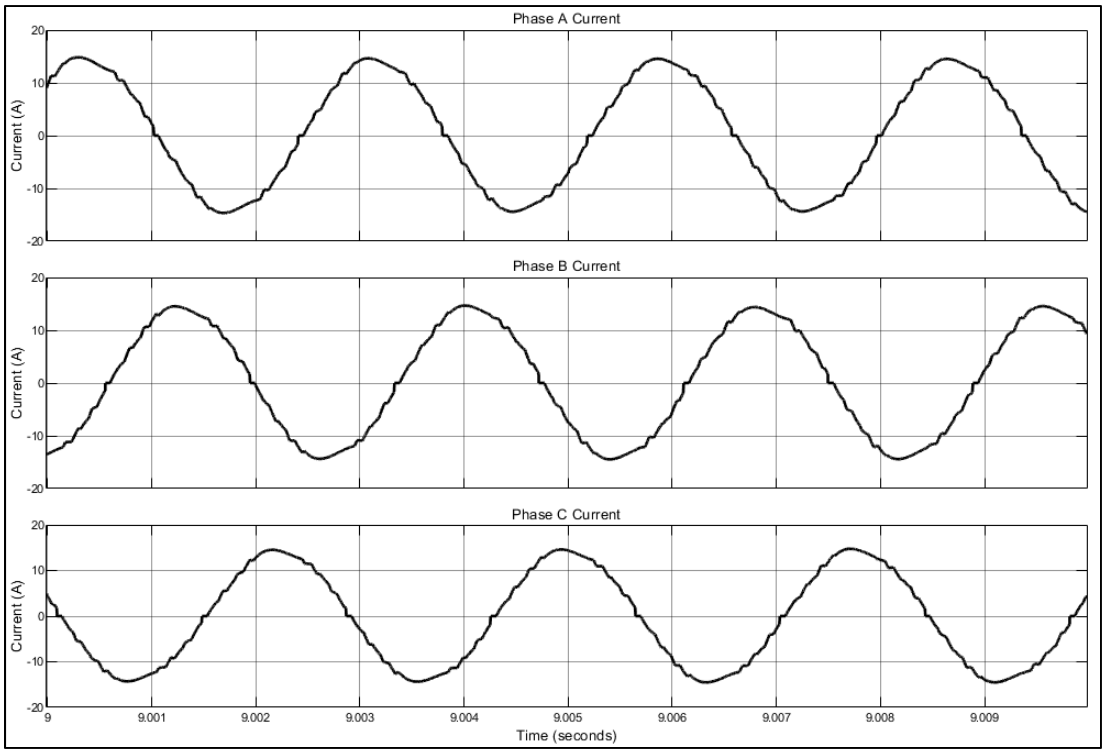

Figure 7.28 Phase Currents During Steady State

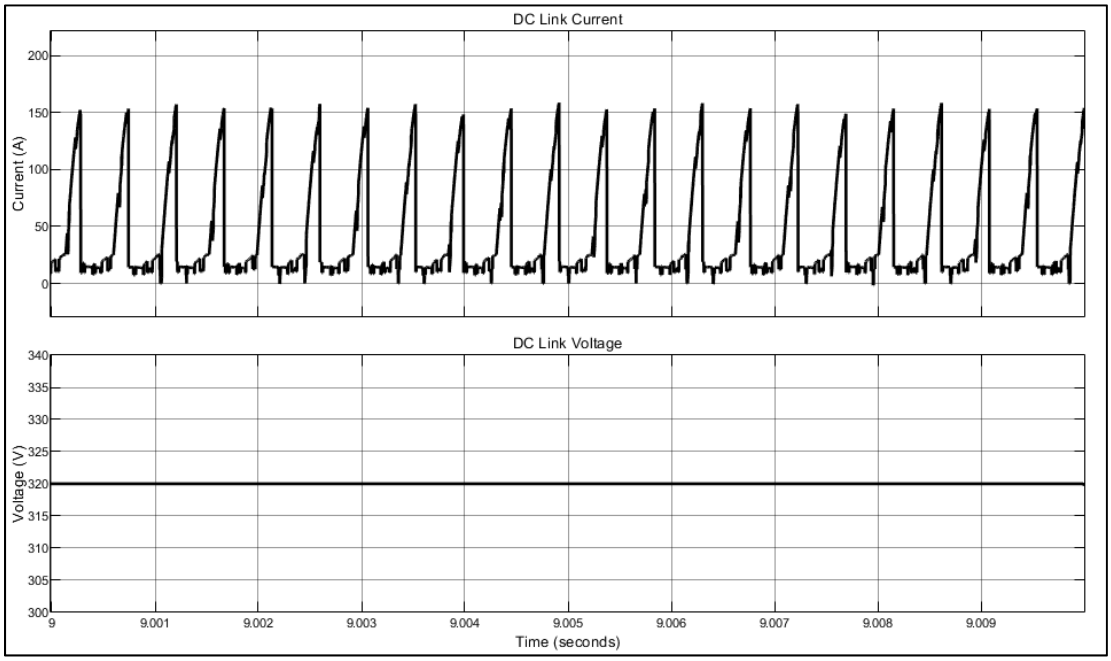

Figure 7.29 DC-Link Current and Voltage during Steady State

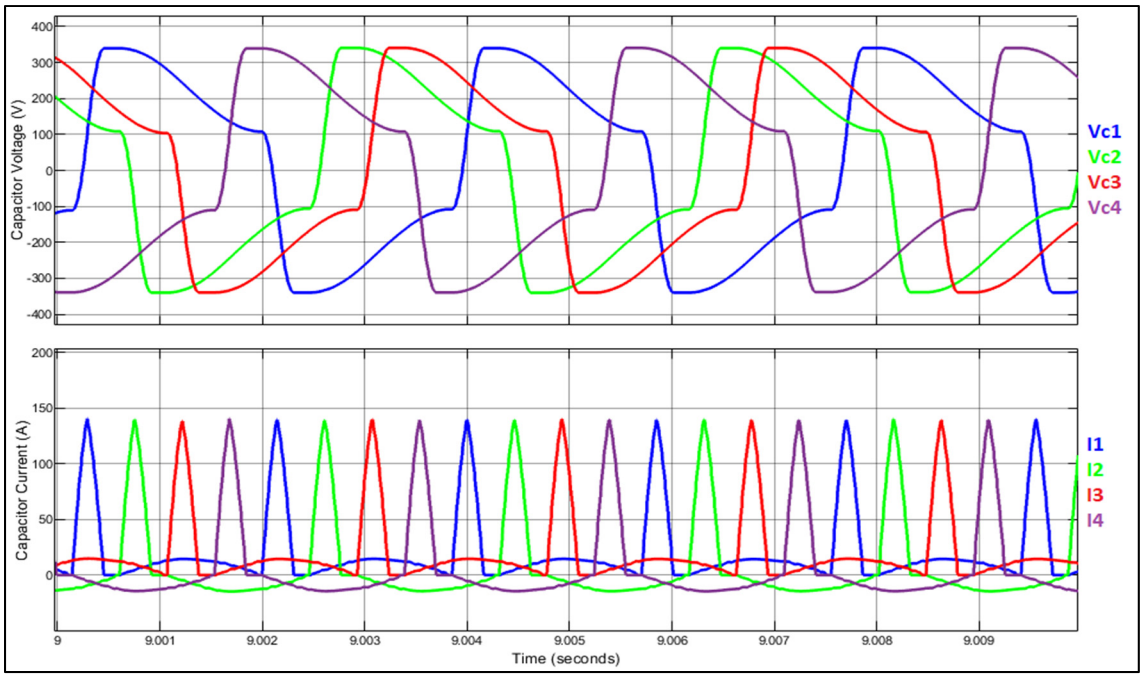

Figure 7.30 Configurable Capacitor Modules voltages and currents during Steady State

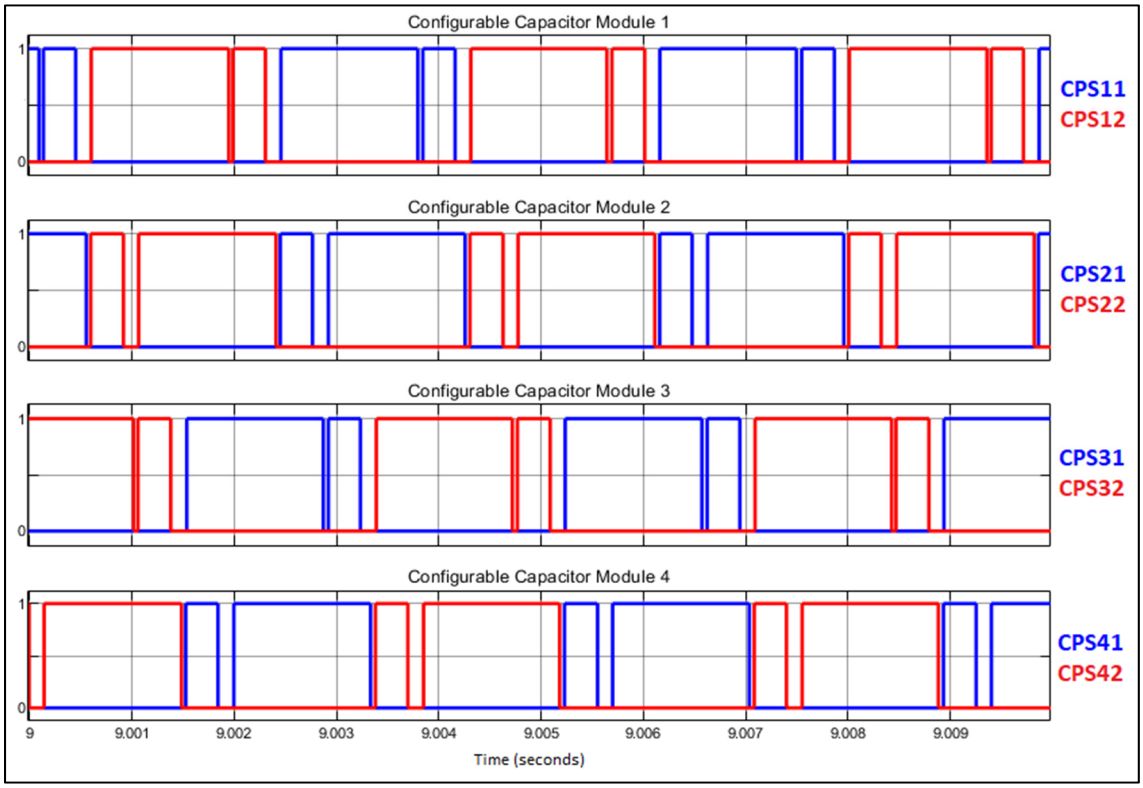

Figure 7.31 Configurable Capacitor Switches CPSX1 and CPSX2 during Steady State

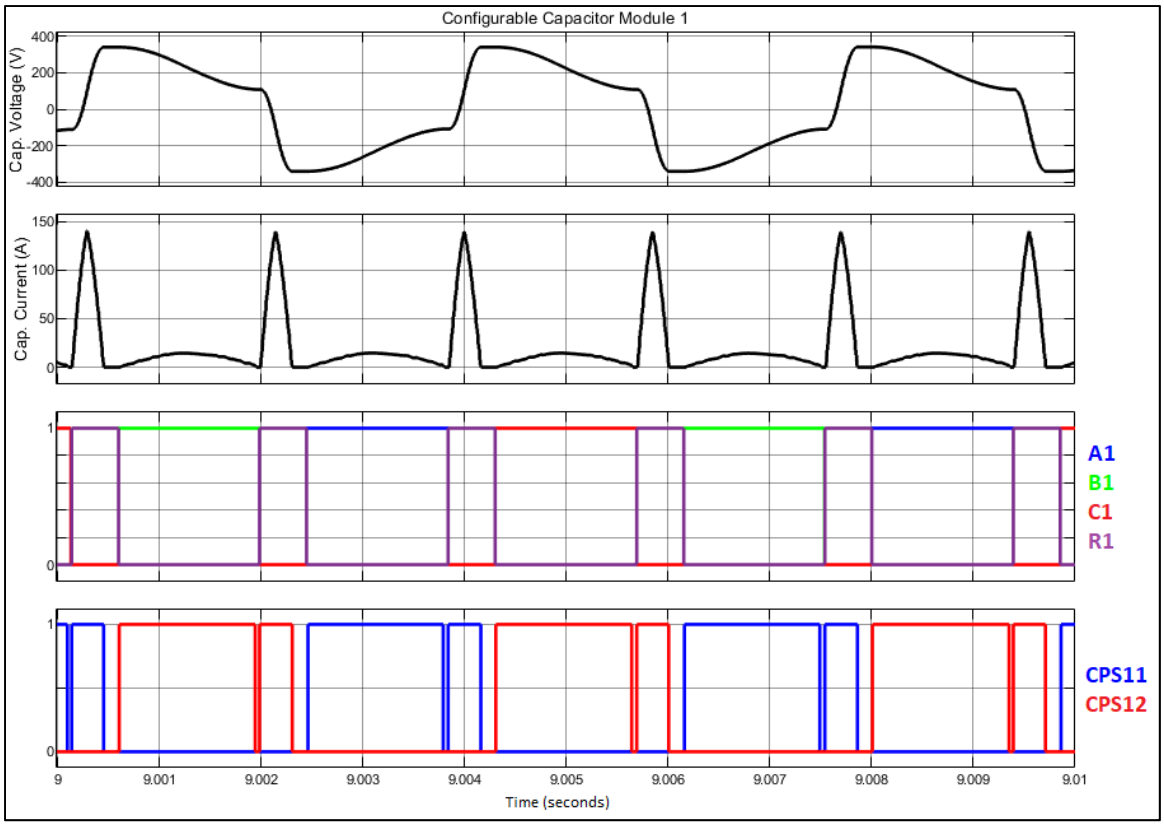

Figure 7.32 Configurable Capacitor Module 1 during Steady State

7.1.5.2 Performance of the system in Steady State

This section presents the performances of the system in steady state. First, the losses in the different components are detailed in the tables 7.1 to 7.5. The losses values and efficiency values in the Tables 7.1 to 7.5 are averaged over 1 second, between 9 and 10 seconds of simulation, where the system is considered in steady state.

Table 7.1 Power Summary of the system

Input DC Power	10602 W
Switching losses	25 W
Output Power (mechanical power)	7908 W
Total system efficiency	74.6 %

Table 7.2 Power summary of the inverter

Inverter input power (DC power)	2605 W
Inverter switching losses	1 W
Inverter conduction losses	336 W
Inverter output AC power	2268 W
Inverter efficiency	87.1%

Table 7.3 Power summary of the RPP (discharge cycles)

RPP input power (inverter output power)	2268 W
Capacitor Discharge power	6172 W
Capacitor discharge conduction losses	375 W
Net Capacitor Discharge power	5797 W
RPP output power (combined capacitors and inverter)	8065 W
RPP discharge cycles efficiency	95.6%

Table 7.4 Power summary of the RPP (recharge cycles)

RPP input recharge power (DC power)	7997 W
Capacitor recharge conduction losses	1578 W
Recharge circuit switching losses	24 W
Recharge circuit conduction losses	515 W
Net Capacitor Recharge Power	6172 W
RPP recharge cycles efficiency	77.2%

Table 7.5 Power summary of the PMSM

Motor input electrical power	8065 W
Motor conduction losses	157 W
Motor output mechanical power	7908 W
Motor efficiency	98.1%

7.1.5.3 Performances of the Control Algorithm

The primary objective of the control algorithm is to control the motor speed to match the speed target. The motor torque, and therefore the phase currents, are automatically adjusted by the control algorithm to maintain the motor speed at the speed target irrelevant of the load torque, unless a limitation prevents the motor speed to reach its target. The following section describe the performance of the control algorithm. Figures 7.33 and 7.34 show the motor speed and

torque in steady state. Tables 7.6 and 7.7 show the statistical data of the speed and torque of the PMSM output shaft, in addition to the control error and stabilization time of the speed control loop.

Table 7.6 Motor speed statistics in Steady State

Parameter	**Value**
Mean Speed	5397.76 rpm
Maximum Speed	5397.82 rpm
Minimum Speed	5397.73 rpm
Standard Deviation of Speed	0.019 rpm
Speed Target	5400.0 rpm
Speed Stabilization Time	0.65 second
Steady State Speed Control Error	2.24 rpm (0.04%)

Table 7.7 Motor torque statistics in Steady State

Parameter	**Value**
Mean Torque	13.99 N.m
Maximum Torque	14.91 N.m
Minimum Torque	13.20 N.m
Peak-to-peak fluctuations	1.71 N.m
Standard Deviation of Torque	0.25 N.m

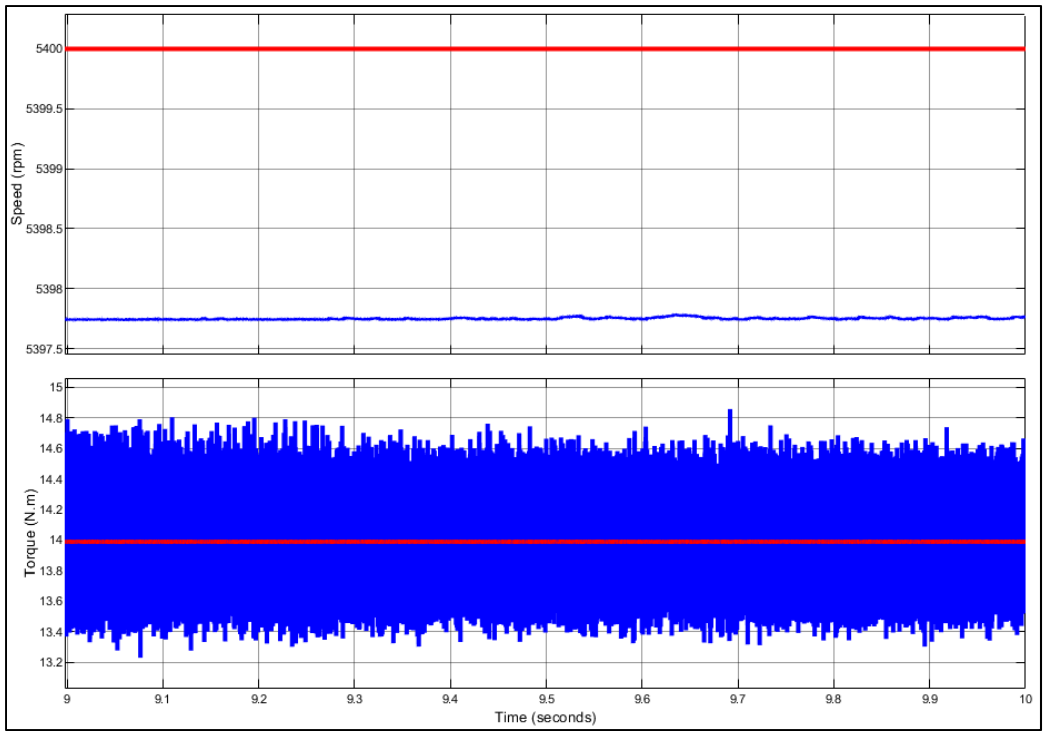

Figure 7.33 Motor Torque and Motor Speed during Steady State

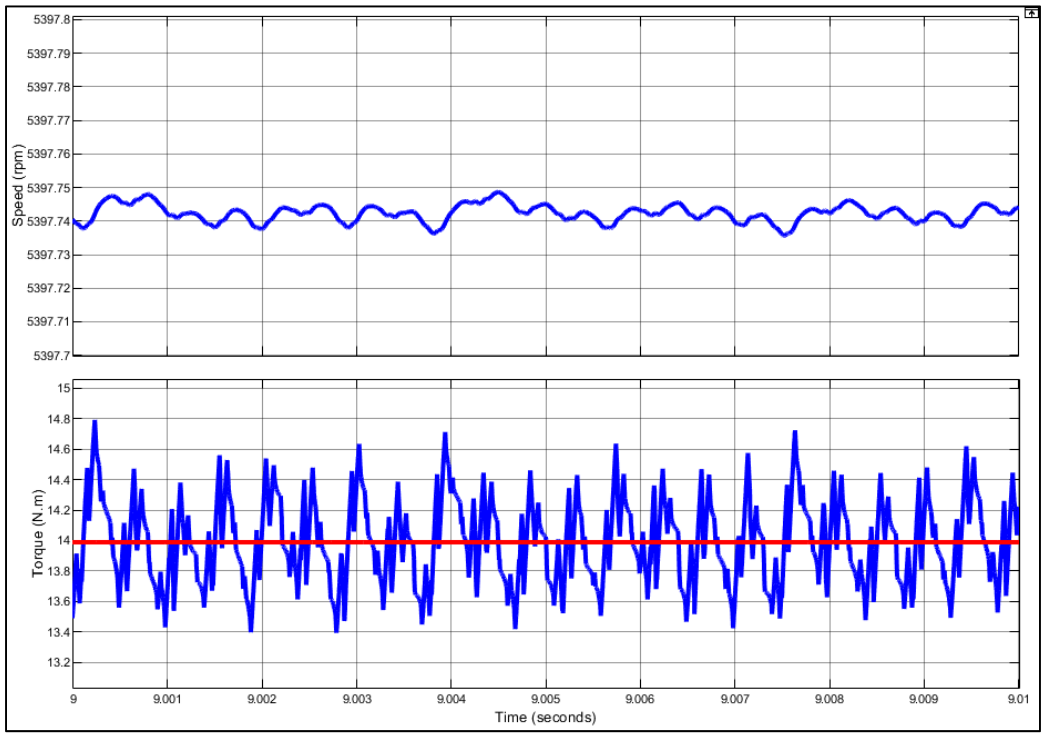

Figure 7.34 Motor Torque and Motor Speed during Steady State (10 ms close-up)

7.1.5.4 Phase current spectral analysis

In order to quantify the phase current harmonics, a FFT analysis has been done on the phase current of phase A during steady state operation. A sample of 10 cycles at a fundamental frequency of 360 Hz (electrical frequency at operating speed) has been used to compute the THD. The following section quantifies the phase current harmonics and THD.

Table 7.8 Total Harmonic Distortion (THD) of Phase Current A

Signal	**THD (%)**
Phase A current	3.69%

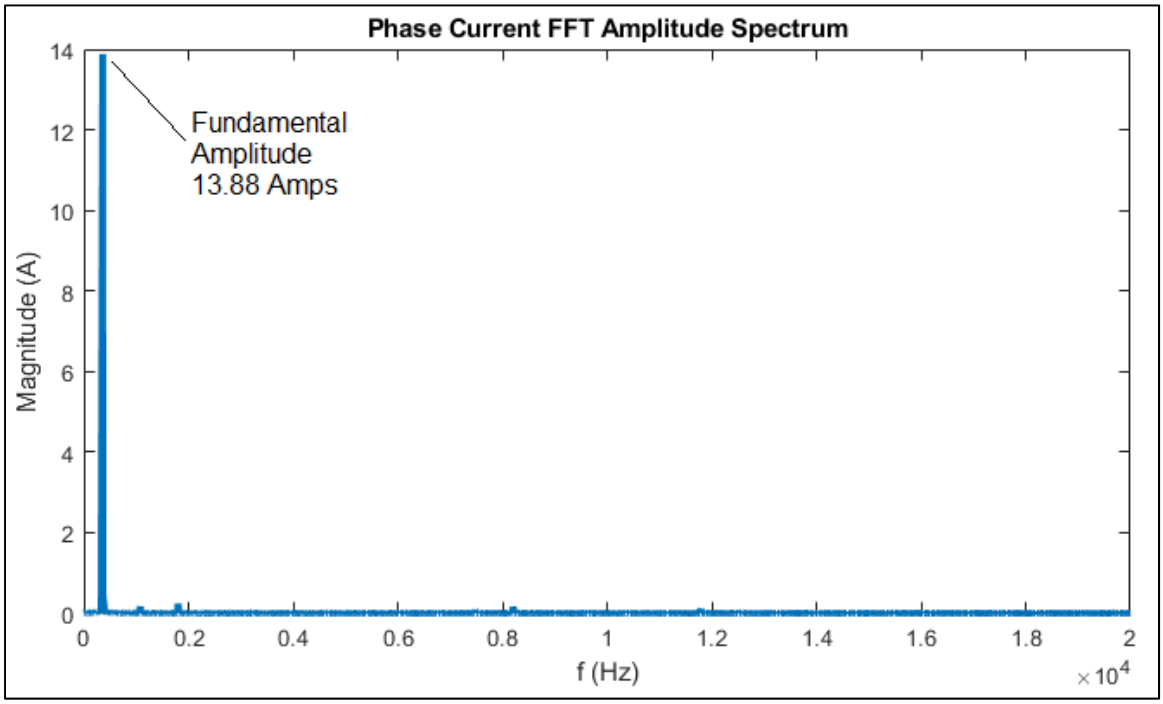

Figure 7.35 FFT amplitude spectrum analysis of phase A current

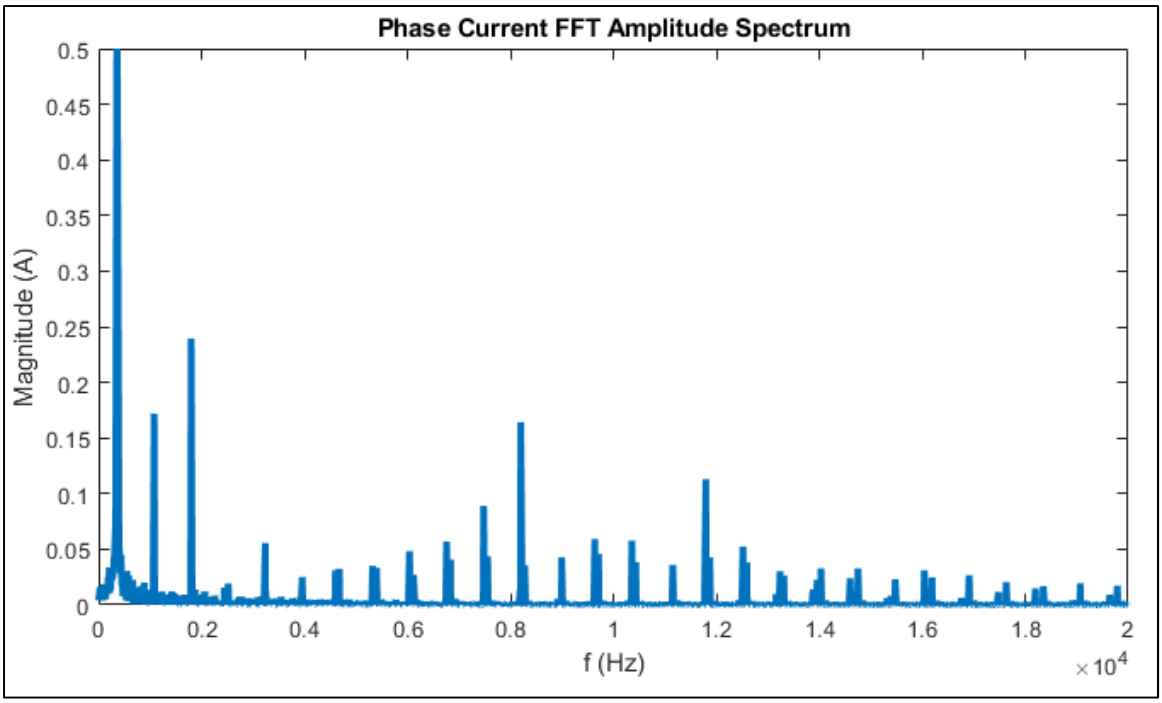

Figure 7.36 FFT amplitude spectrum analysis of phase A current
(Zoomed amplitude for harmonics)

7.2 System weight and power density

In this section, the weight of the PMSM, the inverter and the Resonant Power Processor are calculated from the Bill of Material (BOM) presented in ANNEX III.

Table 7.9 Resonant Power Processor System Power Density Data

Parameter	**Value**
Motor Weight	18.3 Kg
Inverter Weight	604 g
Resonant Power Processor Weight	52.5 Kg
Output Power	7908 W
Power Density	110.8 W/Kg

CHAPTER 8

RESULTS ANALYSIS

This section reviews and analyses the results presented previously in Section 7. The operation of the RPP is first analysed. The performances of the control system are also reviewed and explained. The system efficiency, losses and power density are then reviewed. Finally, the hypothesis of Section 3 are verified with regards to the results presented in the previous section.

For some aspects of the results analysis, a comparison has been made with a baseline system, made of a DC-DC boost converter that brings the DC link voltage from 320 Vdc to 750 Vdc (2.34:1 boost converter). Also, the inverter used for the comparison is a Three-Level Neutral Point Clamped, T-Type, as detailed in Section 1.3.4.2. This baseline system is deemed to be the best solution available with the prior art to supply the electrical power to the PMSM at a speed of 5400 N.m and an output torque of 14 N.m. This baseline system is used to make a fair comparison between the prior art capabilities and the RPP system capabilities. The baseline system Simulink model can be found in ANNEX VII.

8.1 Operation of the Resonant Power Processor (RPP)

8.1.1 Initiation of run-up and operation up to 2700 rpm

Upon run-up initiation (at t=0 second), the standard ZDAC control algorithm ensures the scheduling of the inverter's output voltage in order to maintain the maximum torque of the motor. Before the RPP is activated, the system behaves like a normal inverter fed PMSM drive, with the exception that the inverter is not a classic inverter but is in fact a modified Three-Level Neutral Point Clamped, T-Type inverter, as explained in Section 5.2. During operation with the RPP offline, the Configurable Capacitor Modules 1, 2 and 3 are configured as a pass-through between the inverter and the motor (the currents bypass the capacitors because all CPSX1 and CPSX2 switches are "ON"), and the Configurable Capacitor Modules 4 is completely isolated from the motor phases.

8.1.2 1st transition – Resonant Power Processor transition from Offline to Online

The speed threshold for RPP activation has been set to 2700 rpm with a hysteresis band of +/- 14 rpm. Once the speed threshold has been reached, the RPP control algorithm sets the "BOOST_ON" Boolean to true, sending the command to the 4 Configurable Capacitor Modules to initiate the recharge and discharge cycles. The 4th Configurable Capacitor Module is the first one to enter the recharge cycle as the Configurable Capacitor Module 4 is initially completely isolated from the motor phases. Upon activation, the RPP recharges the 4th Configurable Capacitor Module and waits for the signal to discharge the capacitor in a motor phase. As seen in Section 5.4, the timing of the capacitor discharge cycle is based on the rotor position (zero Back-EMF crossing). When the phase B zero Back-EMF crossing signal occurs, the RPP control disconnects the Configurable Capacitor Module 1 from the phase B then connects the Configurable Capacitor Module 4 to the phase B. The Configurable Capacitor Module 1 then immediately recharges and then waits for the phase A to be ready to accept a recharged capacitor.

The recharged capacitors voltages are added to the inverter output voltage in alternance, ensuring enough phase voltage to counter the increasing Back-EMF. Upon activation of the RPP, the "High Capacitance" configuration (C=112 µF) is selected to match as much as possible the natural frequency of the motor phases' RLC circuits at low speed.

8.1.3 2nd Transition – High Capacitance to Low Capacitance Transition

Once the speed of 4500 rpm is reached, the RPP transitions from the "High Capacitance" configuration (C=112 µF) to the "Low Capacitance" configuration (C=56 µF). During this process, the motor torque is slightly disturbed for a short period of time before it stabilizes again at the maximum torque until the desired speed is reached.

As shown in Section 5.4, the transition from the "High Capacitance" configuration to the "Low Capacitance" configuration is done when the Configurable Capacitor Module control state is at "Discharged". This is for two reasons; first, the transition is done a zero current to limit the losses in the "HX" switches. Second, the transition is done at the minimum capacitor energy

level, again to limit the stress in the “HX” switches. The capacitance reduction from 112 to 56 µF does not generate a significant stress on the “HX” switches because at the moment of the transition, the voltages in both capacitors are equal. However, in the scenario where the motor was decelerating, the transition would have occurred from 56 µF to 112 µF, which would have required to close the “HX” switch with possibly a high voltage difference between the two capacitors.

During this 2nd transition, there is no change in other system status or control state. The FOC continuously operates in ZDAC control mode, and RPP control operates with the same algorithm.

8.1.4 3rd Transition – Stabilization towards Steady State

When the desired speed of 5400 rpm is reached, the closed loop speed control sets the torque request which is required to maintain the speed to the speed target. Steady state operation at 5400 rpm and 14 N.m shows that the control system successfully controls the motor.

During the 3rd transition, only the FOC adjusts the inverter output voltage to adjust the phase current, and therefore the motor torque. The capacitor voltage request is set in open loop as a function of motor speed.

8.1.5 Steady state operation

In steady state, the RPP manages to maintain the motor torque at 14 N.m with a speed of 5400 rpm. At this torque and speed, the output power is 7.9 kW.

8.2 Torque Ripples in Steady State

The torque ripple in steady state is a good indicator of the output power quality of the system. Large torque ripples may increase the speed oscillations and may induce increased vibratory

stresses in the propeller or to the load attached to the output shaft. For those reasons, the torque ripples need to be reduced as mush as possible.

To make a comparison between the prior art solution and the Resonant Power Processor system, the model defined in ANNEX VII has been used as a baseline. The torque ripples comparison shows that the output torque quality of the Resonant Power Processor is superior to the 3 Level inverter with a DC-DC Boost converter.

Table 8.1 Output torque quality comparison between RPP system and baseline system.

Parameter	**RPP 320V**	**3L Inv. 750V**
Mean Torque	13.99 N.m	14.00 N.m
Maximum Torque	14.91 N.m	15.32 N.m
Minimum Torque	13.20 N.m	12.48 N.m
Peak-to-peak torque fluctuations	1.71 N.m	2.84 N.m
Standard Deviation of Torque	0.25 N.m	0.60 N.m

8.3 Current Harmonics in Steady State

The phase current harmonics are also a good indicator of the output power quality of the system. High amplitude phase current harmonics, especially at high frequency, induce iron losses in the motor's rotor and stator, which in turns increase the motor temperature. For this reason, the phase current harmonics need to be reduced as mush as possible.

To make a comparison between the prior art solution and the Resonant Power Processor system, the model defined in ANNEX VII has been used as a baseline. Table 8.2 shows the comparison of THD between the RPP and the baseline system. Figures 8.1 to 8.3 show FFT analysis frequency spectrum used to make the current harmonics comparison.

Table 8.2 Phase current THD comparison between RPP system and baseline system

Signal	**THD (%)**
Phase A current (RPP system at 320 Vdc)	3.69%
Phase A current (3-Level Inverter at 750 Vdc)	4.87%

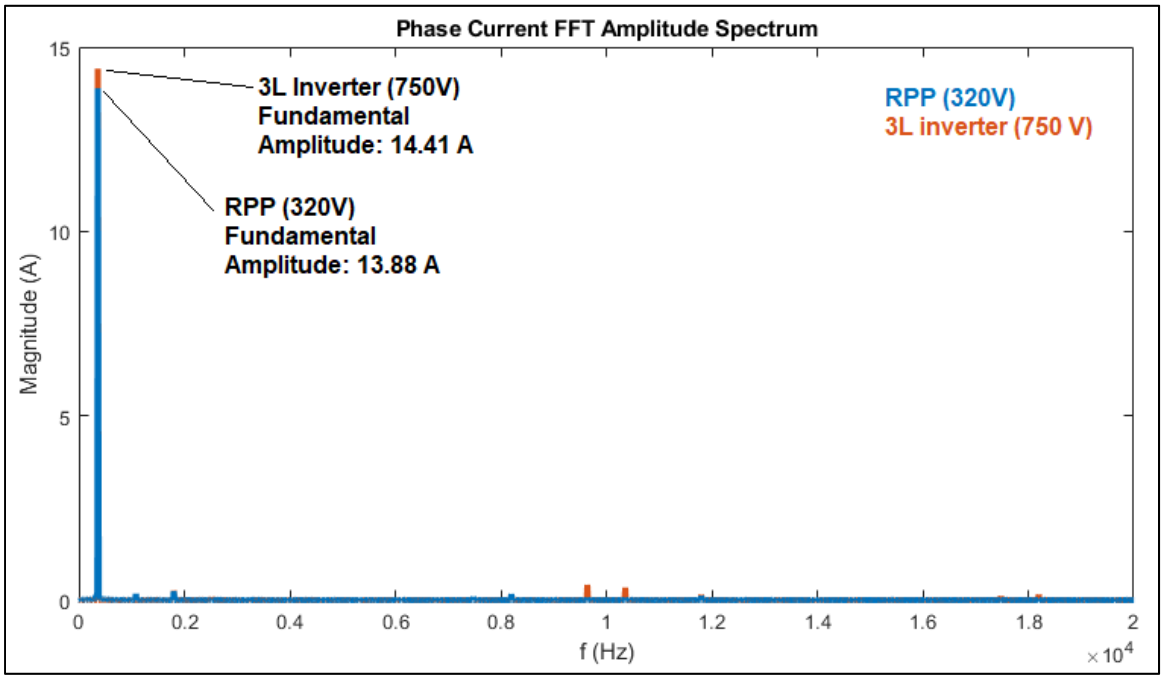

Figure 8.1 FFT amplitude spectrum analysis of phase A current (RPP vs baseline)

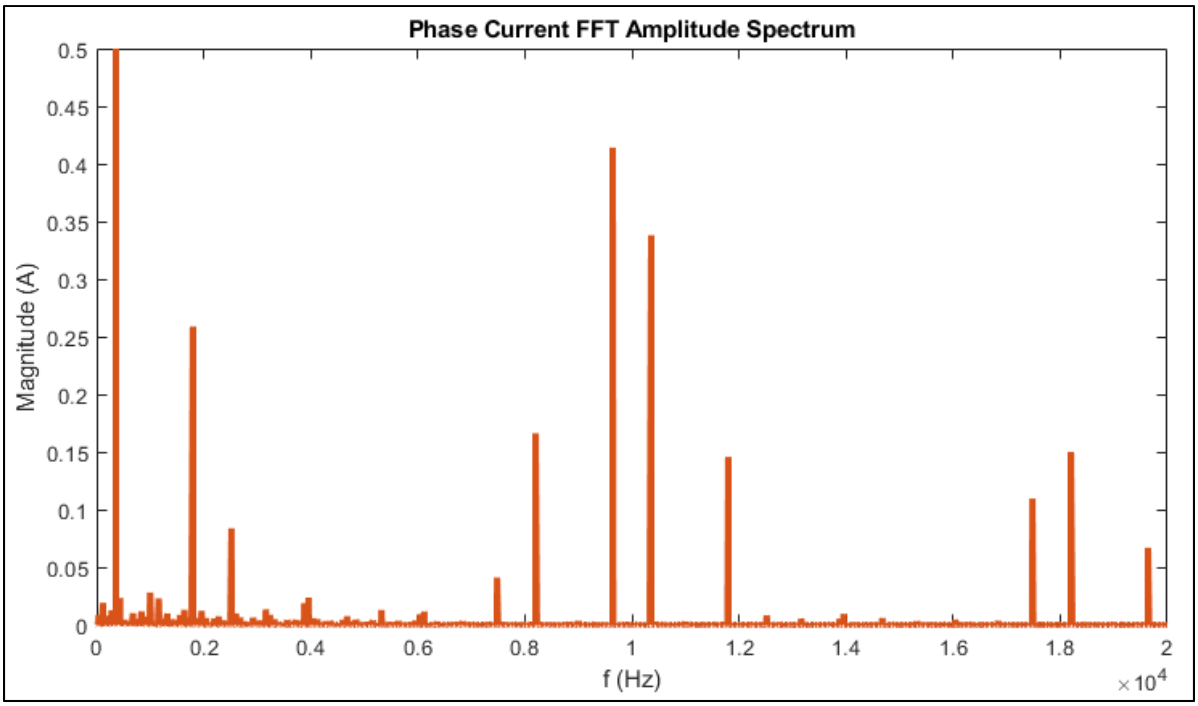

Figure 8.2 FFT amplitude spectrum analysis of phase A current (Baseline system)

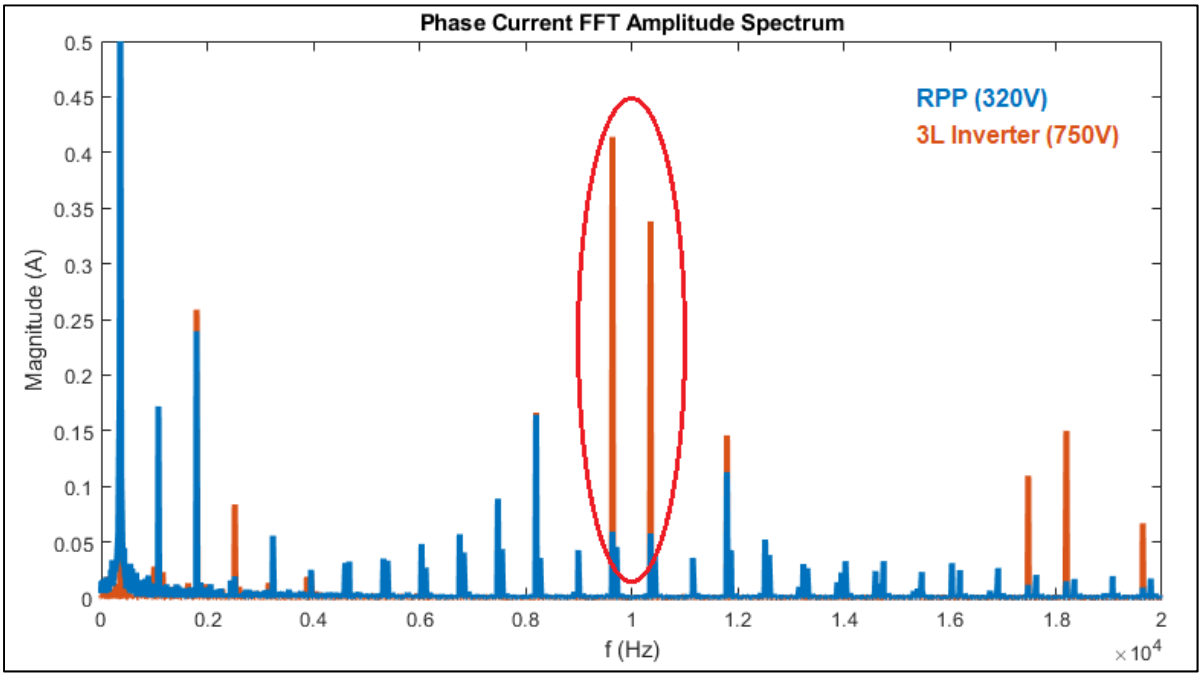

Figure 8.3 FFT amplitude spectrum analysis of phase A current
(RPP vs baseline, zoomed amplitude for harmonics)

The frequency spectrum analysis of the phase current shows that the current harmonics induced by the 10 kHz PWM switching of the inverter are of greater magnitude on the baseline system when compared to the RPP (Circled in red on Figure 8.3). However, the RPP shows many small amplitude parasitic harmonics which cannot be observed on the Baseline system. To better understand the root cause of the parasitic harmonics on the FFT, a time-domain analysis and comparison of the phase currents is shown on Figure 8.4. It can be observed that the baseline system current sinewave almost perfectly matches the reference sine wave, and the PWM induced current oscillations are clearly distinguishable.

With the RPP, two discontinuities occur. First, during the transition between capacitors, the phase current is momentarily interrupted to allow the change of configuration of the RPP. This current interruption time is 50 µs. Because the FPGA processing frequency is 1 MHz and because the input signals are processed by the control system at 200 kHz, this delay period could be reduced to 15 µs or less without risking an overrun of the phase selection algorithm. This would reduce the current harmonics generated by the current step near zero current. See Figure 8.4 where the phase current interruption near zero current is circled in red.

Second, the phase current of the RPP near peak current slightly undershoots the reference sine wave (Circled in red on Figure 8.4). It can be observed in the Figure 7.27 that at peak voltage, the inverter is saturated and cannot provide the required voltage to maintain a perfect sinusoidal current profile. This can be improved by charging the capacitors to a higher voltage. Charging the capacitors to a higher voltage would reduce the required inverter output voltage to generate the perfectly sinusoidal current profile. It is to be noted that the recharge cycle is used at only ~70%, with ~30% of dead time. This allows to charge the capacitors to a higher voltage without risking of overrunning the recharge process.

The phase current harmonics comparison shows that the THD is better with the RPP compared to the baseline system. It can be observed on Figure 8.4 that the phase current profile is smoother with the RPP compared to the baseline system.

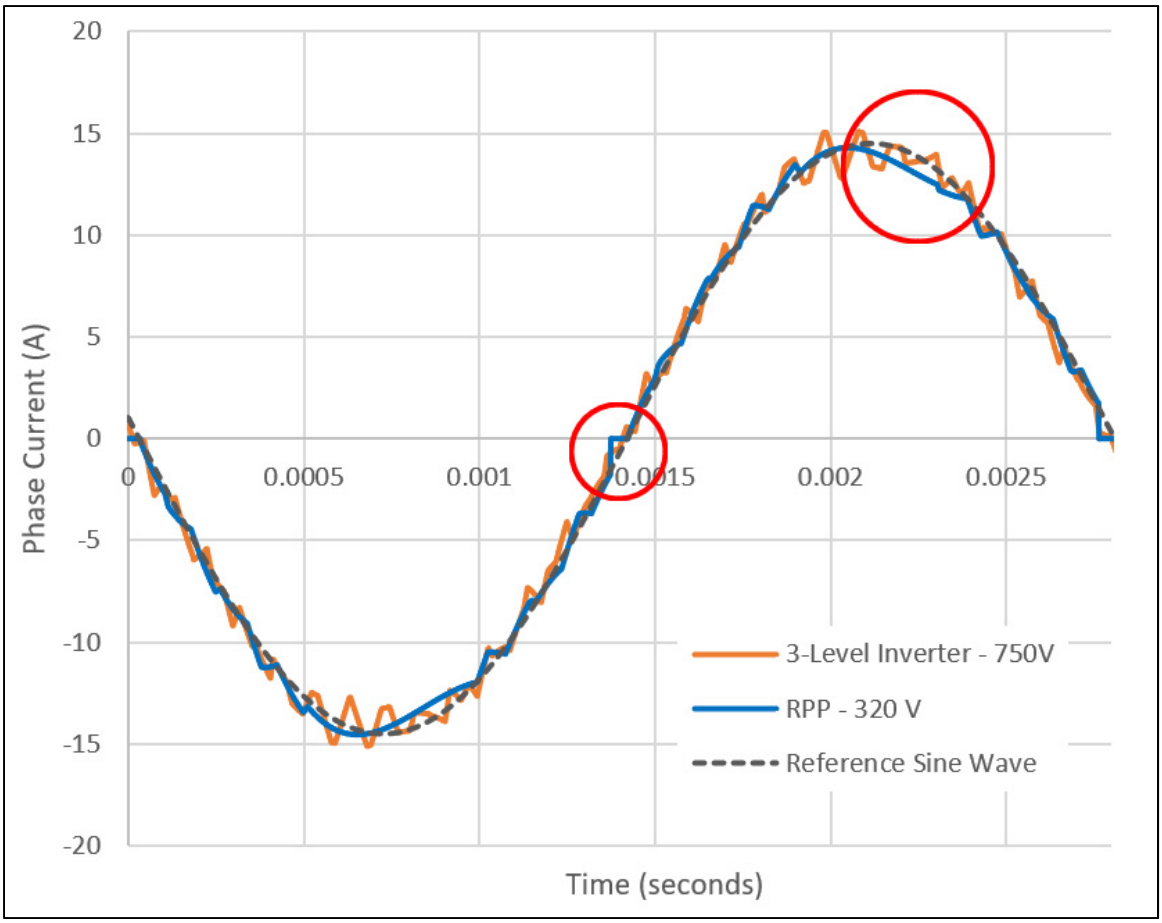

Figure 8.4 Phase current profile comparison between RPP and Baseline

8.4 General observations

8.4.1 Electric Machine Phase/Recharge Circuit Selection (EMPRCS)

The control algorithm successfully manages the Electric Machine Phase/Recharge Circuit Selection (EMPRCS) throughout the system run-up. In no occurrence the control algorithm allows to connect a Configurable Capacitor Module to more than one motor phase or recharge circuit simultaneously, even during transitions from one phase to the other. Also, the control algorithm successfully manages the recharge cycles timing, never commanding two Configurable Capacitor Modules to be recharged simultaneously.

The control algorithm manages the transitions between states, and the associated motor phase or recharge circuit as expected. In all cases the discharge process is properly timed with the triggering events, which are the back-EMF zero crossings of the half period. Also, in all cases the recharge process is properly timed with triggering events, which are the recharge available flag and recharge current zero-crossing.

8.4.2 Capacitor Polarity Selection (CPS)

The control algorithm successfully manages the Capacitor Polarity switches. Through the run-up process, the capacitors' polarities are always set properly to either provide discharge energy to the motor phase or to benefit from the discharged capacitor's residual energy for the recharge cycle.

The control algorithm ensures that both CPSX1 and CPSX2 switches are closed simultaneously only when the RPP is offline to create a pass-through circuit directly linking the inverter to the motor. Once the RPP is active, in no occurrence both CPSX1 and CPSX2 switches are closed simultaneously, as this would cause a short circuit between both terminals of the capacitor.

As expected, both CPSX1 and CPSX2 switches are open (OFF) during transitions in order to lock the capacitor's energy and provide zero current switching capability.

8.4.3 Capacitance Setting (CS)

The control algorithm successfully change the Configurable Capacitor Modules' capacitance as expected by commanding the "HX" switches according to the motor speed and Configurable Capacitor Module's state. As mentioned previously, the transition occurs when the capacitors are in discharged state, which minimize the stress on the "HX" switches.

8.4.4 Zero Current Switching in the RPP

The Resonant Power Processor control algorithm has been designed to ensure Zero Current Switching in all phase selection switches (AX, BX, CX and RX), capacitor polarity switches (CPSX1 and CPSX2) and capacitance selection switches (HX). The test results show that this objective is largely met.

First, the ZDAC control aligns the phase current vector with the Back-EMF vector. This ensures that the triggers for initiating and terminating the discharge cycle in the motor phases can be timed directly by the Back-EMF zero crossing criteria. Figure 8.5 below shows a close-up of the discharge cycle initiation and termination with regards to the phase current. One can observe that in steady state, the phase current at discharge initiation and termination are below 2 A. It is important to switch the phase selection switches at the lowest current possible as in all cases, switches are connected to either the motor phases inductances or the recharge circuit inductances. It is known that the current circulating in an inductance has an inertia, similar to a moving mass. Suddenly opening circuit of an inductive circuit in which current circulates may generate a high voltage peak, which will ultimately increase the switching losses. At 2 A of phase current, the energy stored in the motor phase inductance is 7 mJ. As previously mentioned in Section 8.3, the zero-current switching performance could be improved by reducing the RPP configuration time between capacitor discharge cycles.

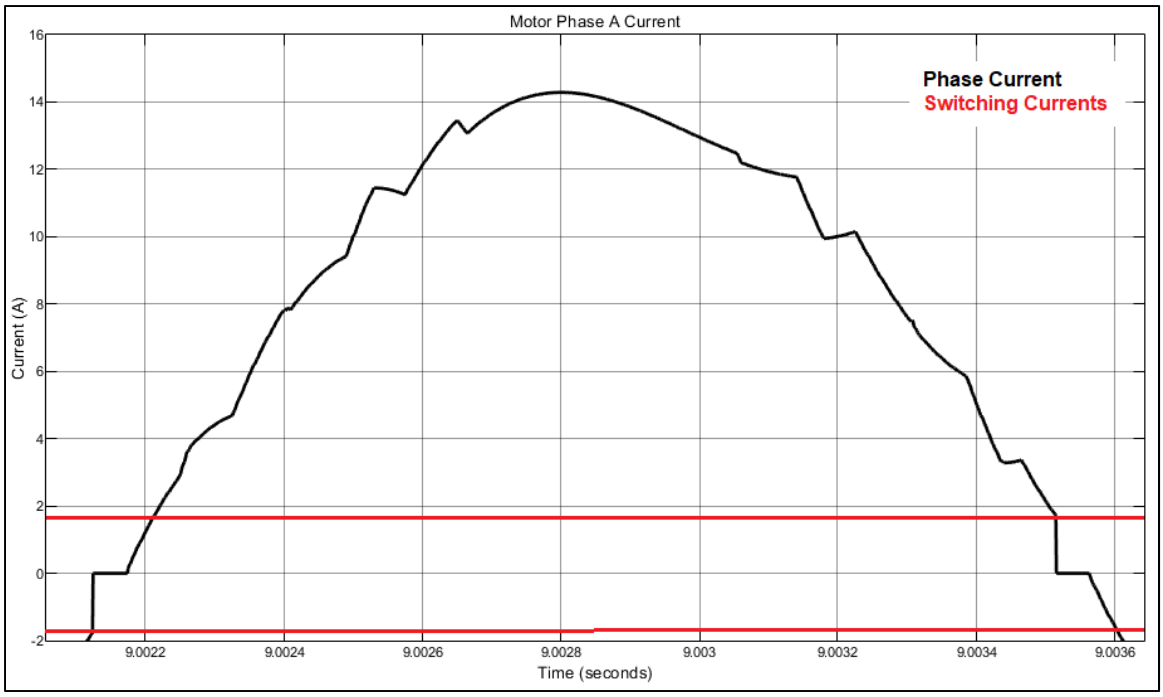

Figure 8.5 Phase current during discharge cycle initiation and termination

Second, the CPSX1 and CPSX2 switches change configuration only in the discharged or recharged state, where the current is null. As previously mentioned, in no circumstance both CPSX1 and CPSX2 switches are ON simultaneously. Also, the CPSX1 and CPSX2 switching is performed when the Configurable Capacitor module is open circuit by the phase selection switches, ensuring ZCS.

Finally, as previously mentioned, the HX switches change state in Discharged state, where current is null.

It is to be noted that the recharge circuit MOSFET (R_ON) switches at zero current half of the time. During turn-on, the recharge current is null therefore ZCS is achieved. However, during turn-off, the recharge current is maximal. In order to prevent a high voltage surge at the recharge MOSFET, a free-wheeling path is available for the recharge current through the bypass diode.

8.4.5 Neutral Current

Because the neutral of the motor is not floating, the sum of all phase currents are not automatically equal to zero. Theoretically, when all phase currents are perfectly sinusoidal and of exact same magnitude, the sum of all currents always equals zero, even when the motor neutral is not floating. However, because the phase currents are not perfectly sinusoidal and not exactly of the same magnitude, a current circulates in the Motor Neutral lead. Connecting the motor neutral to the battery zero-volt reference creates the advantage that the phase currents can be controlled independently. This is particularly useful when the control must manage capacitor voltages in the phase voltage equation.

From Figure 7.7, it can be observed that during the run-up, the neutral current can reach up to 25 A peak. However, in steady state, the neutral current is only 0.67 A rms, which indicates that the phase currents are properly balanced.

8.4.6 Battery Current

The battery current during the run-up process is shown in Figure 7.6. it can be observed that before the RPP activation, the battery current is stable. However, after activation of the RPP, the battery current draws significant current spikes, up to approximately 200 A. The battery current spikes are caused by the capacitor recharge cycles.

8.5 Compliance with design requirements

It has been verified that the components requirements described in ANNEX I are met throughout the system run-up process. The simulation results show that most components of the system have been properly sized for the operation, with the exceptions described below:

- The AX, BX and CX switches maximum current requirement is 20 A peak, but the maximum phase current reached during the run-up process is 23 A peak. However, it is to

be noted that the selected bi-directional switches can withstand up to 150 A peak. Therefore, implementation ensures proper functioning of the system.

- The inverter MOSFETs maximum current requirement is 20 A peak, but the maximum phase current reached during the run-up process is 23 A peak. However, it is to be noted that the selected inverter MOSFETs can withstand up to 29 A peak. Therefore, implementation ensures proper functioning of the system.

- The recharge MOSFET current reaches 175 A, however the requirement and implementation of the component set the maximum peak current to 150 A.

- The recharge inductance current reaches 175 A, however the requirement and implementation of the component set the maximum peak current to 150 A (50 A per inductor).

- The phase A, B and C phase current sensors maximum current requirement is 20 A peak, but the maximum phase current reached during the run-up process is 23 A peak. However, it is to be noted that the selected phase current transducer range is from -50 A to 50 A. Therefore, implementation ensures proper functioning of the system.

- The 56 µF capacitor bank tolerance is not met. Implementation of the 56 µF capacitor bank makes the nominal capacitance to be 55 µF. The nominal value of the capacitor banks is within the capacitance acceptable tolerance as per ANNEX I, however the components themselves have a tolerance of +/- 5%, which ultimately bring the lowest possible capacitance to 52.7 µF (the lowest acceptable capacitance is 53.2 µF as per ANNEX I). However, as the capacitor banks are made of multiple components, it reduces the probability that all capacitors in the capacitance bank are on the low side, therefore reducing the probabilities that the capacitor banks do not meet the +/- 5% tolerance requirement.

- The implementation of the 0.330 mH recharge inductance does dot meet the tolerance requirements of ANNEX I. The 1 mH inductances used in the implementation have +/- 15% of inductance tolerance. However, enough bandwidth exists in the recharge cycle to allow for a bigger inductance, which will ultimately increase the recharge cycle time. Also, as the inductance is made to 3 identical parts, it reduces the probability that all inductors in the inductance bank are on the low or high side, therefore reducing the probabilities that the inductance bank does not meet the +/- 5% tolerance requirement.

Because the non-compliance to the requirements occurs for very short periods of time, and as the exceedances are not significant and occur only once in the run-up process, it is deemed that the components are able to withstand the exceedances for a proof-of-concept demonstrator prototype.

8.6 Performance of the control system

8.6.1 Performance of the control system during run-up

The simulation results show that the base speed of the motor, with a battery voltage of 320 Vdc, is approximately 2000 rpm. Below 2000 rpm, the motor can maintain its maximum torque and maximum current (or in our case close to maximum torque and maximum current). It is to be noted that the torque limit is set to 15.6 N.m in the motor controller, however the Field Oriented Control is operating in transient during this period because the motor is constantly accelerating. It is shown at Figure 7.3 that the d-q axis voltage commands are in transient state, continuously adjusting for the changing back-EMF and phase impedance. Stronger controller P-I gains could have improved the maximum torque tracking in transient state. However, the controller P-I gains have not been optimized as part of this research project, as the objective is to demonstrate a proof of concept for the Resonant Power Processor.

From approximately 2000 rpm, the phase current, and therefore the motor torque, decreases until the motor reaches almost steady state at approximately 2700 rpm, where the available motor torque is almost equal to the load torque. Within this speed range, the motor power

cannot be increased because the increasing back-EMF counters the phase voltage to a point where the maximum phase current cannot circulate in the motor phases anymore. During this transition period, the integrator of the q-axis current command to q-axis voltage command transfer function constantly decrease the q-axis voltage command until the minimum value of -500 V is reached (the outputs of the integrators are limited within +/- 500V). During this period, the control strategy is still Zero D-Axis Current (ZDAC), so only the q-axis current decrease while the d-axis current remains zero, as shown in Figure 7.3.

At 2700 rpm, the Resonant Power Processor (RPP) activates, and the motor torque momentarily reaches 19 N.m of torque. This transient torque overshoot is because the d-q axis voltage commands were high from the previous operational condition where the Back-EMF was preventing the full phase current, as shown in Figure 7.3. As the commanded phase currents can be reached, the FOC integrators de-saturate and converge to the proper voltage operating set point.

For the rest of the run-up, the motor torque is maintained to a maximum value of 15.4 N.m, which is only 0.2 N.m lower than the maximum torque of 15.6 N.m set in the controller (1.3% lower than maximum value).

8.6.2 Performance of the control system during steady state operation

Once the target speed is reached or exceeded, it can be observed that the closed loop speed control is able to manage the motor torque, and therefore the phase currents, to stabilize the motor speed at the speed target in 0.65 second, and within 0.04% of speed control error. The motor speed ripples remain within 0.09 rpm peak-to-peak. The inertial load of the propeller being 0.1 $Kg.m^2$, it helps damping the torque ripples and maintaining the speed fluctuations at low amplitude. It is to be noted that the performance of the control algorithm has not been tested with a varying load, as the load has been assumed to be a pure function of motor speed squared.

8.6.3 Performance of the Capacitor Voltage Control

The capacitor voltage request is an open loop parameter which is function of motor speed. As the Back-EMF is function of motor speed, also setting the capacitor voltage request as a function of motor speed is equivalent to setting the capacitor voltage request as a function of the motor Back-EMF. This is justified by the fact that the purpose of the recharged capacitors is to counter the motor back-EMF, allowing phase currents to reach the desired values with sufficient margin to generate a sinusoidal current profile. The value of the Capacitor Voltage Request is generated by the Main Sequencer as per Figure 5.11.

The controller that ensures that the recharged capacitor voltage is part of the individual Capacitor Module Controls. The control of the recharged capacitor voltage is based on the calculation of the initial capacitor energy and energy input. As seen previously, in a LC resonant circuit, the energy is exchanged between the capacitor (in the form of potential energy) and the inductance (in the form of kinetic energy). The recharge cycle allows to convert the residual capacitor energy into kinetic energy in the inductance before it is converted to potential energy again at the end of the recharge cycle.

The control algorithm that schedules the “R_ON” MOSFET to properly charge the capacitor can be found in Figure 5.9. The algorithm subtracts the initial capacitor energy from the total capacitor energy request in order to determine the energy input required. The control algorithm monitors the input energy by integrating the instantaneous power from the battery minus the instantaneous power losses of the RPP (estimated to the losses in the Configurable Capacitor Module). This approach has been selected in order to benefit from the resonant dynamics of the recharge current, which allows to harvest the inductance energy in the form of current and convert it to capacitor energy in the form of capacitor voltage.

Figure 8.6 below shows the recharged capacitor voltage compared to the capacitor voltage request through the run-up process.

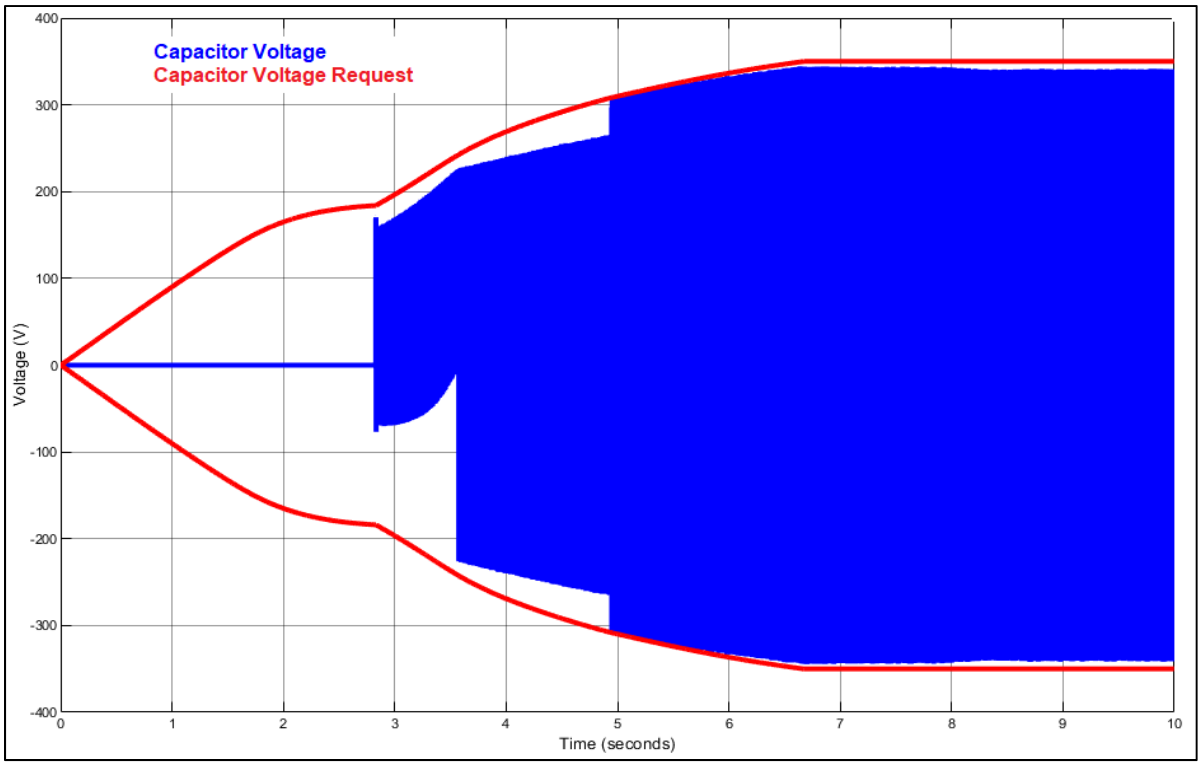

Figure 8.6 Capacitor Voltage vs Capacitor Voltage Request (Config. Cap. Module 1 shown)

One can observe that in the High Capacitance configuration, the recharged capacitor voltage error is larger than in the Low Capacitance configuration. This is mainly due to the fact that the losses estimation equation is based on the Low Capacitance configuration (HX OFF). When in the High Capacitance configuration is selected, the conduction losses are superior compared to the conduction losses in Low Capacitance configuration. The conduction losses are therefore underestimated when in High Capacitance configuration, causing the recharged capacitor voltage to be below the target.

As previously explained in the Section 5.3.1.1, the implementation of the capacitor banks makes their high and low nominal values to be 110 µF and 55 µF respectively. As the control algorithm considers that the nominal high and low capacitance values are 112 µF and 56 µF respectively, the capacitor recharge algorithm overestimates the amount of energy required to achieve the requested recharged capacitor voltage. However, because only the RPP conduction losses are considered in the input energy calculation request, the effect of overestimating the

capacitor energy in the recharge control algorithm is partially cancelled. The performance of the capacitor recharge control is deemed acceptable, especially because the fine-tuning of the phase voltage is performed by the inverter.

8.7 Efficiency, power losses and power density

The performance of an electrodynamic system is mainly driven by its efficiency and power density. Therefore, those aspects need to be deeply analysed in order to make a judgement on the advantages and disadvantages of the RPP with regards to the prior art. The following sub section analyses the performances of the RPP system and compares it with the baseline system.

8.7.1 Efficiency and power losses

8.7.1.1 Baseline System DC-DC boost conversion efficiency and power losses

As previously mentioned, the baseline system configuration requires to increase the DC-link voltage from 320 Vdc to 750 Vdc. This energy conversion always involves losses, and without a suitable DC-DC converter model, these losses are difficult to quantify. To have an approximation of the DC-DC conversion losses and efficiency, off-the-shelf components have been assumed. The commercially available DC-DC converters come with a data sheet which quantify the efficiency of the component.

A research on the website www.digikey.ca to find a suitable DC-DC boost converter concluded that high power DC-DC converters are not common. Actually, only one DC-DC converter was available in the range of 10 kW to 12 kW, and no higher power DC-DC converter was available. This converter is the TDK-Lambda EZA11K320240 (https://product.tdk.com/en/system/files?file=dam/doc/product/power/switching-power/bidirect-converter/catalog/eza11k_e.pdf). The datasheet of the converter mentions that this DC-DC converter can provide a boost ratio of 4:3, can operate at 240V nominal input voltage and 320V nominal output voltage, and has a power rating of 11 kW.

Assuming that this DC-DC converter can be used with the same boost ratio at higher voltages and higher power, one finds that 3 DC-DC converters in series are required to increase the DC link voltage from 320 Vdc to 750 Vdc. The output power is assumed to be the input power of the inverter (See Tables 8.3 and 8.4). The conversion efficiency of all stages is 95%, which is the efficiency claimed by the supplier in the data sheet. See Table 8.3 for the power summary of the baseline system DC-DC conversion.

Table 8.3 Power Summary of the baseline DC-DC conversion

Parameter	**Value**
1st Boost stage input voltage	320 Vdc
1st Boost stage input power	9930 W
1st Boost stage output voltage / 2nd Boost stage input voltage	426.7 Vdc
1st Boost stage output power / 2nd Boost stage input power	9433 W
2nd Boost stage output voltage / 3rd Boost stage input voltage	568.7 Vdc
2nd Boost stage output power / 3rd Boost stage input power	8962 W
3rd Boost stage output voltage	750 Vdc
3rd Boost stage output power	8514 W
Global DC-DC conversion efficiency	85.7 %

8.7.1.2 Inverter efficiency and power losses

The Three-Level Neutral Point Clamped, T-Type inverter topology has been used for both the RPP system and the baseline system. Only the external connections to the inverter have been modified for the RPP system to allow all 3 phases to output negative or positive voltages simultaneously.

Because for the same phase current the Baseline system DC-link is 750 Vdc compared to 320 with the RPP's inverter, the inverter input power is significantly increased, as well as the inverter output power.

To make the baseline system's inverter power summary, the inverter output AC power as been measured on the simulation results, and the losses (switching and conduction) losses have been calculated with the same inverter loss model as used for the RPP power summary of Section

7.1.5.2. It can be observed that the conduction losses in the inverter is very similar between the RPP's inverter and the baseline system's inverter. This is because the phase current is the same in both configurations. Because the conduction losses are only function of current, the higher input voltage increase the input power but not the losses, increasing the baseline inverter's efficiency. The switching losses have been calculated based on the data sheets of the semi-conductors supplier. See Table 8.4 for the summary of the inverter losses for both the RPP system and the baseline system.

Table 8.4 Power summary of the inverter (RPP system vs baseline system)

	RPP 320V	**3L Inv. 750V**
Inverter input power (DC power)	2605 W	8514 W
Inverter switching losses	1 W	1 W
Inverter conduction losses	336 W	339 W
Inverter output AC power	2268 W	8174 W
Inverter efficiency	87.1%	96.7%

8.7.1.3 RPP efficiency and power losses

The RPP losses account for the most significant part of the losses in the RPP electrodynamic system. As seen in Section 7.1.5.2, the recharge cycle efficiency of the RPP is as low as 77.2%, but the discharge cycle efficiency is good with 95.6%. The difference of efficiency between the recharge and discharge cycles is for two reasons. First, the recharge current goes through the recharge inductance, recharge diodes and recharge MOSFET in addition to the Configurable Capacitor Modules, when the discharge current only goes through the Configurable Capacitor Modules. Second, the recharge current is significantly above the phase current, as the peak phase current reaches 15 Amps and the peak recharge current reaches 140 Amps. Because the voltage drops in the semi-conductors increase with current, and because the power losses are the product of the voltage drops and current, the increased currents have a double effect on the conduction losses.

Referring to the Tables 7.2 to 7.4 of Section 7.1.5.2, one finds that the conduction losses account for 99% of the total losses. Fortunately, there are ways to improve the conduction

losses in the RPP. First, using multiple IGBTs in parallel for the implementation of the bi-directional switches is an interesting option. Doing so, the current in each IGBT will be divided by the amount of parallel IGBTs. Dividing the current in many IGBTs will reduce the voltage drop across the IGBTs, and therefore the conduction losses will be decreased. Using multiple IGBTs in parallel is also interesting in terms of safety and reliability, as failure of one IGBT will not disable the whole system. Second, using more performant semi-conductor devices, like Silicon-Carbide (SiC) IGBTs, may reduce even more the conduction losses.

Looking at the power summary of the RPP discharge cycle, it can be observed that the summary does not balance, as there is an excess of 292 W. An analysis of the energy balance in the recharge cycle has been done to understand the root cause of this power balance error.

First the resonant energy balance between the capacitor and the recharge inductance has been checked. The capacitor energy is measured from the simulation results using the standard capacitor energy equation, which is function of the capacitance and the capacitor voltage squared. The inductive energy is also measured from the simulation results using the standard inductance energy equation, which is function of the inductance and current squared. One can see at Figure 8.7 below that the resonant energy is properly balancing in the capacitor and inductance.

Second, the input energy and the losses have been checked. The input energy and the losses have been measured from the simulation results. The Net Input Energy is the difference between the input energy and the losses during the recharge process. See Figure 8.8 for a graphic of the input energy and losses.

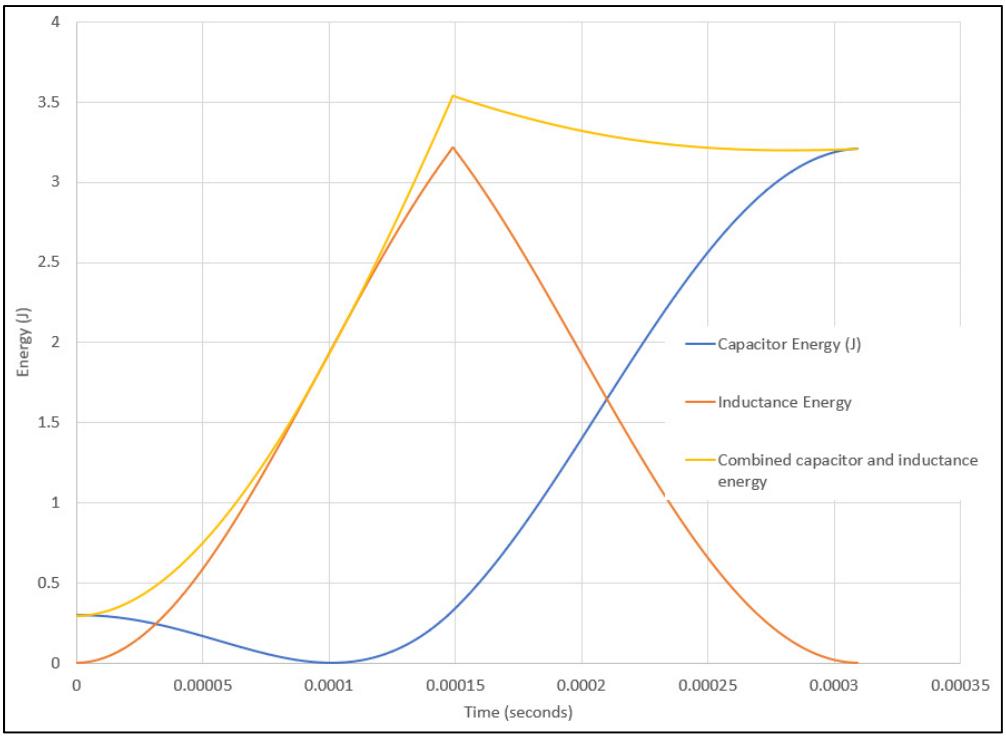

Figure 8.7 Resonant energy balance between the inductor and the capacitor

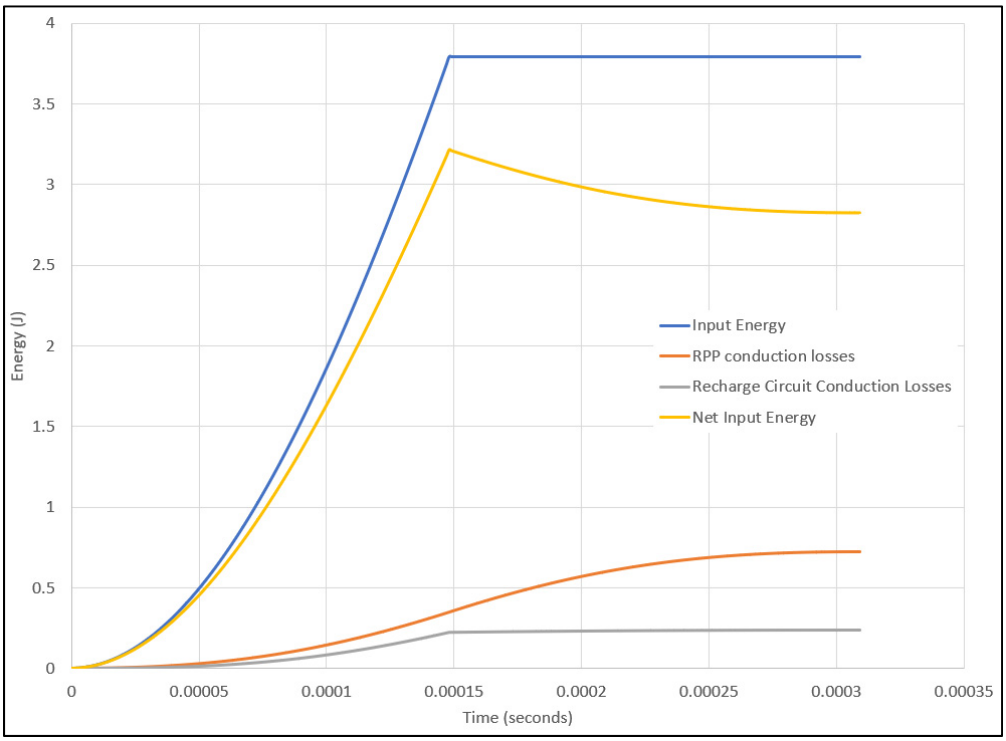

Figure 8.8 Input energy and losses during the recharge process

Theoretically, the resonant energy and the Net input energy should match perfectly. However, as shown in Figure 8.9, there is a small discrepancy between the resonant energy (combined capacitor and inductance energy) and the Net input energy. It is to be noted that the initial capacitor energy has been added to the input energy in the Figure 8.9 because the residual capacitor energy at the beginning of the recharge cycle is re-used during the recharge cycle and therefore contributes to the input energy.

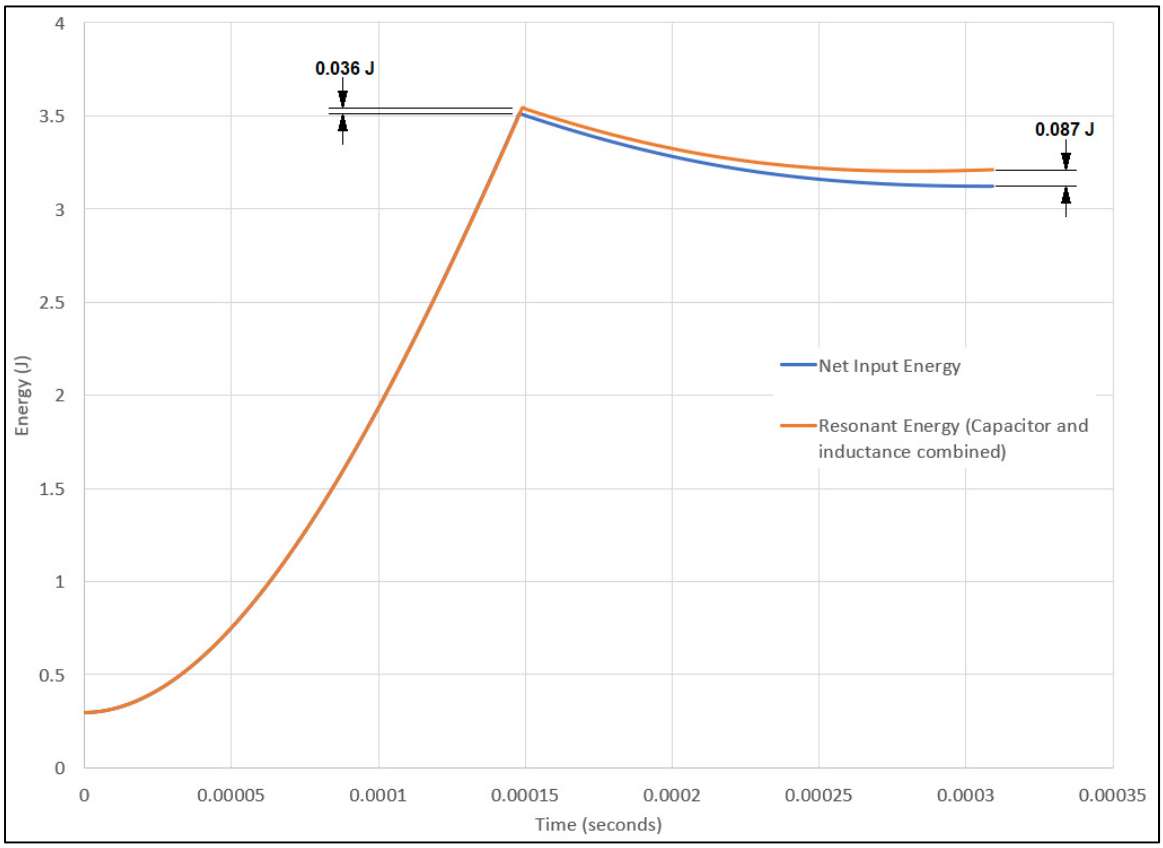

Figure 8.9 Comparison between resonant energy and Net input energy

In the simulation model, the recharge current is generated by the recharge circuit model. However, to prevent algebraic loops in the simulation model, the capacitor models use the last pass value of the current value generated by the recharge circuit model. For this reason, at the end of the energy input cycle, where the "R_ON" MOSFET is turned off, the capacitor model is still being recharged with the peak current while the inductance model current already stated decreasing. This causes the initial energy error of 0.036 J. Once the energy input cycle is

completed, the inductance energy in the form of current is gradually transferred to the capacitor in the form of voltage. Again, because the capacitor model uses the last pass value, the capacitor is always charged with a higher current than the current generated by the recharge circuit model. This generates the additional 0.051 J of error. For the cycle analyzed, the total energy error at the end of the recharge cycle is 0.087 J, which is an error of 2.72%. As the recharge cycle occurs at 2160 Hz, the calculated power error based on the analyzed recharge cycle is 188 W. Because all the recharge cycles are not identical, the error from cycle to cycle may vary. The loss error of 292 W in the RPP recharge cycle power summary (Table 7.4) is the averaged value over 1 second. This represents an error of 3.65% of error on the recharge process energy. This error is undesirable, however it does not invalidate the proof of concept of the RPP.

It is to be noted that only the RPP recharge cycle generates such a power error. All other dynamic simulation models perfectly balance between the measured input energy, calculated losses and output energy. Testing a real hardware prototype will remove the uncertainty related to the energy balance of the recharge cycles.

8.7.1.4 Motor Efficiency and losses

The same Permanent Magnet Synchronous Machine has been used for both the RPP system and the baseline system. The electrical input power and the mechanical output power have been measured directly from the simulation results. The motor conduction losses have also been calculated directly from the simulation results, using the standard resistive losses equation, function of phase resistance and phase current squared.

As it can be seen in Table 8.5 below, the test simulation results show that the PMSMs used with either the RPP system or the baseline system have similar performances. One finds comparable input power (voltages and currents) and output power with both configurations, as it can be seen in Tables 8.5 and 8.6 below. It is to be reminded that the PMSM models used in this research project do not have a thermal model and therefore cannot quantify the effect of the harmonics reduction observed in Section 8.3 above cannot be quantified in terms of

efficiency improvement. However, it has been previously mentioned that the high frequency harmonics are particularly harmful at high frequency.

Table 8.5 Power summary of the PMSM (RPP system vs baseline system)

	RPP 320V	**3L Inv. 750V**
Motor input electrical power	8065 W	8174 W
Motor conduction losses	157 W	156 W
Motor output mechanical power	7908 W	7917 W
Motor efficiency	98.1%	96.9%

Table 8.6 Motor input voltage and current (RPP system vs baseline system)

	RPP 320V	**3L Inv. 750V**
Line-Line Voltage (rms)	485.7 V	491.8 V
Phase Current (rms)	10.19 A	10.20 A

8.7.1.5 Global system efficiency comparison

Accounting for all the losses in all the components, as well as the input and output energy of the system, the global efficiency of both the RPP system and the baseline system are shown in Table 8.7 below.

Table 8.7 Power Summary of the system (RPP system vs baseline system)

	RPP 320V	**3L Inv. 750V**
Input DC Power	10602 W	9930 W
Output Power (mechanical power)	7908 W	7917 W
Total system efficiency	74.6 %	79.7%

The data shows that the global system efficiency is better with the baseline system compared to the RPP system.

8.7.2 Power Density

Being a very important parameter for airborne propulsion, the power density of the RPP is compared with the power density of the baseline system. As previously mentioned in Section 8.7.1.1 above, finding a turnkey DC-DC boost converter for the baseline system was not possible, as high-power DC-DC boost converters are not commonly available. To overcome the lack of solution, and in order to have access to a real-life DC-DC power conversion power density, 3 copies of the most powerful boost DC-DC converter that could be found commercially have been used for the DC-DC boost conversion function. The 3 DC-DC converters, model TDK-Lambda EZA11K320240, have been connected in series to increase the DC link voltage from 320 V to 750 V. Using 3 TDK-Lambda EZA11K320240 DC-DC converters for the intended purpose exceed the capabilities of the converters, both in terms of power and input voltage range. However, for the power density calculation, it is assumed that the hardware can withstand excessive usage. Table 8.8 below compares the power densities of the RPP system and the baseline system.

Table 8.8 Power density comparison between RPP system and baseline system

Parameter	**RPP 320V**	**3L Inv. 750V**
Motor Weight	18.3 Kg	18.3 Kg
Inverter Weight	604 g	604 g
Resonant Power Processor Weight	52.5 Kg	
DC-DC Boost Converter 320V/750V		60.0 Kg
Output Power	7908 W	7917 W
Power Density	110.8 W/Kg	100.3 W/Kg

The RPP has been designed with off the shelf components and a true design optimization effort has not been done for this proof-of-concept virtual prototype. A significant part of the RPP weight is due to the passive components. The total inductors weight is 19.7 Kg (37.6% of total RPP weight) and the total capacitors weight is 32.7 Kg (62.2% of total RPP weight). Together, the passive components account for 99% of the weight of the RPP. Custom inductors and capacitors may help to reduce the weight of the RPP and therefore increase the power density.

Also, it is to be noted that half of the capacitors are used only during the low speed portion of the run-up, and they become dead weight once the low capacitance configuration is set. Accounting for only the active capacitors for the calculation of the power density would bring it to ~143 W/Kg.

Finally, connecting both 56 μF capacitor banks in series instead of in parallel would create a 3rd capacitance value of 28 μF. The corresponding natural frequency would be 510.6 Hz, equivalent to a speed of 7659 rpm. Assuming that 14 N.m of torque would be achievable, the output power would be 11.2 kW, and the resulting power density could reach up to 157.3 W/Kg.

The weight of each TDK-Lambda DC-DC converter is 20 Kg. However, unlike the TDK-Lambda DC-DC converter, the RPP weight estimation does not include the control electronics, wiring, cooling system and packaging. Accounting for such material, the power density of the RPP and DC-DC boost converters would probably be similar.

8.8 Verification of initial hypotheses

In this section, the 4 initial hypotheses that support the elaboration of the concept, and that have been formulated in Section 3, are verified and discussed according to the simulation results.

8.8.1 Verification of initial hypothesis #1

Hypothesis #1: “Current and voltage sinusoidal behavior of the resonant RLC circuit may reduce PWM induced current harmonics, therefore improve motor efficiency.”

Referring to the data shown in Section 7 and analyzed in Section 8, the use of the resonant behavior of the RLC system successfully reduced the PWM induced harmonics in the phase current, and the THD value is better with the RPP compared to the baseline system. Therefore, the test results show that the hypothesis #1 is verified.

8.8.2 Verification of initial hypothesis #2

Hypothesis #2: “The Current/Voltage gain of an RLC circuit at the natural frequency being that of the DC gain of the RL circuit, lower AC input voltage may be required to reach the desired current, therefore improving efficiency.”

As it can be seen in Section 8.7.1.4 above, the input electrical power to the motor of the RPP system is very slightly lower than the input electrical power to the motor of the baseline system. The difference between both input power is less than 1.4%, therefore one can assume that the difference comes from simulation errors of both simulation models. At the motor terminals, the electrical circuit remains an inductive and resistive (RL) electrical circuit, where the back-EMF voltage is applied. It is therefore expected that at the motor terminals, the electrical power required for the PMSM to operate at the required rating is identical.

The real effect of the RL vs RLC circuit on the input phase voltage should have been measured at the terminals of the RL vs RLC circuit. However, with the conduction losses generated in the RPP circuits, this effect could not be isolated from the global electrical behavior of the system.

Therefore, the test results show that the hypothesis #3 cannot be directly verified. However, the dynamics of RL vs RLC circuits well known, and it is also known that at the resonance frequency the RLC circuit gain is the same as the RL circuit DC gain. Despites that this hypothesis could not be verified with the test results, it can be verified theoretically as seen in Section 3.

8.8.3 Verification of initial hypothesis #3

Hypothesis #3: “The voltage amplification capability of the RLC circuit may bring the capacitor’s voltage above the battery voltage, and therefore allow operating the motor at higher speeds while in MTPA.”

The test results show that despites the fact that the battery voltage is only 320 V, the charged capacitor voltage reaches above 340 V. It is to be noted that the full recharge capability is not used, because only ~70% of the recharge cycle is used and ~30% of the recharge cycle is idle. This means that potentially, the recharged capacitor voltage could reach voltages well above 320 V. The test results also show that the capacitor voltage. Therefore, the test results show that the hypothesis #3 is verified.

8.8.4 Verification of initial hypothesis #4

Hypothesis #4: “Unitary power factor at the natural frequency of the RLC circuit simplify the capacitor energy release schedule.”

In the present concept, the capacitor energy release is timed with the Back-EMF zero crossing. The Back-EMF zero crossing corresponds to an alignment with the d-axis. Because the RLC circuit has a unitary power factor, the zero phase current switching is allowed because the capacitor discharge does not need to occur with a phase lead or phase lag compared to the Back-EMF vector. Therefore, the test results show that the hypothesis #4 is verified.

CONCLUSION

In the aviation industry, the solutions to achieve a fully electric commercial airplane do not exist yet. Aside the required improvements to the batteries energy density and power density, improvements are required for the electrodynamic systems themselves. As previously mentioned, this research project focuses on the improvement of the electrodynamic systems performances. This research project started with the hypothesis that the electrical resonance phenomenon could help improving the performances of a PMSM based electrodynamic system.

In this research project, a novel resonant converter has been developed to verify the potential advantages and/or improvements relative to the exploitation of the electrical resonance phenomenon. This novel resonant converter, named Resonant Power Processor (RPP), turns the motor phases electrical circuits into RLC circuits, which have their natural frequencies matching the electrical frequency of the PMSM at the desired operating speed. The concept system consists of a three phase PMSM, a modified three phases three-level inverter and the Resonant Power Processor. The Resonant Power Processor includes four Configurable Capacitor Modules and one recharge circuit. At all times during operation, three pre-charged capacitors are connected in series while one capacitor is being recharged in the recharge circuit. Each configurable capacitor module goes through recharge and discharge cycles in alternance. In this master's thesis, the RPP concept has evolved to a detailed design consisting of the power electronics, control electronics and control algorithm, fully synthesizable in VHDL code for implementation in a FPGA. The system has then been successfully simulated in the Matlab/Simulink environment.

The simulation results show that the Resonant Power Processor design, including the control algorithm, successfully controls the PMSM at the desired speed and desired torque (5400 rpm and 14 N.m), with improved phase current THD and improved torque ripples. The motor's mechanical output power reached during operation is about 263% of the baseline configuration with the same battery voltage of 320 V.

The simulation results show that the power density and global efficiency of the system are not improved compared to the baseline system, which is made of cascaded DC-DC boost converters and a three-level inverter. Effectively, the weight of the passive components (capacitors and inductors) is quite significant and does not provide a significative power density improvement for the RPP compared to the prior art. Also, the conduction losses in the semiconductor devices of the RPP are significant, therefore reducing the efficiency of the system, mainly during the capacitor recharge process. Fortunately, solutions exist to improve the power density and efficiency of the proposed system. First, as mentioned earlier, off the shelf capacitors and inductors have been used to develop the virtual prototype. Those off the shelf components are not optimized for the needs of the RPP and may be heavier than custom parts that are developed especially for the RPP implementation. Custom inductors and capacitors may significantly improve the power density of the system. Second, the conduction losses in the RPP may be significantly reduced by using multiple semi-conductors in parallel instead of a single semi-conductor. As seen previously, 99% of the RPP losses consist of conduction losses in the semi-conductors. Splitting the currents into multiple semi-conductors for the implementation of the bi-directional switches will reduce the voltage drop across the semi-conductor devices, and therefore reduce the conduction losses. Also, using more performant semi-conductor devices, such as Silicon-Carbide (SiC) IGBTs and MOSFETs, will improve the performances of the system.

In conclusion, the proposed Resonant Power Processor developed in this master's thesis is a promising concept that may allow to improve the performances, power density and efficiency of a PMSM based electrodynamic system at high speed and high torque operation, if the proposed improvements are made to the design.

RECOMMENDATIONS

Considering the results and conclusions of this research project, the following recommendations are made:

Study of the energy density of the capacitors and inductors

In order to have a clearer picture of the potential improved power density of the system, the energy density of the passive components (capacitors and inductors) should be studied.

Verify the effect of the recharge current surges on the battery

As seen in the results section, the recharge process generates high current surges from the battery. This effect on the battery longevity should be assessed. If it is found that the recharge current surges may be damageable to the battery, a system to equilibrate the battery current during the capacitor recharge process should be considered.

Design a RPP variant that connects the two 56 μF capacitor banks in series

As mentioned earlier, connecting both 56 μF capacitor banks in series would bring the configurable capacitor module's capacitance to 28 μF, potentially allowing to reach speeds up to 7659 rpm. However, this configuration has not been designed nor simulated. It would be interesting to evaluate the power density of this configuration.

Evaluate and optimize the control algorithm for operation at variable torque as a function of speed

This research project developed a control algorithm optimized for operation at 14 N.m at 5400 rpm. It is to be assumed that a real life operation of the RPP will require operation at various torques for a given speed. The air density decreasing with altitude, the propeller torque will decrease as the aircraft climbs if the speed is steady. Therefore, the control algorithm should be improved accordingly.

ANNEX I

RESONANT POWER PROCESSOR PARTS REQUIREMENTS

Table-A I-1 Functional requirements of the capacitors

Capacitance	56 µF +/- 5%	
Current Direction	Bidirectional	
Voltage Polarity	Bipolar	
Max Current. (rms)	45 A	
Max Current. (peak)	150 A	
Max Voltage. (rms)	250 V	
Max Voltage. (peak)	350 V	
Number of units	8	

Table-A I-2 Functional requirements of the recharge inductance

Inductance	330 µH +/- 5%	
Current Direction	Unidirectionnal	
Voltage Polarity	Bipolar	
Max Current. (rms)	80 A	
Max Current. (peak)	150 A	
Max Voltage. (rms)	275 V	
Max Voltage. (peak)	475 V	
Number of units	1	

Table-A I-3 Functional requirements of the AX, BX and CX switches

Current Direction	Bidirectionnal	
Voltage Polarity	Bipolar	
Max Current. (rms)	6 A	
Max Current. (peak)	20 A	
Breakout Voltage	750 V	
Maximum Opening Time.	2 µs	
Maximum Closing Time.	2 µs	
Switching Frequency (max)	1000 Hz	
Number of units	24	

Table-A I-4 Functional requirements of the RX switches

Current Direction	Bidirectionnal	
Voltage Polarity	Bipolar	
Max Current. (rms)	35 A	
Max Current. (peak)	150 A	
Breakout Voltage	750 V	
Maximum Opening Time.	2 µs	
Maximum Closing Time.	2 µs	
Switching Frequency (max)	3000 Hz	
Number of units	8	

Table-A I-5 Functional requirements of the CPSX1 and CPSX2 switches

Current Direction	Bidirectionnal	
Voltage Polarity	Bipolar	
Max Current. (rms)	35 A	
Max Current. (peak)	150 A	
Breakout Voltage	750 V	
Maximum Opening Time.	2 µs	
Maximum Closing Time.	2 µs	
Switching Frequency (max)	2000 Hz	
Number of units	16	

Table-A I-6 Functional requirements of the HX switches

Current Direction	Bidirectionnal	
Voltage Polarity	Bipolar	
Courant max. (A,rms)	25 A	
Courant max. (A,peak)	100 A	
Breakout Voltage	750 V	
Maximum Opening Time.	2 µs	
Maximum Closing Time.	2 µs	
Switching Frequency (max)	< 1 Hz	
Number of units	4	

Table-A I-7 Functional requirements of the inverter's transistors and embedded diodes

Transistor Max Current (rms)	6 A	
Transistor Max Current (peak)	20 A	
Diode Max Current (rms)	6 A	
Diode Max Current (peak)	20 A	
Breakout Voltage	750 V	
Maximum Opening Time.	2 µs	
Maximum Closing Time.	2 µs	
Switching Frequency (max)	10000 Hz	Fixed Frequency
Number of units	6	

Table-A I-8 Functional requirements of the Recharge Circuit transistor and embedded diode

Transistor Max Current (rms)	50 A	
Transistor Max Current (peak)	150 A	
Diode Max Current (rms)	0 A	
Diode Max Current (peak)	0 A	
Breakout Voltage	750 V	
Maximum Opening Time.	2 µs	
Maximum Closing Time.	2 µs	
Switching Frequency (max)	3000 Hz	
Number of units	1	

Table-A I-9 Functional requirements of the Recharge circuit diodes

Max. Current (rms)	75 A	
Max. Current (peak)	150 A	
Breakout voltage	750 V	
Number of units	2	

Table-A I-10 Functional requirements of the VcX Voltage sensors

Voltage Polarity	Bipolar	
Operating Range	-400 / 400 V	
Number of units	4	

Table-A I-11 Functional requirements of the Vdc voltage sensor

Voltage Polarity	Unipolar	
Operating Range	0 / 400 V	
Number of units	1	

Table-A I-12 Functional requirements of the phase current sensors (Ia, Ib and Ic)

Current Direction	Bidirectionnal	
Operating Range	-30/+30 A	
Minimum Resolution	0.05 A	
Number of units	3	

Table-A I-13 Functional requirements of the recharge current sensor (Ir)

Current Direction	Bidirectionnal	
Operating Range	0/200 A	
Minimum Resolution	0.1 A	
Number of units	1	

ANNEX II

DETAILED DESIGN OF THE RESONANT POWER PROCESSOR (POWER ELECTRONICS)

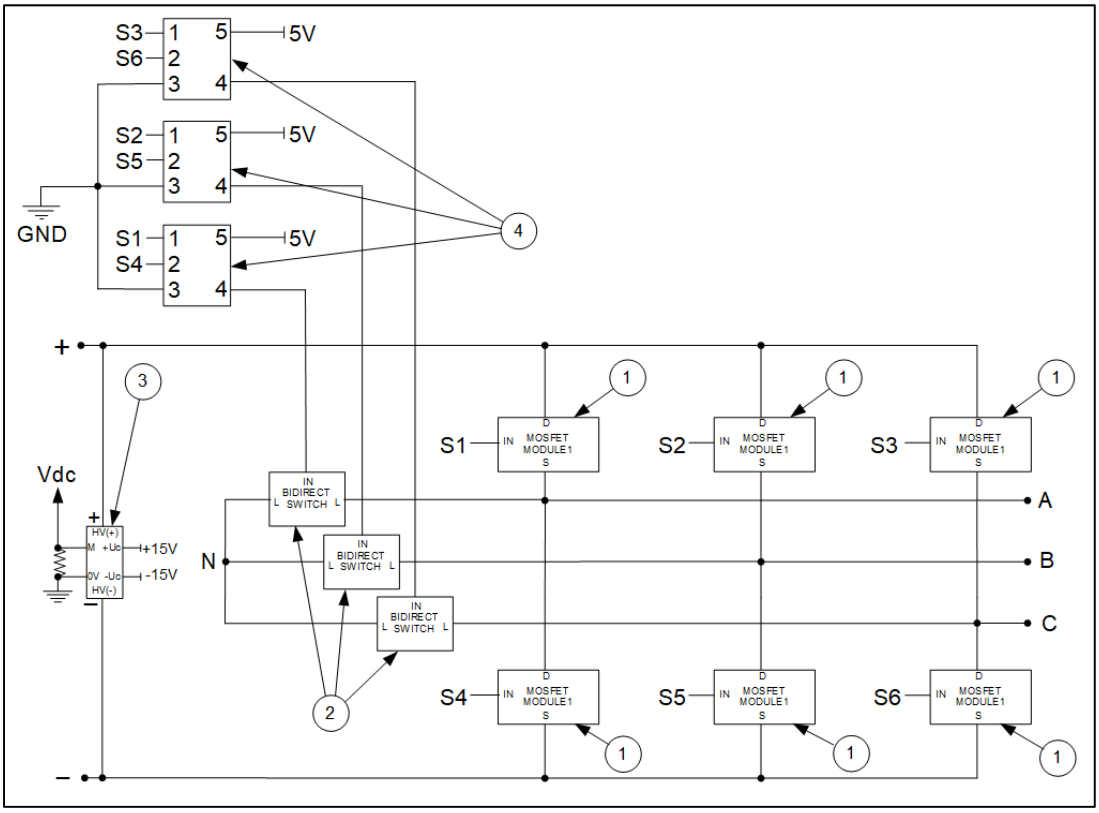

Figure-A II-1 Modified 3 phases - 2 levels inverter

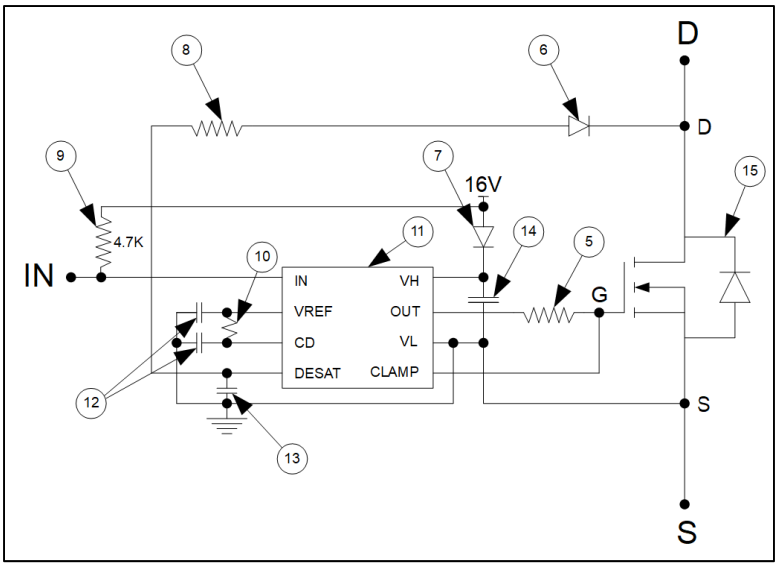

Figure-A II-2 MOSFET MODULE1 sub-assembly
(including MOSFET and gate driver)

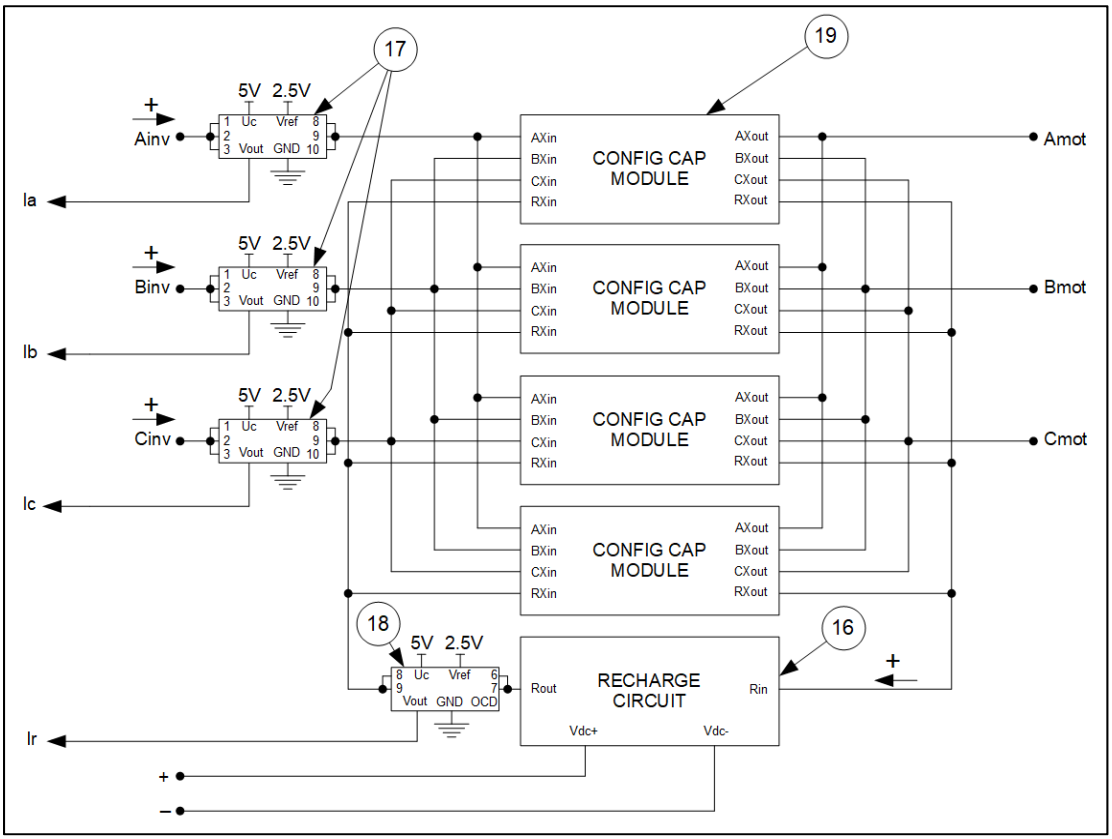

Figure-A II-3 Resonant Power Processor Detailed Architecture
(Power Electronics and Instrumentation)

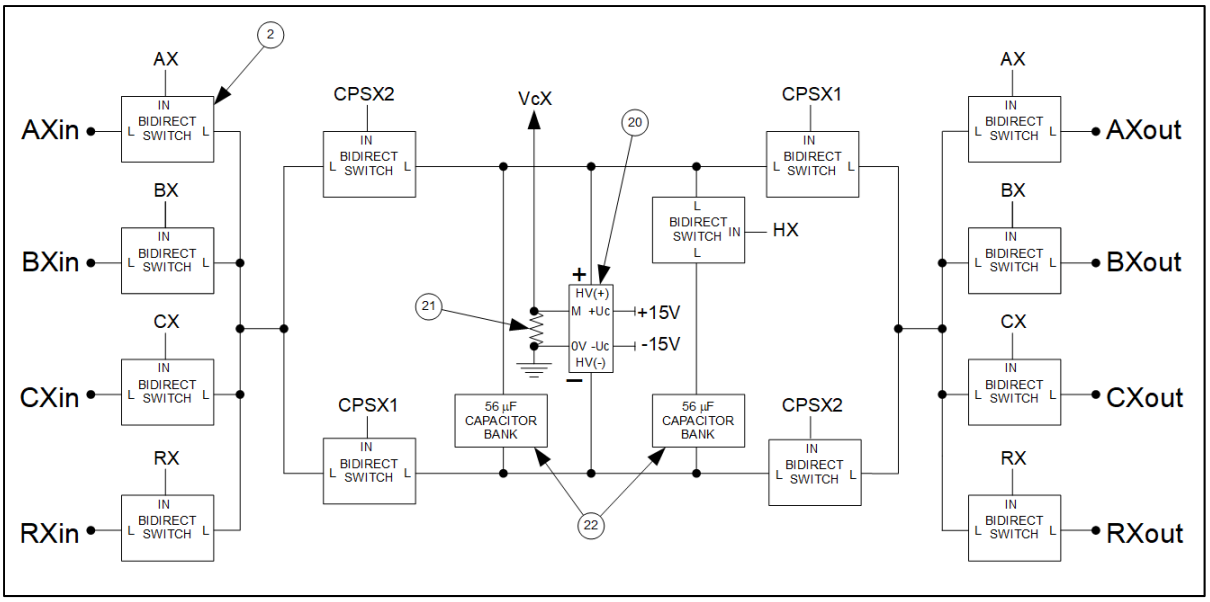

Figure-A II-4 CONFIG CAP MODULE - Configurable Capacitor Module sub-assembly
(Power Electronics, instrumentation and control signals)

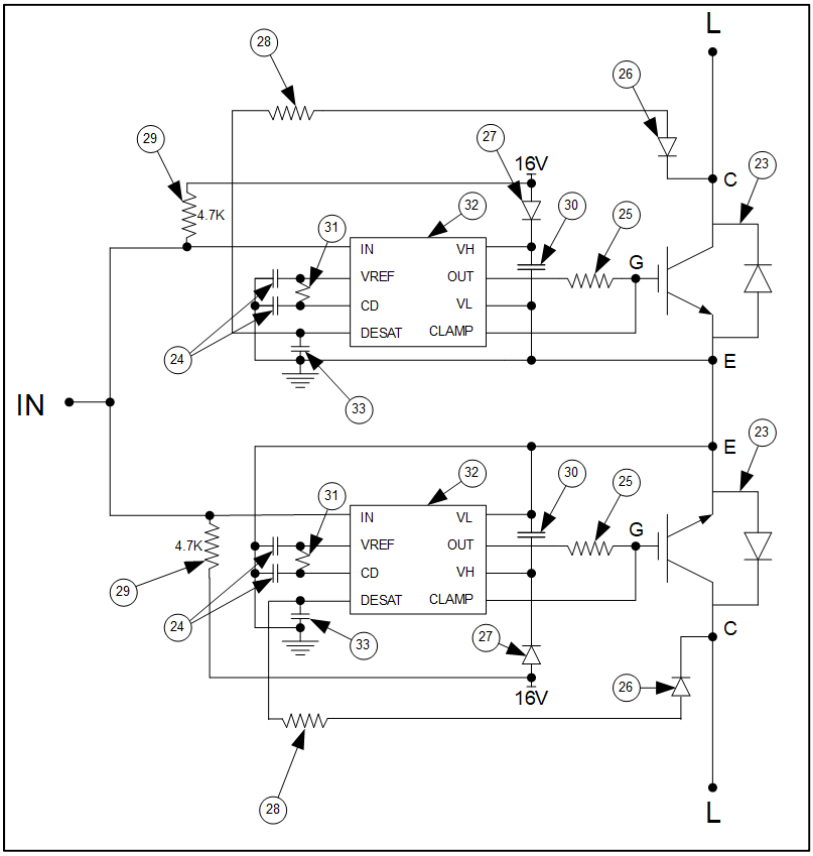

Figure-A II-5 BIDIRECT SWITCH Sub-Assembly
(Including IGBTs and Gate Drivers)

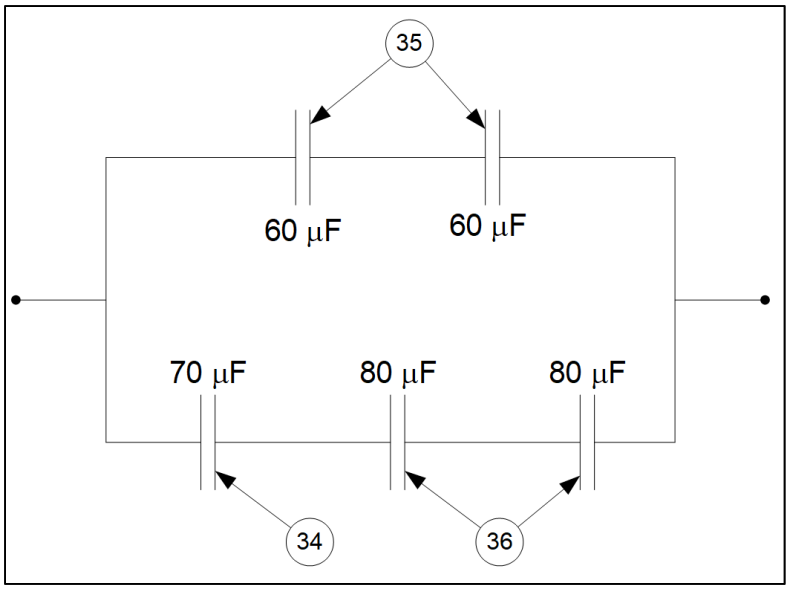

Figure-A II-6 56 µF Capacitor Bank.

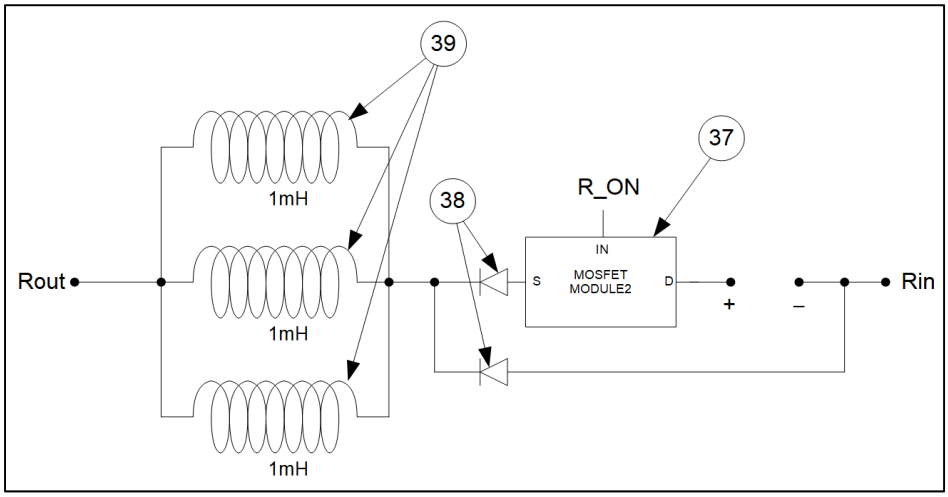

Figure-A II-7 Topology of the Recharge Circuit.

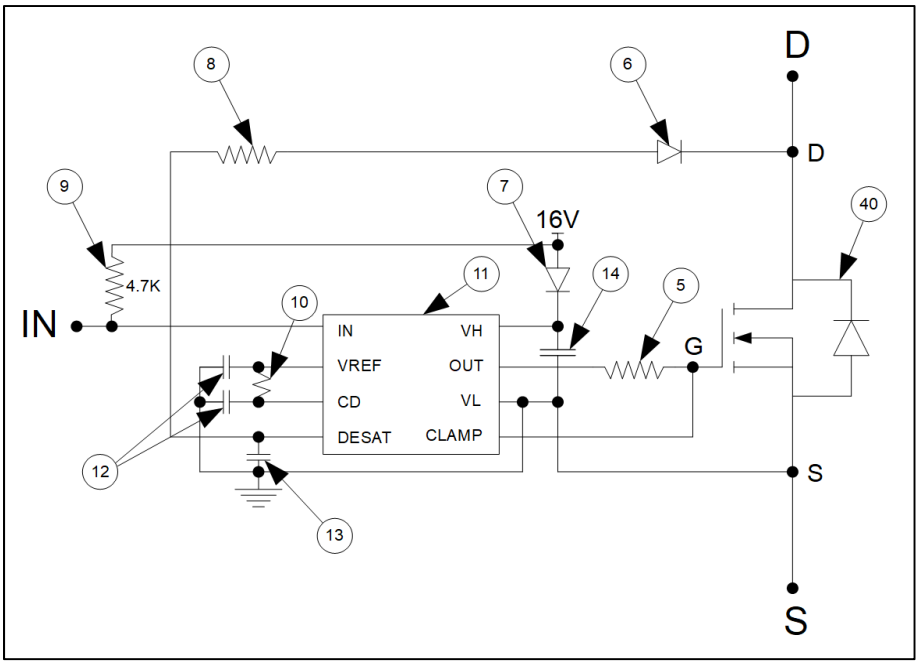

Figure-A II-8 MOSFET MODULE2 Sub-Assembly
(Including MOSFET and Gate Driver)

ANNEX III

BILL OF MATERIAL OF THE SYSTEM

Table-A III-1 Bill of Material of the System

ID \ BOM Level	1	2	3	4	5	Part Number	Part Name	Supplier	Unit Weight (g)	Total Weight (g)
-	1					BSM33C-6177MHQ	Permanent Magnet Synchronous Motor	ABB/Baldor	18300	18300
-	1					N/A	Modified 3 phases - 2 Level Inverter	N/A	603.68	603.68
1		6				N/A	MOSFET MODULE 1	N/A	6.74	40.44
5			1			TBD	Resistor (TBD)	TBD		
6			1			TBD	Diode	TBD		
7			1			TBD	Diode	TBD		
8			1			TBD	Resistor (TBD)	TBD		
9			1			TBD	Resistor (4.7K)	TBD		
10			1			TBD	Resistor (TBD)	TBD		
11			1			TD352ID	Gate Driver	STMicroelectronics	0.54	0.54
12			2			TBD	Capacitor (TBD)	TBD		
13			1			TBD	Capacitor (TBD)	TBD		
14			1			TBD	Capacitor (TBD)	TBD		
15			1			APT28M120L	MOSFET	Microchip Technology	6.2	6.2
2		3				N/A	BIDIRECT SWITCH	N/A	1.08	3.24
23			2			NGTB40N120FL2WAG	IGBT	ON Semiconductors		
24			4			TBD	Capacitor (TBD)	TBD		
25			2			TBD	Resistor (TBD)	TBD		
26			2			TBD	Diode	TBD		
27			2			TBD	Diode	TBD		
28			2			TBD	Resistor (TBD)	TBD		
29			2			TBD	Resistor (4.7K)	TBD		
30			2			TBD	Capacitor (TBD)	TBD		
31			2			TBD	Resistor (TBD)	TBD		
32			2			TD352ID	Gate Driver	STMicroelectronics	0.54	1.08
33			2			TBD	Capacitor (TBD)	TBD		
3		1				CV 3-1500	Voltage Transducer	LEM	560	560
4		3				SN74AHC1G02-EP	NOR Gate	Texas Instruments		
-	1					N/A	Resonant Power Processor	N/A	52484.6	52484.6
16		1				N/A	Recharge Circuit	N/A	19733.1	19733.1
37			1			N/A	MOSFET MODULE 2	N/A	2.14	2.14
5				1		TBD	Resistor (TBD)	TBD		
6				1		TBD	Diode	TBD		
7				1		TBD	Diode	TBD		
8				1		TBD	Resistor (TBD)	TBD		
9				1		TBD	Resistor (4.7K)	TBD		
10				1		TBD	Resistor (TBD)	TBD		
11				1		TD352ID	Gate Driver	STMicroelectronics	0.54	0.54
12				2		TBD	Capacitor (TBD)	TBD		
13				1		TBD	Capacitor (TBD)	TBD		
14				1		TBD	Capacitor (TBD)	TBD		
40				1		IXFB70N100X	MOSFET	IXYS	1.6	1.6
38			2			RHRG75120	Diode	On Semiconductor		
39			3			195C50	1 mH inductor	Hammond Manufacturing	6577	19731
19		4				N/A	Configurable Capacitor Module	N/A	8163.12	32652.5
2			13			N/A	BIDIRECT SWITCH	N/A	1.08	14.04
23				2		NGTB40N120FL2WAG	IGBT	ON Semiconductors		
24				4		TBD	Capacitor (TBD)	TBD		
25				2		TBD	Resistor (TBD)	TBD		
26				2		TBD	Diode	TBD		
27				2		TBD	Diode	TBD		
28				2		TBD	Resistor (TBD)	TBD		
29				2		TBD	Resistor (4.7K)	TBD		
30				2		TBD	Capacitor (TBD)	TBD		
31				2		TBD	Resistor (TBD)	TBD		
32				2		TD352ID	Gate Driver	STMicroelectronics	0.54	1.08
33				2		TBD	Capacitor (TBD)	TBD		
20			1			CV 3-1500	Voltage Transducer	LEM	560	560
21			1			TBD	Resistor (TBD)	TBD		
22			2			N/A	56 µF Capacitor Bank	N/A	3794	7588
34				1		C44PMGR5600RASJ	60 µF Capacitor	Kemet	600	600
35				2		C44PMGR5700RASJ	70 µF Capacitor	Kemet	730*	1460*
36				2		C44PMGR5800RASJ	80 µF Capacitor	Kemet	867	1734
17		3				LESR 50-NP	Current Transducer	LEM	10	30
18		1				LZSR 200-TP/SP1	Current Transducer	LEM	69	69

* The weight of the 70 µF capacitor has been estimated because the data could not be found on the data sheet.

ANNEX IV

INVERTER LOSS MODEL (MATLAB CODE)

```
function [VinvAn, VinvBn, VinvCn, Inv_Cond_Loss, Inv_Sw_Loss] =
fcn(VinvAnRaw, VinvBnRaw, VinvCnRaw, S1, S2, S3, S4, S5, S6, Ia, Ib, Ic)

%Initialization of persistent variables

persistent S1_LP
if isempty(S1_LP)
  S1_LP=false;
end

persistent S2_LP
if isempty(S2_LP)
  S2_LP=false;
end

persistent S3_LP
if isempty(S3_LP)
  S3_LP=false;
end

persistent S4_LP
if isempty(S4_LP)
  S4_LP=false;
end

persistent S5_LP
if isempty(S5_LP)
  S5_LP=false;
end

persistent S6_LP
if isempty(S6_LP)
  S6_LP=false;
end

persistent S1S4_LP
if isempty(S1S4_LP)
  S1S4_LP=false;
end

persistent S2S5_LP
if isempty(S2S5_LP)
  S2S5_LP=false;
end

persistent S3S6_LP
```

```
if isempty(S3S6_LP)
  S3S6_LP=false;
end

%%Calculation of conduction losses%%

%%Inverter losses calculation for phase A%%

if S1 == true

    if Ia > 0

        VlossA = 1.06*Ia;

    elseif Ia < 0

        VlossA = -1.5;

    else

        VlossA = 0.0;

    end

elseif S4 == true

    if Ia > 0

        VlossA = 1.5;

    elseif Ia < 0

        VlossA = 1.06*Ia;

    else

        VlossA = 0.0;

    end

else

    if Ia > 0.1

        VlossA = 1.5+1.06*Ia;

    elseif Ia < -0.1

        VlossA = -1.5+1.06*Ia;
```

```
    else
        VlossA = 0.0;
    end
end

%%Inverter losses calculation for phase B%%
if S2 == true
    if Ib > 0
        VlossB = 1.06*Ib;
    elseif Ib < 0
        VlossB = -1.5;
    else
        VlossB = 0.0;
    end
elseif S5 == true
    if Ib > 0
        VlossB = 1.5;
    elseif Ib < 0
        VlossB = 1.06*Ib;
    else
        VlossB = 0.0;
    end
else
    if Ib > 0.1
        VlossB = 1.5+1.06*Ib;
    elseif Ib < -0.1
```

```
        VlossB = -1.5+1.06*Ib;
    else
        VlossB = 0.0;
    end
end
%%Inverter losses calculation for phase C%%
if S3 == true
    if Ic > 0
        VlossC = 1.06*Ic;
    elseif Ic < 0
        VlossC = -1.5;
    else
        VlossC = 0.0;
    end
elseif S6 == true
    if Ic > 0
        VlossC = 1.5;
    elseif Ic < 0
        VlossC = 1.06*Ic;
    else
        VlossC = 0.0;
    end
else
    if Ic > 0.1
        VlossC = 1.5+1.06*Ic;
```

```
    elseif Ic < -0.1

        VlossC = -1.5+1.06*Ic;

    else

        VlossC = 0.0;

    end

end


VinvAn = VinvAnRaw - VlossA;
VinvBn = VinvBnRaw - VlossB;
VinvCn = VinvCnRaw - VlossC;

Inv_Cond_LossA = abs(VlossA*Ia);
Inv_Cond_LossB = abs(VlossB*Ib);
Inv_Cond_LossC = abs(VlossC*Ic);

Inv_Cond_Loss = Inv_Cond_LossA + Inv_Cond_LossB + Inv_Cond_LossC;


%%Calculation of switching losses

%Semiconductor status parameters

%Bi-Directional switch status

if S1 == false && S4 == false
    S1S4 = true;
else
    S1S4 = false;
end

if S2 == false && S5 == false
    S2S5 = true;
else
    S2S5 = false;
end

if S3 == false && S6 == false
    S3S6 = true;
else
    S3S6 = false;
end

%MOSFET turn on
```

```
if S1 == true && S1_LP ==  false
    S1_ON = true;
else
    S1_ON = false;
end

if S2 == true && S2_LP ==  false
    S2_ON = true;
else
    S2_ON = false;
end

if S3 == true && S3_LP ==  false
    S3_ON = true;
else
    S3_ON = false;
end

if S4 == true && S4_LP ==  false
    S4_ON = true;
else
    S4_ON = false;
end

if S5 == true && S5_LP ==  false
    S5_ON = true;
else
    S5_ON = false;
end

if S6 == true && S6_LP ==  false
    S6_ON = true;
else
    S6_ON = false;
end


%MOSFET turn off

if S1 == false && S1_LP ==  true
    S1_OFF = true;
else
    S1_OFF = false;
end

if S2 == false && S2_LP ==  true
    S2_OFF = true;
else
    S2_OFF = false;
end

if S3 == false && S3_LP ==  true
    S3_OFF = true;
```

```
else
    S3_OFF = false;
end

if S4 == false && S4_LP ==  true
    S4_OFF = true;
else
    S4_OFF = false;
end

if S5 == false && S5_LP ==  true
    S5_OFF = true;
else
    S5_OFF = false;
end

if S6 == false && S6_LP ==  true
    S6_OFF = true;
else
    S6_OFF = false;
end


%Bi-Directional turn on

if S1S4 == true && S1S4_LP ==  false
    S1S4_ON = true;
else
    S1S4_ON = false;
end

if S2S5 == true && S2S5_LP ==  false
    S2S5_ON = true;
else
    S2S5_ON = false;
end

if S3S6 == true && S3S6_LP ==  false
    S3S6_ON = true;
else
    S3S6_ON = false;
end

%Bi-Directional turn off

if S1S4 == false && S1S4_LP ==  true
    S1S4_OFF = true;
else
    S1S4_OFF = false;
end

if S2S5 == false && S2S5_LP ==  true
    S2S5_OFF = true;
```

```
else
    S2S5_OFF = false;
end

if S3S6 == false && S3S6_LP ==  true
    S3S6_OFF = true;
else
    S3S6_OFF = false;
end

%Calculation of inverter switching losses (MOSFET transition to ON)

if S1_ON == true
    S1_ON_LOSS = abs(0.6187*Ia);
else
    S1_ON_LOSS = 0.0;
end

if S2_ON == true
    S2_ON_LOSS = abs(0.6187*Ib);
else
    S2_ON_LOSS = 0.0;
end

if S3_ON == true
    S3_ON_LOSS = abs(0.6187*Ic);
else
    S3_ON_LOSS = 0.0;
end

if S4_ON == true
    S4_ON_LOSS = abs(0.6187*Ia);
else
    S4_ON_LOSS = 0.0;
end

if S5_ON == true
    S5_ON_LOSS = abs(0.6187*Ib);
else
    S5_ON_LOSS = 0.0;
end

if S6_ON == true
    S6_ON_LOSS = abs(0.6187*Ic);
else
    S6_ON_LOSS = 0.0;
end

%Calculation of inverter switching losses (MOSFET transition to OFF)

if S1_OFF == true
    S1_OFF_LOSS = abs(0.928*Ia);
else
```

```
    S1_OFF_LOSS = 0.0;
end

if S2_OFF == true
    S2_OFF_LOSS = abs(0.928*Ib);
else
    S2_OFF_LOSS = 0.0;
end

if S3_OFF == true
    S3_OFF_LOSS = abs(0.928*Ic);
else
    S3_OFF_LOSS = 0.0;
end

if S4_OFF == true
    S4_OFF_LOSS = abs(0.928*Ia);
else
    S4_OFF_LOSS = 0.0;
end

if S5_OFF == true
    S5_OFF_LOSS = abs(0.928*Ib);
else
    S5_OFF_LOSS = 0.0;
end

if S6_OFF == true
    S6_OFF_LOSS = abs(0.928*Ic);
else
    S6_OFF_LOSS = 0.0;
end

%Calcultation of inverter switching losses (Bi-directional switch transition
to ON)

if S1S4_ON == true
    S1S4_ON_LOSS = abs(0.6187*Ia);
else
    S1S4_ON_LOSS = 0.0;
end

if S2S5_ON == true
    S2S5_ON_LOSS = abs(0.6187*Ib);
else
    S2S5_ON_LOSS = 0.0;
end

if S3S6_ON == true
    S3S6_ON_LOSS = abs(0.6187*Ic);
else
    S3S6_ON_LOSS = 0.0;
end
```

```
%Calcultation of inverter switching losses (Bi-directional switch transition
to ON)

if S1S4_OFF == true
    S1S4_OFF_LOSS = abs(0.6187*Ia);
else
    S1S4_OFF_LOSS = 0.0;
end

if S2S5_OFF == true
    S2S5_OFF_LOSS = abs(0.6187*Ib);
else
    S2S5_OFF_LOSS = 0.0;
end

if S3S6_OFF == true
    S3S6_OFF_LOSS = abs(0.6187*Ic);
else
    S3S6_OFF_LOSS = 0.0;
end

% MOSFET switching losses

S1_Sw_Loss = S1_ON_LOSS + S1_OFF_LOSS;
S2_Sw_Loss = S2_ON_LOSS + S2_OFF_LOSS;
S3_Sw_Loss = S3_ON_LOSS + S3_OFF_LOSS;
S4_Sw_Loss = S4_ON_LOSS + S4_OFF_LOSS;
S5_Sw_Loss = S5_ON_LOSS + S5_OFF_LOSS;
S6_Sw_Loss = S6_ON_LOSS + S6_OFF_LOSS;

% Bi-Directional switches losses

S1S4_Sw_Loss = S1S4_ON_LOSS + S1S4_OFF_LOSS;
S2S5_Sw_Loss = S2S5_ON_LOSS + S2S5_OFF_LOSS;
S3S6_Sw_Loss = S3S6_ON_LOSS + S3S6_OFF_LOSS;

% Modified inverter switching losses

Inv_Sw_Loss = S1_Sw_Loss + S2_Sw_Loss + S3_Sw_Loss + S4_Sw_Loss + S5_Sw_Loss
+ S6_Sw_Loss + S1S4_Sw_Loss + S2S5_Sw_Loss + S3S6_Sw_Loss;


%Setting of last pass values

S1_LP = S1;
S2_LP = S2;
S3_LP = S3;
S4_LP = S4;
S5_LP = S5;
S6_LP = S6;
```

```
S1S4_LP = S1S4;
S2S5_LP = S2S5;
S3S6_LP = S3S6;

end
```

ANNEX V

CONFIGURABLE CAPACITOR MODULES LOSS MODEL (MATLAB CODE)

```
function [VcA, VcB, VcC, VcR, RPPXCondLoss, CapXCondLoss,CapModXSwLoss,
VcALossRPP, VcBLossRPP, VcCLossRPP, VcRLossRPP] = fcn(AX, BX, CX, RX, CPSX1,
CPSX2, HX, VcARaw, VcBRaw, VcCRaw, VcRRaw, Ia, Ib, Ic, Ir)

%Conduction Losses Calculation

% Phase A Conduction Losses Calculation

if AX == true

    if CPSX1 == true && CPSX2 == true

        if Ia > 0

            VcALossRPP = 2*(2.9+0.044*Ia)+(2.9+0.044*Ia/2);

        elseif Ia < 0

            VcALossRPP = -2*(2.9-0.044*Ia)-(2.9-0.044*Ia/2);

        else

            VcALossRPP = 0.0;

        end

    VcALossCap = 0.0;

    elseif HX == true

        if Ia > 0

            VcALossRPP = 4*(2.9+0.044*Ia)+(2.9+0.044*Ia/2);

        elseif Ia < 0

            VcALossRPP = -4*(2.9-0.044*Ia)-(2.9-0.044*Ia/2);

        else

            VcALossRPP = 0.0;

        end
```

```
    VcALossCap = 0.0023*Ia/2;

    else

        if Ia > 0

            VcALossRPP = 4*(2.9+0.044*Ia);

        elseif Ia < 0

            VcALossRPP = -4*(2.9-0.044*Ia);

        else

            VcALossRPP = 0.0;

        end

    VcALossCap = 0.0023*Ia;

    end

    VcBLossRPP = 0.0;
    VcCLossRPP = 0.0;
    VcRLossRPP = 0.0;

    VcBLossCap = 0.0;
    VcCLossCap = 0.0;
    VcRLossCap = 0.0;

% Phase B Conduction Losses Calculation

elseif BX == true

    if CPSX1 == true && CPSX2 == true

        if Ib > 0

            VcBLossRPP = 2*(2.9+0.044*Ib)+(2.9+0.044*Ib/2);

        elseif Ib < 0

            VcBLossRPP = -2*(2.9-0.044*Ib)-(2.9-0.044*Ib/2);

        else

            VcBLossRPP = 0.0;

        end

    VcBLossCap = 0.0;
```

```
    elseif HX == true

        if Ib > 0

            VcBLossRPP = 4*(2.9+0.044*Ib)+(2.9+0.044*Ib/2);

        elseif Ib < 0

            VcBLossRPP = -4*(2.9-0.044*Ib)-(2.9-0.044*Ib/2);

        else

            VcBLossRPP = 0.0;

        end

    VcBLossCap = 0.0023*Ib/2;

    else

        if Ib > 0

            VcBLossRPP = 4*(2.9+0.044*Ib);

        elseif Ib < 0

            VcBLossRPP = -4*(2.9-0.044*Ib);

        else

            VcBLossRPP = 0.0;

        end

    VcBLossCap = 0.0023*Ib;

    end

    VcALossRPP = 0.0;
    VcCLossRPP = 0.0;
    VcRLossRPP = 0.0;

    VcALossCap = 0.0;
    VcCLossCap = 0.0;
    VcRLossCap = 0.0;

% Phase C Conduction Losses Calculation

elseif CX == true
```

```
if CPSX1 == true && CPSX2 == true
    if Ic > 0
        VcCLossRPP = 2*(2.9+0.044*Ic)+(2.9+0.044*Ic/2);
    elseif Ic < 0
        VcCLossRPP = -2*(2.9-0.044*Ic)-(2.9-0.044*Ic/2);
    else
        VcCLossRPP = 0.0;
    end
VcCLossCap = 0.0;
elseif HX == true
    if Ic > 0
        VcCLossRPP = 4*(2.9+0.044*Ic)+(2.9+0.044*Ic/2);
    elseif Ic < 0
        VcCLossRPP = -4*(2.9-0.044*Ic)-(2.9-0.044*Ic/2);
    else
        VcCLossRPP = 0.0;
    end
VcCLossCap = 0.0023*Ic/2;
else
    if Ic > 0
        VcCLossRPP = 4*(2.9+0.044*Ic);
    elseif Ic < 0
        VcCLossRPP = -4*(2.9-0.044*Ic);
    else
        VcCLossRPP = 0.0;
```

```
        end

    VcCLossCap = 0.0023*Ic;

    end

    VcALossRPP = 0.0;
    VcBLossRPP = 0.0;
    VcRLossRPP = 0.0;

    VcALossCap = 0.0;
    VcBLossCap = 0.0;
    VcRLossCap = 0.0;

% Phase R Conduction Losses Calculation

elseif RX == true

    if Ir > 0.0

        if CPSX1 == true && CPSX2 == true

            VcRLossRPP = 2*(2.9+0.044*Ir)+(2.9+0.044*Ir/2);

            VcRLossCap = 0.0;

        elseif HX == true

            VcRLossRPP = 4*(2.9+0.044*Ir)+(2.9+0.044*Ir/2);

            VcRLossCap = 0.0023*(Ir/2)^2;

        else

        VcRLossRPP = 4*(2.9+0.044*Ir);

        VcRLossCap = 0.0023*Ir;

        end

    else

    VcRLossRPP = 0.0;
    VcRLossCap = 0.0;

    end

    VcALossRPP = 0.0;
    VcBLossRPP = 0.0;
    VcCLossRPP = 0.0;
```

```
    VcALossCap = 0.0;
    VcBLossCap = 0.0;
    VcCLossCap = 0.0;

else

    VcALossRPP = 0.0;
    VcBLossRPP = 0.0;
    VcCLossRPP = 0.0;
    VcRLossRPP = 0.0;

    VcALossCap = 0.0;
    VcBLossCap = 0.0;
    VcCLossCap = 0.0;
    VcRLossCap = 0.0;

end

VcA = VcARaw - VcALossRPP - VcALossCap;
VcB = VcBRaw - VcBLossRPP - VcBLossCap;
VcC = VcCRaw - VcCLossRPP - VcCLossCap;
VcR = VcRRaw - VcRLossRPP - VcRLossCap;

RPPXCondLoss   =   VcALossRPP*Ia   +   VcBLossRPP*Ib   +   VcCLossRPP*Ic   +
VcRLossRPP*Ir;

CapXCondLoss   =   VcALossCap*Ia   +   VcBLossCap*Ib   +   VcCLossCap*Ic   +
VcRLossCap*Ir;

%Switching losses calculation

CapModXSwLoss = 0.0;
```

ANNEX VI

RECHARGE CIRCUIT SEMICONDUCTORS LOSS MODEL (MATLAB CODE)

```
function [VL, RecCondLoss, RecSwLoss] = fcn(VLRaw, Ir, R_ON)

%Initalization of last pass values

persistent R_ON_LP
if isempty(R_ON_LP)
  R_ON_LP=false;
end

%Recharge Conduction Losses

if R_ON == true

    VLLoss = 0.178*Ir + (0.8+0.0017*Ir);

else

    VLLoss = (0.8+0.0017*Ir);

end

VL = VLRaw - VLLoss;

RecCondLoss = VLLoss*Ir;

%Recharge Switching Losses

if R_ON == true && R_ON_LP == false
    R_ON_ON = true;
else
    R_ON_ON = false;
end

if R_ON == false && R_ON_LP == true
    R_ON_OFF = true;
else
    R_ON_OFF = false;
end

if R_ON_ON == true
    RecSwLoss_ON = 0.9683*Ir;
else
    RecSwLoss_ON = 0.0;
end
```

```
if R_ON_OFF == true
    RecSwLoss_OFF = 3*Ir;
else
    RecSwLoss_OFF = 0.0;
end

RecSwLoss = RecSwLoss_ON + RecSwLoss_OFF;
```

ANNEX VII

BASELINE 750V 3-LEVEL INVERTER SIMULATION MODEL

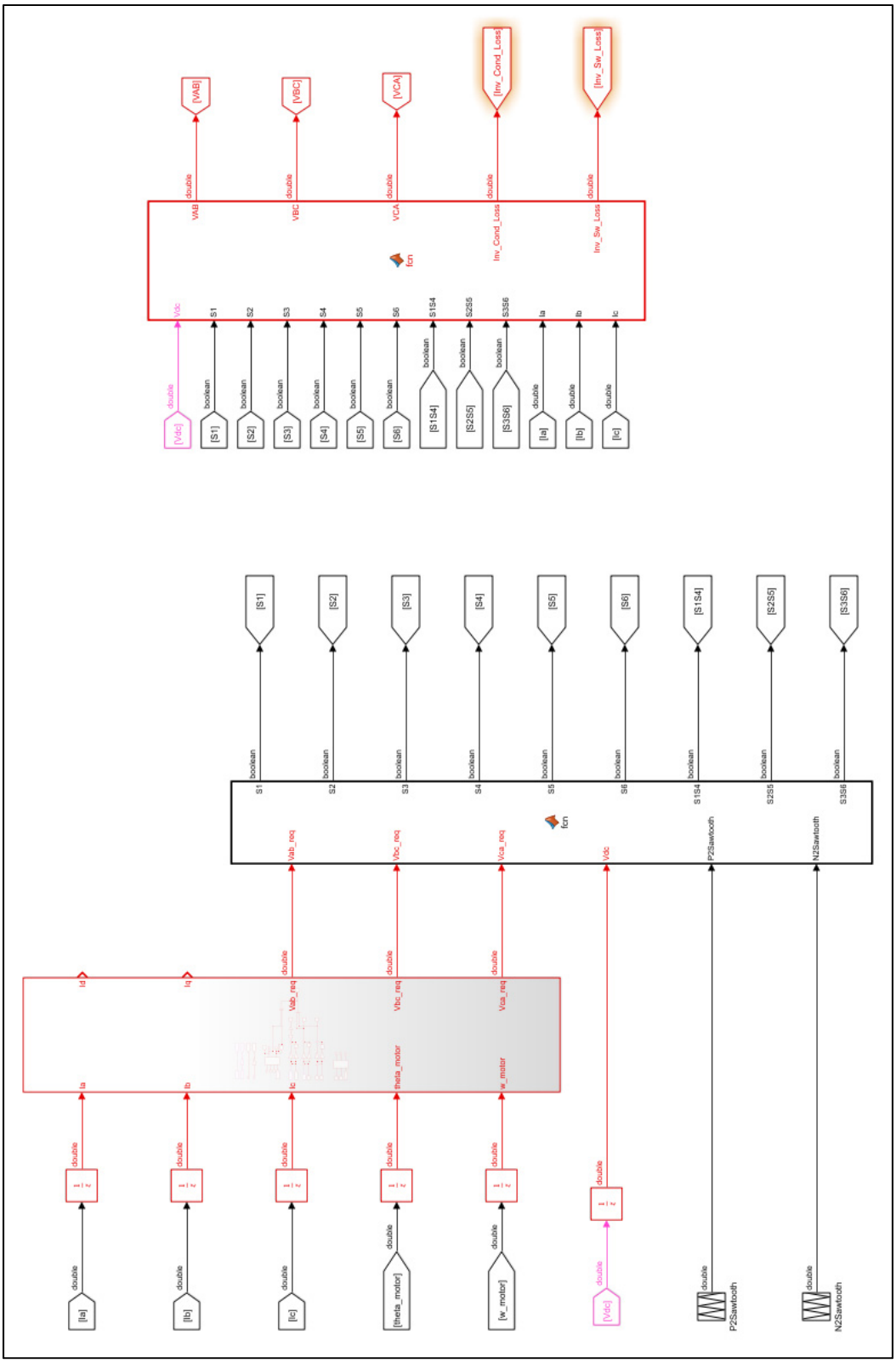

Figure-A VII-1.1 Top level baseline simulation architecture

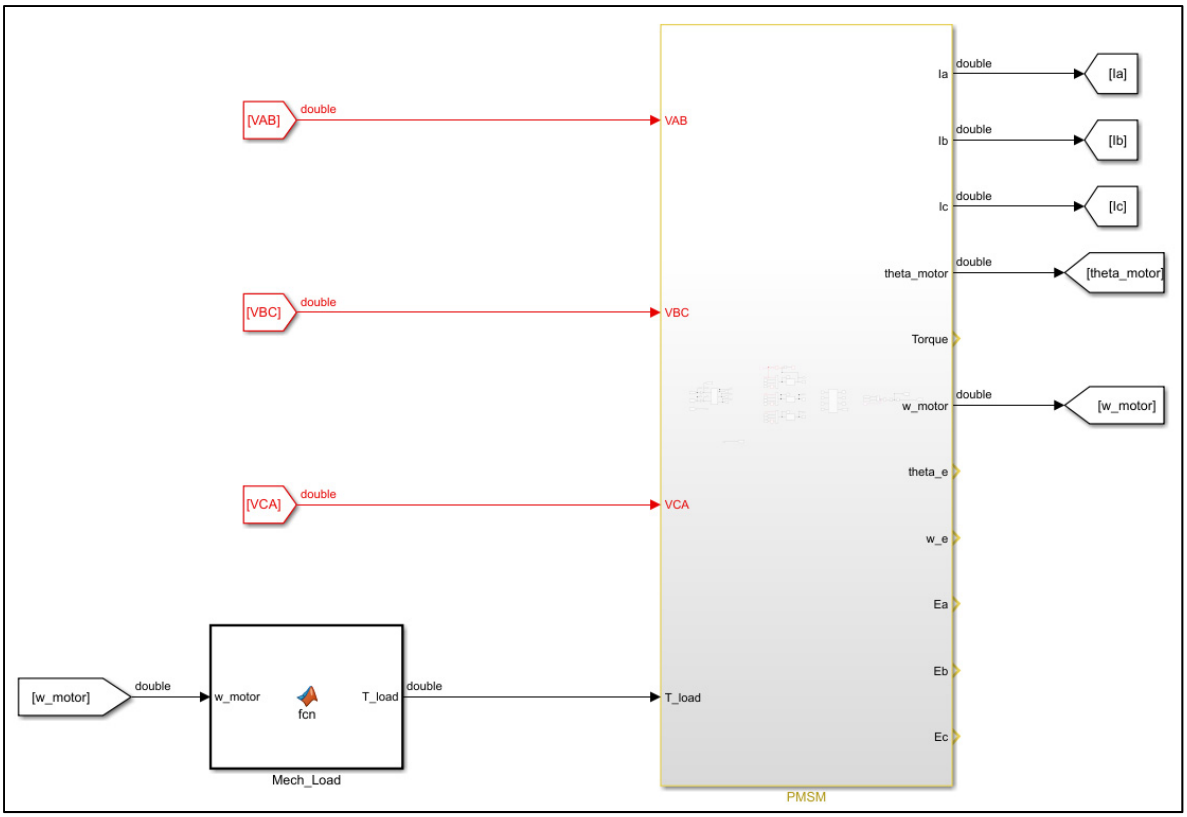

Figure-A VII-1.2 Top level baseline simulation architecture (continued)

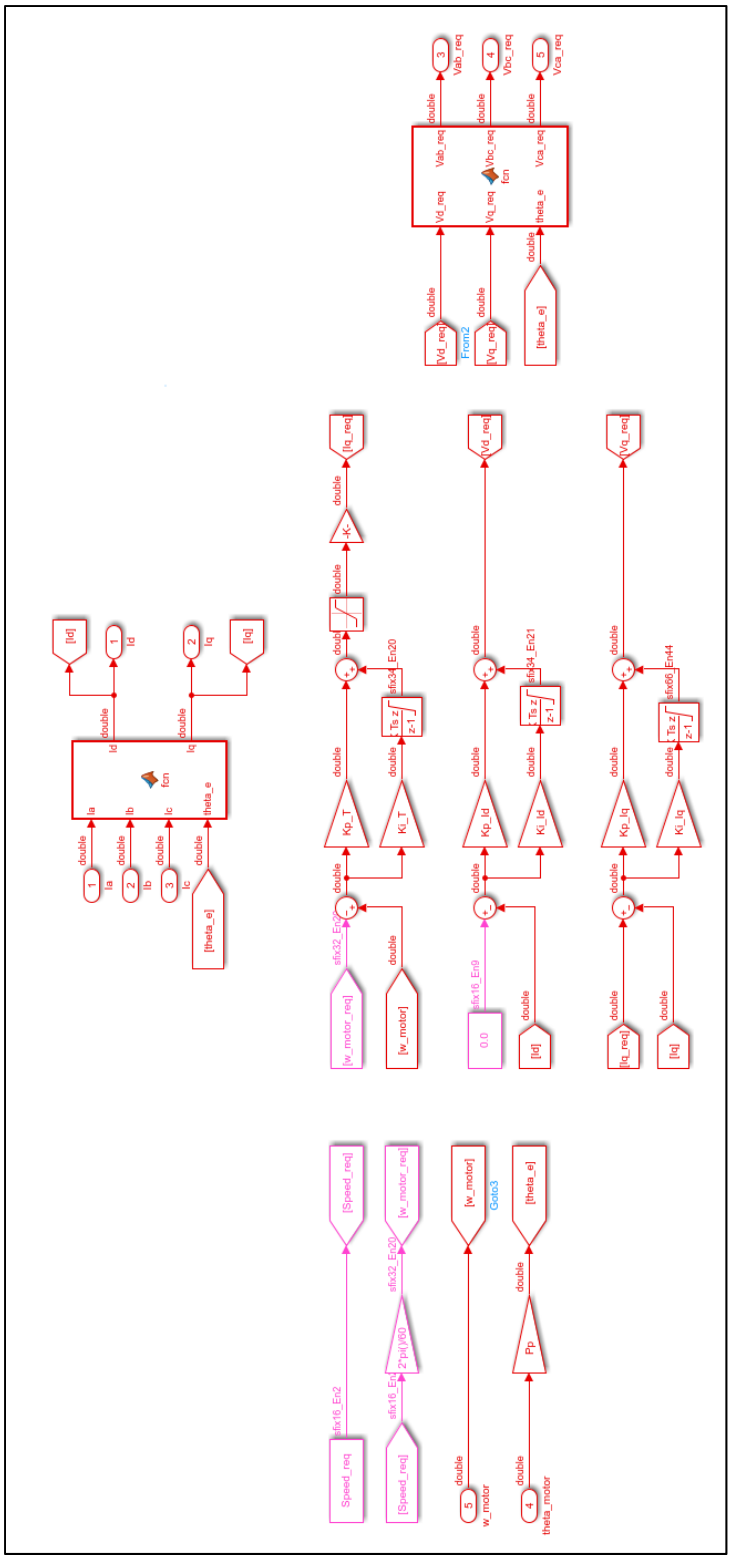

Figure-A VII-2 Field Oriented Control subsystem

VII.1 – 3-Level Inverter command algorithm

```
function [S1, S2, S3, S4, S5, S6, S1S4, S2S5, S3S6] = fcn(Vab_req, Vbc_req,
Vca_req, Vdc, P2Sawtooth, N2Sawtooth)

if Vab_req/Vdc >= P2Sawtooth

    S1 = true;
    S4 = false;
    S1S4 = false;

elseif Vab_req/Vdc <= N2Sawtooth

    S1 = false;
    S4 = true;
    S1S4 = false;

else

    S1 = false;
    S4 = false;
    S1S4 = true;

end



if Vbc_req/Vdc >= P2Sawtooth

    S2 = true;
    S5 = false;
    S2S5 = false;

elseif Vbc_req/Vdc <= N2Sawtooth

    S2 = false;
    S5 = true;
    S2S5 = false;

else

    S2 = false;
    S5 = false;
    S2S5 = true;

end



if Vca_req/Vdc >= P2Sawtooth
```

```
    S3 = true;
    S6 = false;
    S3S6 = false;

elseif Vca_req/Vdc <= N2Sawtooth

    S3 = false;
    S6 = true;
    S3S6 = false;

else

    S3 = false;
    S6 = false;
    S3S6 = true;

end
```

VII.2 – 3-Level Inverter model function (with losses)

```
function [VAB, VBC, VCA, Inv_Cond_Loss, Inv_Sw_Loss] = fcn(Vdc, S1, S2, S3,
S4, S5, S6, S1S4, S2S5, S3S6, Ia, Ib, Ic)

%Initialization of persistent variables

persistent S1_LP
if isempty(S1_LP)
  S1_LP=false;
end

persistent S2_LP
if isempty(S2_LP)
  S2_LP=false;
end

persistent S3_LP
if isempty(S3_LP)
  S3_LP=false;
end

persistent S4_LP
if isempty(S4_LP)
  S4_LP=false;
end

persistent S5_LP
if isempty(S5_LP)
  S5_LP=false;
end

persistent S6_LP
if isempty(S6_LP)
  S6_LP=false;
end

persistent S1S4_LP
if isempty(S1S4_LP)
  S1S4_LP=false;
end

persistent S2S5_LP
if isempty(S2S5_LP)
  S2S5_LP=false;
end

persistent S3S6_LP
if isempty(S3S6_LP)
  S3S6_LP=false;
end
```

```
if S1 == true && S4 == false && S1S4 == false && S2 == true && S5 == false
&& S2S5 == false && S3 == true && S6 == false && S3S6 == false

    VABRaw = 0;
    VBCRaw = 0;
    VCARaw = 0;

elseif S1 == false && S4 == true && S1S4 == false && S2 == true && S5 ==
false && S2S5 == false && S3 == true && S6 == false && S3S6 == false

    VABRaw = -Vdc;
    VBCRaw = 0;
    VCARaw = Vdc;

 elseif S1 == false && S4 == false && S1S4 == true && S2 == true && S5 ==
false && S2S5 == false && S3 == true && S6 == false && S3S6 == false

    VABRaw = -Vdc/2;
    VBCRaw = 0;
    VCARaw = Vdc/2;

elseif S1 == true && S4 == false && S1S4 == false && S2 == false && S5 ==
true && S2S5 == false && S3 == true && S6 == false && S3S6 == false

    VABRaw = Vdc;
    VBCRaw = -Vdc;
    VCARaw = 0;

elseif S1 == false && S4 == true && S1S4 == false && S2 == false && S5 ==
true && S2S5 == false && S3 == true && S6 == false && S3S6 == false

    VABRaw = 0;
    VBCRaw = -Vdc;
    VCARaw = Vdc;

elseif S1 == false && S4 == false && S1S4 == true && S2 == false && S5 ==
true && S2S5 == false && S3 == true && S6 == false && S3S6 == false

    VABRaw = Vdc/2;
    VBCRaw = -Vdc;
    VCARaw = Vdc/2;

elseif S1 == true && S4 == false && S1S4 == false && S2 == false && S5 ==
false && S2S5 == true && S3 == true && S6 == false && S3S6 == false

    VABRaw = Vdc/2;
    VBCRaw = -Vdc/2;
    VCARaw = 0;

elseif S1 == false && S4 == true && S1S4 == false && S2 == false && S5 ==
false && S2S5 == true && S3 == true && S6 == false && S3S6 == false
```

```
    VABRaw = -Vdc/2;
    VBCRaw = -Vdc/2;
    VCARaw = Vdc;

elseif S1 == false && S4 == false && S1S4 == true && S2 == false && S5 ==
false && S2S5 == true && S3 == true && S6 == false && S3S6 == false

    VABRaw = 0;
    VBCRaw = -Vdc/2;
    VCARaw = Vdc/2;

elseif S1 == true && S4 == false && S1S4 == false && S2 == true && S5 ==
false && S2S5 == false && S3 == false && S6 == true && S3S6 == false

    VABRaw = 0;
    VBCRaw = Vdc;
    VCARaw = -Vdc;

elseif S1 == false && S4 == true && S1S4 == false && S2 == true && S5 ==
false && S2S5 == false && S3 == false && S6 == true && S3S6 == false

    VABRaw = -Vdc;
    VBCRaw = Vdc;
    VCARaw = 0;

elseif S1 == false && S4 == false && S1S4 == true && S2 == true && S5 ==
false && S2S5 == false && S3 == false && S6 == true && S3S6 == false

    VABRaw = -Vdc/2;
    VBCRaw = Vdc;
    VCARaw = -Vdc/2;

elseif S1 == true && S4 == false && S1S4 == false && S2 == false && S5 ==
true && S2S5 == false && S3 == false && S6 == true && S3S6 == false

    VABRaw = Vdc;
    VBCRaw = 0;
    VCARaw = -Vdc;

elseif S1 == false && S4 == true && S1S4 == false && S2 == false && S5 ==
true && S2S5 == false && S3 == false && S6 == true && S3S6 == false

    VABRaw = 0;
    VBCRaw = 0;
    VCARaw = 0;

elseif S1 == false && S4 == false && S1S4 == true && S2 == false && S5 ==
true && S2S5 == false && S3 == false && S6 == true && S3S6 == false

    VABRaw = Vdc/2;
    VBCRaw = 0;
```

```
    VCARaw = -Vdc/2;

elseif S1 == true && S4 == false && S1S4 == false && S2 == false && S5 ==
false && S2S5 == true && S3 == false && S6 == true && S3S6 == false

    VABRaw = Vdc/2;
    VBCRaw = Vdc/2;
    VCARaw = -Vdc;

elseif S1 == false && S4 == true && S1S4 == false && S2 == false && S5 ==
false && S2S5 == true && S3 == false && S6 == true && S3S6 == false

    VABRaw = -Vdc/2;
    VBCRaw = Vdc/2;
    VCARaw = 0;

elseif S1 == false && S4 == false && S1S4 == true && S2 == false && S5 ==
false && S2S5 == true && S3 == false && S6 == true && S3S6 == false

    VABRaw = 0;
    VBCRaw = Vdc/2;
    VCARaw = -Vdc/2;

elseif S1 == true && S4 == false && S1S4 == false && S2 == true && S5 ==
false && S2S5 == false && S3 == false && S6 == false && S3S6 == true

    VABRaw = 0;
    VBCRaw = Vdc/2;
    VCARaw = -Vdc/2;

elseif S1 == false && S4 == true && S1S4 == false && S2 == true && S5 ==
false && S2S5 == false && S3 == false && S6 == false && S3S6 == true

    VABRaw = -Vdc;
    VBCRaw = Vdc/2;
    VCARaw = Vdc/2;

elseif S1 == false && S4 == false && S1S4 == true && S2 == true && S5 ==
false && S2S5 == false && S3 == false && S6 == false && S3S6 == true

    VABRaw = -Vdc/2;
    VBCRaw = Vdc/2;
    VCARaw = 0;

elseif S1 == true && S4 == false && S1S4 == false && S2 == false && S5 ==
true && S2S5 == false && S3 == false && S6 == false && S3S6 == true

    VABRaw = Vdc;
    VBCRaw = -Vdc/2;
    VCARaw = -Vdc/2;
```

```
elseif S1 == false && S4 == true && S1S4 == false && S2 == false && S5 ==
true && S2S5 == false && S3 == false && S6 == false && S3S6 == true

    VABRaw = 0;
    VBCRaw = -Vdc/2;
    VCARaw = Vdc/2;

elseif S1 == false && S4 == false && S1S4 == true && S2 == false && S5 ==
true && S2S5 == false && S3 == false && S6 == false && S3S6 == true

    VABRaw = Vdc/2;
    VBCRaw = -Vdc/2;
    VCARaw = 0;

elseif S1 == true && S4 == false && S1S4 == false && S2 == false && S5 ==
false && S2S5 == true && S3 == false && S6 == false && S3S6 == true

    VABRaw = Vdc/2;
    VBCRaw = 0;
    VCARaw = -Vdc/2;

elseif S1 == false && S4 == true && S1S4 == false && S2 == false && S5 ==
false && S2S5 == true && S3 == false && S6 == false && S3S6 == true

    VABRaw = -Vdc/2;
    VBCRaw = 0;
    VCARaw = Vdc/2;

elseif S1 == false && S4 == false && S1S4 == true && S2 == false && S5 ==
false && S2S5 == true && S3 == false && S6 == false && S3S6 == true

    VABRaw = 0;
    VBCRaw = 0;
    VCARaw = 0;

else

    VABRaw = 0;
    VBCRaw = 0;
    VCARaw = 0;

end



%%Calculation of conduction losses%%

%%Inverter losses calculation for phase A%%

if S1 == true

    if Ia > 0
```

```
        VlossA = 1.06*Ia;
    elseif Ia < 0
        VlossA = -1.5;
    else
        VlossA = 0.0;
    end
elseif S4 == true
    if Ia > 0
        VlossA = 1.5;
    elseif Ia < 0
        VlossA = 1.06*Ia;
    else
        VlossA = 0.0;
    end
else
    if Ia > 0.1
        VlossA = 1.5+1.06*Ia;
    elseif Ia < -0.1
        VlossA = -1.5+1.06*Ia;
    else
        VlossA = 0.0;
    end
end

%%Inverter losses calculation for phase B%%
```

```
if S2 == true
    if Ib > 0
        VlossB = 1.06*Ib;
    elseif Ib < 0
        VlossB = -1.5;
    else
        VlossB = 0.0;
    end
elseif S5 == true
    if Ib > 0
        VlossB = 1.5;
    elseif Ib < 0
        VlossB = 1.06*Ib;
    else
        VlossB = 0.0;
    end
else
    if Ib > 0.1
        VlossB = 1.5+1.06*Ib;
    elseif Ib < -0.1
        VlossB = -1.5+1.06*Ib;
    else
        VlossB = 0.0;
    end
end
```

```
%%Inverter losses calculation for phase C%%
if S3 == true
    if Ic > 0
        VlossC = 1.06*Ic;
    elseif Ic < 0
        VlossC = -1.5;
    else
        VlossC = 0.0;
    end
elseif S6 == true
    if Ic > 0
        VlossC = 1.5;
    elseif Ic < 0
        VlossC = 1.06*Ic;
    else
        VlossC = 0.0;
    end
else
    if Ic > 0.1
        VlossC = 1.5+1.06*Ic;
    elseif Ic < -0.1
        VlossC = -1.5+1.06*Ic;
    else
        VlossC = 0.0;
    end
```

```
end


VAB = VABRaw - (VlossA-VlossB);
VBC = VBCRaw - (VlossB-VlossC);
VCA = VCARaw - (VlossC-VlossA);

Inv_Cond_LossA = abs(VlossA*Ia);
Inv_Cond_LossB = abs(VlossB*Ib);
Inv_Cond_LossC = abs(VlossC*Ic);

Inv_Cond_Loss = Inv_Cond_LossA + Inv_Cond_LossB + Inv_Cond_LossC;


%%Calculation of switching losses

%Semiconductor status parameters

%Bi-Directional switch status

%MOSFET turn on

if S1 == true && S1_LP ==  false
    S1_ON = true;
else
    S1_ON = false;
end

if S2 == true && S2_LP ==  false
    S2_ON = true;
else
    S2_ON = false;
end

if S3 == true && S3_LP ==  false
    S3_ON = true;
else
    S3_ON = false;
end

if S4 == true && S4_LP ==  false
    S4_ON = true;
else
    S4_ON = false;
end

if S5 == true && S5_LP ==  false
    S5_ON = true;
else
    S5_ON = false;
end
```

```
if S6 == true && S6_LP ==  false
    S6_ON = true;
else
    S6_ON = false;
end


%MOSFET turn off

if S1 == false && S1_LP ==  true
    S1_OFF = true;
else
    S1_OFF = false;
end

if S2 == false && S2_LP ==  true
    S2_OFF = true;
else
    S2_OFF = false;
end

if S3 == false && S3_LP ==  true
    S3_OFF = true;
else
    S3_OFF = false;
end

if S4 == false && S4_LP ==  true
    S4_OFF = true;
else
    S4_OFF = false;
end

if S5 == false && S5_LP ==  true
    S5_OFF = true;
else
    S5_OFF = false;
end

if S6 == false && S6_LP ==  true
    S6_OFF = true;
else
    S6_OFF = false;
end


%Bi-Directional turn on

if S1S4 == true && S1S4_LP ==  false
    S1S4_ON = true;
else
    S1S4_ON = false;
end
```

```
if S2S5 == true && S2S5_LP ==  false
    S2S5_ON = true;
else
    S2S5_ON = false;
end

if S3S6 == true && S3S6_LP ==  false
    S3S6_ON = true;
else
    S3S6_ON = false;
end

%Bi-Directional turn off

if S1S4 == false && S1S4_LP ==  true
    S1S4_OFF = true;
else
    S1S4_OFF = false;
end

if S2S5 == false && S2S5_LP ==  true
    S2S5_OFF = true;
else
    S2S5_OFF = false;
end

if S3S6 == false && S3S6_LP ==  true
    S3S6_OFF = true;
else
    S3S6_OFF = false;
end

%Calcultation of inverter switching losses (MOSFET transition to ON)

if S1_ON == true
    S1_ON_LOSS = abs(1.45*Ia);
else
    S1_ON_LOSS = 0.0;
end

if S2_ON == true
    S2_ON_LOSS = abs(1.45*Ib);
else
    S2_ON_LOSS = 0.0;
end

if S3_ON == true
    S3_ON_LOSS = abs(1.45*Ic);
else
    S3_ON_LOSS = 0.0;
end
```

```
if S4_ON == true
    S4_ON_LOSS = abs(1.45*Ia);
else
    S4_ON_LOSS = 0.0;
end

if S5_ON == true
    S5_ON_LOSS = abs(1.45*Ib);
else
    S5_ON_LOSS = 0.0;
end

if S6_ON == true
    S6_ON_LOSS = abs(1.45*Ic);
else
    S6_ON_LOSS = 0.0;
end

%Calcultation of inverter switching losses (MOSFET transition to OFF)

if S1_OFF == true
    S1_OFF_LOSS = abs(2.175*Ia);
else
    S1_OFF_LOSS = 0.0;
end

if S2_OFF == true
    S2_OFF_LOSS = abs(2.175*Ib);
else
    S2_OFF_LOSS = 0.0;
end

if S3_OFF == true
    S3_OFF_LOSS = abs(2.175*Ic);
else
    S3_OFF_LOSS = 0.0;
end

if S4_OFF == true
    S4_OFF_LOSS = abs(2.175*Ia);
else
    S4_OFF_LOSS = 0.0;
end

if S5_OFF == true
    S5_OFF_LOSS = abs(2.175*Ib);
else
    S5_OFF_LOSS = 0.0;
end

if S6_OFF == true
    S6_OFF_LOSS = abs(2.175*Ic);
else
```

```
    S6_OFF_LOSS = 0.0;
end

%Calcultation of inverter switching losses (Bi-directional switch transition
to ON)

if S1S4_ON == true
    S1S4_ON_LOSS = abs(1.45*Ia);
else
    S1S4_ON_LOSS = 0.0;
end

if S2S5_ON == true
    S2S5_ON_LOSS = abs(1.45*Ib);
else
    S2S5_ON_LOSS = 0.0;
end

if S3S6_ON == true
    S3S6_ON_LOSS = abs(1.45*Ic);
else
    S3S6_ON_LOSS = 0.0;
end

%Calcultation of inverter switching losses (Bi-directional switch transition
to ON)

if S1S4_OFF == true
    S1S4_OFF_LOSS = abs(1.45*Ia);
else
    S1S4_OFF_LOSS = 0.0;
end

if S2S5_OFF == true
    S2S5_OFF_LOSS = abs(1.45*Ib);
else
    S2S5_OFF_LOSS = 0.0;
end

if S3S6_OFF == true
    S3S6_OFF_LOSS = abs(1.45*Ic);
else
    S3S6_OFF_LOSS = 0.0;
end

% MOSFET switching losses

S1_Sw_Loss = S1_ON_LOSS + S1_OFF_LOSS;
S2_Sw_Loss = S2_ON_LOSS + S2_OFF_LOSS;
S3_Sw_Loss = S3_ON_LOSS + S3_OFF_LOSS;
S4_Sw_Loss = S4_ON_LOSS + S4_OFF_LOSS;
S5_Sw_Loss = S5_ON_LOSS + S5_OFF_LOSS;
S6_Sw_Loss = S6_ON_LOSS + S6_OFF_LOSS;
```

```
% Bi-Directional switches losses

S1S4_Sw_Loss = S1S4_ON_LOSS + S1S4_OFF_LOSS;
S2S5_Sw_Loss = S2S5_ON_LOSS + S2S5_OFF_LOSS;
S3S6_Sw_Loss = S3S6_ON_LOSS + S3S6_OFF_LOSS;

% Modified inverter switching losses

Inv_Sw_Loss = S1_Sw_Loss + S2_Sw_Loss + S3_Sw_Loss + S4_Sw_Loss + S5_Sw_Loss
+ S6_Sw_Loss + S1S4_Sw_Loss + S2S5_Sw_Loss + S3S6_Sw_Loss;


%Setting of last pass values

S1_LP = S1;
S2_LP = S2;
S3_LP = S3;
S4_LP = S4;
S5_LP = S5;
S6_LP = S6;

S1S4_LP = S1S4;
S2S5_LP = S2S5;
S3S6_LP = S3S6;

end
```

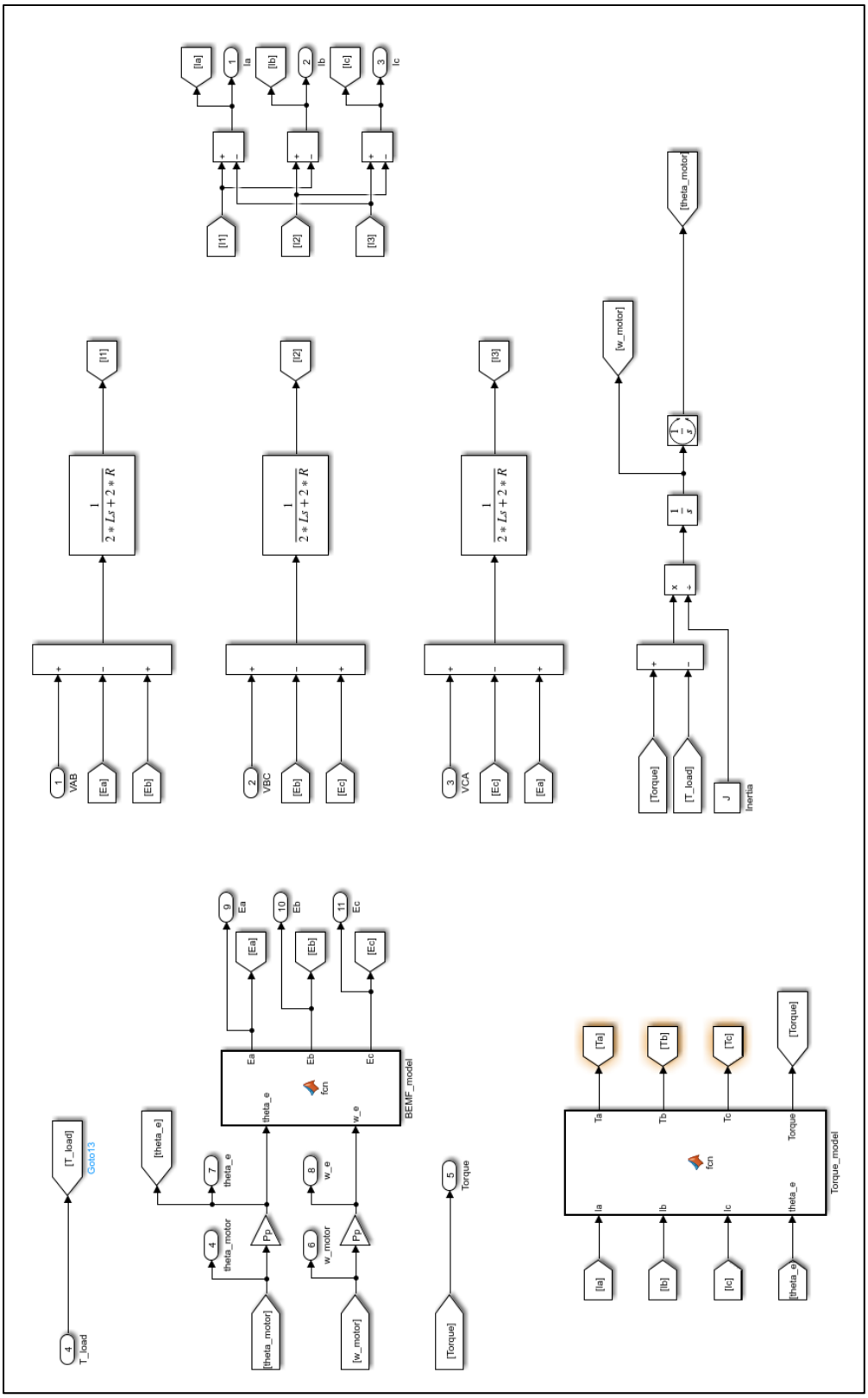

Figure-A VII-5 PMSM Model of the baseline system simulation model

ANNEX VIII

FFT MATLAB CODE

```
FFTdata(:,1)=SS_Current_3L_750V.time(:,1);
FFTdata(:,2)=SS_Current_3L_750V.signals(1).values(:,1);

FFTdataR(:,1)=SS_Current_RPP.time(:,1);
FFTdataR(:,2)=SS_Current_RPP.signals(1).values(:,1);


FFTI = FFTdata(:,2);
FFTIR = FFTdataR(:,2);

L=1000000;
Fs=1000000;

Y = fft(FFTI);
YR = fft(FFTIR);

P2 = abs(Y/L);
P1 = P2(1:L/2+1);
P1(2:end-1) = 2*P1(2:end-1);

P2R = abs(YR/L);
P1R = P2R(1:L/2+1);
P1R(2:end-1) = 2*P1R(2:end-1);

f = Fs*(0:(L/2))/L;
plot(f,P1)
hold on
plot(f,P1R)
title('Phase Current FFT Amplitude Spectrum')
xlabel('f (Hz)')
ylabel('Magnitude (A)')
```

LIST OF BIBLIOGRAPHICAL REFERENCES

Lithium-ion battery (2021, July 8). In *Wikipedia*. https://en.wikipedia.org/wiki/Lithium-ion_battery

Jet fuel (2021, July 4). In *Wikipedia.* https://en.wikipedia.org/wiki/Jet_fuel

T. Finken, M. Felden & K. Hameyer (2008). Comparison and design of different electrical machine types regarding their applicability in hybrid electrical vehicles. *2008 18th International Conference on Electrical Machines*, pp. 1-5, doi: 10.1109/ICELMACH.2008.4800044.

Wildi, T. (2003). *Électrotechnique* (3rd ed., pp. 421-424). Quebec, Canada: Les presses de l'université Laval.

D. Liang, J. Li, R. Qu, P. Zheng and B. Song (2015). Evaluation of high-speed permanent magnet synchronous machine drive with three-level and two-level inverter. *2015 IEEE International Electric Machines & Drives Conference (IEMDC)*, pp. 1586-1592, doi: 10.1109/IEMDC.2015.7409275.

Baïlon, J.-P., Dorlot, J.-M. (2000). *Des Matériaux* (3rd ed., pp. 446-460). Montreal, Canada: Presses Internationales Polytechnique.

L. Ma, M. Sanada, S. Morimoto and Y. Takeda (2003). Prediction of iron loss in rotating machines with rotational loss included. *IEEE Transactions on Magnetics*, vol. 39, no. 4, pp. 2036-2041, doi: 10.1109/TMAG.2003.812706.

K. Yamamoto, K. Shinohara and H. Makishima (2002). Comparison between flux weakening and PWM inverter with voltage booster for permanent magnet synchronous motor drive. *Proceedings of the Power Conversion Conference-Osaka 2002 (Cat. No.02TH8579)*, pp. 161-166 vol.1, doi: 10.1109/PCC.2002.998540.

J. Joseph, R. M. Patel and H. R. Pathak (2018). Analysis and Comparison of DC - DC Converter Topologies for the Design and Development of a Solar Based Inverterless System. *2018 Second International Conference on Electronics, Communication and Aerospace Technology (ICECA)*, pp. 1429-1434, doi: 10.1109/ICECA.2018.8474867.

A. Thiyagarajan, S. G. Praveen Kumar and A. Nandini (2014). Analysis and comparison of conventional and interleaved DC/DC boost converter. *Second International Conference on Current Trends In Engineering and Technology - ICCTET 2014*, pp. 198-205, doi: 10.1109/ICCTET.2014.6966287.

N. Boujelben, F. Masmoudi, M. Djemel and N. Derbel (2017). Design and comparison of quadratic boost and double cascade boost converters with boost converter. *2017 14th International Multi-Conference on Systems, Signals & Devices (SSD)*, pp. 245-252, doi: 10.1109/SSD.2017.8167022.

P. Nandankar, A. Dasarwar and G. Kachare (2018). Comparison of improved converter topologies for high voltage gain. *2018 International Conference on Communication information and Computing Technology (ICCICT)*, pp. 1-6, doi: 10.1109/ICCICT.2018.8325893.

M. Tiapkin, S. Volkov and G. Tiapkin (2017). Selection of three-level low voltage inverter circuit topology for a high speed electric drive. *2017 International Conference on Industrial Engineering, Applications and Manufacturing (ICIEAM)*, pp. 1-5, doi: 10.1109/ICIEAM.2017.8076333.

J. Rodriguez, S. Bernet, P. K. Steimer and I. E. Lizama (2010). A Survey on Neutral-Point-Clamped Inverters. *IEEE Transactions on Industrial Electronics*, vol. 57, no. 7, pp. 2219-2230, doi: 10.1109/TIE.2009.2032430.

N. Karnik, D. Singla and P. R. Sharma (2012). Comparative analysis of harmonic reduction in multilevel inverter. *2012 IEEE Fifth Power India Conference*, pp. 1-5, doi: 10.1109/PowerI.2012.6479521.

J. Itoh, D. Sato and T. Tanaka (2012). Investigation of optimal operation method for Permanent Magnet Synchronous Motor drive system with 3-level inverter. *2012 International Conference on Renewable Energy Research and Applications (ICRERA)*, pp. 1-6, doi: 10.1109/ICRERA.2012.6477377.

M. Haris, M. K. Pathak and P. Agarwal (2014). Comparison of SPWM multilevel inverter fed PMSM drive with two level inverter fed drive. *International Conference on Recent Advances and Innovations in Engineering (ICRAIE-2014)*, pp. 1-5, doi: 10.1109/ICRAIE.2014.6909123.

S. Morimoto, M. Sanada and Y. Takeda (1994). Wide-speed operation of interior permanent magnet synchronous motors with high-performance current regulator. *IEEE Transactions on Industry Applications*, vol. 30, no. 4, pp. 920-926, doi: 10.1109/28.297908.

S. Halder, P. Agarwal and S. P. Srivastava (2015). Comparative analysis of MTPA and ZDAC control in PMSM drive. *2015 Annual IEEE India Conference (INDICON)*, pp. 1-5, doi: 10.1109/INDICON.2015.7443809.

Xin Zhao and Hui Liang (2009). Flux-weakening control of permanent magnet synchronous motor using in electric vehicles. *2009 IEEE 6th International Power Electronics and Motion Control Conference*, pp. 1050-1054, doi: 10.1109/IPEMC.2009.5157540.

D. Pohlenz and J. Böcker (2010). Efficiency improvement of an IPMSM using Maximum Efficiency operating strategy. *Proceedings of 14th International Power Electronics and Motion Control Conference EPE-PEMC 2010*, pp. T5-15-T5-19, doi: 10.1109/EPEPEMC.2010.5606831.

R. Ni, D. Xu, G. Wang, L. Ding, G. Zhang and L. Qu (2015). Maximum Efficiency Per Ampere Control of Permanent-Magnet Synchronous Machines. *IEEE Transactions on Industrial Electronics*, vol. 62, no. 4, pp. 2135-2143, doi: 10.1109/TIE.2014.2354238.

Q. Guo, C. Zhang, L. Li, J. Zhang, J. Liu and T. Wang (2016). Efficiency Optimization Control of Permanent-Magnet Synchronous Machines for Electric Vehicle Traction Systems. *2016 IEEE Vehicle Power and Propulsion Conference (VPPC)*, pp. 1-5, doi: 10.1109/VPPC.2016.7791672.

J. Lee, M. Kim, H. Jeong and S. Choi (2016). Single switch ZCS resonant converter with high step-up ratio. *2016 IEEE 8th International Power Electronics and Motion Control Conference (IPEMC-ECCE Asia)*, pp. 3495-3500, doi: 10.1109/IPEMC.2016.7512856.

A. Van den Bossche, R. Stoyanov, N. Dukov, V. Valchev and A. Marinov (2016). Analytical simulation and experimental comparison of the losses in resonant DC/DC converter with Si and SiC switches. *2016 IEEE International Power Electronics and Motion Control Conference (PEMC)*, pp. 934-939, doi: 10.1109/EPEPEMC.2016.7752119.

T. Mishima, Y. Takeuchi and M. Nakaoka (2011). A new high step-up voltage ratio soft switching PWM boost DC-DC power converter with edge resonant switched capacitor modular. *Proceedings of the 2011 14th European Conference on Power Electronics and Applications*, pp. 1-10.

S. Hori and K. Matsuse (1999). Characteristics of series-resonant AC link inverter for capacitor motor drives. *IECON'99. Conference Proceedings. 25th Annual Conference of the IEEE Industrial Electronics Society (Cat. No.99CH37029)*, pp. 1386-1390 vol.3, doi: 10.1109/IECON.1999.819427.

A. N. Rahman, H. Chiu and Y. Hsieh (2018). Design of wide input voltage range high step-up DC-DC converter based on secondary-side resonant tank full bridge LLC. *2018 3rd International Conference on Intelligent Green Building and Smart Grid (IGBSG)*, pp. 1-6, doi: 10.1109/IGBSG.2018.8393557.

M. Marchesoni, L. Puglisi and A. Rebora (1995). Analysis and modelling of the auxiliary quasi-resonant DC link inverter applied to AC electric vehicle drives. *1995 Proceedings of the IEEE International Symposium on Industrial Electronics*, pp. 558-563 vol.2, doi: 10.1109/ISIE.1995.497246.

M. M. Alaee, E. Afjei and S. Ataei (2007). A New Resonant Driver for Switched Reluctance Motor. *2007 International Conference on Electrical Engineering*, pp. 1-3, doi: 10.1109/ICEE.2007.4287304.

M. M. Shahbazi, S. M. Madani and A. Ebrahimi (2009). New resonant pole inverter for battery fed brushless dc motor drive. *2009 IEEE International Electric Machines and Drives Conference*, pp. 352-356, doi: 10.1109/IEMDC.2009.5075229.

A. K. Kapoor and A. N. Tripathi (1996). A novel soft-switched PWM inverter for induction motor drives. *Proceedings of International Conference on Power Electronics, Drives and Energy Systems for Industrial Growth*, pp. 7-12 vol.1, doi: 10.1109/PEDES.1996.537274.

F. Z. Peng and D. J. Adams (2000). An auxiliary quasi-resonant tank soft-switching inverter. *Conference Record of the 2000 IEEE Industry Applications Conference. Thirty-Fifth IAS Annual Meeting and World Conference on Industrial Applications of Electrical Energy (Cat. No.00CH37129)*, pp. 2397-2403 vol.4, doi: 10.1109/IAS.2000.883159.

M. M. Peretz and S. Ben-Yaakov (2005). Analysis of the Current-Fed Push-Pull Parallel Resonant Inverter Implemented with Unidirectional Switches. *2005 IEEE 36th Power Electronics Specialists Conference*, pp. 880-884, doi: 10.1109/PESC.2005.1581731.

H. Wei, G. Zhu, I. Bartarseh and J. Vaidya (1998). Analysis, design and simulation of a resonant DC link inverter for high power, high frequency brushless DC motor. *Proceedings IEEE Southeastcon '98 'Engineering for a New Era'*, pp. 109-113, doi: 10.1109/SECON.1998.673304.

K. K. Law, K. W. E. Cheng and Y. P. B. Yeung (2005). Design and analysis of switched-capacitor-based step-up resonant converters. *IEEE Transactions on Circuits and Systems I: Regular Papers*, vol. 52, no. 5, pp. 943-948, doi: 10.1109/TCSI.2004.840482.

A. Pholsriphim, S. Nurach and W. Lenwari (2017). Half-bridge resonance inverter for induction heating using digital-controlled pulse density modulation technique. *2017 12th IEEE Conference on Industrial Electronics and Applications (ICIEA)*, pp. 1084-1086, doi: 10.1109/ICIEA.2017.8283001.

H. Kernstock and B. Plassnegger (2012). High efficiency soft switched 3-level MOSFET Inverter for an Electric Vehicle PMSM Drive. *2012 15th International Power Electronics and Motion Control Conference (EPE/PEMC)*, pp. DS1b.9-1-DS1b.9-5, doi: 10.1109/EPEPEMC.2012.6397210.

Y. Murai, H. Ishikawa and T. A. Lipo (1994). New series resonant DC link inverter for electric vehicle drives. *Proceedings of 1994 IEEE Industry Applications Society Annual Meeting*, pp. 443-447 vol.1, doi: 10.1109/IAS.1994.345446.

H. Hucheng, L. Weiguo, D. Manfeng and M. Ruiqing (2007). Novel Resonant DC Link Soft Switching Inverter for Brushless DC Motor Drive System. *EUROCON 2007 - The International Conference on "Computer as a Tool"*, pp. 1746-1751, doi: 10.1109/EURCON.2007.4400338.

O. A. Eno, D. S. Thompson and J. Coppin (2005). High power resonant topology for DC-DC converter. *2005 European Conference on Power Electronics and Applications*, pp. 7 pp.-P.7, doi: 10.1109/EPE.2005.219209.

B. A. Potter, S. A. Shirsavar and M. D. McCulloch (2003). Optimal inverter design for an induction machine using resonant frequency matching. *IEEE International Electric Machines and Drives Conference, 2003. IEMDC'03.*, pp. 1972-1977 vol.3, doi: 10.1109/IEMDC.2003.1210721.

K. Fathy *et al*. (2005). PWM/PDM dual mode controlled soft switching multi resonant high-frequency inverter. *2005 IEEE International Conference on Industrial Technology*, pp. 1450-1455, doi: 10.1109/ICIT.2005.1600863.

K. Taniguchi, S. Saegusa and T. Morizane (2005). PAM Inverter System with Soft-Switching PFC Converter suitable for PM Motor Drives. *2005 International Conference on Power Electronics and Drives Systems*, pp. 793-798, doi: 10.1109/PEDS.2005.1619793.

Duk-Bae Suh, Jong-Woo Choi and Seung-Ki Sul (1996). Voltage gradient suppression in application of voltage-fed PWM inverter to AC motor drives-resonant DC link inverter approach. *Proceedings of Applied Power Electronics Conference. APEC '96*, pp. 601-606 vol.2, doi: 10.1109/APEC.1996.500502.

B. Saha, H. W. Lee and M. Nakaoka (2006). Series Load Resonant Soft-Switched PWM and PDM High Frequency Inverter using Auxiliary Active Edge-Resonant Snubber. *2006 IEEE International Conference on Industrial Technology*, pp. 288-293, doi: 10.1109/ICIT.2006.372224.

Y. P. Benny Yeung (2004). *Resonant Switched Reluctance Motor Drive and Its Power Conditioning with Switched-Capacitor Techniques*. (Ph. D. Thesis, The Hong Kong Polytechnic University, Hong Kong).

K. Choo, I. Won, S. Hong, J. Lee and C. Won (2017). Novel DC-link voltage variation method for interior permanent magnet synchronous motor drive system with high-efficient DC-DC converter. *2017 20th International Conference on Electrical Machines and Systems (ICEMS)*, pp. 1-6, doi: 10.1109/ICEMS.2017.8056204.

J. O. Estima and A. J. Marques Cardoso (2012). Efficiency Analysis of Drive Train Topologies Applied to Electric/Hybrid Vehicles. *IEEE Transactions on Vehicular Technology*, vol. 61, no. 3, pp. 1021-1031, doi: 10.1109/TVT.2012.2186993.

F. Al-Jilani, D. Godin-Lebreux, R. Myrtil (2020). *ELE795-01: Rapport final de projet, Conception d'un convertisseur statique résonant destiné à une machine synchrone à aimant permanent*. Montreal, Canada: École de technologie Supérieure.

F. Binette, G. Huard-Desjardins, S. Lavoie (2021). *ELE795-01: Rapport final de projet, Conception du contrôle d'un convertisseur statique résonant destiné à une machine synchrone à aimant permanent*. Montreal, Canada: École de technologie Supérieure.

On Semiconductors (2021). Hyperfast Diode, 75 A, 1200 V RHRG75120 Specification. Retrieved from https://www.onsemi.com/pdf/datasheet/rhrg75120-d.pdf

H. Raee, A. Rabiei and T. Thirnger (2013). Analytical prediction of switching losses in MOSFETs for variable drain-source voltage and current applications. *2013 IEEE 8th Conference on Industrial Electronics and Applications (ICIEA)*, pp. 705-709, doi: 10.1109/ICIEA.2013.6566458.

X. Yu and P. Yeaman (2013). Temperature-related MOSFET power loss modeling and optimization for DC-DC converter. *2013 Twenty-Eighth Annual IEEE Applied Power Electronics Conference and Exposition (APEC)*, pp. 2788-2792, doi: 10.1109/APEC.2013.6520692.

IXYS (2021). X-Class HiPerFETTM Power MOSFET IXFB70N100X Specification. Retrieved from https://www.littelfuse.com/~/media/electronics/datasheets/discrete_mosfets/littelfuse_discrete_mosfets_n-channel_ultra_junction_ixfb70n100x_datasheet.pdf.pdf

On Semiconductor (2021). Field Stop II / 4 Lead NGTB40N120FL2WAG Specification. Retrieved from https://www.onsemi.com/pdf/datasheet/ngtb40n120fl2wa-d.pdf

Z. Chen, L. Yuan, Z. Zhao and X. Sun (2012). Power losses in two- and three-level three phase photovoltaic inverters equipped with IGBTs. *2012 15th International Conference on Electrical Machines and Systems (ICEMS)*, pp. 1-6.

ABB/Baldor (2021). Motor BSM33C-3177MHQ Specifications. Retrieved from https://www.baldor.com/catalog/BSM33C-3177MHQ.

TDK-Lambda (2021). 11,000W Bi-Directional DC-DC Converter EZA11K-320240 Specification. Retrieved from https://product.tdk.com/en/system/files?file=dam/doc/product/power/switching-power/bidirect-converter/catalog/eza11k_e.pdf.